

5-16-2024

# $H^1$ -conforming Finite Elements on Nonstandard Meshes

Samuel Edward Reynolds  
*Portland State University*

Follow this and additional works at: [https://pdxscholar.library.pdx.edu/open\\_access\\_etds](https://pdxscholar.library.pdx.edu/open_access_etds)



Part of the [Applied Mathematics Commons](#), and the [Mathematics Commons](#)

Let us know how access to this document benefits you.

---

## Recommended Citation

Reynolds, Samuel Edward, " $H^1$ -conforming Finite Elements on Nonstandard Meshes" (2024).  
*Dissertations and Theses*. Paper 6619.  
<https://doi.org/10.15760/etd.3751>

This Dissertation is brought to you for free and open access. It has been accepted for inclusion in Dissertations and Theses by an authorized administrator of PDXScholar. Please contact us if we can make this document more accessible: [pdxscholar@pdx.edu](mailto:pdxscholar@pdx.edu).

$H^1$ -conforming Finite Elements on Nonstandard Meshes

by

Samuel Edward Reynolds

A dissertation submitted in partial fulfillment of the  
requirements for the degree of

Doctor of Philosophy  
in  
Mathematical Sciences

Dissertation Committee:  
Jeffrey Oval, Chair  
Jay Gopalakrishnan  
Gerardo Lafferriere  
Oscar Bruno

Portland State University  
2024

## Abstract

We present a finite element method for linear elliptic partial differential equations on bounded planar domains that are meshed with cells that are permitted to be curvilinear and multiply connected. We employ Poisson spaces, as used in virtual element methods, consisting of globally continuous functions that locally satisfy a Poisson problem with polynomial data. This dissertation presents four peer-reviewed articles concerning both the theory and computation of using such spaces in the context of finite elements. In the first paper, we propose a Dirichlet-to-Neumann map for harmonic functions by way of computing the trace of a harmonic conjugate by numerically solving a second-kind integral equation; with the trace of a given harmonic function and its conjugate, we may obtain interior values and derivatives (such as the gradient). In the second paper, we establish some properties of a local Poisson space (i.e. when restricted to a single mesh cell), including its dimension, and provide a construction of a basis of this space. An interpolation operator for this space is introduced, and bounds on the interpolation error are proved and verified computationally in the lowest order case. In the third paper, we demonstrate that computations with higher-order spaces are computationally feasible by showing that both the  $H^1$  semi-inner product and the  $L^2$  inner product can be computed in the local Poisson space using only path integrals over boundary of the mesh cell, without need for any volumetric quadrature. Reducing the  $L^2$  inner product to a boundary integral involves determining an “anti-Laplacian” of a harmonic function, i.e. a bi-

harmonic function whose Laplacian is given; we provide a construction of the trace and normal derivative of such a function. In the fourth paper, we show that the  $H^1$  semi-inner product and  $L^2$  inner product can be likewise computed on mesh cells that are “punctured”, i.e. multiply connected. The primary difficulty arises due to the fact that a given harmonic function is not guaranteed to have a harmonic conjugate, but can be corrected for by introducing logarithmic singularities centered at chosen points in the holes. In addition to these four papers, we also provide a brief update on ongoing extensions of this work, including a full implementation of the finite element method and application to computing terms that arise in problems with advection terms and generalized diffusion operators.

## Dedication

For my nieces and nephews:

Oceana, Ariana, Easton, Mason, & Briella

## Acknowledgements

I am deeply grateful for the many years of generous support, guidance, and encouragement of my advisor, Jeffrey O'vall. Special thanks to Jay Gopalakrishnan for his patience in teaching me the fundamentals of finite element analysis, and for sharing his knowledge and expertise on many topics. I would like to sincerely thank Gerardo Lafferriere, who instructed me in real and functional analysis, and helped foster an environment of growth in his time as the Department Chair. I am also thankful to Oscar Bruno, who gave feedback on an early version of part of this work and subsequently agreed to serve on my dissertation committee. I learned many useful technical skills that made the implementation of this work possible from my internship mentors, Richard Tran Mills at Argonne National Laboratory and Julian Andrej at Lawrence Livermore National Laboratory. I had the pleasure of collaborating with Akash Anand and Steffen Weißer on a portion of this work, and I am grateful for their contributions. Lastly, I would like to thank the National Science Foundation for partially funding the research presented in this dissertation through the following NSF grants:

- DMS-1414365
- DMS-1522471
- DMS-1624776
- DMS-2012285
- RTG grant DMS-2136228

## Contents

<b>Abstract</b> . . . . .	<b>i</b>
<b>Dedication</b> . . . . .	<b>iii</b>
<b>Acknowledgements</b> . . . . .	<b>iv</b>
<b>List of Figures</b> . . . . .	<b>vii</b>
<b>List of Tables</b> . . . . .	<b>ix</b>
<b>1. Introduction</b> . . . . .	<b>1</b>
1.1. Preliminaries . . . . .	1
1.2. Structure of This Dissertation . . . . .	3
<b>2. A High-order Method for Evaluating Derivatives of Harmonic Functions in Planar Domains</b> . . . . .	<b>6</b>
2.1. Introduction . . . . .	7
2.2. Smooth Boundary and Data . . . . .	10
2.3. Piecewise Smooth Boundary and Data . . . . .	17
2.3.1. Domains with a Single Corner . . . . .	19
2.3.2. Domains with Multiple Corners . . . . .	27
2.4. Conclusion . . . . .	36
2.5. References . . . . .	37
<b>3. Trefftz Finite Elements on Curvilinear Polygons</b> . . . . .	<b>39</b>
3.1. Introduction . . . . .	41
3.2. Local and Global Spaces . . . . .	45
3.3. Interpolation . . . . .	53
3.4. Computing with Curved Trefftz Finite Elements . . . . .	63
3.5. Numerical Experiments . . . . .	67
3.6. Conclusions . . . . .	79
3.7. References . . . . .	81
<b>4. Quadrature for Implicitly-defined Finite Element Functions on Curvilinear Polygons</b> . . . . .	<b>88</b>

4.1.	Introduction . . . . .	89
4.2.	Preliminary Results . . . . .	95
4.3.	Reducing Volumetric Integrals to Boundary Integrals . . . . .	100
4.4.	Numerical Illustrations . . . . .	104
4.5.	Additional Details . . . . .	117
4.6.	Concluding Remarks . . . . .	123
4.7.	References . . . . .	124
<b>5.</b>	<b>Evaluation of Inner Products of Implicitly-defined Finite Element Functions on Multiply Connected Planar Mesh Cells . . . . .</b>	<b>128</b>
5.1.	Introduction . . . . .	130
5.2.	Simply Connected Mesh Cells . . . . .	133
5.2.1.	The $H^1$ Semi-inner Product . . . . .	133
5.2.2.	A Dirichlet-to-Neumann Map . . . . .	135
5.2.3.	The $L^2$ Inner Product . . . . .	136
5.2.4.	Anti-Laplacians of Harmonic Functions . . . . .	137
5.2.5.	Piecewise Smooth Boundaries . . . . .	140
5.2.6.	Summary of Simply Connected Case . . . . .	142
5.3.	Punctured Cells . . . . .	143
5.3.1.	A Dirichlet-to-Neumann Map for Punctured Cells . . . . .	145
5.3.2.	Anti-Laplacians of Harmonic Functions on Punctured Cells . . . . .	147
5.3.3.	Summary of Multiply Connected Case . . . . .	152
5.4.	Numerical Examples . . . . .	154
5.5.	Conclusion . . . . .	160
5.6.	References . . . . .	162
<b>6.</b>	<b>Conclusion . . . . .</b>	<b>166</b>
6.1.	Summary . . . . .	166
6.2.	Future Work . . . . .	167
6.2.1.	Comparison Studies . . . . .	167
6.2.2.	$hp$ -Refinement . . . . .	167
6.2.3.	Applications to Time-dependent Problems . . . . .	167
6.2.4.	$H(\text{div})$ - and $H(\text{curl})$ -conforming Spaces . . . . .	168
6.2.5.	3-dimensional Domains . . . . .	168
	<b>Appendix A. Extensions . . . . .</b>	<b>169</b>
A.1.	Advection Terms . . . . .	169
A.2.	Generalized Diffusion Operators . . . . .	170
	<b>Appendix B. Implementation . . . . .</b>	<b>173</b>

## List of Figures

2.1.	The Bean Domain (left) and the Five-Petal Domain. . . . .	14
2.2.	Five-Petal: The errors, $V(t_i) - \tilde{V}(t_i)$ , in approximating the Dirichlet trace of $v$ for $n = 32$ (left) and $n = 64$ (right). . . . .	17
2.3.	The Teardrop (left) and Boomerang domains. Below each domain are parametric plots of $u, v$ and $\partial u/\partial \mathbf{t}$ , $\partial v/\partial \mathbf{t}$ for the conjugate pair from (2.24). For the Teardrop, $\alpha = 3/2$ . For the Boomerang, $\alpha = 2/3$ . . . . .	20
2.4.	Plots of $V$ and $W$ , and $V'$ and $W'$ , for the Boomerang, with $\alpha = 2/3$ , $p = 7$ and $v = r^\alpha \sin(\alpha\theta)$ . . . . .	25
2.5.	L-shaped Polygon: The hexagonal domain $\Omega$ used in Example 2.3.3. . . . .	27
2.6.	L-shaped Polygon: Contour plots of $\phi_k$ (left column) and $ \nabla\phi_k $ (center column) for piecewise linear data considered in Example 2.3.4. The normal derivative $\partial\phi_k/\partial\mathbf{n}$ is plotted in the right column. Rows correspond to $k = 0, 1, 2, 3$ , respectively. . . . .	34
3.1.	Shuriken (quadrilateral), Half-Washer (hexagon), Two-Edge Circle (bigon). . . . .	47
3.2.	At left, the edge $e$ and associated triangle (dashed) for Example 3.2.6. At right, plots of a basis for $\mathbb{P}_3(e)$ with respect to a parametrization, $x = x(t)$ , of $e$ . . . . .	51
3.3.	The Shuriken, Pegboard and Jigsaw meshes for $r = 16$ , as well as the computed finite element solution $\hat{u} \in V_1(\mathcal{T})$ on these meshes. . . . .	69
3.4.	Reference elements (top) for the Perturbed Triangle meshes (bottom), shown with $r = 8$ , for $a = 1/4, 1, 4, 16$ from left to right. The dashed lines are straight ( $a = \infty$ ). . . . .	71
3.5.	Log-Log plots of $ u - \hat{u} _{H^1(\Omega)}$ (left column) and $\kappa_2(A)$ (right column) with respect to the mesh parameter $r$ (horizontal axis), for Type 1 (dashed) and Type 2 (solid) elements on Perturbed Triangle mesh families $a = 1/4, 1, 4, 16$ (from top to bottom). . . . .	73
3.6.	The L-shaped domain together with the meshes and contour plots of the computed solutions $\hat{u} \in \tilde{V}_1(\mathcal{T})$ corresponding to $r = 4$ (left) and $r = 8$ . . . . .	74

3.7.	Sub-triangulations of the L-shaped element $K_L$ that are geometrically graded toward the origin, corresponding to $r = 4$ (left) and $r = 8$ . These sub-triangulations are used merely as part of the argument to justify the interpolation error estimate, and are not used in the computation of $\hat{u}$ . . . . .	77
4.1.	Top panel: a “background” mesh of squares cut by a curved interface, and two curved cells generated by this cutting, the second of which obtained by merging two smaller cells. Bottom panel: A domain with multiple small circular “inclusions” with a fitted mesh, and the two resultant cell types, the second of which is regarded as having two edges.	91
4.2.	Top Left: The puzzle piece mesh cell considered in Example 4.4.4 (and Example 4.4.1). Top Right: The fictitious point $z$ and equilateral triangle used to define $\mathbb{P}_1(e)$ for the circular arc of the right tab; this construction was used to provide boundary values in the for the vertex functions $v_4$ and $v_5$ , and the edge function $u_1$ . Bottom Panel: Contour plots of $v_3, v_4, u_1 \in V_1^{\partial K}(K) = V_1(K)$ , left to right. . . . .	113
4.3.	Top: Two examples of a shuriken $K_a$ , as considered in Example 4.4.5. On the left, $a = 0.25$ , and on the right, $a = 0.45$ . Bottom: Contour plots of $v_0, u_0$ , and $w_0$ , left to right, for $a = 0.25$ . . . . .	116
5.1.	Left: A curvilinear mesh of a square domain featuring a curvilinear interface. Center: A curvilinear mesh of a square domain with circular punctures. Right: A few of the cells found in these meshes. . . . .	132
5.2.	Punctured cells used for numerical experiments in Section 5.4. . . . .	154
5.3.	Interior values of $v$ and $\nabla v$ in Example 5.4.3. In the left column, we have the computed values of $v$ on top, and the base 10 logarithm of the absolute error on bottom. This setup is repeated in the middle and right columns for the components of the gradient. . . . .	160

## List of Tables

2.1. Bean: Errors in approximating the normal derivative of $u$ on $\partial\Omega$ , and its values and first and second partial derivatives at two points, $P_1 = (4, 1/2)$ and $P_2 = (3, 9/4)$ , in $\Omega$ . Below this are the exact values of $u$ and its first and second partial derivatives at these points. . . . .	16
2.2. Five-Petal: Errors in approximating the normal derivative of $u$ on $\partial\Omega$ , and its values and first and second partial derivatives at two points, $P_1 = (2, 1/2)$ and $P_2 = (7/2, 1)$ , in $\Omega$ . Below this are the exact values of $u$ and its first and second partial derivatives at these points. . . . .	18
2.3. Errors in the quadrature (2.29) for $\int_{-1}^1 F(t) dt$ for some singular and “nearly singular” $F$ . For the final, “nearly singular”, integrand, Gauss-Legendre quadrature errors are given for comparison. . . . .	22
2.4. Teardrop: Errors in approximating $W'(\tau)$ on $\partial\Omega$ , and the values of $u$ and its first and second partial derivatives at two points, $P_1 = (1/4, -1/4)$ and $P_2 = (3/2, 1/2)$ , in $\Omega$ . Below this are the exact values of $u$ and its first and second partial derivatives at these points. . . . .	26
2.5. Boomerang: Errors in approximating $W'(\tau)$ on $\partial\Omega$ , and the values of $u$ and its first and second partial derivatives at two points, $P_1 = (0, 1/5)$ and $P_2 = (1/5, -2/5)$ , in $\Omega$ . Below this are the exact values of $u$ and its first and second partial derivatives at these points. . . . .	28
2.6. L-shaped Polygon: Errors in approximating $W'(\tau)$ on $\partial\Omega$ , and the values of $u$ and its first and second partial derivatives at two points, $P_1 = (1/4, 9/10)$ and $P_2 = (-1/20, 1/20)$ , in $\Omega$ . Below this are the exact values of $u$ and its first and second partial derivatives at these points. . . . .	30
2.7. L-shaped Polygon: Absolute errors in computing the function values, gradients and Hessians for the L-shaped domain at two points using an hp-adaptive finite element method. . . . .	32
2.8. L-shaped Polygon: Errors in computing $I_k$ , $k = 0, 1, 2, 3$ . . . . .	35
3.1. Discretization errors, $ u - \widehat{u} _1$ , and error ratios for the Shuriken, Peg-board, and Jigsaw meshes. For the Shuriken meshes, both Type 1 and Type 2 elements are used. For the other meshes, only Type 2 elements are used. . . . .	70

3.2.	Discretization errors, $ u - \widehat{u} _{H^1(\Omega)}$ , and error ratios for the sequence of meshes having one L-shaped cell of fixed size and increasingly fine square cells. Also included are the spectral condition numbers of the global (sparse) stiffness matrix $A$ and the small (dense) stiffness matrix $A_L$ associated with the basis functions on the L-shaped cell. . . . .	78
4.1.	An enumeration of multiindices for $ \alpha  \leq 6$ , together with the indices and values of the non-zero coefficients of $P_\alpha$ from Proposition 4.2.1. . . . .	96
4.2.	Absolute errors in the approximation of $ K $ via (4.15) in Example 4.4.1, for which $\Delta v = \Delta w = 0$ in $K$ and $v = w = 1$ on $\partial K$ . . . . .	105
4.3.	Absolute errors for computing the $L^2$ inner product $\int_K vw \, dx$ and the $H^1$ semi-inner product $\int_K \nabla v \cdot \nabla w \, dx$ on the unit square, as described in Example 4.4.2. Following the notation in that example, $v_j$ denotes the “vertex” functions, $w_j$ denotes the “edge” functions, and $\tilde{w}$ denotes the “bubble” function. . . . .	107
4.4.	Absolute errors for computing the $L^2$ inner product $\int_K v_\alpha v_\beta \, dx$ and the $H^1$ semi-inner product $\int_K \nabla v_\alpha \cdot \nabla v_\beta \, dx$ on the unit square, as described in Example 4.4.2. . . . .	109
4.5.	Absolute errors for the Pac-Man domain considered in Example 4.4.3, using $v_1 = r^\mu \sin \mu\theta$ and $v_2 = r^\nu \sin \nu\theta$ and $v_3 = (1 - r^2)r^2 \sin(\theta) \sin(\theta - \pi/\mu)$ , with $\mu = 4/7$ and $\nu = 2/7$ . . . . .	111
4.6.	Computed values of the $L^2$ inner product $\int_K vw \, dx$ and the $H^1$ semi-inner product $\int_K \nabla v \cdot \nabla w \, dx$ on the Puzzle Piece, as described in Example 4.4.4. Following the notation in that example, $v_j$ denotes the linear vertex functions, $u_j$ denotes the linear edge functions, $w_j$ denotes the quadratic edge functions, and $\tilde{w}$ denotes the bubble function. . . . .	115
4.7.	Computed values of the $L^2$ inner product $\int_{K_a} vw \, dx$ and the $H^1$ semi-inner product $\int_{K_a} \nabla v \cdot \nabla w \, dx$ on two shuriken domains $K_a$ , with $a = 0.25$ and $a = 0.45$ , as described in Example 4.4.5. As before, $v_j$ denotes the linear vertex functions, $u_j$ denotes the linear edge functions, $w_j$ denotes the quadratic edge functions, and $\tilde{w}$ denotes the bubble function. . . . .	118
4.8.	An enumeration of multiindices for $7 \leq  \alpha  \leq 10$ , together with the indices and values of the non-zero coefficients of $P_\alpha$ from Proposition 4.2.1. . . . .	122
5.1.	Errors in intermediate quantities for $v$ on the square with a circular hole in Example 5.4.1: the logarithmic coefficient $a_1$ , the trace of the harmonic conjugate $\widehat{\psi}$ , the weighted normal derivative $wnd$ , and the trace of the anit-Laplacian $\Phi$ . The latter three are given in the $L^2$ boundary norm. . . . .	155
5.2.	Absolute errors in the $H^1$ semi-inner product and $L^2$ inner product for the Punctured Square (Example 5.4.1), Pac-Man (Example 5.4.2), and Ghost (Example 5.4.3). . . . .	158

## 1. Introduction

### 1.1. Preliminaries

Consider the weak problem of determining  $u \in H_0^1(\Omega)$  satisfying

$$\int_{\Omega} \nabla u \cdot A \nabla v \, dx + \int_{\Omega} (b \cdot \nabla u) v \, dx + \int_{\Omega} c u v \, dx = \int_{\Omega} f v \, dx \quad (1.1)$$

for all  $v \in H_0^1(\Omega)$  with  $\Omega \subset \mathbb{R}^2$  an open, bounded domain with a piecewise  $C^2$  boundary without slits or cusps,  $A$  a symmetric, positive definite  $2 \times 2$  piecewise constant matrix,  $b$  a piecewise constant vector,  $c$  a piecewise constant scalar, and  $f$  a piecewise polynomial. Choosing an appropriate finite-dimensional subspace  $V_h \subset H_0^1(\Omega)$ , and taking  $\{v_i : 1 \leq i \leq n\}$  to be a basis of  $V_h$ , we seek the finite element solution  $u \approx \tilde{u} = \sum_j \alpha_j v_j$  satisfying

$$\sum_j \alpha_j \int_{\Omega} \nabla v_j \cdot A \nabla v_i \, dx + \int_{\Omega} (b \cdot \nabla v_j) v_i \, dx + \int_{\Omega} c v_j v_i \, dx = \int_{\Omega} f v_i \, dx, \quad (1.2)$$

for all  $1 \leq i \leq n$ . The choice of the finite element space  $V_h$  determines the quality of the approximate solution  $\hat{u} \approx u$ .

A conventional choice is the Lagrange finite element space, consisting of continuous piecewise polynomials defined in terms of a tetrahedral (in this case, triangular) mesh of  $\Omega$ . Due to the geometry of  $\Omega$ , a triangular mesh may be a suboptimal choice, especially if  $\Omega$  has a curved boundary or a curved internal interface along which some of the parameters  $A, b, c, f$  have a discontinuity. A conventional approach would refine the mesh in the region near the curvature in order for the mesh boundary to

approximate the curved boundary  $\partial\Omega$  as a collection of straight line segments. Such refinement can dramatically increase the dimension of the finite element space, and therefore nonlinearly increase the computational cost in solving the finite element system (1.2).

By a *curvilinear mesh*  $\mathcal{T}$  we mean a collection of connected open subdomains  $K \subset \Omega$  with the cell boundary  $\partial K$  being  $C^2$  smooth without slits or cusps, such that  $K_i \cap K_j = \emptyset$  and  $\bigcup_{K \in \mathcal{T}} \overline{K} = \overline{\Omega}$ . Most of our discussion will additionally assume that  $K$  is simply connected, but as we will see in Chapter 5 this assumption can be relaxed to allow multiply connected mesh cells. Clearly, greater flexibility of curvilinear meshes allows us to fully capture domains with a curved boundary or interface in a way that a polygonal mesh can only approximate, and potentially with much less refinement and therefore with a more computationally attractive linear system size.

A significant hurdle to using a curvilinear mesh in practice is that using a Lagrange-like space of polynomials will not in general be  $H^1$ -conforming, since imposing continuity of distinct first degree polynomials across a curved facet cannot succeed. In recent years, the virtual element method (VEM) has surged in popularity in part because it solves this problem by using a finite element space not of piecewise polynomials but a larger space of functions that are locally defined as solutions to Poisson problems with polynomial data. Specifically, for a mesh cell  $K$ , we take  $V_p(K)$  to denote the *local Poisson space*, a subspace of  $H^1(K)$  whose elements have a Laplacian that is a polynomial of degree at most  $p - 2$  and have a Dirichlet trace on the cell boundary  $\partial K$  that is “piecewise polynomial” in a sense that will be made precise later. It is already apparent that  $V_p(K)$  contains the space of polynomials of degree at most  $p$ , but we will see later on that the space is considerably richer and has approximation properties well-suited for many problems.

The *global Poisson space*  $V_p(\mathcal{T})$  consists of the continuous functions in  $H^1(\Omega)$  whose restriction to any mesh cell  $K$  lies in  $V_p(K)$ . The final challenge to implementing a finite element method with these functions then is to compute the volumetric integrals

$$\int_{\Omega} \nabla v \cdot A \nabla w \, dx \, , \tag{1.3}$$

$$\int_{\Omega} (b \cdot \nabla v) w \, dx \, , \tag{1.4}$$

$$\int_{\Omega} c v w \, dx \tag{1.5}$$

for  $v, w \in V_p(\mathcal{T})$ , so that the global matrix and load vector in (1.2) can be computed and the resulting linear system can be solved using existing methods. Note that  $\int_{\Omega} f v \, dx$  is of the form (1.5) since  $f \in V_q(\mathcal{T})$  for some  $q \in \mathbb{N}$ .

The method proposed in this work departs from the VEM framework insofar that it is *nonvirtual*, i.e. we work with the implicitly-defined functions in  $V_p(\mathcal{T})$  directly, whereas VEMs, as the name suggests, deal with these functions “virtually” by projecting them onto polynomial spaces and correcting for this sin by introducing so-called stabilization terms.

## 1.2. Structure of This Dissertation

The body of this dissertation consists of four peer-reviewed papers, each presented in a separate chapter.

In Chapter 2, we propose a Dirichlet-to-Neumann map for harmonic functions by way of numerically solving a second-kind integral equation to obtain the trace of a harmonic conjugate, whose tangential derivative is the normal derivative of the given

harmonic function. Special attention is given to the case when the boundary has corners, which presents a significant numerical challenge. With the normal derivative in hand, we are able to compute the  $H^1$  semi-inner product

$$\int_K \nabla \phi \cdot \nabla \psi \, dx = \int_K \phi \frac{\partial \psi}{\partial n} \, ds$$

of two harmonic functions  $\phi, \psi$ . Furthermore, the interior values and derivatives of a harmonic function can be obtained with Cauchy’s integral formula.

Chapter 3 presents the general framework of a FEM method using Poisson spaces. We provide a method of constructing a basis of such spaces, determine their dimension, and prove some preliminary results on their approximation power. We also present some numerical experiments for the global problem with  $A = I$ ,  $b = 0$ ,  $c = 0$ , and  $f = 1$ , using the results of the previous paper to compute  $H^1$  semi-inner products on the lowest order case  $p = 1$ , and verify that convergence rates are consistent with that predicted in theory.

The computation of  $H^1$  semi-inner products and  $L^2$  inner products for the arbitrary order  $p \geq 1$  case is considered in Chapter 4. We find that both types of volumetric integral can be reduced to boundary integrals along the boundary of the mesh cell. In the case of the  $L^2$  inner product, we construct an “anti-Laplacian”  $\Phi$  of a harmonic function  $\phi$ , so that  $\Delta \Phi = \phi$ , and thereby compute

$$\int_K \phi \psi \, dx = \int_K \psi \Delta \Phi \, dx = \int_{\partial K} \left( \psi \frac{\partial \Phi}{\partial n} - \Phi \frac{\partial \psi}{\partial n} \right) \, ds$$

by applying Green’s identities.

The techniques discussed thus far for computing  $H^1$  and  $L^2$  (semi-)inner products fail on mesh cells that are “punctured,” i.e. multiply connected, because a given harmonic function can fail to have a harmonic conjugate in such a case—for instance,  $\ln|x|$  does not have a harmonic conjugate on an annulus centered at the origin. In

Chapter 4, we introduce a modification of the previous work to incorporate punctured mesh cells by introducing logarithmic singularities centered at the holes of the cell.

We address the case of  $A, b$  being nontrivial in Appendix A, but the majority of our discussion will concern the case with  $b = 0$  and  $A = a I$  being a scalar multiple of the identity, in which case (1.2) reduces to

$$\sum_j \alpha_j \int_{\Omega} a \nabla v_j \cdot \nabla v_i \, dx + \int_{\Omega} c v_j v_i \, dx = \int_{\Omega} f v_i \, dx, \quad 1 \leq i \leq n. \quad (1.6)$$

In Appendix B, we provide some remarks on the implementation of our method.

## 2. A High-order Method for Evaluating Derivatives of Harmonic Functions in Planar Domains

### Full citation information:

Jeffrey S. Ovall and Samuel E. Reynolds. A high-order method for evaluating derivatives of harmonic functions in planar domains. *SIAM Journal on Scientific Computing*, 40(3):A1915–A1935, 2018.

**Authors:** *Jeffrey S. Ovall*<sup>1</sup> and *Samuel E. Reynolds*<sup>1</sup>

### Author contribution statement:

- Jeffrey S. Ovall: developed algorithms, drafted the paper
- Samuel E. Reynolds: implemented numerical examples, investigation, review and editing

**DOI:** 10.1137/17M1141825

### Hyperlink to the publication in PDXScholar:

<https://archives.pdx.edu/ds/psu/26690>

**Additional information:** Ovall was partially supported by the NSF Grant DMS-1414365.

---

<sup>1</sup>Fariborz Maseeh Department of Mathematics and Statistics, Portland State University, Portland, OR 97201

## Abstract

We propose a high-order integral equation based method for evaluating interior and boundary derivatives of harmonic functions that are specified by their Dirichlet data in planar domains. The tangential derivative of the given Dirichlet data is used to form a complementary Neumann problem, whose solution is a harmonic conjugate of the function whose derivatives we seek. We use a high-order Nyström method to compute the Dirichlet trace of the harmonic conjugate on the domain boundary. The tangential derivative of this harmonic conjugate, effected via an FFT, is the normal derivative of the original function. Because the original and conjugate harmonic functions are the real and imaginary parts of a complex analytic function, we are able to use Cauchy's integral formulas to compute function values and derivatives inside the domain. Several numerical experiments, on smooth domains and domains with corners, illustrate the rapid convergence and high accuracy of the proposed approach.

### 2.1. Introduction

Let  $\Omega \subset \mathbb{R}^2$  be a bounded, open and simply connected domain, whose boundary  $\partial\Omega$  is either smooth or consists of a finite number of smooth closed arcs that intersect only at corners having interior angles strictly between 0 and  $2\pi$  (no slits or cusps). Given data  $f \in C(\partial\Omega)$  that is also smooth or piecewise smooth, we consider the Dirichlet problem

$$\Delta u = 0 \text{ in } \Omega \quad , \quad u = f \text{ on } \partial\Omega . \tag{2.1}$$

This paper concerns the efficient and accurate approximation of derivatives of  $u$  at points in  $\Omega$ , as well as the normal derivative  $\partial u / \partial \mathbf{n}$  at points on  $\partial\Omega$  (the Dirichlet-to-Neumann map  $f \mapsto \partial u / \partial \mathbf{n}$ ), by doing computations only on  $\partial\Omega$ . Throughout,  $\mathbf{n}$

and  $\mathbf{t}$  (where they are defined) are, respectively, the outward unit normal vector and the unit tangent vector in the counter-clockwise direction on  $\partial\Omega$ .

A motivation for developing an efficient and high-order solver for (2.1) having these features comes from Boundary Element-Based Finite Element Methods (BEM-FEM) (cf. [6, 9, 10, 17, 18, 21–23]), an approach to solving boundary value problems on fairly general polygonal or polyhedral partitions (meshes) of the given domain. BEM-FEM employs local spaces of functions that are defined implicitly on each mesh cell in terms of boundary value problems—typically Poisson problems having polynomial righthand side and Dirichlet data, which can be reduced to computing harmonic functions with prescribed (polynomial) Dirichlet data. Functions in these local spaces, together with their interior derivatives (at least gradients) and their boundary normal derivatives, are evaluated in the formation of the associated finite element linear systems. We propose an integral equation based approach that efficiently provides high-quality approximations of each of these quantities of interest, also allowing for more general cell shapes and boundary conditions in a natural way.

Two key ingredients of the proposed approach are Cauchy’s integral formulas and the notion of harmonic conjugates. Recall that functions  $u, v$  are called harmonic conjugates in  $\Omega$  when  $\Delta u = \Delta v = 0$  in  $\Omega$ , and they satisfy the Cauchy-Riemann equations

$$\nabla u = R\nabla v \text{ in } \Omega, \text{ where } R = \begin{pmatrix} 0 & 1 \\ -1 & 0 \end{pmatrix}. \quad (2.2)$$

In other words, the gradients of  $u$  and  $v$  are orthogonal in  $\Omega$ , with  $\nabla u$  being a clockwise rotation of  $\nabla v$  by  $\pi/2$ . Given  $u$  that is harmonic in  $\Omega$ , it is guaranteed a family of harmonic conjugates that only differ by additive constants. We identify  $\Omega$  with a subset of  $\mathbb{C}$  in the natural way via  $z = x_1 + \mathbf{i}x_2$  for  $x = (x_1, x_2) \in \Omega$ . Given a harmonic conjugate  $v$  of  $u$ , the function  $w(z) = u(x) + \mathbf{i}v(x)$  is analytic in  $\Omega$ , and we

have the Cauchy integral formulas

$$w^{(k)}(z_0) = \frac{k!}{2\pi i} \int_{\partial\Omega} \frac{w(z)}{(z - z_0)^{k+1}} dz . \quad (2.3)$$

From (2.3) we can extract values and derivatives of  $u$  (and  $v$ ) at  $x_0 = (x_{0,1}, x_{0,2})$  by looking at the real and imaginary parts of this integral. For example,

$$w'(z_0) = u_{x_1}(x_0) - iu_{x_2}(x_0) = v_{x_2}(x_0) + iv_{x_1}(x_0) , \quad (2.4)$$

$$w''(z_0) = u_{x_1x_1}(x_0) - iu_{x_1x_2}(x_0) = v_{x_1x_2}(x_0) + iv_{x_1x_1}(x_0) . \quad (2.5)$$

The remaining second partials of  $u$  and  $v$  are clear from the fact that they are harmonic.

The orthogonality of the gradients of  $u$  and  $v$  imply that

$$\frac{\partial u}{\partial \mathbf{n}} = \frac{\partial v}{\partial \mathbf{t}} \quad , \quad \frac{\partial v}{\partial \mathbf{n}} = -\frac{\partial u}{\partial \mathbf{t}} = -\frac{\partial f}{\partial \mathbf{t}} \quad \text{on } \partial\Omega . \quad (2.6)$$

Using the latter of these, a specific harmonic conjugate of  $u$  is given as the solution of a complementary Neumann problem for (2.1),

$$\Delta v = 0 \text{ in } \Omega \quad , \quad \frac{\partial v}{\partial \mathbf{n}} = g = -\frac{\partial f}{\partial \mathbf{t}} \text{ on } \partial\Omega \quad , \quad \int_{\partial\Omega} v dS = 0 . \quad (2.7)$$

The final condition is a convenient way of selecting a specific harmonic conjugate. The proposed strategy for computing  $\partial u/\partial \mathbf{n}$  on  $\partial\Omega$ , and derivatives of  $u$  in  $\Omega$ , may be summarized as follows:

- (a) Compute the solution of (2.7) on  $\partial\Omega$  (a Neumann-to-Dirichlet map  $g \mapsto v$ ).

This is done in the present work by solving a second-kind integral equation via a Nyström method.

- (b) Use  $\partial v/\partial \mathbf{t}$  to compute  $\partial u/\partial \mathbf{n}$  on  $\partial\Omega$ .

- (c) Use (2.3) to compute derivatives of  $u$  in  $\Omega$ .

Some of the key computational tools are quadratures based on the trapezoid rule, and the Fast Fourier Transform.

The combination of harmonic conjugates with Cauchy's integral formulas and high-order numerical methods for integral equations provides a straight-forward algorithm for computing function values and derivatives of harmonic functions that only requires computations on the boundary of the domain. We are aware of no other method that yields high-resolution approximations of all these quantities of interest in such a unified way. In Section 2.2 we describe the approach outlined above in the case of smooth boundaries and data, and numerically demonstrate the high-order nature of the algorithm. In Section 2.3, we do the same in the case of piecewise smooth boundaries and data, highlighting the challenges when corners are present, and how we deal with them.

## 2.2. Smooth Boundary and Data

We assume here that  $\partial\Omega$  and  $f$  are smooth (at least  $C^2$ ). A direct application of Green's Theorem shows that the solution of (2.7) satisfies

$$v(x) = \int_{\partial\Omega} \Phi(x, y)g(y) dS(y) - \int_{\partial\Omega} \frac{\partial\Phi(x, y)}{\partial\mathbf{n}(y)} v(y) dS(y) \text{ for } x \in \Omega , \quad (2.8)$$

where  $\Phi(x, y) = -(2\pi)^{-1} \ln |x - y|$  is the fundamental solution of the Laplacian. From (2.8), we obtain the following second-kind integral equation for the Dirichlet trace of  $v$ ,

$$\frac{v(x)}{2} + \int_{\partial\Omega} \frac{\partial\Phi(x, y)}{\partial\mathbf{n}(y)} v(y) dS(y) = \int_{\partial\Omega} \Phi(x, y)g(y) dS(y) \text{ for } x \in \partial\Omega . \quad (2.9)$$

The operator on the left of (2.9) has a one-dimensional kernel, consisting of the constant functions, so we use the fact that  $\int_{\partial\Omega} v dS = 0$  to obtain a well-posed problem,

$$\frac{v(x)}{2} + \int_{\partial\Omega} \left( \frac{\partial\Phi(x, y)}{\partial\mathbf{n}(y)} + 1 \right) v(y) dS(y) = \int_{\partial\Omega} \Phi(x, y)g(y) dS(y) \text{ for } x \in \partial\Omega . \quad (2.10)$$

As proposed, we solve (2.10) to obtain  $v$  on  $\partial\Omega$ . Note that

$$\begin{aligned} \Phi(x, y) &= -(4\pi)^{-1} \ln|x - y|^2 \quad , \\ \frac{\partial\Phi(x, y)}{\partial\mathbf{n}(y)} &= \frac{(x - y) \cdot \mathbf{n}(y)}{2\pi|x - y|^2} = \frac{(x - y) \cdot (R\mathbf{t}(y))}{2\pi|x - y|^2} . \end{aligned} \quad (2.11)$$

We parametrize (2.10) as follows. Let  $x = x(t) : [0, 2\pi] \rightarrow \partial\Omega$  be a smooth (at least  $C^2$ ) and  $2\pi$ -periodic parametrization of  $\partial\Omega$  that traverses the boundary counter-clockwise, such that  $|x'(t)| \geq \sigma$  for some  $\sigma > 0$ . Take  $V(t) = v(x(t))$ ,  $G(t) = g(x(t))|x'(t)|$ . Since  $g = -\partial f/\partial\mathbf{t}$ , it holds that  $G(t) = -F'(t)$ , where  $F(t) = f(x(t))$ . The parametrized form of (2.10) is

$$\begin{aligned} \frac{V(t)}{2} + \int_0^{2\pi} K(t, s)V(s) ds \\ = \int_0^{2\pi} L_1(t, s)G(s) ds + \int_0^{2\pi} L_2(t, s)G(s) ds \text{ for } t \in [0, 2\pi) , \end{aligned} \quad (2.12)$$

where the integral kernels are given by

$$K(t, s) = \frac{(x(t) - x(s)) \cdot (Rx'(s))}{2\pi|x(t) - x(s)|^2} + |x'(s)| , \quad (2.13)$$

$$L_1(t, s) = -\frac{1}{4\pi} \ln\left( \frac{|x(t) - x(s)|^2}{4\sin^2((t - s)/2)} \right) , \quad (2.14)$$

$$L_2(t, s) = -\frac{1}{4\pi} \ln(4\sin^2((t - s)/2)) . \quad (2.15)$$

Simple Taylor series arguments show that the diagonal entries of  $K$  and  $L_1$  are

$$K(t, t) = \frac{x''(t) \cdot (Rx'(t))}{4\pi|x'(t)|^2} + |x'(t)| \quad , \quad L_1(t, t) = -\frac{1}{4\pi} \ln|x'(t)|^2 , \quad (2.16)$$

so it is not difficult to see that, for any fixed  $t$ , both  $K(t, s)$  and  $L_1(t, s)$  are smooth

(at least  $C^2$ ) and  $2\pi$ -periodic. It is clear that  $L_2(t, s)$  is singular, but its singularity is integrable and of a very particular type that is independent of the parametrization. The splitting of the kernel on the righthand side of (2.12) as a sum allows us to isolate the periodic logarithmic singularity,  $L_2$ , and treat it by suitable means as described below.

Nyström discretizations (cf. [12, 15, 16]) of (2.12) involve replacing the integrals with suitable quadratures, and then sampling the corresponding equations at the quadrature points to obtain a square system. The integrals involving  $K$  and  $L_1$  will be treated using the uniform trapezoid rule, which is of high order for (very) smooth periodic functions. Fixing  $n$ , and taking  $t_j = \pi j/n$  for  $0 \leq j \leq 2n$ ,

$$\begin{aligned} \int_0^{2\pi} K(t, s)V(s) ds &\approx \frac{\pi}{n} \sum_{j=0}^{2n-1} K(t, t_j)V(t_j) \\ \int_0^{2\pi} L_1(t, s)G(s) ds &\approx \frac{\pi}{n} \sum_{j=0}^{2n-1} L_1(t, t_j)G(t_j) . \end{aligned}$$

Following Martensen [14] and Kussmaul [13] (see also [12]), we use a quadrature for the integral involving  $L_2$  that exploits the specific nature of the singularity,

$$\int_0^{2\pi} L_2(t, s)G(s) ds \approx \sum_{j=0}^{2n-1} \omega_j(t)G(t_j) \quad , \quad \omega_j(t) = \frac{1}{2n} \sum_{m=1}^n \frac{\cos(m(t-t_j))}{m} . \quad (2.17)$$

This quadrature can be derived, for example, by integrating the Fourier series of  $G(s)$  term-by-term against  $-(4\pi)^{-1} \ln(4 \sin^2((t-s)/2))$ , truncating the resulting series at term  $n$ , and using the trapezoid rule on  $2n$  subintervals to approximate each of the Fourier coefficients in the finite sum. Key to this derivation is the fact that (cf. [8]),

$$-\frac{1}{2\pi} \int_0^{2\pi} \ln(4 \sin^2((t-s)/2)) e^{ims} ds = \begin{cases} 0 & , m = 0 \\ e^{imt}/|m| & , m \neq 0 \end{cases} .$$

We also note that

$$\omega_j(t_i) = \widehat{\omega}_{|i-j|} \quad , \quad \widehat{\omega}_k = \frac{1}{2n} \sum_{m=1}^n \frac{\cos(mt_k)}{m} \quad , \quad (2.18)$$

which reduces computational costs in computing the weights when integrals involving  $L_2$  are to be approximated at each  $t_i$ .

The Nyström method corresponding to these quadratures defines the approximations  $V_i \approx V(t_i)$  as the solution of the linear system

$$\frac{V_i}{2} + \frac{\pi}{n} \sum_{j=0}^{2n-1} K(t_i, t_j) V_j = \sum_{j=0}^{2n-1} \left( \frac{\pi}{n} L_1(t_i, t_j) + \widehat{\omega}_{|i-j|} \right) G(t_j) \quad , \quad 0 \leq i \leq 2n-1 \quad . \quad (2.19)$$

Because the  $\{(t_i, V_i)\}$  data approximates a smooth periodic function at equispaced points, it is natural to interpolate it with a trigonometric polynomial,

$$\widetilde{V}(t) = \sum_{j=-n}^n d_j e^{ijt} \quad , \quad (2.20)$$

for which we use a Fast Fourier Transform (FFT) to efficiently obtain the coefficients  $\{d_j\}$ . The values  $\widetilde{V}'(t_j)$  are obtained by an inverse FFT (IFFT), using the coefficients  $\{j d_j\}$ . From this, we obtain our approximation of the normal derivative of  $u$  at  $x_i = x(t_i)$  as

$$\frac{\partial u}{\partial \mathbf{n}}(x_i) = \frac{\partial v}{\partial \mathbf{t}}(x_i) = \frac{V'(t_i)}{|x'(t_i)|} \approx \frac{\widetilde{V}'(t_i)}{|x'(t_i)|} \quad . \quad (2.21)$$

For  $x_0 \in \Omega$  and its complex counterpart  $z_0 = x_0 \cdot (1, i)$ , the parametrized form of the Cauchy integral formulas (2.3), and their Nyström-based approximations, are

$$\begin{aligned} w^{(k)}(z_0) &= \frac{k!}{2\pi i} \int_0^{2\pi} \frac{[F(t) + iV(t)]x'(t) \cdot (1, i)}{[(x(t) - x_0) \cdot (1, i)]^{k+1}} dt \\ &\approx \frac{k!}{2\pi i} \int_0^{2\pi} \frac{[F(t) + i\widetilde{V}(t)]x'(t) \cdot (1, i)}{[(x(t) - x_0) \cdot (1, i)]^{k+1}} dt \quad . \end{aligned} \quad (2.22)$$

The integral involving  $\widetilde{V}(t)$  in (2.22) is also approximated by the trapezoid rule.

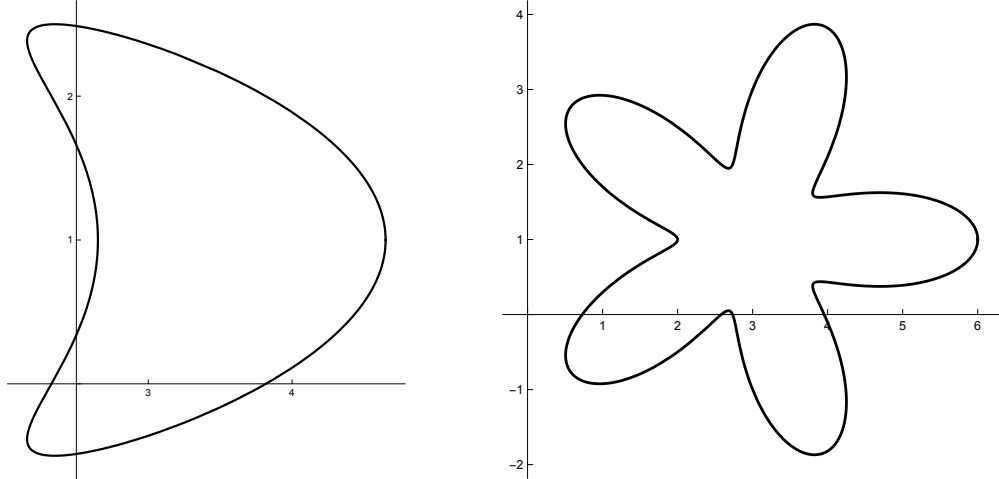


Figure 2.1: The Bean Domain (left) and the Five-Petal Domain.

We already have the data  $\{V_j\}$  on hand for the trapezoid rule on  $2n$  subintervals, but we can cheaply double or quadruple (etc.) the number of subintervals via the FFT/IFFT approach to “fill in” data at the new nodes. In several of the experiments in this section and the next, we report how these richer versions of the trapezoid rule compare with the baseline trapezoid rule.

For both examples in this section we use the harmonic conjugate pair

$$u(x) = \ln |x| \quad , \quad v(x) = \arctan(x_2/x_1) - v_{ave} \quad , \quad (2.23)$$

where  $v_{ave}$  is the constant such that  $\int_{\partial\Omega} v \, dS = 0$ . Both domains, which are pictured in Figure 2.1, are in right half-plane. These experiments were done in MATLAB, using its built-in “backslash” direct solver for the linear system (2.19) and FFT/IFFT for computing the trigonometric interpolant  $\tilde{V}$  and its derivative.

*Example 2.2.1* (Bean Shape). We consider the domain  $\Omega$  bounded by the curve

$$x(t) = (\cos t + 0.65 \cos(2t), 1.5 \sin t) + P \quad , \quad P = (3, 1) \quad .$$

In this case,  $v_{ave} \approx 0.286124639031644347606124552$ , correct in all digits shown, up

to rounding in the last digit. In Table 2.1 we report various errors with respect the problem-size parameter  $n$  from (2.19). These errors are:

- (a) The maximum absolute error in the approximation of  $\partial u / \partial \mathbf{n}$  at the nodes  $x_i = x(t_i)$ .
- (b) The absolute error in the approximation of  $u$ , its first partial derivatives and its second partial derivatives at two points in  $\Omega$ .

For the errors in (b), we experiment with three different levels of resolution for the trapezoid rule in the approximation (2.22). The lowest level of resolution, indicated by the label  $\zeta = 1$ , uses exactly the data  $\{(t_i, V_i)\}$  computed in (2.19). The next level of resolution, indicated by  $\zeta = 2$ , corresponds to augmenting the original data with interpolated data at the midpoints,  $t_{i+1/2} = (t_i + t_{i+1})/2$ . The finest level of resolution we will consider, indicated by  $\zeta = 4$ , corresponds to further augmenting the level-two data with interpolated data at the quarter-points,  $t_{i+1/4} = (3t_i + t_{i+1})/4$  and  $t_{i+3/4} = (t_i + 3t_{i+1})/4$ . The computed spectral condition numbers of the matrices associated with (2.19) remain fixed at 5.9686e+00 for  $n = 16, 32, 64$ .

The high-order nature of the algorithm is apparent, with significant decreases in each measure of error as the number of points is doubled, reaching machine precision in many cases for  $n = 64$ . We also note that, for this problem, significant reductions in error are achieved for interior values by interpolating the computed data for the trapezoid approximation of (2.22).

*Example 2.2.2 (Five-Petal Shape).* We consider the domain  $\Omega$  bounded by the curve

$$x(t) = (2 + \cos(mt))(\cos t, \sin t) + P \quad , \quad m = 5 \quad , \quad P = (3, 1) \quad .$$

We use the same harmonic conjugates as were used in the Bean example, Example 2.2.1. In this case,  $v_{ave} \approx 0.289910246091888587979329869$ , correct in all digits

Table 2.1: Bean: Errors in approximating the normal derivative of  $u$  on  $\partial\Omega$ , and its values and first and second partial derivatives at two points,  $P_1 = (4, 1/2)$  and  $P_2 = (3, 9/4)$ , in  $\Omega$ . Below this are the exact values of  $u$  and its first and second partial derivatives at these points.

		$n = 16$	$n = 32$	$n = 64$
	$\partial u / \partial \mathbf{n}$	1.4989e-04	1.0888e-08	9.3328e-13
$\zeta = 1$	$u(P_1)$	1.8243e-03	3.9705e-05	5.1622e-10
	$u(P_2)$	7.8176e-05	1.1441e-07	9.3259e-15
	$u_{x_1}(P_1)$	1.3305e-01	1.3028e-05	6.8491e-08
	$u_{x_2}(P_1)$	4.4526e-02	1.6231e-03	8.3801e-08
	$u_{x_1}(P_2)$	4.4379e-03	1.0111e-06	1.2859e-13
	$u_{x_2}(P_2)$	3.4742e-03	3.7146e-06	6.9197e-13
	$u_{x_1 x_1}(P_1)$	1.8676e+00	4.7321e-02	7.3981e-06
	$u_{x_1 x_2}(P_1)$	1.4898e+00	2.9545e-02	9.5720e-07
	$u_{x_1 x_1}(P_2)$	8.6408e-02	8.5098e-05	4.1156e-11
	$u_{x_1 x_2}(P_2)$	7.1994e-02	7.2353e-05	1.2868e-11
$\zeta = 2$	$u(P_1)$	3.9653e-05	5.0881e-10	4.4409e-16
	$u(P_2)$	1.8213e-06	1.6698e-11	8.8818e-16
	$u_{x_1}(P_1)$	1.4315e-05	6.8485e-08	1.0825e-15
	$u_{x_2}(P_1)$	1.6223e-03	8.3802e-08	1.7486e-15
	$u_{x_1}(P_2)$	3.2456e-06	1.5828e-11	1.6653e-16
	$u_{x_2}(P_2)$	6.8505e-07	4.1912e-12	0
	$u_{x_1 x_1}(P_1)$	4.7319e-02	7.3981e-06	3.2960e-15
	$u_{x_1 x_2}(P_1)$	2.9546e-02	9.5720e-07	1.3543e-14
	$u_{x_1 x_1}(P_2)$	7.9112e-05	4.9585e-11	5.3429e-16
	$u_{x_1 x_2}(P_2)$	7.2458e-05	4.5001e-11	1.3878e-17
$\zeta = 4$	$u(P_1)$	5.2294e-08	7.4061e-12	1.7764e-15
	$u(P_2)$	1.7069e-06	1.6707e-11	8.8818e-16
	$u_{x_1}(P_1)$	1.2210e-06	5.8367e-12	1.9429e-16
	$u_{x_2}(P_1)$	9.0129e-07	1.3441e-12	1.4155e-15
	$u_{x_1}(P_2)$	4.2567e-06	1.5956e-11	2.4980e-16
	$u_{x_2}(P_2)$	3.0296e-06	4.8828e-12	1.3878e-16
	$u_{x_1 x_1}(P_1)$	9.0848e-06	3.9098e-12	1.4433e-15
	$u_{x_1 x_2}(P_1)$	1.7443e-06	4.1441e-13	3.3567e-15
	$u_{x_1 x_1}(P_2)$	5.9859e-06	8.4289e-12	1.0408e-16
	$u_{x_1 x_2}(P_2)$	1.0520e-07	3.2132e-11	4.0246e-16

	$u(P_j)$	$u_{x_1}(P_j)$	$u_{x_2}(P_j)$	$u_{x_1 x_1}(P_j)$	$u_{x_1 x_2}(P_j)$
$P_1$	1.3940e+00	2.4615e-01	3.0769e-02	-5.9645e-02	-1.5148e-02
$P_2$	1.2524e+00	2.4510e-01	1.4706e-01	-3.8447e-02	-7.2088e-02

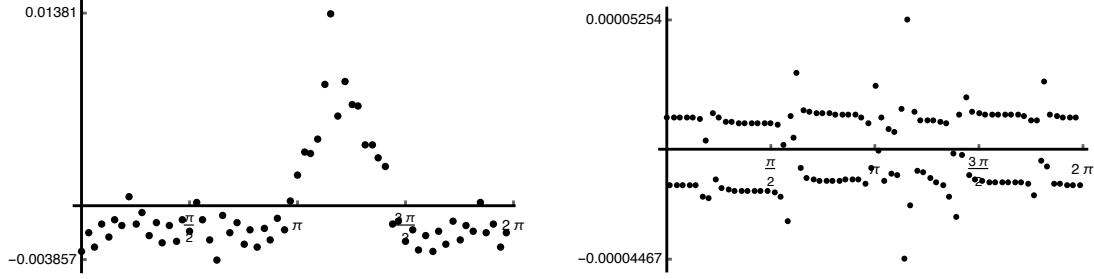


Figure 2.2: Five-Petal: The errors,  $V(t_i) - \tilde{V}(t_i)$ , in approximating the Dirichlet trace of  $v$  for  $n = 32$  (left) and  $n = 64$  (right).

shown. Plots of the errors,  $V(t_i) - \tilde{V}(t_i)$ , in the approximations of the Dirichlet trace of  $v$ , computed from the Nyström linear system (2.19) when  $n = 32$  and  $n = 64$ , are given in Figure 2.2. For  $n = 128$ , the magnitude of maximal error is approximately  $1.083 \times 10^{-8}$ , while the mean magnitude of the errors is approximately  $3.222 \times 10^{-9}$ . We report the same kinds of errors as in the Bean example, for the choice  $\zeta = 2$ , in Table 2.2. There was modest improvement in errors by increasing from  $\zeta = 1$  to  $\zeta = 2$ , but no further improvement for  $\zeta = 4$ . Because of the greater curvature of the domain, more points are needed to reach machine precision, but the same high-order convergence is clear. The computed spectral condition numbers of the associated matrices monotonically decrease from  $9.7013e+00$  when  $n = 16$  to  $9.0344e+00$  when  $n = 256$ .

### 2.3. Piecewise Smooth Boundary and Data

We briefly describe the key difficulties that arise when  $\Omega$  has corners. The first is that neither of the integrands in (2.10) is a smooth periodic function for fixed  $x$ . More specifically, if  $z \in \partial\Omega$  is a corner point where the interior angle is  $\pi/\alpha$ , and  $x, y \in \partial\Omega$

Table 2.2: Five-Petal: Errors in approximating the normal derivative of  $u$  on  $\partial\Omega$ , and its values and first and second partial derivatives at two points,  $P_1 = (2, 1/2)$  and  $P_2 = (7/2, 1)$ , in  $\Omega$ . Below this are the exact values of  $u$  and its first and second partial derivatives at these points.

		$n = 16$	$n = 32$	$n = 64$	$n = 128$	$n = 256$
	$\partial u / \partial \mathbf{n}$	5.5351e-01	1.2496e-01	3.5390e-03	3.4062e-6	2.9735e-12
$\zeta = 2$	$u(P_1)$	2.1926e-02	8.1485e-04	6.8438e-07	1.0090e-11	5.5511e-16
	$u(P_2)$	2.1976e-03	4.2675e-05	2.1450e-06	2.9139e-11	1.5543e-15
	$u_{x_1}(P_1)$	4.6939e-02	2.4008e-03	2.1684e-06	5.0886e-11	2.7756e-16
	$u_{x_2}(P_1)$	3.3170e-02	2.2415e-03	2.1590e-07	5.0079e-11	2.0817e-16
	$u_{x_1}(P_2)$	9.0903e-03	2.9921e-06	1.9011e-06	5.9653e-11	2.7756e-16
	$u_{x_2}(P_2)$	1.6139e-02	6.4784e-04	1.0570e-08	2.8182e-11	3.8858e-16
	$u_{x_1 x_1}(P_1)$	1.1008e-01	4.4535e-03	3.8472e-06	2.1866e-10	6.3838e-16
	$u_{x_1 x_2}(P_1)$	1.0526e-01	1.3734e-04	6.2953e-06	2.0828e-11	1.4710e-15
	$u_{x_1 x_1}(P_2)$	1.3452e-02	2.9259e-04	3.5473e-06	2.0290e-10	8.3267e-17
	$u_{x_1 x_2}(P_2)$	1.2613e-02	4.0277e-04	6.4810e-07	1.8877e-11	2.4286e-16

	$u(P_j)$	$u_{x_1}(P_j)$	$u_{x_2}(P_j)$	$u_{x_1 x_1}(P_j)$	$u_{x_1 x_2}(P_j)$
$P_1$	7.2346e-01	4.7059e-01	1.1765e-01	-2.0761e-01	-1.1073e-01
$P_2$	1.2920e+00	2.6415e-01	7.5472e-02	-6.4080e-02	-3.9872e-02

are on opposite sides of the corner, then

$$\lim_{y \rightarrow z} \frac{\partial \Phi(x, y)}{\partial \mathbf{n}(y)} = \frac{\sin(\pi/\alpha)}{2\pi|x - z|}.$$

This is clearly unbounded as  $x \rightarrow z$ . Additionally,  $u$  and  $v$  are typically only Hölder continuous near  $z$ , with unbounded partial derivatives (cf. [7, 24, 25]). Again, more specifically,

$$|u(x) - u(z)| \sim a|x - z|^\alpha \text{ for } x \in \bar{\Omega} \quad , \quad |\partial u / \partial \mathbf{n}(x)| \sim b|x - z|^{\alpha-1} \text{ for } x \in \partial\Omega \quad ,$$

for some constants  $a, b$  that are typically non-zero. The same holds for  $v$ . If the corner angle at  $z$  is obtuse,  $0 < \alpha < 1$ , then we expect the normal derivatives of  $u$  and  $v$  to be unbounded near  $z$ . Because of the assumption that  $u$  has piecewise smooth Dirichlet data, its tangential derivative will be bounded near  $z$ , but the tangential derivative of  $v$ , which is the normal derivative of  $u$ , will typically be unbounded in the case of obtuse angles. This singular behavior of  $u, v$  is illustrated in the Teardrop and Boomerang examples below (cf. [5, 11]), both of which have a single corner, at

the origin, with angle  $\pi/\alpha$ , see Figure 2.3. For these examples we take the harmonic conjugate pair

$$u = r^\alpha \cos(\alpha\theta) \quad , \quad v = r^\alpha \sin(\alpha\theta) \quad , \quad (2.24)$$

where  $r = |x|$  and  $\theta$  are the standard polar coordinates.

The second difficulty is that the integral equation (2.10) is no longer valid, when viewed pointwise, at corners. It is well-known that

$$\int_{\partial\Omega} \frac{\partial\Phi(x, y)}{\partial\mathbf{n}(y)} dS(y) = \begin{cases} -1/2 & , x \in \partial\Omega \text{ not at corner} \\ -1/(2\alpha) & , x \in \partial\Omega \text{ at } \pi/\alpha \text{ corner} \end{cases} \quad ,$$

and a consequence of this is that, for  $z \in \partial\Omega$  a corner with interior angle  $\pi/\alpha$ ,

$$\frac{v(z)}{2\alpha} + \int_{\partial\Omega} \left( \frac{\partial\Phi(z, y)}{\partial\mathbf{n}(y)} + 1 \right) v(y) dS(y) = \int_{\partial\Omega} \Phi(z, y)g(y) dS(y) \quad . \quad (2.25)$$

A simple modification removes the  $\alpha$ -dependency in the integral operator (cf. [11]),

$$\begin{aligned} |\partial\Omega|v(z) + \frac{v(x) - v(z)}{2} + \int_{\partial\Omega} \left( \frac{\partial\Phi(x, y)}{\partial\mathbf{n}(y)} + 1 \right) (v(y) - v(z)) dS(y) \\ = \int_{\partial\Omega} \Phi(x, y)g(y) dS(y) \quad , \end{aligned} \quad (2.26)$$

for  $x = z$  and any  $x \in \partial\Omega$  that is not at a corner. If  $z$  is the only corner, we may take (2.26) for all  $x \in \partial\Omega$ . We will focus on that case for much of the discussion of how the approach from Section 2.2 must be modified. After developing an approach to treat domains with a single corner, we will briefly describe how it can be adjusted to accommodate multiple corners.

**2.3.1. Domains with a Single Corner:** Taking a smooth parametrization  $x = x(t) : [0, 2\pi] \rightarrow \partial\Omega$  of  $\partial\Omega$  as before, with  $x(0) = x(2\pi) = z$ , and using the same

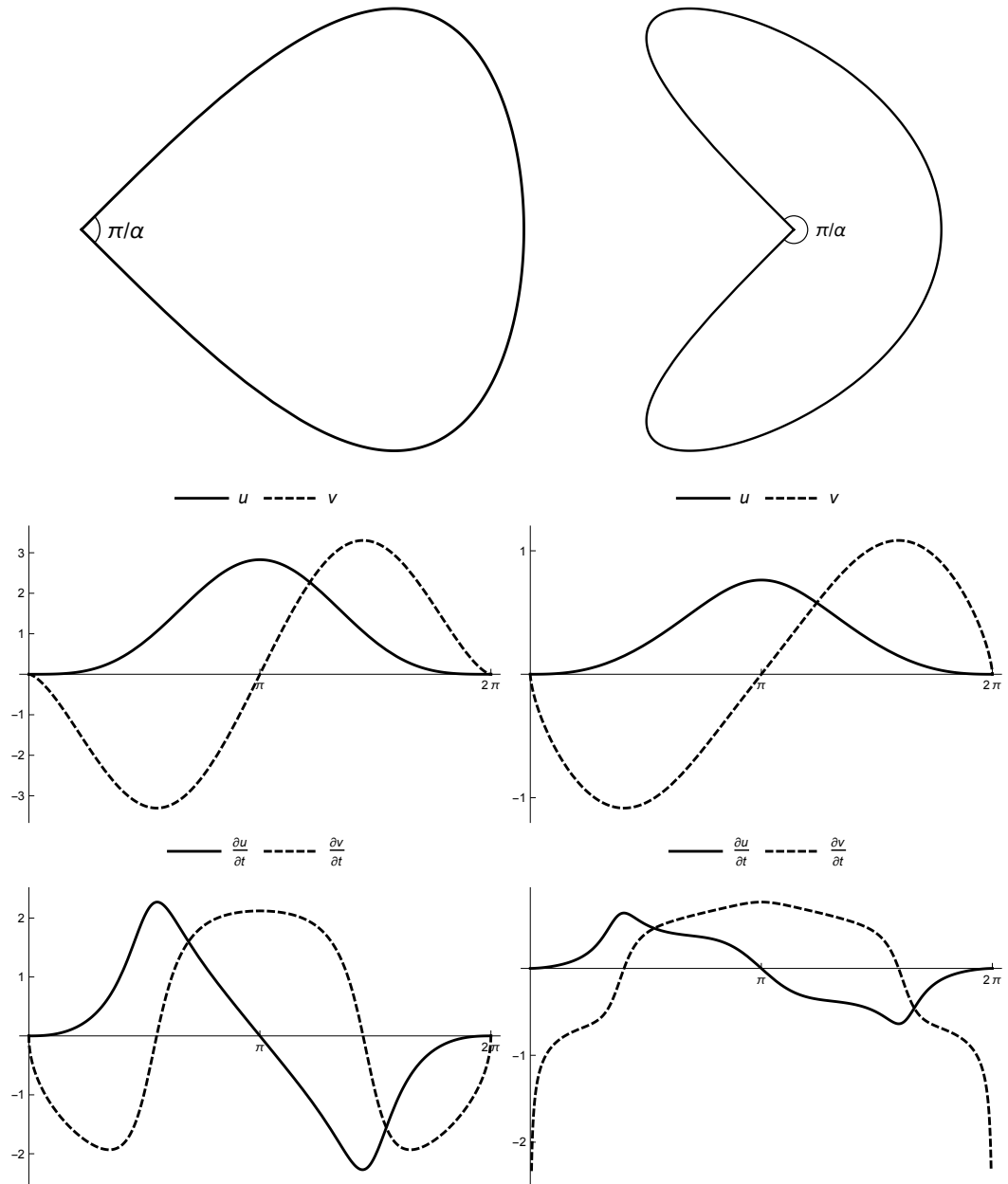


Figure 2.3: The Teardrop (left) and Boomerang domains. Below each domain are parametric plots of  $u, v$  and  $\partial u/\partial t, \partial v/\partial t$  for the conjugate pair from (2.24). For the Teardrop,  $\alpha = 3/2$ . For the Boomerang,  $\alpha = 2/3$ .

notation as in Section 2.2, the parametrized version of (2.26) is

$$\begin{aligned} |\partial\Omega|V(0) + \frac{V(t) - V(0)}{2} + \int_0^{2\pi} K(t, s)(V(s) - V(0)) ds \\ = \int_0^{2\pi} (L_1(t, s) + L_2(t, s)) G(s) ds \end{aligned} \quad (2.27)$$

Both integrands in (2.27) are more challenging than in the smooth case, but both will be addressed by essentially the same quadratures as before (trapezoid and Martensen), after a suitable change-of-variable.

The relevant quadrature for the first integral in (2.27) is analyzed in [11], and we briefly describe it for a generic interval  $[a, b]$ . Given an integer  $p \geq 2$ , let  $\lambda : [a, b] \rightarrow [a, b]$  be given by

$$\begin{aligned} \lambda(t) &= (b - a) \frac{[c(t)]^p}{[c(t)]^p + [1 - c(t)]^p} + a \quad , \\ c(t) &= \left(\frac{1}{2} - \frac{1}{p}\right) \left(\frac{2t - a - b}{b - a}\right)^3 + \frac{1}{p} \left(\frac{2t - a - b}{b - a}\right) + \frac{1}{2} . \end{aligned} \quad (2.28)$$

The function  $\lambda$  is strictly increasing, and  $\lambda(t) - a$  and  $b - \lambda(t)$  have roots of multiplicity  $p$  at  $a$  and  $b$ , respectively. Letting  $h = (b - a)/m$  and  $\tau_k = a + kh$ , an  $(m + 1)$ -point quadrature associated with this is based on the change of variable  $t = \lambda(\tau)$ ,

$$\begin{aligned} \int_a^b F(t) dt &= \int_a^b F(\tau) \lambda'(\tau) d\tau \approx \sum_{k=0}^m w_k F(t_k) \quad , \\ t_k &= \lambda(\tau_k) \quad , \quad w_k = h \lambda'(\tau_k) . \end{aligned} \quad (2.29)$$

Here  $F \in C(a, b)$  is integrable, and typically very smooth in  $(a, b)$ . Since  $\lambda'(a) = \lambda'(b) = 0$ , we can omit the points/weights  $(t_0, w_0)$  and/or  $(t_m, w_m)$ , and this is necessary when  $F$  is unbounded at  $a$  or  $b$ . We refer to the quadrature described in (2.28)-(2.29) as *Kress Quadrature*, due to its introduction in [11].

In very general terms, increasing  $p$  increases the order of the quadrature, but for a fixed  $m$  a smaller  $p$  may give a better result. Because this quadrature may be

Table 2.3: Errors in the quadrature (2.29) for  $\int_{-1}^1 F(t) dt$  for some singular and “nearly singular”  $F$ . For the final, “nearly singular”, integrand, Gauss-Legendre quadrature errors are given for comparison.

$m$	$F(t) = (1 - t^2)^{1/3}$		$F(t) = (1 - t^2)^{-1/3}$		$F(t) = (1 + 10^{-4} - t^2)^{-1/2}$		
	$p = 5$	$p = 7$	$p = 5$	$p = 7$	$p = 5$	$p = 7$	Gauss
2	3.174e-01	3.174e-01	5.871e-01	5.871e-01	1.122e+00	1.122e+00	6.722e-01
4	1.020e-01	2.579e-01	4.682e-02	1.945e-02	5.924e-03	1.181e-01	3.665e-01
8	4.213e-04	2.057e-03	1.557e-03	5.915e-04	7.467e-03	1.242e-02	1.854e-01
16	5.184e-08	1.863e-07	1.341e-04	5.415e-06	3.412e-03	1.089e-03	8.678e-02
32	7.938e-10	7.244e-12	1.246e-05	2.600e-07	6.863e-06	2.188e-05	3.607e-02
64	9.114e-12	9.104e-15	1.197e-06	1.112e-08	8.817e-08	9.773e-09	1.181e-02
128	9.570e-14	4.441e-16	1.168e-07	4.535e-10	3.137e-10	4.268e-13	2.260e-03
256	0	8.882e-16	1.150e-08	2.301e-11	4.914e-12	1.332e-15	1.271e-04
512	2.220e-16	4.441e-16	1.135e-09	1.245e-10	7.860e-14	7.638e-14	5.468e-07
1024	1.332e-15	0	1.143e-10	6.871e-11	1.776e-15	3.464e-14	1.390e-11

unfamiliar, we illustrate its performance in Table 2.3 on a few integrals,  $\int_{-1}^1 F(t) dt$ , that are challenging for many quadratures. The first integrand,  $F(t) = (1 - t^2)^{1/3}$ , has stronger singular behavior than what would arise in the integration of  $u, v$  along  $\partial\Omega$ . The second integrand,  $F(t) = (1 - t^2)^{-1/3}$ , has stronger singular behavior than what would arise in the integration of the tangential or normal derivatives of  $u, v$  along  $\partial\Omega$ . Though one could, in principle, derive Gaussian quadratures integrals involving these kinds of singularities, the approach (2.29) does not require a priori knowledge of the particular kind of singularity, and is effective on a wide range of integrands by adjusting  $m$  and/or  $p$ , so it is more of a multi-purpose quadrature scheme. The third integrand,  $F(t) = (1 + 10^{-4} - t^2)^{-1/2}$ , has singularities just outside the interval of integration, and we refer to it as being “nearly singular”, because its extremely large derivatives near  $\pm 1$  make it essentially singular for numerical purposes. The integrand  $F(s) = K(t, s)(V(s) - V(0))$  in (2.27), exhibits similar nearly singular behavior for  $s$  near  $2\pi$  when  $t$  is close to 0, and for  $s$  near 0 when  $t$  is close to  $2\pi$ . For the final integrand, we compare the performance of (2.29) with Gauss-Legendre quadrature.

For integrands of the form  $F(t) = (1 - t^2)^q Q(t)$ , where  $q > -1$  and  $Q \in C^\infty(-1, 1) \cap C[-1, 1]$ , one can see that the integrand after the change-of-variable

$t = \lambda(\tau)$  has the form,

$$F(\lambda(\tau))\lambda'(\tau) = (1 - \tau^2)^{p(q+1)-1}R(\tau) ,$$

for some  $R \in C^\infty(-1, 1) \cap C[-1, 1]$ . It is well-known (cf. [20]) that error in the  $(m+1)$ -point trapezoid rule decays like the  $m^{\text{th}}$  Fourier coefficient of the integrand. In our case, that error is  $\mathcal{O}(m^{-p(q+1)})$ , which is consistent with the convergence behavior seen for the first two integrands in Table 2.3, until the effects of double-precision arithmetic begin to dominate. This kind of analysis yields a somewhat stronger convergence result than that given in [11, Theorem 2.1], where only odd integer orders of convergence are established—an artifact of the use of the Euler-Maclaurin formula in the proof.

The quadrature (2.29) will be used to approximate the integral on the left-hand side of (2.27), so we must approximate the integral on the right-hand side at these quadrature points,  $t_k = \lambda(\tau_k)$ . After the change-of-variable  $t = \lambda(\tau)$ ,  $s = \lambda(\sigma)$ , the integral on the right-hand side of (2.27) becomes

$$\begin{aligned} J(\tau) &= -\frac{1}{4\pi} \int_0^{2\pi} \ln(|x(\lambda(\tau)) - x(\lambda(\sigma))|^2) G(\lambda(\sigma))\lambda'(\sigma) d\sigma \\ &= -\frac{1}{4\pi} \int_0^{2\pi} \ln\left(\frac{|x(\lambda(\tau)) - x(\lambda(\sigma))|^2}{4 \sin^2((\tau - \sigma)/2)}\right) G(\lambda(\sigma))\lambda'(\sigma) d\sigma \\ &\quad - \frac{1}{4\pi} \int_0^{2\pi} \ln(4 \sin^2((\tau - \sigma)/2)) G(\lambda(\sigma))\lambda'(\sigma) d\sigma , \end{aligned}$$

and we write  $J(\tau) = J_1(\tau) + J_2(\tau)$  to correspond to this decomposition of the integral. The first of these,  $J_1(t)$ , is handled via the trapezoid rule in  $\sigma$ , which corresponds to (2.29) in  $s$ . We note that

$$\begin{aligned} \lim_{\sigma \rightarrow \tau} \tilde{L}_1(\tau, \sigma) &= 2 \ln(|x'(\lambda(\tau))| \lambda'(\tau)) \\ \text{where } \tilde{L}_1(\tau, \sigma) &= \ln\left(\frac{|x(\lambda(\tau)) - x(\lambda(\sigma))|^2}{4 \sin^2((\tau - \sigma)/2)}\right) . \end{aligned} \tag{2.30}$$

The integral  $J_2(\tau)$  is handled by Martensen quadrature, as before. These quadrature choices yield a natural analogue of the Nyström linear system (2.19), given by

$$\begin{aligned} |\partial\Omega|V_0 + \frac{V_i - V_0}{2} + \sum_{j=0}^{2n-1} K(t_i, t_j)w_j(V_j - V_0) \\ = \sum_{j=0}^{2n-1} \left( \tilde{L}_1(\tau_i, \tau_j)w_j + \hat{\omega}_{|i-j|}\lambda'(\tau_j) \right) G(t_j) , \end{aligned} \quad (2.31)$$

for  $0 \leq i \leq 2n - 1$ , where  $w_j, t_j, \tau_j$  are described between (2.28) and (2.29), with  $(a, b) = (0, 2\pi)$  and  $m = 2n - 1$ . Since  $w_j = (\pi/n)\lambda'(\tau_j)$  in this case, we may re-express the terms in the second sum as

$$\left( \tilde{L}_1(\tau_i, \tau_j)w_j + \hat{\omega}_{|i-j|}\lambda'(\tau_j) \right) G(t_j) = \left( \tilde{L}_1(\tau_i, \tau_j) + (n/\pi)\hat{\omega}_{|i-j|} \right) w_j G(t_j) .$$

The structure of the linear system (2.31) suggests that an iterative linear solver such as GMRES [19] is a natural choice, and that is what we use in our experiments below.

Let  $W(\tau) = V(\lambda(\tau)) = V(t)$ . The values  $V_i \approx V(t_i) = W(\tau_i)$  are associated with an even spacing in  $\tau$ , not  $t$ , so it makes sense to use the data  $\{(\tau_i, V_i)\}$  to construct a trigonometric polynomial  $\tilde{W}(\tau) \approx W(\tau)$  and evaluate it and its derivative using the same FFT/IFFT approach as in the smooth boundary case. We have the obvious relationship, for  $x = x(t)$ ,

$$\frac{\partial u}{\partial \mathbf{n}}(x) = \frac{\partial v}{\partial \mathbf{t}}(x) = \frac{V'(t)}{|x'(t)|} = \frac{W'(\tau)}{|x'(t)|\lambda'(\tau)} . \quad (2.32)$$

Working with  $W$ , instead of  $V$ , is very natural for a few reasons. The first is that  $W$  has greater Hölder regularity than  $V$ . More specifically,  $V'$  is typically unbounded near 0 and  $2\pi$  when the interior angle at the corner is obtuse, whereas  $W'$  is not. This is illustrated in Figure 2.4 for the Boomerang domain (see Figure 2.3 and Example 2.3.2), with  $\alpha = 2/3$ ,  $p = 7$  and  $v = r^\alpha \sin(\alpha\theta)$ . Moreover, for sufficiently

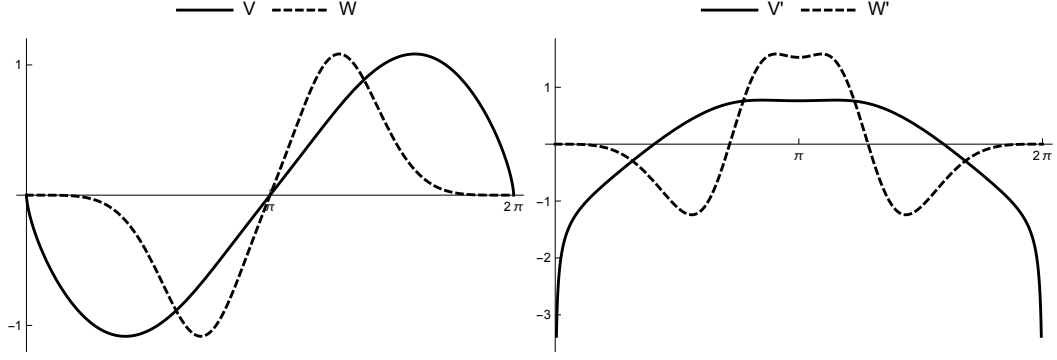


Figure 2.4: Plots of  $V$  and  $W$ , and  $V'$  and  $W'$ , for the Boomerang, with  $\alpha = 2/3$ ,  $p = 7$  and  $v = r^\alpha \sin(\alpha\theta)$ .

smooth  $\psi$  we have

$$\begin{aligned} \int_{\Omega} \nabla u(x) \cdot \nabla \psi(x) dx &= \int_{\partial\Omega} \frac{\partial u}{\partial \mathbf{n}}(x) \psi(x) dS(x) \\ &= \int_0^{2\pi} V'(t) \tilde{\psi}(t) dt = \int_0^{2\pi} W'(\tau) \tilde{\psi}(\lambda(\tau)) d\tau, \end{aligned} \quad (2.33)$$

where  $\tilde{\psi}(t) = \psi(x(t))$ . For example, taking  $\psi = u$ , we may obtain an accurate approximation of the  $H^1(\Omega)$  seminorm of  $u$  by computing the boundary integral.

*Example 2.3.1* (Teardrop Domain). The boundary of the Teardrop domain is parametrized by

$$x(t) = (2 \sin(t/2), -\beta \sin t) \quad , \quad \beta = \tan(\pi/(2\alpha)) \quad ,$$

for some fixed  $\alpha > 1$ , and  $t \in [0, 2\pi)$ . Choosing  $\alpha = 3/2$  results in  $|\partial\Omega| \approx 8.488331067320425334480158779233$ , correct to all digits shown. Since  $\partial u/\partial \mathbf{n}$  is unbounded, in Table 2.4 we instead report the maximal error in the approximation of  $W'$  at the nodes  $x_i = x(\lambda(\tau_i))$ , along with the errors in the approximations of  $u$  and those of its derivatives at two test points, for  $n = 32, 64, 128$ . Because increasing the interpolation parameter  $\zeta$  yields some improvements in the approximation of  $u$  and its derivatives in the interior, we report the results for  $\zeta = 1, 2, 4$ . In each case we fix

the Kress quadrature parameter  $p = 7$ .

*Example 2.3.2* (Boomerang Domain). The boundary of the Boomerang domain is

Table 2.4: Teardrop: Errors in approximating  $W'(\tau)$  on  $\partial\Omega$ , and the values of  $u$  and its first and second partial derivatives at two points,  $P_1 = (1/4, -1/4)$  and  $P_2 = (3/2, 1/2)$ , in  $\Omega$ . Below this are the exact values of  $u$  and its first and second partial derivatives at these points.

		$n = 32$	$n = 64$	$n = 128$
	$W'(\tau)$	2.4757e-08	1.1834e-10	2.2128e-11
$\zeta = 1$	$u(P_1)$	7.9294e-04	3.6510e-05	7.5064e-09
	$u(P_2)$	9.5304e-05	2.8453e-09	8.5709e-14
	$u_{x_1}(P_1)$	1.2030e-01	4.1148e-03	2.5001e-07
	$u_{x_1}(P_2)$	2.0874e-03	1.2807e-07	2.3204e-13
	$u_{x_2}(P_1)$	6.7333e-02	5.1754e-04	1.7720e-06
	$u_{x_2}(P_2)$	2.5234e-03	4.8239e-07	9.4480e-14
	$u_{x_1x_1}(P_1)$	6.0023e+00	2.4731e-01	1.8116e-04
	$u_{x_1x_1}(P_2)$	4.5915e-02	5.7993e-06	1.9174e-13
	$u_{x_1x_2}(P_1)$	1.4401e+00	2.8889e-01	2.7358e-04
	$u_{x_1x_2}(P_2)$	5.1692e-02	1.9819e-05	1.3299e-13
$\zeta = 2$	$u(P_1)$	3.6509e-05	7.5065e-09	1.7902e-13
	$u(P_2)$	2.7874e-09	7.8826e-14	8.4155e-14
	$u_{x_1}(P_1)$	4.1148e-03	2.5002e-07	4.8361e-13
	$u_{x_1}(P_2)$	1.2798e-07	2.1649e-13	2.3292e-13
	$u_{x_2}(P_1)$	5.1754e-04	1.7720e-06	7.9381e-14
	$u_{x_2}(P_2)$	4.8240e-07	2.2787e-13	9.8588e-14
	$u_{x_1x_1}(P_1)$	2.4731e-01	1.8116e-04	8.1177e-12
	$u_{x_1x_1}(P_2)$	5.7994e-06	1.7342e-13	7.6605e-14
	$u_{x_1x_2}(P_1)$	2.8889e-01	2.7358e-04	5.8813e-11
	$u_{x_1x_2}(P_2)$	1.9819e-05	6.1282e-13	5.4222e-13
$\zeta = 4$	$u(P_1)$	7.4665e-09	2.8486e-13	1.7918e-13
	$u(P_2)$	5.7809e-11	7.8604e-14	8.2157e-14
	$u_{x_1}(P_1)$	2.4997e-07	1.1471e-12	5.8287e-13
	$u_{x_1}(P_2)$	9.7181e-11	2.2204e-13	2.3470e-13
	$u_{x_2}(P_1)$	1.7719e-06	3.7526e-14	5.3346e-14
	$u_{x_2}(P_2)$	4.6493e-12	2.3209e-13	9.8088e-14
	$u_{x_1x_1}(P_1)$	1.8116e-04	1.1985e-11	3.0287e-12
	$u_{x_1x_1}(P_2)$	1.0911e-11	9.3148e-14	7.6272e-14
	$u_{x_1x_2}(P_1)$	2.7358e-04	5.6236e-11	2.0127e-12
	$u_{x_1x_2}(P_2)$	2.3542e-11	1.0200e-12	5.4058e-13

	$u(P_j)$	$u_{x_1}(P_j)$	$u_{x_2}(P_j)$	$u_{x_1x_1}(P_j)$	$u_{x_1x_2}(P_j)$
$P_1$	8.0449e-02	8.2401e-01	3.4132e-01	1.1653e+00	-4.8270e-01
$P_2$	1.7611e+00	1.8618e+00	-3.0213e-01	5.8875e-01	9.5541e-02

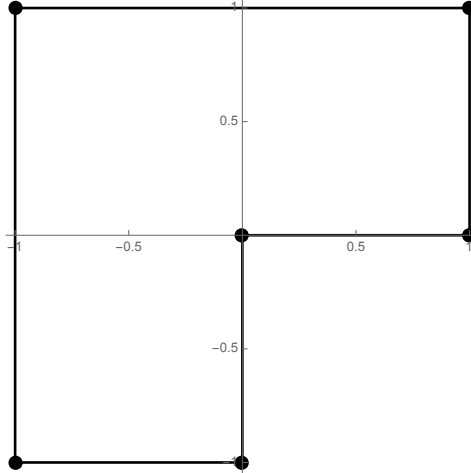


Figure 2.5: L-shaped Polygon: The hexagonal domain  $\Omega$  used in Example 2.3.3.

parametrized by

$$x(t) = (-(2/3) \sin(3t/2), \beta \sin t) \quad , \quad \beta = \tan(\pi/(2\alpha)) \quad ,$$

for some fixed  $1/2 < \alpha < 1$ , and  $t \in [0, 2\pi)$ . In this case choosing  $\alpha = 2/3$  gives a boundary length of  $|\partial\Omega| \approx 6.038382737179698567469163685137$ , correct to all digits shown. For  $n = 32, 64, 128$  and fixed Kress quadrature parameter  $p = 7$ , we report the maximal errors in  $W'$ , as well as pointwise errors in the approximation of  $u$  and its derivatives at two test points in  $\Omega$ , in Table 2.5. Increasing the interpolation parameter to  $\zeta = 4$  only yielded significant improvement of the approximation of the second derivatives at one of the points,  $P_2$ , when  $n = 32$ . The errors in this case were  $2.6027\text{e-}07$  and  $1.1944\text{e-}07$  for  $u_{x_1x_1}(P_2)$  and  $u_{x_1x_2}(P_2)$ , respectively.

**2.3.2. Domains with Multiple Corners:** We now consider domains with  $m$  corners. Proceeding counterclockwise along  $\partial\Omega$ , label the successive corner points  $z_0, \dots, z_{m-1} \in \partial\Omega$ , taking  $z_m = z_0$  for convenience. Let  $\partial\Omega_k$  be the arc (edge) of  $\partial\Omega$  having endpoints  $z_k$  and  $z_{k+1}$ . For the  $k$ th edge, we introduce the parameteri-

zation  $x_k : [0, 2\pi] \rightarrow \partial\Omega_k$ . The overall parameterization  $x : [0, 2m\pi] \rightarrow \partial\Omega$ , taken counterclockwise, may then be described by

$$x(t) = x_k(t - 2k\pi) \text{ when } t \in [2k\pi, 2(k+1)\pi] , \text{ for } k = 0, \dots, m-1 . \quad (2.34)$$

The remaining modification to make in (2.26) is to choose  $z = z(x)$  to be to the nearest corner point for each  $x \in \partial\Omega$ . More specifically, if  $x$  is a corner point, then  $z(x) = x$ ; otherwise, if  $x \in \partial\Omega_k$ ,  $z(x)$  is the nearer of the two endpoints  $z_k$  and  $z_{k+1}$ .

Table 2.5: Boomerang: Errors in approximating  $W'(\tau)$  on  $\partial\Omega$ , and the values of  $u$  and its first and second partial derivatives at two points,  $P_1 = (0, 1/5)$  and  $P_2 = (1/5, -2/5)$ , in  $\Omega$ . Below this are the exact values of  $u$  and its first and second partial derivatives at these points.

		$n = 32$	$n = 64$	$n = 128$
	$W'(\tau)$	9.4803e-05	7.0329e-06	3.7774e-07
$\zeta = 1$	$u(P_1)$	2.5641e-06	4.7332e-11	9.2051e-13
	$u(P_2)$	1.1966e-04	4.6305e-08	1.6187e-13
	$u_{x_1}(P_1)$	1.7859e-04	1.1043e-09	5.4297e-12
	$u_{x_1}(P_2)$	1.3322e-03	3.8414e-06	3.0368e-12
	$u_{x_2}(P_1)$	3.3131e-05	2.2396e-09	1.4309e-12
	$u_{x_2}(P_2)$	6.2385e-03	9.5505e-07	2.2362e-12
	$u_{x_1x_1}(P_1)$	1.2630e-02	3.8802e-08	5.8864e-12
	$u_{x_1x_1}(P_2)$	1.9192e-01	1.0969e-04	3.1104e-11
	$u_{x_1x_2}(P_1)$	5.2302e-03	3.9446e-07	2.5246e-11
	$u_{x_1x_2}(P_2)$	9.6834e-02	2.4007e-04	9.4683e-11
$\zeta = 2$	$u(P_1)$	1.0626e-07	5.5637e-11	9.2112e-13
	$u(P_2)$	8.6896e-08	2.7288e-11	1.6676e-13
	$u_{x_1}(P_1)$	5.7167e-08	3.1948e-10	5.4287e-12
	$u_{x_1}(P_2)$	3.6962e-06	3.5486e-11	2.2881e-12
	$u_{x_2}(P_1)$	2.8798e-07	2.6696e-10	1.4291e-12
	$u_{x_2}(P_2)$	7.8038e-07	1.3160e-10	1.9919e-12
	$u_{x_1x_1}(P_1)$	1.4949e-06	1.9932e-09	5.8825e-12
	$u_{x_1x_1}(P_2)$	1.0943e-04	4.7297e-10	5.1005e-12
	$u_{x_1x_2}(P_1)$	2.2716e-06	3.1653e-09	2.5230e-11
	$u_{x_1x_2}(P_2)$	2.4019e-04	3.1828e-11	3.1751e-12

	$u(P_j)$	$u_{x_1}(P_j)$	$u_{x_2}(P_j)$	$u_{x_1x_1}(P_j)$	$u_{x_1x_2}(P_j)$
$P_1$	1.7100e-01	9.8726e-01	5.6999e-01	9.4999e-01	-1.6454e+00
$P_2$	4.3261e-01	8.1308e-01	-3.1447e-01	-6.1376e-02	6.4688e-01

In light of these modifications, the parameterized version of (2.26) is

$$\begin{aligned} |\partial\Omega|c(t) + \frac{V(t) - c(t)}{2} + \int_0^{2m\pi} K(t, s) (V(s) - c(t)) ds \\ = \int_0^{2m\pi} (L_1(t, s) + L_2(t, s)) G(s) ds \end{aligned} \quad (2.35)$$

where  $c(t) = v(z(x(t)))$ . We again approximate these integrals by employing a combination of Kress and Martensen quadratures, as in the single corner case, on each edge. Interpolation of the computed data is done over the whole boundary, not over the individual edges.

*Example 2.3.3 (L-shaped Polygon Domain).* Let  $\Omega$  be the non-convex hexagon having vertices

$$\{z_0, z_1, z_2, z_3, z_4, z_5\} = \{(0, 0), (1, 0), (1, 1), (-1, 1), (-1, -1), (0, -1)\} ,$$

listed in counter-clockwise order—see Figure 2.5. The (initial) parameterization of the boundary is given by (2.34), with

$$x_k(t) = \frac{2\pi - t}{2\pi} z_k + \frac{t}{2\pi} z_{k+1} .$$

We consider the harmonic conjugate pair

$$u = r^\alpha \sin(\alpha\theta) \quad , \quad v = -r^\alpha \cos(\alpha\theta) \quad , \quad (2.36)$$

where  $\alpha = 2/3$ . Note that the average value of  $v$  on  $\partial\Omega$  is 0. The singular behavior of  $u$  (and  $v$ ) near the re-entrant corner is typical for the interior angle  $\pi/\alpha = 3\pi/2$ . As with the previous examples, we use the Kress quadrature parameter  $p = 7$ , and vary both the level of discretization  $n$  and the level of interpolation  $\zeta$ . The high-order convergence with respect to  $n$  is again observed in Table 2.6.

As a point of comparison, we consider an hp-adaptive finite element (hp-FEM) algorithm provided in the software package PLTMG [2] (<http://www.netlib.org/>)

Table 2.6: L-shaped Polygon: Errors in approximating  $W'(\tau)$  on  $\partial\Omega$ , and the values of  $u$  and its first and second partial derivatives at two points,  $P_1 = (1/4, 9/10)$  and  $P_2 = (-1/20, 1/20)$ , in  $\Omega$ . Below this are the exact values of  $u$  and its first and second partial derivatives at these points.

		$n = 16$	$n = 32$	$n = 64$	$n = 128$
	$W'(\tau)$	3.7987e-04	2.9270e-05	2.2814e-06	1.8316e-07
$\zeta = 1$	$u(P_1)$	6.6297e-03	5.7811e-05	4.1972e-09	3.3307e-16
	$u(P_2)$	3.0510e-06	9.8255e-09	1.4598e-11	1.4516e-14
	$u_{x_1}(P_1)$	1.9742e-01	2.4367e-03	1.1353e-07	1.3878e-15
	$u_{x_1}(P_2)$	2.1543e-05	6.9194e-08	1.0207e-10	1.0525e-13
	$u_{x_2}(P_1)$	3.3264e-01	5.6750e-03	8.1358e-07	1.4211e-14
	$u_{x_2}(P_2)$	2.1543e-05	6.9194e-08	1.0207e-10	1.0392e-13
	$u_{x_1x_1}(P_1)$	1.6738e+01	5.5570e-01	1.5752e-04	2.5633e-12
	$u_{x_1x_1}(P_2)$	1.6844e-10	3.2620e-13	7.1688e-15	1.3943e-16
	$u_{x_1x_2}(P_1)$	9.3136e+00	2.2078e-01	1.7471e-05	1.1505e-12
	$u_{x_1x_2}(P_2)$	7.0487e-04	2.2598e-06	3.3216e-09	3.8849e-12
$\zeta = 2$	$u(P_1)$	5.7766e-05	4.0115e-09	1.6342e-13	1.3323e-15
	$u(P_2)$	3.0512e-06	9.8256e-09	1.4599e-11	1.4766e-14
	$u_{x_1}(P_1)$	2.4366e-03	1.1324e-07	6.1684e-13	3.1641e-15
	$u_{x_1}(P_2)$	2.1526e-05	6.9194e-08	1.0207e-10	1.0547e-13
	$u_{x_2}(P_1)$	5.6756e-03	8.1548e-07	3.3369e-12	5.5511e-15
	$u_{x_2}(P_2)$	2.1526e-05	6.9194e-08	1.0207e-10	1.0703e-13
	$u_{x_1x_1}(P_1)$	5.5570e-01	1.5752e-04	3.1078e-12	1.1713e-14
	$u_{x_1x_1}(P_2)$	1.6563e-10	3.2620e-13	2.4326e-15	1.3243e-15
	$u_{x_1x_2}(P_1)$	2.2078e-01	1.7475e-05	2.5347e-12	2.4127e-14
	$u_{x_1x_2}(P_2)$	7.0008e-04	2.2598e-06	3.3216e-09	3.9009e-12
$\zeta = 4$	$u(P_1)$	4.0601e-08	1.8587e-10	1.6220e-13	2.5535e-15
	$u(P_2)$	3.0512e-06	9.8256e-09	1.4598e-11	1.3295e-14
	$u_{x_1}(P_1)$	1.8599e-08	2.9745e-10	6.1462e-13	4.9405e-15
	$u_{x_1}(P_2)$	2.1526e-05	6.9194e-08	1.0206e-10	1.0569e-13
	$u_{x_2}(P_1)$	1.4181e-06	1.9045e-09	3.3290e-12	7.3275e-15
	$u_{x_2}(P_2)$	2.1526e-05	6.9194e-08	1.0207e-10	1.0569e-13
	$u_{x_1x_1}(P_1)$	1.5719e-04	1.0940e-09	5.3479e-13	1.8707e-14
	$u_{x_1x_1}(P_2)$	1.6563e-10	3.1780e-13	7.4333e-15	3.5177e-15
	$u_{x_1x_2}(P_1)$	1.8419e-05	3.3071e-09	3.6607e-12	1.8985e-14
	$u_{x_1x_2}(P_2)$	7.0008e-04	2.2598e-06	3.3216e-09	3.8858e-12
	$u(P_j)$	$u_{x_1}(P_j)$	$u_{x_2}(P_j)$	$u_{x_1x_1}(P_j)$	$u_{x_1x_2}(P_j)$
$P_1$	7.2824e-01	-2.8634e-01	6.1897e-01	2.4018e-01	3.9335e-02
$P_2$	1.7100e-01	-1.1400e+00	1.1400e+00	-2.4443e-15	7.5999e+00

pltmg/). In [1], it is shown that such methods can achieve exponential convergence with respect to the number of degrees of freedom (DOF), with errors on the order of  $e^{-cDOF^{1/3}}$ , for some  $c > 0$ , for problems in 2D having singular solutions, such as the one considered in this example. In brief, ( $H^1$ -conforming) hp-FEM approximates the solution of (2.1) using spaces of globally continuous, piecewise polynomials, on a sequence of meshes. These approximation spaces are generated by an adaptive feedback loop (SOLVE-ESTIMATE-MARK-REFINE) in which the current approximation is used to compute local estimates of error that are then used to mark certain elements for “refinement”. This refinement consists of some combination of further subdivisions of mesh cells ( $h$ -refinement) and increasing local polynomial degrees ( $p$ -refinement). The error estimates and adaptive strategy used in PLTMG are described in [3, 4], and more briefly in [2].

Starting from an initial mesh consisting of six right triangles, and polynomials of degree one in each triangle, the adaptive feedback loop was run until the problem size reached approximately 100K DOF. This entailed 24 refinements (25 solves). Using built-in routines in PLTMG, the function value, gradient and Hessian were computed at the same two points as were reported for our method in Table 2.6. The errors in these computations are reported in Table 2.7. In order to save space, the data corresponding to 8, 21 and 40 DOF are not shown. Although the adaptive method is designed to drive down the approximation error at the optimal (exponential) rate with respect to the global  $H^1(\Omega)$ -norm, we observe that the pointwise errors are also consistent with exponential convergence, at least until they reach their minimum levels. The optimal errors achieved by the finite element algorithm are orders of magnitude larger than those achieved by our approach, and required significantly more computational effort.

*Example 2.3.4 (L-shaped Polygon Domain, Revisited).* This example is motivated by

Table 2.7: L-shaped Polygon: Absolute errors in computing the function values, gradients and Hessians for the L-shaped domain at two points using an hp-adaptive finite element method.

	DOF	$u$	$u_{x_1}$	$u_{x_2}$	$u_{x_1x_1}$	$u_{x_1x_2}$
$P_1 = (0.25, 0.9)$	65	2.58e-04	5.91e-03	1.29e-02	7.64e-03	1.13e-02
	195	1.18e-04	2.63e-04	1.20e-03	1.05e-04	1.82e-03
	256	7.03e-05	1.81e-04	7.17e-04	1.54e-04	1.16e-03
	460	2.97e-05	6.04e-05	3.02e-04	5.73e-05	7.53e-04
	773	1.15e-05	1.98e-05	1.17e-04	2.38e-05	2.27e-04
	1408	4.58e-06	7.28e-06	4.60e-05	6.60e-06	7.53e-05
	2501	1.82e-06	2.87e-06	1.83e-05	2.44e-06	2.97e-05
	3151	6.65e-07	1.03e-06	6.69e-06	6.22e-07	1.05e-05
	4900	2.59e-07	4.11e-07	2.61e-06	6.48e-07	4.28e-06
	9200	9.99e-08	1.59e-07	1.00e-06	1.53e-07	1.65e-06
	12771	3.58e-08	5.72e-08	3.60e-07	4.50e-08	5.91e-07
	18066	1.34e-08	2.15e-08	1.35e-07	1.04e-08	2.19e-07
	24278	4.60e-09	7.21e-09	4.62e-08	4.85e-08	7.97e-08
	27834	1.84e-09	2.79e-09	1.85e-08	1.87e-08	3.09e-08
	30060	7.27e-10	1.02e-09	7.37e-09	2.04e-08	1.26e-08
	34637	2.86e-10	3.48e-10	2.93e-09	2.45e-08	4.07e-09
	39402	1.18e-10	7.40e-11	1.24e-09	2.43e-08	1.01e-09
54074	6.16e-11	1.09e-10	6.03e-10	3.40e-08	5.69e-09	
58064	1.19e-11	5.66e-11	1.12e-10	4.32e-08	1.65e-08	
68404	1.24e-12	7.29e-11	3.29e-11	4.65e-08	1.92e-08	
75923	4.16e-12	8.11e-11	6.41e-11	4.76e-08	1.97e-08	
110080	4.76e-12	8.01e-11	7.01e-11	4.76e-08	1.97e-08	
$P_2 = (-0.05, 0.05)$	65	4.07e-02	3.21e-01	1.80e-01	3.32e-00	5.44e-00
	195	1.70e-02	4.41e-01	6.91e-02	8.66e-00	4.05e-00
	256	6.50e-03	3.16e-01	5.96e-03	9.55e-00	1.17e-00
	460	6.28e-04	4.82e-03	8.34e-03	7.26e-00	1.75e-00
	773	1.06e-03	2.21e-04	1.71e-02	7.62e-00	6.48e-01
	1408	2.31e-04	1.66e-03	3.85e-03	1.26e-00	8.10e-01
	2501	9.35e-05	1.03e-03	3.62e-04	1.81e-01	1.18e-01
	3151	3.41e-05	1.48e-04	3.46e-04	2.51e-02	5.26e-02
	4900	1.33e-05	6.82e-05	1.21e-04	1.41e-02	1.83e-02
	9200	5.12e-06	1.61e-06	5.88e-05	1.18e-02	1.43e-02
	12771	1.84e-06	1.02e-05	1.58e-05	2.63e-03	2.18e-03
	18066	6.88e-07	5.14e-06	4.54e-06	2.19e-04	1.84e-05
	24278	2.36e-07	1.66e-06	1.66e-06	1.03e-06	5.34e-05
	27834	9.43e-08	6.65e-07	6.59e-07	2.99e-06	1.62e-05
	30060	3.74e-08	2.67e-07	2.58e-07	4.67e-06	1.52e-06
	34637	1.49e-08	1.03e-07	1.03e-07	6.66e-06	4.88e-06
	39402	6.21e-09	4.36e-08	4.36e-08	1.23e-07	1.57e-06
54074	3.36e-09	2.36e-08	2.36e-08	2.52e-09	7.72e-07	
58064	8.50e-10	5.97e-09	5.97e-09	2.60e-09	1.99e-07	
68404	1.86e-10	1.30e-09	1.30e-09	4.61e-09	4.75e-08	
75923	4.23e-11	2.96e-10	2.96e-10	5.22e-09	1.30e-08	
110080	1.17e-11	8.16e-11	8.22e-11	1.67e-09	4.34e-09	

BEM-FEM discretizations, as discussed in the Introduction. Let  $\Omega$  be as in Example 2.3.3. In the present context, we view  $\Omega$  as being a (non-convex) mesh cell in a polygonal mesh, and we compute a local finite element stiffness matrix as described below. We note that rigid body motions and dilations of  $\Omega$  do not effect the element stiffness matrix in this case.

For  $0 \leq k \leq 5$ , let  $f_k \in C(\partial\Omega)$  be the piecewise linear function defined by the relations  $f_k(z_j) = \delta_{jk}$ . Taking  $f_k$  to be the Dirichlet data for the harmonic function  $\phi_k$ , the corresponding Neumann data for the harmonic conjugate is piecewise constant. The analytical solutions are unknown, but we numerically estimate  $\phi_k$ ,  $|\nabla\phi_k|$ , and  $\partial\phi_k/\partial\mathbf{n}$  and report the results in Figure 2.6, for the cases  $k = 0, 1, 2, 3$ . The cases  $k = 4, 5$  can be obtained by using the symmetry of the domain. We use  $n = 32$ ,  $p = 7$ , and  $\zeta = 8$ , and evaluate  $\phi_k$  and  $|\nabla\phi_k|$  on a uniform grid with spacing  $1/64$  to obtain the contour plots. Using  $n = 128$  and  $p = 7$  ( $\zeta$  is irrelevant in this case), the normal derivative is approximated as suggested in (2.32), and plotted versus the parameter  $t$  over  $[0, 12\pi]$ . We see that  $\partial\phi_k/\partial\mathbf{n}$  is unbounded at the non-convex corner ( $t = 0, 12\pi$ ) in each case, as is typically expected, and has jump discontinuities at some of the remaining corners. Increasing the parameters made no difference in these plots.

The  $6 \times 6$  element stiffness matrix  $A$  is defined by

$$a_{ij} = \int_{\Omega} \nabla\phi_j \cdot \nabla\phi_i \, dx = \int_{\partial\Omega} \frac{\partial\phi_j}{\partial\mathbf{n}} \phi_i \, ds .$$

Using the computed approximation of  $\partial\phi_j/\partial\mathbf{n}$ , we approximate  $a_{ij}$  as suggested in (2.32)-(2.33), employing trapezoid quadrature. To provide some indication of discretization parameters that will yield a good approximation of  $A$ , we approximate

the integrals

$$I_k = \int_{\partial\Omega} \frac{\partial u}{\partial \mathbf{n}} \phi_k ds ,$$

$0 \leq k \leq 5$ , where  $u$  is given in (2.36), using the same approach as that to compute the entries of  $A$ . The integrand  $\frac{\partial u}{\partial \mathbf{n}} \phi_k$  exhibits the same (asymptotic) singular behavior as each of the integrands  $\frac{\partial \phi_j}{\partial \mathbf{n}} \phi_i$ , and we can integrate it exactly, so it provides a reasonable benchmark for the integrals we really want to compute. For reference, the

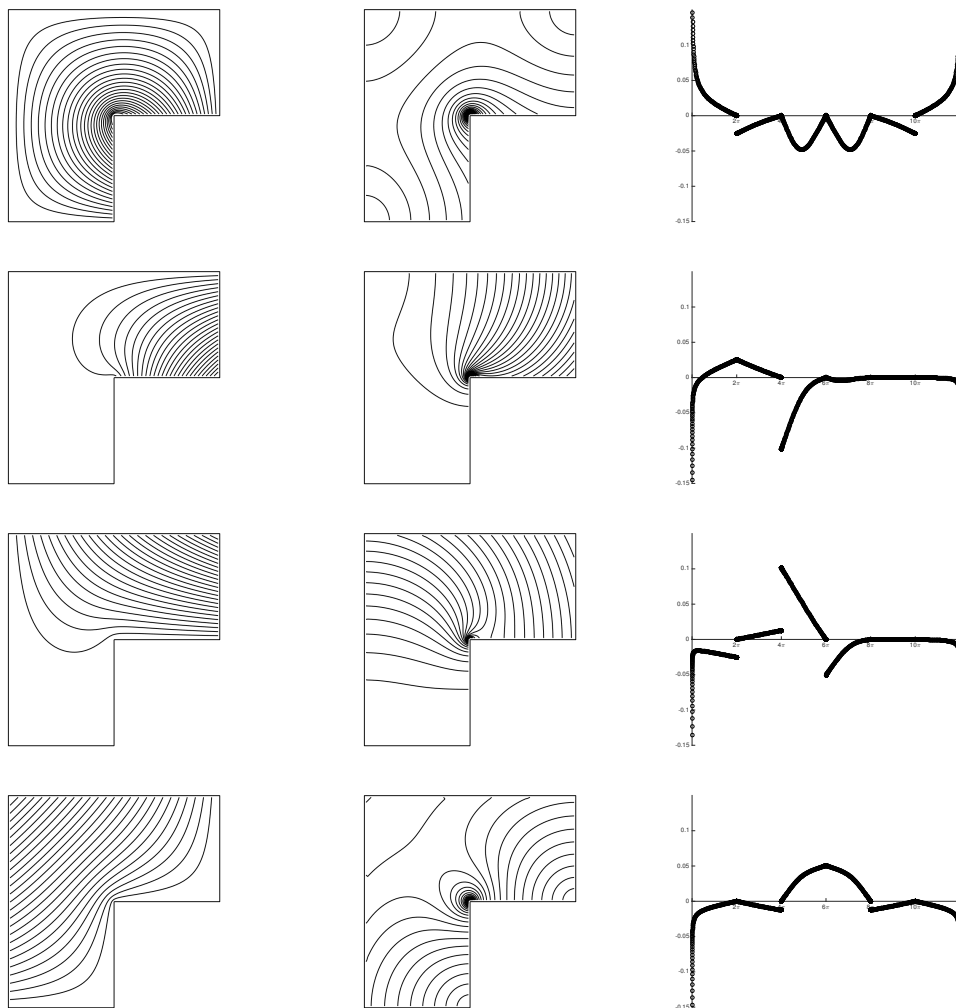


Figure 2.6: L-shaped Polygon: Contour plots of  $\phi_k$  (left column) and  $|\nabla \phi_k|$  (center column) for piecewise linear data considered in Example 2.3.4. The normal derivative  $\frac{\partial \phi_k}{\partial \mathbf{n}}$  is plotted in the right column. Rows correspond to  $k = 0, 1, 2, 3$ , respectively.

Table 2.8: L-shaped Polygon: Errors in computing  $I_k$ ,  $k = 0, 1, 2, 3$ .

$n$	$I_0$	$I_1$	$I_2$	$I_3$
8	1.5911e-03	8.7883e-06	3.2315e-05	1.9000e-04
16	7.0835e-05	8.2103e-07	4.5187e-07	9.4359e-07
32	2.8614e-06	2.1710e-09	1.1642e-09	2.7526e-09
64	1.1197e-07	4.4634e-12	5.3857e-13	2.4745e-12
128	4.4953e-09	1.1108e-13	1.4778e-12	4.5253e-13
256	7.0143e-11	2.5469e-13	8.9928e-15	5.4601e-13

exact values of  $I_k$  are given here:

$$I_0 = -6/5 = -1.2$$

$$I_1 = I_5 = -\frac{3}{5} - \frac{3}{5} \left( \frac{5 + 3\sqrt{3}}{2} \right)^{1/3} \approx -0.43265049655149479157 ,$$

$$I_2 = I_4 = \frac{3(1 + \sqrt{3})}{10(2)^{2/3}} \approx 0.51632524827574739578$$

$$I_3 = \frac{3(1 + \sqrt{3})}{5(2)^{2/3}} \approx 1.0326504965514947916 .$$

The errors in our approximations are given in Table 2.8. For these computations we fix  $p = 7$  and increase  $n$ .

We give the computed stiffness matrix for  $n = 256$  below, showing only 8 digits after the decimal due to space considerations.

$$A \approx \begin{pmatrix} 1.56907050 & -0.05893429 & -0.44613381 & -0.55893429 & -0.44613381 & -0.05893429 \\ -0.05893429 & 0.62426538 & -0.33906579 & -0.19359976 & -0.02120064 & -0.01146490 \\ -0.44613381 & -0.33906579 & 0.82273301 & 0.06986679 & -0.08619956 & -0.02120064 \\ -0.55893429 & -0.19359976 & 0.06986679 & 0.80640024 & 0.06986679 & -0.19359976 \\ -0.44613381 & -0.02120064 & -0.08619956 & 0.06986679 & 0.82273301 & -0.33906579 \\ -0.05893429 & -0.01146490 & -0.02120064 & -0.19359976 & -0.33906579 & 0.62426538 \end{pmatrix}$$

Although  $A$  is symmetric, we computed  $a_{ij}$  and  $a_{ji}$  independently to provide further indication that computations are working as expected. For  $n = 128$  and  $n = 256$ , the maximum entrywise errors of the computed  $A - A^T$  are  $2.54e-09$  and  $4.02e-11$ , respectively, with the worst errors being all of the same magnitude and occurring in the first row and column; all other errors are at least three orders of magnitude smaller. Since it holds that the nullspace of  $A$  is spanned by the vector of

ones,  $\mathbf{e} \in \mathbb{R}^6$ , we also consider  $A\mathbf{e}$  for the computed  $A$ . For  $n = 128$  and  $n = 256$ , the maximum entrywise errors of the computed  $A\mathbf{e}$  are  $1.02\text{e-}8$  and  $1.59\text{e-}10$ , respectively, and these occur in the first entry.

## 2.4. Conclusion

We have provided an efficient, high-order method for computing the normal derivative and interior derivatives of a harmonic function with prescribed Dirichlet data in planar domains that may have corners. Using the notion of harmonic conjugates and Cauchy's integral formulas, the computation of each of the quantities of interest was reduced to computations along the boundary of the domain, with the dominant cost being the solution of a second-kind Fredholm equation to compute the Dirichlet trace of a harmonic conjugate. This integral equation was solved using a high-order Nyström method, employing appropriate quadratures. The rapid convergence and high accuracy of the method was demonstrated through several examples for smooth and non-smooth domains, and a comparison with an hp-adaptive finite element was also provided. As a further application of our approach, we considered the formation of matrices associated with non-standard finite element methods on polygonal meshes, and this application will be pursued further in subsequent work.

## 2.5. References

- [1] I. Babuška and B. Q. Guo. Approximation properties of the  $h$ - $p$  version of the finite element method. *Comput. Methods Appl. Mech. Engrg.*, 133(3-4):319–346, 1996.
- [2] R. E. Bank. PLTMG: A software package for solving elliptic partial differential equations. Users' guide 12.0. Technical report, Department of Mathematics, University of California, San Diego, 2016.
- [3] R. E. Bank and H. Nguyen.  $hp$  adaptive finite elements based on derivative recovery and superconvergence. *Comput. Vis. Sci.*, 14(6):287–299, 2011.
- [4] R. E. Bank, J. Xu, and B. Zheng. Superconvergent derivative recovery for Lagrange triangular elements of degree  $p$  on unstructured grids. *SIAM J. Numer. Anal.*, 45(5):2032–2046 (electronic), 2007.
- [5] O. P. Bruno, J. S. Owall, and C. Turc. A high-order integral algorithm for highly singular PDE solutions in Lipschitz domains. *Computing*, 48(3):149–181, 2009.
- [6] D. Copeland, U. Langer, and D. Pusch. From the boundary element domain decomposition methods to local Trefftz finite element methods on polyhedral meshes. In *Domain decomposition methods in science and engineering XVIII*, volume 70 of *Lect. Notes Comput. Sci. Eng.*, pages 315–322. Springer, Berlin, 2009.
- [7] P. Grisvard. *Elliptic problems in nonsmooth domains*, volume 24 of *Monographs and Studies in Mathematics*. Pitman (Advanced Publishing Program), Boston, MA, 1985.
- [8] P. Henrici. Fast Fourier methods in computational complex analysis. *SIAM Rev.*, 21(4):481–527, 1979.
- [9] C. Hofreither.  $L_2$  error estimates for a nonstandard finite element method on polyhedral meshes. *J. Numer. Math.*, 19(1):27–39, 2011.
- [10] C. Hofreither, U. Langer, and C. Pechstein. Analysis of a non-standard finite element method based on boundary integral operators. *Electron. Trans. Numer. Anal.*, 37:413–436, 2010.
- [11] R. Kress. A Nyström method for boundary integral equations in domains with corners. *Numer. Math.*, 58(2):145–161, 1990.
- [12] R. Kress. *Linear integral equations*, volume 82 of *Applied Mathematical Sciences*. Springer, New York, third edition, 2014.

- [13] R. Kussmaul. Ein numerisches Verfahren zur Lösung des Neumannschen Aussenraumproblems für die Helmholtzsche Schwingungsgleichung. *Computing (Arch. Elektron. Rechnen)*, 4:246–273, 1969.
- [14] E. Martensen. Über eine Methode zum räumlichen Neumannschen Problem mit einer Anwendung für torusartige Berandungen. *Acta Math.*, 109:75–135, 1963.
- [15] E. J. Nyström. Über Die Praktische Auflösung von Integralgleichungen mit Anwendungen auf Randwertaufgaben der Potentialtheorie. *Soc. Sci. Fenn. Comment. Phys.-Math.*, 4(15):1–52, 1928.
- [16] E. J. Nyström. Über Die Praktische Auflösung von Integralgleichungen mit Anwendungen auf Randwertaufgaben. *Acta Math.*, 54(1):185–204, 1930.
- [17] S. Rjasanow and S. Weißer. Higher order BEM-based FEM on polygonal meshes. *SIAM J. Numer. Anal.*, 50(5):2357–2378, 2012.
- [18] S. Rjasanow and S. Weißer. FEM with Trefftz trial functions on polyhedral elements. *J. Comput. Appl. Math.*, 263:202–217, 2014.
- [19] Y. Saad and M. H. Schultz. GMRES: a generalized minimal residual algorithm for solving nonsymmetric linear systems. *SIAM J. Sci. Statist. Comput.*, 7(3):856–869, 1986.
- [20] L. Trefethen and J. Weideman. The exponentially convergent trapezoidal rule. *SIAM Review*, 56(3):385–458, 2014.
- [21] S. Weißer. Residual error estimate for BEM-based FEM on polygonal meshes. *Numer. Math.*, 118(4):765–788, 2011.
- [22] S. Weißer. Arbitrary order Trefftz-like basis functions on polygonal meshes and realization in BEM-based FEM. *Comput. Math. Appl.*, 67(7):1390–1406, 2014.
- [23] S. Weißer. Residual based error estimate and quasi-interpolation on polygonal meshes for high order BEM-based FEM. *Comput. Math. Appl.*, 73(2):187–202, 2017.
- [24] N. M. Wigley. Asymptotic expansions at a corner of solutions of mixed boundary value problems. *J. Math. Mech.*, 13:549–576, 1964.
- [25] S. S. Zargaryan and V. G. Maz'ya. The asymptotic form of the solutions of integral equations of potential theory in the neighbourhood of the corner points of a contour. *Prikl. Mat. Mekh.*, 48(1):169–174, 1984.

### 3. Trefftz Finite Elements on Curvilinear Polygons

#### Full citation information:

Akash Anand, Jeffrey S. Owall, Samuel E. Reynolds, and Steffen Weißer.  
Trefftz finite elements on curvilinear polygons. *SIAM Journal on Scientific Computing*, 42(2):A1289–A1316, 2020.

**Authors:** Akash Anand<sup>1</sup>, Jeffrey S. Owall<sup>2</sup>, Samuel E. Reynolds<sup>2</sup>, and Steffen Weißer<sup>3</sup>

#### Author contribution statement:

- Akash Anand: investigation, review and editing
- Jeffrey S. Owall: established theoretical results, developed algorithms, drafted the paper
- Samuel E. Reynolds: implemented numerical examples, investigation, review and editing
- Steffen Weißer: investigation, review and editing

**DOI:** 10.1137/19M1294046

---

<sup>1</sup>Indian Institute of Technology, Kanpur, UP 208016, India

<sup>2</sup>Fariborz Maseeh Department of Mathematics and Statistics, Portland State University, Portland, OR 97201

<sup>3</sup>Department of Mathematics, Saarland University, 66041 Saarbrücken, Germany

**Hyperlink to the publication in PDXScholar:**

<https://archives.pdx.edu/ds/psu/29392>

**Additional information:** This work was partially supported by the NSF Grants DMS-1522471 and DMS-1624776. Numerical studies were facilitated by the Portland Institute for Computational Sciences.

## Abstract

We present a Trefftz-type finite element method on meshes consisting of curvilinear polygons. Local basis functions are computed using integral equation techniques that allow for the efficient and accurate evaluation of quantities needed in the formation of local stiffness matrices. To define our local finite element spaces in the presence of curved edges, we must also properly define what it means for a function defined on a curved edge to be “polynomial” of a given degree on that edge. We consider two natural choices, before settling on the one that yields the inclusion of complete polynomial spaces in our local finite element spaces, and discuss how to work with these edge polynomial spaces in practice. An interpolation operator is introduced for the resulting finite elements, and we prove that it provides optimal order convergence for interpolation error under reasonable assumptions. We provide a description of the integral equation approach used for the examples in this paper, which was recently developed precisely with these applications in mind. A few numerical examples illustrate this optimal order convergence of the finite element solution on some families of meshes in which every element has at least one curved edge. We also demonstrate that it is possible to exploit the approximation power of locally singular functions that may exist in our finite element spaces in order to achieve optimal order convergence without the typical adaptive refinement toward singular points.

### 3.1. Introduction

Polygonal and polyhedral meshes in finite element analysis for the numerical treatment of boundary value problems have attracted a lot of interest during the last few years due to their enormous flexibility. They resolve the paradigm of a small class of element shapes (e.g. triangles, quadrilaterals, tetrahedra, etc.) in finite element

methods (FEM) and therefore open the possibility for very problem adapted mesh handling. This comes with an easy realization of local mesh refinement, coarsening and adaptation near singularities and interfaces. In particular, the notion of such general meshes naturally deal with “hanging nodes”—allowing two edges of a polygon to meet at a straight angle removes the notion of hanging nodes altogether. Virtual Element Methods (VEM) (cf. [2, 4–6, 9–14, 25, 40]), which have drawn inspiration from mimetic finite difference schemes, constitute one active line of research in this direction. Another involves Boundary Element-Based Finite Element Methods (BEM-FEM) (cf. [27, 50–52, 68, 69, 81–86]), which have looked more toward the older Trefftz methods for motivation. A similar strategy has been followed in our previous work [3], where a Nyström approximation is applied for the treatment of local boundary integral equations instead of a boundary element method. The gained insights and flexibilities in that work build the basis of the development in this paper. A third line of research involves generalized barycentric coordinates (cf. [38, 42, 43, 59, 67, 72] and the references in [39]), that mimic certain key properties of standard barycentric coordinates over general element shapes. The before mentioned approaches yield globally-conforming discretizations, which is challenging on general meshes. However, there has also been significant interest in various non-conforming methods for polyhedral meshes. We mention Compatible Discrete Operator (CDO), Hybrid High-Order (HHO) schemes (cf. [18–21, 32–34]) and Weak Galerkin (WG) schemes (cf. [62–64, 77–80]), as well as the recent adaptations of the discontinuous Petrov-Galerkin method (cf. [75]), in this regard.

The present work builds upon [3] for second-order, linear, elliptic boundary value problems posed on possibly curved domains  $\Omega \subset \mathbb{R}^2$ : Find  $u \in \mathcal{H}$  such that

$$\int_{\Omega} A \nabla u \cdot \nabla v + (\mathbf{b} \cdot \nabla u + cu)v \, dx = \int_{\Omega} f v \, dx + \int_{\partial\Omega_N} g v \, ds \text{ for all } v \in \mathcal{H}, \quad (3.1)$$

where  $\mathcal{H}$  is some appropriate subspace of  $H^1(\Omega)$  incorporating homogeneous Dirichlet boundary conditions, and standard assumptions on the data  $A, \mathbf{b}, c, f, g$  ensure that the problem is well-posed. Although polygonal meshes are quite flexible and have been studied intensively in recent years, there are relatively few results in this direction that allow for curved elements in the spirit of polygonal meshes, despite their natural appeal in fitting curved domain boundaries and interfaces. Early efforts at treating curved boundaries in the finite element context, such as isoparametric elements (cf. [15, 56, 71]), involve (local) mappings of standard mesh cells to fit curved boundaries, and these methods remain popular today. More recently, isogeometric analysis (cf. [28]), which integrates the use of splines both for modeling complex (curved) geometries and in constructing finite elements on the resulting meshes. This remains an active area of research. Two recent contributions employing non-conforming methods over curved polygonal elements are described in [21, 24]. In terms of conforming methods for treating curved boundaries that are in the same vein as the conforming polygonal methods mentioned in the first paragraph, we mention four, all of which are very recent. In [16], the curved boundary of the domain is approximated by polygonal elements with straight edges and a stabilization is constructed such that optimal rates of convergence are retained for high order methods. In contrast, [10] gives a first study of VEM with polygonal elements having curved edges in 2D for the treatment of curved boundaries and interfaces, but the construction results in  $\mathbb{P}_p(K) \not\subset V_p(K)$ , i.e. the polynomials of degree smaller or equal  $p$  are locally not contained in the local approximation space of order  $p$ . This introduces additional difficulties in the study of approximation properties. More recently, these authors work with a richer finite element space of functions for which  $\mathbb{P}_p(K) \subset V_p(K)$ , see [8]. This richer space is referred to as “Type 2 elements” in our previous contribution [3], which considered the natural incorporation of Dirichlet data on curved (or straight) portions. Our present

work provides a practical realization, as well as supporting interpolation theory, for Type 2 elements on very general planar meshes consisting of curvilinear polygons. As both our work and [8] must address many of the same theoretical and practical concerns, it is unsurprising that there are strong similarities between the approaches, and comparisons between them will be of interest as both are developed further.

The paper is organized as follows: In Section 3.2 we describe local and global finite element spaces allowing for mesh cells that are fairly general curvilinear polygons. As is done in VEM and BEM-FEM, as well as our previous Trefftz-Nyström contribution [3], the local spaces are defined in terms of Poisson problems with polynomial data on the mesh cells. For curved edges, we discuss two natural choices (those suggested in [3]) for what it means to have polynomial boundary data on curved edges. The one that we believe is the more appropriate of the two requires further explanation concerning how these edge polynomial spaces and their bases can be constructed in practice, and the bulk of Section 3.2 is devoted to doing so. Having defined the local and global spaces, Section 3.3 provides an interpolation operator, and establishes that interpolation in these spaces is at least as good as interpolation by polynomials in more standard (e.g. triangular, quadrilateral) meshes, as well as interpolation in straight-edged polygonal meshes. In brief, it is established that the inclusion of  $\mathbb{P}_p(K)$  in our local spaces  $V_p(K)$  provides the expected approximation power, and the presence of other (possibly singular) functions in  $V_p(K)$  is not detrimental. In [3], an example illustrated that such locally singular functions can even be beneficial for approximation, and we develop that argument further in the final example of Section 3.5. Section 3.4 provides a description of the integral equation approach we use for computing the information about our basis functions that is needed in forming finite element stiffness matrices. This approach, which was developed with our present application in mind, is discussed in detail in our previous work [65], so

we here provide a broader description of the approach and some of its key features. Finally, Section 3.5 provides several examples illustrating the convergence of the finite element solution on different families of meshes whose elements each have at least one curved edge, including a comparison of convergence and conditioning for Type 1 and Type 2 elements on families of meshes whose curved edges are very close to being straight. As mentioned above, in the final example of this section we both argue and demonstrate that it is possible to exploit the approximation power of locally singular functions that may exist in our finite element spaces in order to achieve optimal order convergence without the typical adaptive refinement toward singular points.

### 3.2. Local and Global Spaces

Following [26, 36], let  $K$  be a connected subset of  $\mathbb{R}^2$ , with non-empty interior and compact closure, whose Lipschitz boundary,  $\partial K$ , is a simple closed contour consisting of a finite union of smooth arcs, see Figure 3.1. We will refer to  $K$  as a *mesh cell*, the arcs as *edges*, and will implicitly assume that adjacent edges meet at an (interior) angle strictly between 0 and  $2\pi$ , i.e.  $K$  has no slits or cusps. We allow adjacent edges to meet at a straight angle. The *vertices* of  $K$  are those points where two adjacent edges meet. Given an integer  $p$  and a mesh cell  $K$ , we define the space  $\mathbb{P}_p(K)$  to be the polynomials of (total) degree at most  $p$  on  $K$ , with  $\mathbb{P}_p(K) = \{0\}$  for  $p < 0$ , and the space  $\mathbb{P}_p(\partial K)$  to be continuous functions on  $\partial K$  whose trace on each edge  $e$  is the trace of a function from  $\mathbb{P}_p(K)$  (equivalently, from  $\mathbb{P}_p(\mathbb{R}^2)$ ) on  $e$ , and we denote by  $\mathbb{P}_p(e)$  this edge trace space. In [3], we refer to this definition of  $\mathbb{P}_p(e)$  as its *Type 2* version; the *Type 1* version consists of functions on  $e$  that are polynomials with respect to a natural parameter, such as arc length, in a parametrization of  $e$ . In order to avoid unnecessary complications in our description, we will assume that no edge is a closed contour, i.e. each edge has two distinct endpoints, and that  $K$  is

simply-connected. This is not a necessary constraint in practice, but allowing for even more general elements, such as those having no vertices, or those that are not simply-connected (i.e. have holes) requires using different integral equation techniques. We briefly highlight this issue in Section 3.4.

Let  $\Omega \subset \mathbb{R}^2$  be a bounded domain with Lipschitz boundary. Given a partition  $\mathcal{T} = \{K\}$  of  $\Omega$ , we define  $V_p(\mathcal{T})$  by

$$V_p(\mathcal{T}) = \{v \in C(\overline{\Omega}) : v|_K \in V_p(K) \text{ for all } K \in \mathcal{T}\}, \quad (3.2)$$

where we define the space  $V_p(K)$  as follows,

$$v \in V_p(K) \text{ if and only if } \Delta v \in \mathbb{P}_{p-2}(K) \text{ in } K \text{ and } v|_{\partial K} \in \mathbb{P}_p(\partial K). \quad (3.3)$$

The space  $V_p(K)$  clearly contains  $\mathbb{P}_p(K)$ , but it typically contains other functions as well. A natural decomposition of  $V_p(K)$  is  $V_p(K) = V_p^K(K) \oplus V_p^{\partial K}(K)$ , where

$$v \in V_p^K(K) \text{ if and only if } \Delta v \in \mathbb{P}_{p-2}(K) \text{ in } K \text{ and } v = 0 \text{ on } \partial K, \quad (3.4)$$

$$v \in V_p^{\partial K}(K) \text{ if and only if } \Delta v = 0 \text{ in } K \text{ and } v|_{\partial K} \in \mathbb{P}_p(\partial K). \quad (3.5)$$

The dimension of  $V_p(K)$  is

$$\begin{aligned} \dim V_p(K) &= \dim V_p^K(K) + \dim V_p^{\partial K}(K) \\ &= \dim \mathbb{P}_{p-2}(K) + \dim \mathbb{P}_p(\partial K) = \binom{p}{2} + \dim \mathbb{P}_p(\partial K). \end{aligned} \quad (3.6)$$

The dimension of  $\mathbb{P}_p(\partial K)$  depends on the number and nature of the edges of  $K$ . If  $e$  is a straight edge,  $\dim \mathbb{P}_p(e) = p+1$ , but if  $e$  is not a straight edge, the dimension of  $\mathbb{P}_p(e)$  can be as high as  $\binom{p+2}{2}$ , as it is when  $p = 1$ . The dimension of  $\mathbb{P}_p(e)$  more generally is given in the following proposition, a proof of which may be found in [60, Theorem 7.1], for example.

**Proposition 3.2.1.** Suppose that  $f_m \in \mathbb{P}_m(\mathbb{R}^2)$  is an irreducible polynomial of degree

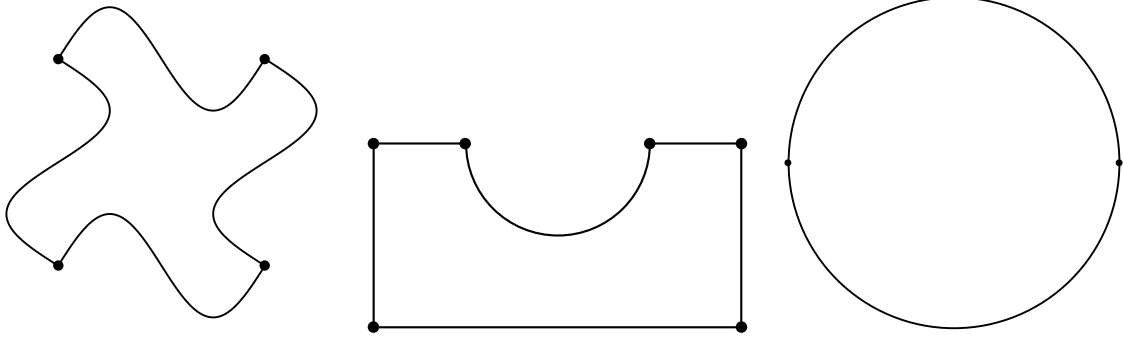


Figure 3.1: Shuriken (quadrilateral), Half-Washer (hexagon), Two-Edge Circle (bigon).

$m$ , and that all points  $x \in e$  satisfy  $f_m(x) = 0$ . It holds that  $\dim \mathbb{P}_p(e) = \binom{p+2}{2} - \binom{p-m+2}{2}$ . If  $e$  does not lie on a real algebraic curve in the plane, then  $\dim \mathbb{P}_p(e) = \binom{p+2}{2}$ .

*Example 3.2.2.* We consider the dimensions of the spaces  $V_p(K) = V_p^K(K) \oplus V_p^{\partial K}(K)$ ,  $p = 1, 2$ , for each of the three mesh cells in Figure 3.1. We have  $\dim V_1^K(K) = 0$  and  $\dim V_2^K(K) = 1$ . The continuity of functions in  $\mathbb{P}_p(\partial K)$  implies that

$$\dim V_p^{\partial K}(K) = \dim \mathbb{P}_p(\partial K) = \sum_{e \subset \partial K} \dim \mathbb{P}_p(e) - \# \text{ edges} . \quad (3.7)$$

This formula holds for arbitrary  $p$ . For  $p = 1, 2$ , we have

$$\begin{aligned} \dim V_1^{\partial K}(K) &= (\# \text{ straight edges}) + 2(\# \text{ curved edges}) , \\ \dim V_2^{\partial K}(K) &= 2(\# \text{ straight edges}) + 4(\# \text{ curved conic edges}) \\ &\quad + 5(\# \text{ curved non-conic edges}) . \end{aligned}$$

For the Half-Washer and Two-Edge Circle, the curved edges are circular arcs. For the Shuriken, the curved edges are not segments of curved conic sections (ellipses, parabolas, hyperbolas). Therefore, the dimensions of these spaces are

	Shuriken	Half-Washer	Two-Edge Circle
$\dim V_1(K)$	$0+(0)+2(4)=8$	$0+(5)+2(1)=7$	$0+(0)+2(2)=4$
$\dim V_2(K)$	$1+2(0)+4(0)+5(4)=21$	$1+2(5)+4(1)+5(0)=15$	$1+2(0)+4(2)+5(0)=9$

A basis for  $\mathbb{P}_{p-2}(K)$  implicitly defines a basis for  $V_p^K(K)$ . In Section 3.4, we describe how we form the associated local finite element linear systems over  $V_p(K)$ , using integral equations to get the relevant information about our basis functions. At this stage, we merely state that it is convenient to compute harmonic functions in this context. To this end, let  $z$  be a point in  $K$ , and  $\alpha = (\alpha_1, \alpha_2)$  be a multi-index. In [54], the authors provide an explicit formula for a polynomial  $q_\alpha \in \mathbb{P}_p(K)$  satisfying  $\Delta q_\alpha = (x - z)^\alpha$ ; see also the beginning of Section 3.4. A basis of  $V_p^K(K)$ ,  $\{\phi_\alpha^K \in \mathbb{P}_p(K) : |\alpha| \leq p\}$ , is given by  $\phi_\alpha^K = \psi_\alpha^K + q_\alpha$ , where

$$\Delta \psi_\alpha^K = 0 \text{ in } K \quad , \quad \psi_\alpha^K = -q_\alpha \text{ on } \partial K \quad . \quad (3.8)$$

Similarly, a basis of  $\mathbb{P}_p(\partial K)$  naturally leads to a basis of  $V_p^{\partial K}(K)$ . Given an edge  $e$  in the mesh, we describe an approach for obtaining a basis of  $\mathbb{P}_p(e)$  that is independent of the mesh cell(s) of which it is an edge. Let  $e$  have vertices  $z_0, z_1$ . We choose a third point  $z_2$  such that  $z_0, z_1, z_2$  are the vertices of an equilateral triangle (see Figure 3.2)—note that  $z_2$  typically has nothing to do with the underlying mesh  $\mathcal{T}$ . Given a global numbering of the vertices of the mesh, this can be done in a consistent way by choosing  $z_2$  such that a counter-clockwise traversal of the boundary of the triangle is consistent with traversing the edge  $e$  from its smaller to its larger vertex numbers. Let  $\ell_0, \ell_1, \ell_2 \in \mathbb{P}_1(\mathbb{R}^2)$  be the three barycentric coordinates associated with these vertices. Formulas for these three functions are given by

$$\ell_j(x) = 1 - \frac{(x - z_j) \cdot R(z_{j-1} - z_{j+1})}{(\sqrt{3}/2)h^2} \quad , \quad (3.9)$$

where we understand the subscripts modulo 3 (i.e.  $z_{-1} = z_2$  and  $z_3 = z_0$ ), and

$$R = \begin{pmatrix} 0 & 1 \\ -1 & 0 \end{pmatrix} \quad , \quad h = |z_1 - z_0| \quad , \quad z_2 = \frac{z_1 + z_0}{2} - R \cdot \frac{\sqrt{3}(z_1 - z_0)}{2} \quad .$$

Any basis for  $\mathbb{P}_p(\mathbb{R}^2)$  yields a spanning set for  $\mathbb{P}_p(e)$  by restriction, and such a basis

may be expressed in terms of linear combinations of products of the barycentric coordinates. We will consider hierarchical bases expressed in this way (cf. [1, 17, 74]). For example, a hierarchical basis for  $\mathbb{P}_3(\mathbb{R}^2)$  is

$$\left\{ \ell_0, \ell_1, \ell_2, 4\ell_1\ell_2, 4\ell_0\ell_2, 4\ell_0\ell_1, \frac{3\sqrt{3}}{2}\ell_1\ell_2(\ell_1 - \ell_2), \right. \\ \left. \frac{3\sqrt{3}}{2}\ell_0\ell_2(\ell_0 - \ell_2), \frac{3\sqrt{3}}{2}\ell_0\ell_1(\ell_0 - \ell_1), 27\ell_0\ell_1\ell_2 \right\}, \quad (3.10)$$

Here, we have chosen the scaling on each function so that its maximum value on the triangle, in magnitude, is 1. In any hierarchical basis for  $\mathbb{P}_p(\mathbb{R}^2)$ , the only functions that do not vanish at both  $z_0$  and  $z_1$  are  $\ell_0$  and  $\ell_1$ . A simple consequence of this fact is that

**Proposition 3.2.3.** For any edge  $e$ , a hierarchical basis of  $\mathbb{P}_p(e)$  contains both  $\ell_0$  and  $\ell_1$ .

As stated in Proposition 3.2.1, if  $e$  lies on an algebraic curve of order  $m$ , we know the dimension of  $\mathbb{P}_p(e)$ . However, it may be undesirable to make this determination in practice. Regardless, we need a practical method for paring down a spanning set for  $\mathbb{P}_p(e)$  to a basis. Let  $N = \binom{p+2}{2}$ , and suppose that  $\{\ell_0, \ell_1, b_1, \dots, b_{N-2}\}$  is a hierarchical spanning set of  $\mathbb{P}_p(e)$ , as described above. The functions are listed in increasing order of degree. The Gram matrix  $m_{ij} = \int_e b_i b_j ds$  may be used to determine the remaining basis functions (in addition to  $\ell_0, \ell_1$ ) for  $\mathbb{P}_p(e)$ . We recall that  $\text{rank}(M) = \dim \text{span}\{b_1, \dots, b_{N-2}\}$  (cf. [53, Theorem 7.2.10]). A basis for  $\text{span}\{b_1, \dots, b_{N-2}\}$  consisting of some subset of these functions may be determined using a rank-revealing Cholesky decomposition of  $M$  (cf. [47–49]). We state a slightly more general version of this result in the following proposition, and then provide a simple algorithm for selecting a basis of  $\text{span}\{b_1, \dots, b_{N-2}\}$ , and hence of  $\mathbb{P}_p(e)$ .

**Proposition 3.2.4.** Let  $m_{ij} = \langle b_j, b_i \rangle$ ,  $1 \leq i, j \leq n$  be the Gram matrix associated

with an inner-product  $\langle \cdot, \cdot \rangle$  and a list of vectors  $(b_1, \dots, b_n)$ . Let  $P^T M P = R^T R$  be a rank-revealing Cholesky decomposition, where  $P$  is a permutation matrix, and  $R = \begin{pmatrix} R_{11} & R_{12} \end{pmatrix}$ , with the  $r \times r$  matrix  $R_{11}$  having strictly positive entries. Then  $\{b_{p(j)} : 1 \leq j \leq r\}$  is a basis for  $\text{span}\{b_1, \dots, b_n\}$ , where  $p$  is the permutation on  $\{1, \dots, n\}$  defined by  $P\mathbf{e}_j = \mathbf{e}_{p(j)}$ , and  $\{\mathbf{e}_1, \dots, \mathbf{e}_n\}$  are the standard coordinate vectors.

The following algorithm is essentially Gaussian elimination with complete pivoting for positive semi-definite matrices, where the pivoting is done in place.

**Algorithm 3.2.5.** Let  $m_{ij} = \langle b_j, b_i \rangle$ ,  $1 \leq i, j \leq n$ , be the Gram matrix associated with an inner-product  $\langle \cdot, \cdot \rangle$  and a list of vectors  $(b_1, \dots, b_n)$ . Upon termination of the following algorithm,  $\text{index} = \{p(j) : 1 \leq j \leq r\}$ , the indices of a basis  $\{b_{p(j)} : 1 \leq j \leq r\}$  of  $\text{span}\{b_1, \dots, b_n\}$ :

```

index = {}
k = arg max{mjj : 1 ≤ j ≤ n}
while mkk > 0
    index = index ∪ {k}
    M = M - mkk-1 mk mkT
    k = arg max{mjj : 1 ≤ j ≤ n}
end

```

Here,  $\mathbf{m}_k$  is the  $k^{\text{th}}$  column of the current  $M$ .

In practice, one replaces the condition  $m_{kk} > 0$  with  $m_{kk} > \tau$  for some suitably small tolerance  $\tau > 0$ . Some speed-up of this basic algorithm may be achieved by exploiting the fact that previous reduction steps,  $M = M - m_{kk}^{-1} \mathbf{m}_k \mathbf{m}_k^T$ , have zeroed out the rows and columns in the index set, so these are no longer needed for further reductions. In the following example, we use  $\tau = 10^{-12}$  in our determination of a basis for  $\mathbb{P}_3(e)$ .

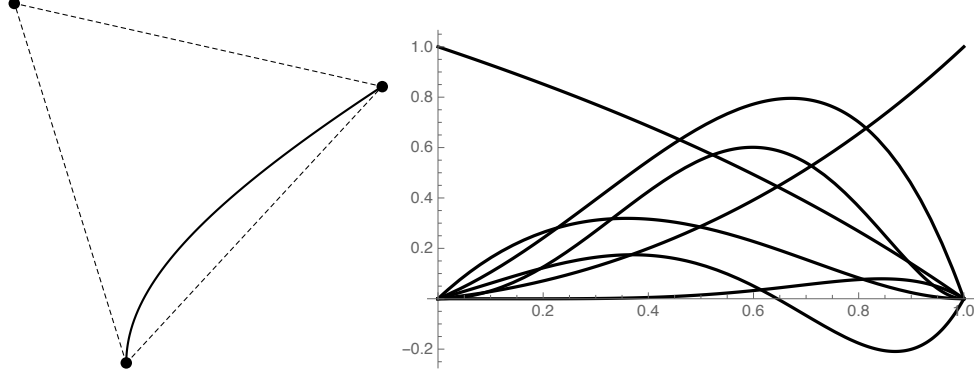


Figure 3.2: At left, the edge  $e$  and associated triangle (dashed) for Example 3.2.6. At right, plots of a basis for  $\mathbb{P}_3(e)$  with respect to a parametrization,  $x = x(t)$ , of  $e$ .

*Example 3.2.6.* For any edge  $e$ , a hierarchical spanning set for  $\mathbb{P}_3(e)$  is given by (3.10) where we have restricted the domains of these functions to  $e$ . Let  $e$  be parameterized by  $x(t) = (\cosh t, (\sinh t)/2)$ ,  $0 \leq t \leq 1$ , so  $e$  is part of the hyperbola  $x^2 - 4y^2 = 1$ . We know in advance that  $\dim \mathbb{P}_3(e) = 10 - 3 = 7$ , and  $\ell_0, \ell_1$  will be part of our basis for  $\mathbb{P}_3(e)$ , so we must select five of the remaining eight functions,

$$\left\{ \ell_2, 4\ell_1\ell_2, 4\ell_0\ell_2, 4\ell_0\ell_1, \frac{3\sqrt{3}}{2}\ell_1\ell_2(\ell_1 - \ell_2), \frac{3\sqrt{3}}{2}\ell_0\ell_2(\ell_0 - \ell_2), \frac{3\sqrt{3}}{2}\ell_0\ell_1(\ell_0 - \ell_1), 27\ell_0\ell_1\ell_2 \right\},$$

to complete our basis. Taking the functions in this order, and forming the associated Gram matrix, we determine that the indices are (given in the order computed): 4, 7, 8, 3, 5; the knowledge that we only needed five functions was not used in this computation. Therefore, our basis for  $\mathbb{P}_3(e)$  is given by

$$\left\{ \ell_0, \ell_1, 4\ell_0\ell_2, 4\ell_0\ell_1, \frac{3\sqrt{3}}{2}\ell_1\ell_2(\ell_1 - \ell_2), \frac{3\sqrt{3}}{2}\ell_0\ell_1(\ell_0 - \ell_1), 27\ell_0\ell_1\ell_2 \right\}.$$

These basis functions are plotted, as functions of the parameter  $t$ , in Figure 3.2, together with the edge  $e$  and associated triangle used to define the barycentric coordinates  $\ell_0, \ell_1, \ell_2$ . As a matter of interest, we note that, when the reduction algorithm

was used, with  $\tau = 10^{-12}$  as before, on the entire spanning set (3.10), a different basis was obtained,

$$\left\{ \ell_0, \ell_1, 4\ell_1\ell_2, 4\ell_0\ell_2, 4\ell_0\ell_1, \frac{3\sqrt{3}}{2}\ell_1\ell_2(\ell_1 - \ell_2), \frac{3\sqrt{3}}{2}\ell_0\ell_2(\ell_0 - \ell_2) \right\} .$$

*Remark 3.2.7.* A natural variant of Algorithm 3.2.5 that may be used if the diagonal entries of  $M$  are all non-zero is to diagonally rescale its entries,  $m_{ij} \leftarrow m_{ij}/\sqrt{m_{ii}m_{jj}}$ , before beginning the elimination loop. If we do this for Example 3.2.6, the resulting basis for  $\mathbb{P}_3(e)$  is

$$\left\{ \ell_0, \ell_1, \ell_2, \frac{3\sqrt{3}}{2}\ell_1\ell_2(\ell_1 - \ell_2), \frac{3\sqrt{3}}{2}\ell_0\ell_2(\ell_0 - \ell_2), \frac{3\sqrt{3}}{2}\ell_0\ell_1(\ell_0 - \ell_1), 27\ell_0\ell_1\ell_2 \right\} ,$$

regardless of whether we use the entire spanning set (3.10), or remove  $\{\ell_0, \ell_1\}$ , in constructing  $M$ .

*Remark 3.2.8.* We describe an alternative to the barycentric coordinates (3.9) associated with  $e$  that acts more like a local cartesian coordinate system. Using the same notation  $z_0, z_1, h$  and  $R$ , we define

$$\begin{aligned} \tilde{\ell}_0(x) &= \frac{(z_1 - x) \cdot (z_1 - z_0)}{h^2} , & \tilde{\ell}_1(x) &= \frac{(x - z_0) \cdot (z_1 - z_0)}{h^2} , \\ \tilde{\ell}_2(x) &= \frac{(z_1 - x) \cdot R(z_1 - z_0)}{h^2} . \end{aligned} \tag{3.11}$$

Straight-forward manipulations reveal that

$$\ell_0 = \tilde{\ell}_0 - \frac{\tilde{\ell}_2}{\sqrt{3}} , \quad \ell_1 = \tilde{\ell}_1 - \frac{\tilde{\ell}_2}{\sqrt{3}} , \quad \ell_2 = \frac{\tilde{\ell}_2}{\sqrt{3}/2} ,$$

so it is simple to translate between coordinate systems if desired.

Having now properly defined  $V_p(\mathcal{T}) \subset H^1(\Omega)$ , the discrete version of (3.1) is to

find  $\widehat{u} \in V_p(\mathcal{T}) \cap \mathcal{H}$  such that

$$\int_{\Omega} A \nabla \widehat{u} \cdot \nabla v + (\mathbf{b} \cdot \nabla u + c \widehat{u}) v \, dx = \int_{\Omega} f v \, dx + \int_{\partial \Omega_N} g v \, ds \quad (3.12)$$

for all  $v \in V_p(\mathcal{T}) \cap \mathcal{H}$ .

The intersection,  $V_p(\mathcal{T}) \cap \mathcal{H}$ , ensures that we respect any homogeneous Dirichlet boundary conditions inherent in  $\mathcal{H}$ . For standard finite elements, as well as those defined on more general polygonal meshes, common assumptions on the data ensure that the finite element error  $\|u - \widehat{u}\|_{H^1(\Omega)}$  is controlled by interpolation error  $\|u - \mathcal{I}u\|_{H^1(\Omega)}$ , where  $\mathcal{I}u \in V_p(\mathcal{T})$  is some appropriately defined interpolant of  $u$ . In the next section, we define a projection-based interpolation operator appropriate for our setting, and prove that it yields the desired approximation properties.

### 3.3. Interpolation

In this section, we describe a local interpolation scheme

$$\mathcal{I}_K : W(K) = \{v \in C(\overline{K}) \cap H^1(K) : \Delta v \in L^2(K)\} \rightarrow V_p(K), \quad (3.13)$$

and establish local error estimates under stronger regularity assumptions. By construction, the local interpolation operator will define a global interpolation operator

$$\mathcal{I} : W = \{v \in C(\overline{\Omega}) \cap H^1(\Omega) : \Delta v \in L^2(\Omega)\} \rightarrow V_p(\mathcal{T}) \quad (3.14)$$

by  $(\mathcal{I}v)|_K = \mathcal{I}_K v$ .

Our definition of  $\mathcal{I}_K$  is motivated by the decomposition  $V_p(K) = V_p^K(K) \oplus V_p^{\partial K}(K)$ . We begin with a related decomposition of  $v$  as  $v = v^K + v^{\partial K}$ , where

$$\begin{cases} \Delta v^K = \Delta v & \text{in } K \\ v^K = 0 & \text{on } \partial K \end{cases}, \quad \begin{cases} \Delta v^{\partial K} = 0 & \text{in } K \\ v^{\partial K} = v & \text{on } \partial K \end{cases}. \quad (3.15)$$

We define  $\mathcal{I}_K$  by an analogous decomposition  $\mathcal{I}_K v = \mathcal{I}_K^K v + \mathcal{I}_K^{\partial K} v$ , where  $\mathcal{I}_K^K v \in V_p^K(K)$  and  $\mathcal{I}_K^{\partial K} v \in V_p^{\partial K}(K)$  are given by

$$\begin{cases} \Delta(\mathcal{I}_K^K v) = q^K & \text{in } K \\ \mathcal{I}_K^K v = 0 & \text{on } \partial K \end{cases}, \quad \begin{cases} \Delta(\mathcal{I}_K^{\partial K} v) = 0 & \text{in } K \\ \mathcal{I}_K^{\partial K} v = q^{\partial K} & \text{on } \partial K \end{cases}. \quad (3.16)$$

In order to complete this definition, we must define  $q^K \in \mathbb{P}_{p-2}(K)$  and  $q^{\partial K} \in \mathbb{P}_p(\partial K)$ .

We define  $q^K$  by

$$\int_K (\Delta v - q^K) \phi \, dx = 0 \text{ for all } \phi \in \mathbb{P}_{p-2}(K). \quad (3.17)$$

We define  $q^{\partial K}$  by defining it on each edge of  $\partial K$ . For a non-trivial open subset  $\Gamma \subset \partial K$ , we use the inner-product

$$(\phi, \psi)_{H^{1/2}(\Gamma)} = \int_{\Gamma} \phi \psi \, ds + \int_{\Gamma} \int_{\Gamma} \frac{(\phi(x) - \phi(y))(\psi(x) - \psi(y))}{|x - y|^2} \, ds(x) \, ds(y), \quad (3.18)$$

with  $\|\cdot\|_{H^{1/2}(\Gamma)}$  as the associated norm. Below, we take  $\Gamma$  to be either the entire boundary,  $\partial K$ , or a single edge,  $e$ . Fix an edge  $e$  of  $\partial K$ , having endpoints  $z_0, z_1$ , and let  $\mathbb{P}_{p,0}(e) = \{w \in \mathbb{P}_p(e) : w(z_0) = w(z_1) = 0\}$ . We define  $q_e \in \mathbb{P}_m(e)$  by the conditions

$$\begin{aligned} q_e(z_0) = v(z_0) \quad , \quad q_e(z_1) = v(z_1) \quad , \\ (v - q_e, w)_{H^{1/2}(e)} = 0 \text{ for all } w \in \mathbb{P}_{p,0}(e). \end{aligned} \quad (3.19)$$

Finally,  $q^{\partial K}$  is defined by  $(q^{\partial K})|_e = q_e$ .

In several places below, it will be convenient to use the following basic result. Suppose that  $\psi, \phi \in H^1(K)$ , and  $\Delta\psi = 0$  in  $K$  and  $\phi = 0$  on  $\partial K$ . Then  $\int_K \nabla\psi \cdot \nabla\phi \, dx = 0$ , so  $|\psi + \phi|_{H^1(K)}^2 = |\psi|_{H^1(K)}^2 + |\phi|_{H^1(K)}^2$ . For example, we have

$$|v - \mathcal{I}_K v|_{H^1(K)}^2 = |v^K - \mathcal{I}_K^K v|_{H^1(K)}^2 + |v^{\partial K} - \mathcal{I}_K^{\partial K} v|_{H^1(K)}^2, \quad (3.20)$$

and we consider both contributions to the interpolation error in turn. In the proofs below, we use  $c$  as a constant that may vary from one appearance to the next. Throughout,  $h_K$  denotes the diameter of  $K$ . We first consider  $v^K - \mathcal{I}_K^K v$ .

**Proposition 3.3.1.** Suppose that  $v \in H^1(K)$  and  $\Delta v \in H^{p-1}(K)$  for some  $p \geq 1$ . There is a scale-invariant constant  $c = c(p, K) > 0$  for which

$$|v^K - \mathcal{I}_K^K v|_{H^1(K)} \leq ch_K^p |\Delta v|_{H^{p-1}(K)} \quad , \quad \|v^K - \mathcal{I}_K^K v\|_{L^2(K)} \leq ch_K^{p+1} |\Delta v|_{H^{p-1}(K)} .$$

*Proof.* It holds that

$$\begin{aligned} |v^K - \mathcal{I}_K^K v|_{H^1(K)}^2 &= - \int_K (\Delta v - q^K)(v^K - \mathcal{I}_K^K v) \, dx \\ &\leq \|\Delta v - q^K\|_{L^2(K)} \|v^K - \mathcal{I}_K^K v\|_{L^2(K)} . \end{aligned}$$

Since  $v^K - \mathcal{I}_K^K v \in H_0^1(K)$ , the Poincaré-Friedrichs Inequality,  $\|w\|_{L^2(K)} \leq h_K |w|_K$  for  $w \in H_0^1(K)$ , ensures that

$$|v^K - \mathcal{I}_K^K v|_{H^1(K)} \leq h_K \|\Delta v - q^K\|_{L^2(K)} = h_K \inf_{\phi \in \mathbb{P}_{p-2}(K)} \|\Delta v - \phi\|_{L^2(K)} . \quad (3.21)$$

The estimate  $|v^K - \mathcal{I}_K^K v|_{H^1(K)} \leq ch_K^p |\Delta v|_{H^{p-1}(K)}$  follows from this by applying the Bramble-Hilbert Lemma. The  $L^2(K)$  norm result follows from this by applying the Poincaré-Friedrichs Inequality again.  $\square$

*Remark 3.3.2.* If  $K$  is convex,  $h_K$  can be replaced by  $h_K/\pi$  in (3.21) (cf. [66]). Furthermore, for convex  $K$ , the dependence on  $K$  of the constant  $c(p, K)$  coming from the Bramble-Hilbert Lemma in Proposition 3.3.1 can be removed, and for non-convex domains that are star-shaped with respect to a point, ball, or more general subdomain, various estimates of how  $c(p, K)$  depends on the shape of  $K$  have been established [29, 30, 35, 76].

For our analysis of  $v^{\partial K} - \mathcal{I}_K^{\partial K} v$  the following result will be useful.

**Proposition 3.3.3.** If  $v \in H^2(K)$  and  $\Delta v = 0$  in  $K$ , there is a scale-invariant constant  $c = c(K)$  for which

$$\|v\|_{L^\infty(K)} \leq c \inf \left\{ \begin{array}{l} h_K |w|_{H^2(K)} + |w|_{H^1(K)} + h_K^{-1} \|w\|_{L^2(K)} \\ : w \in H^2(K) \text{ and } w = v \text{ on } \partial K \end{array} \right\}. \quad (3.22)$$

*Proof.* For  $w \in H^2(K)$ , we have  $\|w\|_{L^\infty(K)} \leq c \|w\|_{H^2(K)}$  by a Sobolev embedding result. A standard scaling argument then yields

$$\|w\|_{L^\infty(K)} \leq c \left( h_K |w|_{H^2(K)} + |w|_{H^1(K)} + h_K^{-1} \|w\|_{L^2(K)} \right),$$

where  $c = c(K)$  is scale-invariant. Now (3.22) follows from the fact that harmonic functions on  $K$  attain their extrema on  $\partial K$ , so, if  $v, w \in H^2(K)$  have the same Dirichlet trace on  $\partial K$ , and  $v$  is harmonic on  $K$ , then  $\|v\|_{L^\infty(K)} \leq \|w\|_{L^\infty(K)}$ .  $\square$

*Remark 3.3.4.* Since we are working in  $\mathbb{R}^2$ ,  $H^{1+s}(K)$  is continuously imbedded in  $C(\overline{K})$  for any  $s \in (0, 1)$ . Therefore, Proposition 3.3.3 is readily generalized to such spaces, with the obvious bound

$$\|v\|_{L^\infty(K)} \leq c \inf \left\{ \begin{array}{l} h_K^s |w|_{H^{1+s}(K)} + |w|_{H^1(K)} + h_K^{-1} \|w\|_{L^2(K)} \\ : w \in H^{1+s}(K) \text{ and } w = v \text{ on } \partial K \end{array} \right\}. \quad (3.23)$$

Typical assumptions on the domain  $\Omega$  and the data for the problem guarantee that  $u \in H^{1+s}(\Omega)$  for some  $s > 0$  (cf. [45, 46, 87]).

We now consider the term  $|v^{\partial K} - \mathcal{I}_K^{\partial K} v|_{1,K}$ . Let  $e$  be an edge of  $\partial K$ , with endpoints  $z_0, z_1$ . We begin with a further decomposition of  $q_e$ , namely  $q_e = q_{e,1} + q_{e,0}$ , where  $q_{e,1} = v(z_0)\ell_0 + v(z_1)\ell_1 \in \mathbb{P}_1(e)$  and  $q_{e,0} = q_e - q_{e,1} \in \mathbb{P}_{p,0}(e)$ . This induces a natural decomposition of  $q^{\partial K}$ ,  $q^{\partial K} = q_1^{\partial K} + q_0^{\partial K}$ , where  $q_1^{\partial K} \in \mathbb{P}_1(\partial K)$  satisfies  $q_1^{\partial K}(z) = v(z)$  at each vertex  $z$  of  $K$ , and  $q_0^{\partial K}$  vanishes at the vertices.

**Proposition 3.3.5.** Suppose that  $v \in H^{p+1}(K)$  for some  $p \geq 1$ . There is a scale-invariant constant  $c = c(p, K)$  for which

$$|v^{\partial K} - \mathcal{I}_K^{\partial K} v|_{H^1(K)} \leq ch_K^p |v|_{H^{p+1}(K)} \quad , \quad \|v^{\partial K} - \mathcal{I}_K^{\partial K} v\|_{L^2(K)} \leq ch_K^{p+1} |v|_{H^{p+1}(K)} .$$

*Proof.* We decompose  $\mathcal{I}_K^{\partial K} v$  as  $\mathcal{I}_K^{\partial K} v = w_1 + w_0$ , where

$$\left\{ \begin{array}{ll} \Delta w_1 = 0 & \text{in } K \\ w_1 = q_1^{\partial K} & \text{on } \partial K \end{array} \right. , \quad \left\{ \begin{array}{ll} \Delta w_0 = 0 & \text{in } K \\ w_0 = q_0^{\partial K} & \text{on } \partial K \end{array} \right. .$$

It follows that  $|\mathcal{I}_K^{\partial K} v|_{H^1(K)} \leq |w_1|_{H^1(K)} + |w_0|_{H^1(K)}$ .

We denote the set of vertices of  $K$  by  $\mathcal{V}(K)$ , and the set of edges of  $K$  by  $\mathcal{E}(K)$ . For  $z \in \mathcal{V}(K)$ , we define  $\ell_z \in \mathbb{P}_1(\partial K)$  as follows: if  $e$  is not adjacent to  $z$ , then  $\ell_z$  vanishes on  $e$ , and if  $e$  is adjacent to  $z$ , then  $\ell_z = \ell_j$  on  $e$ , where  $z = z_j$  for one of the endpoints  $z_0, z_1$  of  $e$ . Let  $\phi_z$  be the harmonic function on  $K$  whose Dirichlet trace on  $\partial K$  is  $\ell_z$ . It follows that  $w_1 = \sum_{z \in \mathcal{V}(K)} v(z) \phi_z$ , so

$$\begin{aligned} |w_1|_{H^1(K)} &\leq \|v^{\partial K}\|_{L^\infty(K)} \sum_{z \in \mathcal{V}(K)} |\phi_z|_{H^1(K)} \leq c \|v^{\partial K}\|_{L^\infty(K)} \\ &\leq c(h_K |v|_{H^2(K)} + |v|_{H^1(K)} + h_K^{-1} \|v\|_{L^2(K)}) , \end{aligned}$$

where we have used (3.22) in the final inequality. A similar argument shows that  $\|w_1\|_{L^2(K)} \leq c(h_K^2 |v|_{H^2(K)} + h_K |v|_{H^1(K)} + \|v\|_{L^2(K)})$ .

From (3.19), we see that  $(q_{e,0}, q_{e,0})_{H^{1/2}(e)} = (v - q_{e,1}, q_{e,0})_{H^{1/2}(e)}$ , so  $\|q_{e,0}\|_{H^{1/2}(e)} \leq \|v - q_{e,1}\|_{H^{1/2}(e)}$ , for each edge  $e$ . Now,

$$\begin{aligned} |w_0|_{H^1(K)}^2 &= \int_{\partial K} (\partial w_0 / \partial n) q_0^{\partial K} ds \leq c \|\partial w_0 / \partial n\|_{H^{-1/2}(\partial K)} \|q_0^{\partial K}\|_{H^{1/2}(\partial K)} \\ &\leq c |w_0|_{H^1(K)} \|q_0^{\partial K}\|_{H^{1/2}(\partial K)} . \end{aligned}$$

Here we have used applied the trace inequality  $\|\partial w_0 / \partial n\|_{H^{-1/2}(\partial K)} \leq c(|w_0|_{H^1(K)} +$

$\|\Delta w_0\|_{L^2(K)} = c|w_0|_{H^1(K)}$  (cf. [70, Theorem A.33]), where  $c = c(K)$  is scale-invariant.

From this it follows that

$$\begin{aligned} |w_0|_{H^1(K)}^2 &\leq c \|q_0^{\partial K}\|_{H^{1/2}(\partial K)}^2 \leq c \sum_{e \in \mathcal{E}(K)} \|q_0^{\partial K}\|_{H^{1/2}(e)}^2 \\ &\leq c \sum_{e \in \mathcal{E}(K)} \|v - q_{e,1}\|_{H^{1/2}(e)}^2 \leq c \|v - q_1^{\partial K}\|_{H^{1/2}(\partial K)}^2 . \end{aligned}$$

The second inequality holds because  $q_0$  vanishes at the vertices, see Remark 3.3.6. At this stage,  $c = c(p, K)$ .

Another standard trace inequality ensures that

$$\|v - q_1^{\partial K}\|_{H^{1/2}(\partial K)} \leq c (|v - w_1|_{H^1(K)} + h_K^{-1} \|v - w_1\|_{L^2(K)}) .$$

Combining this with our estimates above, we obtain

$$\begin{aligned} |w_0|_{H^1(K)} &\leq c (|v - w_1|_{H^1(K)} + h_K^{-1} \|v - w_1\|_{L^2(K)}) \\ &\leq c (h_K |v|_{H^2(K)} + |v|_{H^1(K)} + h_K^{-1} \|v\|_{L^2(K)}) , \end{aligned}$$

and it follows, by applying the estimates for  $|w_0|_{H^1(K)}$  and  $|w_1|_{H^1(K)}$ , that

$$|\mathcal{I}_K^{\partial K} v|_{H^1(K)} \leq c (h_K |v|_{H^2(K)} + |v|_{H^1(K)} + h_K^{-1} \|v\|_{L^2(K)}) . \quad (3.24)$$

A standard inverse inequality, and the fact that our interpolation scheme preserves constants, yields the obvious analogue in  $L^2(K)$ ,

$$\|\mathcal{I}_K^{\partial K} v\|_{L^2(K)} \leq c (h_K^2 |v|_{H^2(K)} + h_K |v|_{H^1(K)} + \|v\|_{L^2(K)}) . \quad (3.25)$$

Now, let  $\phi \in V_p(K)$  and decompose it as  $\phi = \phi^K + \phi^{\partial K}$ , with  $\phi^K \in V_p^K(K)$  and  $\phi^{\partial K} \in V_p^{\partial K}(K)$ . We have  $|v - \phi|_{H^1(K)}^2 = |v^K - \phi^K|_{H^1(K)}^2 + |v^{\partial K} - \phi^{\partial K}|_{H^1(K)}^2$ , so  $|v^{\partial K} - \phi^{\partial K}|_{H^1(K)} \leq |v - \phi|_{H^1(K)}$ . Noting that  $\mathcal{I}_K^{\partial K} \phi = \phi^{\partial K}$ , and applying (3.24) to

$v - \phi$ , we see that

$$\begin{aligned} |v^{\partial K} - \mathcal{I}_K^{\partial K} v|_{H^1(K)} &\leq |v^{\partial K} - \phi^{\partial K}|_{H^1(K)} + |\mathcal{I}_K^{\partial K}(v - \phi)|_{H^1(K)} \\ &\leq c \left( h_K |v - \phi|_{H^2(K)} + |v - \phi|_{H^1(K)} + h_K^{-1} \|v - \phi\|_{L^2(K)} \right) . \end{aligned}$$

Since  $\mathbb{P}_p(K) \subset V_p(K)$ , the Bramble-Hilbert Lemma now implies that  $|v^{\partial K} - \mathcal{I}_K^{\partial K} v|_{H^1(K)} \leq ch_K^p |v|_{H^{p+1}(K)}$ , as claimed. The result for the  $L^2(K)$  norm follows the same pattern, but we briefly lay out the argument anyway. It holds that

$$\begin{aligned} \|v^{\partial K} - \mathcal{I}_K^{\partial K} v\|_{L^2(K)} &\leq \|v^{\partial K} - \phi^{\partial K}\|_{L^2(K)} + \|\mathcal{I}_K^{\partial K}(v - \phi)\|_{L^2(K)} \\ &\leq \|v^{\partial K} - \phi^{\partial K}\|_{L^2(K)} \\ &\quad + c \left( h_K^2 |v - \phi|_{H^2(K)} + h_K |v - \phi|_{H^1(K)} + \|v - \phi\|_{L^2(K)} \right) . \end{aligned}$$

It remains to estimate  $\|v^{\partial K} - \phi^{\partial K}\|_{L^2(K)}$ , for which we have

$$\begin{aligned} \|v^{\partial K} - \phi^{\partial K}\|_{L^2(K)} &\leq \|v - \phi\|_{L^2(K)} + \|v^K - \phi^K\|_{L^2(K)} \\ &\leq \|v - \phi\|_{L^2(K)} + h_K |v^K - \phi^K|_{H^1(K)} \\ &\leq \|v - \phi\|_{L^2(K)} + h_K |v - \phi|_{H^1(K)} . \end{aligned}$$

Combining this with our previous estimate yields,

$$\|v^{\partial K} - \mathcal{I}_K^{\partial K} v\|_{L^2(K)} \leq c \left( h_K^2 |v - \phi|_{H^2(K)} + h_K |v - \phi|_{H^1(K)} + \|v - \phi\|_{L^2(K)} \right) ,$$

and Bramble-Hilbert Lemma completes the argument.  $\square$

*Remark 3.3.6.* The claim that  $\|q_0^{\partial K}\|_{H^{1/2}(\partial K)}^2 \leq c \sum_{e \in \mathcal{E}(K)} \|q_0^{\partial K}\|_{H^{1/2}(e)}^2$  in the proof of Proposition 3.3.5 requires further comment. Superficially, this holds because both quantities are (squares of) norms on the finite dimensional vector space  $\mathbb{P}_{p,0}(\partial K) = \{w \in P_p(\partial K) : w(z) = 0 \text{ for all } z \in \mathcal{V}(K)\}$ . Although such an argument allows for the dependence of  $c$  on  $\dim \mathbb{P}_{p,0}(\partial K)$  (hence on  $p$ ), we want to ensure that  $c$  is

scale-invariant. For that, we look a little closer at the norms. We have  $\|w\|_{H^{1/2}(\Gamma)}^2 = \|w\|_{L^2(\Gamma)}^2 + |w|_{H^{1/2}(\Gamma)}^2$ , where

$$|w|_{H^{1/2}(\Gamma)}^2 = \int_{\Gamma} \int_{\Gamma} \frac{(w(x) - w(y))^2}{|x - y|^2} ds(x) ds(y) .$$

As suggested by the notation,  $|\cdot|_{H^{1/2}(\Gamma)}$  is generally a semi-norm, with constant functions as its kernel. However, for  $w \in \mathbb{P}_{p,0}(\partial K)$ , both  $|w|_{H^{1/2}(\partial K)}$  and

$$\left( \sum_{e \in \mathcal{E}(K)} |w|_{H^{1/2}(e)}^2 \right)^{1/2}$$

are norms, so there is a constant  $c$  such that  $|w|_{H^{1/2}(\partial K)} \leq c \left( \sum_{e \in \mathcal{E}(K)} |w|_{H^{1/2}(e)}^2 \right)^{1/2}$ . Since both norms in this inequality are scale invariant, so is  $c$ . Since  $\|w\|_{L^2(\partial K)}^2 = \sum_{e \in \mathcal{E}(K)} \|w\|_{L^2(e)}^2$ , we have the result that was claimed.

We briefly mention two earlier contributions that have considered some of the same issues that we do here concerning working with the  $H^{1/2}$  norm on all versus individual parts of the boundary of a mesh cell or a polyhedral subdomain, but in the context of standard finite element meshes. The first is [22], and it concerns domain decomposition-type preconditioners for linear solvers. Though we were unable to use the results of Section 3 in that paper related to localization of the  $H^{1/2}$  norm our context, they provide the first discussion and treatment of this issue of which we are aware in the finite element literature. The second contribution is [31], in which the authors set forth projection-based interpolation schemes that are conforming in  $H^1$ ,  $H(\text{curl})$  and  $H(\text{div})$  spaces. Our interpolation scheme is also projection based, but because their results were for standard element shapes, they could not be readily applied in our context.

*Remark 3.3.7.* The proof of Proposition 3.3.5 revealed that

$$|v^{\partial K} - \mathcal{I}_K^{\partial K} v|_{H^1(K)} \leq c \inf_{\phi \in V_p(K)} \left( h_K |v - \phi|_{H^2(K)} + |v - \phi|_{H^1(K)} + h_K^{-1} \|v - \phi\|_{L^2(K)} \right) ,$$

$$\|v^{\partial K} - \mathcal{I}_K^{\partial K} v\|_{L^2(K)} \leq c \inf_{\phi \in V_p(K)} \left( h_K^2 |v - \phi|_{H^2(K)} + h_K |v - \phi|_{H^1(K)} + \|v - \phi\|_{L^2(K)} \right) .$$

In fact, by the same reasoning as discussed in Remark 3.3.4, we have the expected versions for fractional order spaces as well, for  $s \in (0, 1]$ ,

$$\begin{aligned} & |v^{\partial K} - \mathcal{I}_K^{\partial K} v|_{H^1(K)} \\ & \leq c \inf_{\phi \in V_p(K)} \left( h_K^s |v - \phi|_{H^{1+s}(K)} + |v - \phi|_{H^1(K)} + h_K^{-1} \|v - \phi\|_{L^2(K)} \right) , \end{aligned} \quad (3.26)$$

$$\begin{aligned} & \|v^{\partial K} - \mathcal{I}_K^{\partial K} v\|_{L^2(K)} \\ & \leq c \inf_{\phi \in V_p(K)} \left( h_K^{1+s} |v - \phi|_{H^{1+s}(K)} + h_K |v - \phi|_{H^1(K)} + \|v - \phi\|_{L^2(K)} \right) . \end{aligned} \quad (3.27)$$

Combining Propositions 3.3.1 and 3.3.5, we obtain our key interpolation error result,

**Theorem 3.3.8.** *Suppose that  $v \in H^{p+1}(K)$  for some  $p \geq 1$ . There is a scale-invariant constant  $c = c(p, K)$  for which*

$$|v - \mathcal{I}_K v|_{H^1(K)} \leq c h_K^p |v|_{H^{p+1}(K)} \quad , \quad \|v - \mathcal{I}_K v\|_{L^2(K)} \leq c h_K^{p+1} |v|_{H^{p+1}(K)} .$$

Once a proper notion of “shape regularity” is determined for families of meshes  $\{\mathcal{T}_h\}$  consisting of curvilinear polygons, a result such as  $|v - \mathcal{I}v|_{H^1(\Omega)} \leq c h^p |v|_{H^{p+1}(\Omega)}$ , where  $c = c(p)$  and  $h = \max\{h_K : K \in \mathcal{T}_h\}$ , follows immediately. A meaningful analysis of how the constant  $c(p, K)$  in Theorem 3.3.8 depends on  $p$  and the geometric features of  $K$  is beyond the scope of the present work. One might expect measures such as a “chunkiness parameter” (a natural generalization of aspect ratio, cf. [23, Definition 4.2.16]), the number of edges, the curvature of edges, and the length of edges with respect to the element diameter, to play an important role in determining

the dependence of  $c = c(K)$  on element geometry. Indeed, the number of edges of  $K$  clearly arises in the proof of Proposition 3.3.5, when we bound  $|w_1|_{H^1(K)}$  using a sum of seminorms of functions associated the vertices; see also Remark 3.3.6, in which a sum over edges is used. In contrast, the special analysis given for the L-shaped elements of Example 3.5.3, which have fixed size but increasing number of edges as the mesh is “refined”, provides an example in which neither the number of edges nor their relation to the diameter of the element have any bearing on the associated interpolation constant. In each of the other examples in Section 3.5, the maximal curvature of edges grows without bound as the diameters of the elements shrink, and this has no apparent negative effect on the convergence of the discretization error, which suggests that edge curvature may not ultimately play such an important role in interpolation error analysis either. Additionally, some of the families of meshes in Section 3.5 consist entirely of elements that are not star-shaped with respect to any ball, in which case discussion of a chunkiness parameter is either meaningless, or would have to take on a different form if it were to be applicable at all. In summary, a thorough analysis of how local interpolation error depends (or does not depend) on geometric features of elements is needed. Further extensions of our interpolation error analysis of interest include:

- (a) Estimates that directly involve both the element diameter  $h_K$  and a local “polynomial degree”  $p_K$ , in the manner of standard  $hp$ -finite element analysis.
- (b) Estimates that exploit the fact that  $V_p(K)$  is a richer space than  $\mathbb{P}_p(K)$ , often containing singular functions that may allow similar convergence results for interpolation under weaker regularity assumptions on  $v$ , as suggested by Remarks 3.3.4 and 3.3.7.

We plan to pursue these extensions in subsequent work.

### 3.4. Computing with Curved Trefftz Finite Elements

We recall that the functions that we wish to compute in  $V_p(K)$  satisfy one of two types of equations:

$$\left\{ \begin{array}{l} \Delta v = f \quad \text{in } K \\ v = 0 \quad \text{on } \partial K \end{array} \right. , \quad \left\{ \begin{array}{l} \Delta v = 0 \quad \text{in } K \\ v = g \quad \text{on } \partial K \end{array} \right. , \quad (3.28)$$

where  $f \in \mathbb{P}_{p-2}(K)$  and  $g \in \mathbb{P}_p(\partial K)$ . The first type of equation is readily converted to the second type as follows. Given  $f \in \mathbb{P}_{p-2}(K)$ , one can explicitly construct a  $\hat{f} \in \mathbb{P}_p(K)$  such that  $\Delta \hat{f} = f$ . With such a function in hand, the first type of problem is reduced to finding  $\hat{v}$  satisfying  $\Delta \hat{v} = 0$  in  $K$  and  $\hat{v} = -\hat{f}$  on  $\partial K$ . Then  $v = \hat{v} + \hat{f}$  satisfies the first problem. In [54, Theorem 2], the authors show that, if  $p$  is a homogeneous polynomial of degree  $j$ , then the polynomial  $q$  of degree  $j+2$  given by

$$q(x) = \sum_{k=0}^{[j/2]} \frac{(-1)^k (j-k)!}{(j+1)!(k+1)!} \left( \frac{|x|^2}{4} \right)^{k+1} \Delta^k p(x) ,$$

where  $[j/2]$  denotes the integer part of  $j/2$ , satisfies  $\Delta q = p$ . Having reduced either type of problem to the computation of a harmonic function with piecewise smooth boundary data, we may now employ any number of boundary integral equation techniques to compute such functions. One such technique is to use Boundary Element Methods for first-kind integral equations, as is done in BEM-FEM, to directly compute the outward normal derivative  $\partial v / \partial n$ ; interior point values are computed from layer potentials, as needed, for quadrature approximation of the element stiffness matrix. The limitations in extending this kind of approach to curved element boundaries in a natural way was one of the reasons that we opted for Nyström discretizations in [3]. In that work, we employed second-kind integral equations, which do not directly

yield  $\partial v/\partial n$ , but offered greater flexibility in other areas that offset this downside.

Before describing the approach we use in the current work, we recall the types of integrals we must compute in order to form the finite element stiffness matrix. They include integrals of the following forms,

$$\int_K A \nabla v \cdot \nabla w \, dx \quad , \quad \int_K \mathbf{b} \cdot \nabla v w \, dx \quad , \quad \int_K c v w \, dx \quad , \quad \int_K f v \, dx \quad , \quad \int_e g v \, ds \quad ,$$

where  $v, w \in V_p(K)$ . It is sometimes advantageous to use integration-by-parts on the first of these integrals, yielding integrals of the forms

$$\int_K (\nabla \cdot A \nabla v) w \, dx \quad , \quad \int_{\partial K} (A \nabla v \cdot \mathbf{n}) w \, ds \quad .$$

The benefits of such an approach become clear when  $A$  is a constant scalar on  $K$ , in which case the two integrals above simplify to

$$A \int_K \Delta v w \, dx \quad , \quad A \int_{\partial K} \frac{\partial v}{\partial n} w \, ds \quad .$$

We note that  $\Delta v \in \mathbb{P}_{p-2}(K)$  and  $w \in \mathbb{P}_p(\partial K)$ . Further simplifications occur when  $v \in V_p^{\partial K}(K)$  or  $w \in V_p^K(K)$ —at least one of these two integrals vanishes. We see then that, in quadrature approximations of these kinds of integrals, we should have access to function values and derivatives (up to second partials) of functions in  $V_p(K)$  in the interior of  $K$ , and normal derivatives of such functions on  $\partial K$ —function values and tangential derivatives of such functions on  $\partial K$  are straightforward.

With these goals in mind, in [65] we developed an approach that delivers each of these quantities efficiently and with very high accuracy, *while performing all computations on the boundary  $\partial K$* . The method is based on the fact that, on simply-connected domains  $K \subset \mathbb{R}^2$ , for each harmonic function  $u$ , there is a family of *harmonic conjugates* that differ from each other only by additive constants. We recall that  $v$  is a harmonic conjugate of  $u$  on  $K$  when  $\Delta v = 0$  in  $K$  and  $R \nabla v = \nabla u$  in  $K$ , where

the matrix  $R$  rotates vectors clockwise by  $\pi/2$ . Such a pair of harmonic functions satisfy the Cauchy-Reimann equations, and thus can be taken as the real and imaginary parts of a complex analytic function in  $K$ . More precisely, making the natural identification between  $z = x_1 + ix_2 \in \mathbb{C}$  and  $x = (x_1, x_2) \in K$ , the function defined by  $w(z) = u(x) + iv(x)$  is analytic in  $K$ . Given both  $u$  and  $v$  on the boundary  $\partial K$ , the value  $w$  and its derivatives at points inside  $K$  can be obtained via Cauchy's integral formula,

$$w^{(k)}(z) = \frac{k!}{2\pi i} \oint_{\partial K} \frac{w(\xi)}{(\xi - z)^{k+1}} d\xi ,$$

and the desired  $k$ th partial derivatives of  $u$  (or  $v$ ) can be extracted from the real and imaginary parts of  $w^{(k)}(z)$ . For example,  $w'(z) = u_{x_1}(x) - iu_{x_2}(x)$ , where  $u_{x_j}$  denotes the partial derivative of  $u$  in its  $j$ th argument. For the second partials, we have  $w''(z) = u_{x_1x_1}(x) - iu_{x_1x_2}(x)$ , with  $u_{x_2x_1}(x) = u_{x_1x_2}(x)$  and  $u_{x_2x_2}(x) = -u_{x_1x_1}(x)$ . Furthermore, the orthogonality of  $\nabla u$  and  $\nabla v$  in  $K$  ensures the following relationship between the normal and tangential derivatives of  $u$  and  $v$  on  $\partial K$ .

$$\frac{\partial u}{\partial n} = \frac{\partial v}{\partial t} \quad , \quad \frac{\partial v}{\partial n} = -\frac{\partial u}{\partial t} \quad , \quad (3.29)$$

where  $\partial v/\partial t$  denotes the tangential derivative along  $\partial K$  in the counter-clockwise direction. With these relationships, we see that it is possible to compute the normal derivative of one harmonic function as the (much more convenient) tangential derivative of a harmonic conjugate. Therefore, this general approach allows us to compute all of the quantities of interest related to our harmonic function while performing all computations on the boundary  $\partial K$ , as claimed.

Given the piecewise smooth boundary Dirichlet data  $g$  of a harmonic function  $u$ ,

any harmonic conjugate  $v$  satisfies the complementary Neumann problem

$$\Delta v = 0 \text{ in } K \quad , \quad \frac{\partial v}{\partial n} = -\frac{\partial g}{\partial t} . \quad (3.30)$$

As stated earlier, solutions of (3.30) are only unique up to additive constants, and we fix a particular member by specifying that  $\int_{\partial K} v \, ds = 0$ . The trace of  $v$  on  $\partial K$  is computed as the solution of the following second-kind integral equation,

$$\begin{aligned} \frac{v(x)}{2} + \int_{\partial K} \left( \frac{\partial \Phi(x, y)}{\partial n(y)} + 1 \right) v(y) \, ds(y) \\ = - \int_{\partial K} \Phi(x, y) \frac{\partial g}{\partial t}(y) \, ds(y) \text{ for } x \in \partial K , \end{aligned} \quad (3.31)$$

where  $\Phi(x, y) = -(2\pi)^{-1} \ln |x - y|$  is the fundamental solution of Laplace's equation. The addition of 1 to the integral kernel  $\partial \Phi(x, y)/\partial n(y)$  above, ensures that (3.31) is well-posed by enforcing that  $\int_{\partial K} v \, ds = 0$ . Since  $K$  will typically have corners, the integral equation must be modified in their vicinity if we are to understand the equation pointwise. More specifically, if  $x_c \in \partial K$  is a corner point, and  $x \in \partial K$  is not a corner point, then

$$\begin{aligned} |\partial K|v(x_c) + \frac{v(x) - v(x_c)}{2} + \int_{\partial K} \left( \frac{\partial \Phi(x, y)}{\partial n(y)} + 1 \right) (v(y) - v(x_c)) \, ds(y) \\ = - \int_{\partial K} \Phi(x, y) \frac{\partial g}{\partial t}(y) \, ds(y) . \end{aligned} \quad (3.32)$$

The case of multiple corners is handled similarly. In the present work, as in [65], we solve (3.31) via a Nyström discretization. Key to the practical success of this approach is the choice of quadrature schemes that are well-suited for the types of singularities present in the integrands. The interested reader may find the details in that paper [65]. Having computed  $v$  on  $\partial K$ , we now have access to the quantities of interest for  $u$  as described above.

*Remark 3.4.1* (Multiply connected mesh cells). If  $K$  is not simply connected, the

existence of harmonic conjugate pairs is not guaranteed, so the approach described above cannot be used. In such cases, one can employ different integral equation techniques to efficiently and accurately compute the quantities necessary for assembling local stiffness matrices. We mention the contribution [44] (and references therein) in this regard. The discussion in that work assumes smooth boundaries (at least  $C^2$ ), so their approach must be modified in order to handle mesh cells having corners. We intend to pursue this in subsequent work.

### 3.5. Numerical Experiments

The experiments in this section illustrate the linear convergence rate indicated by Theorem 3.3.8 ( $p = 1$ ) for  $|u - \widehat{u}|_{H^1(\Omega)}$  on simple model problems which nonetheless illustrate the theoretical claims are achieved in practical computations. In the first set of experiments, three increasingly complex families of meshes are used for the same problem on the unit square. In the second set of experiments, we explore the effects of “nearly straight” edges on convergence and conditioning for Type 1 and Type 2 elements. For the final set of experiments, we consider a problem for which the exact solution is known to have a singularity due to a non-convex corner of the domain, and use it to illustrate the approximation power of locally singular functions in our finite element spaces.

*Example 3.5.1* (Three Curved Mesh Families). Let  $\Omega = (0, 1) \times (0, 1)$ , and suppose that  $u$  satisfies

$$-\Delta u = 1 \text{ in } \Omega \quad , \quad u = 0 \text{ on } \partial\Omega \text{ .}$$

Series representations of  $u$  and  $|u|_{H^1(\Omega)}^2$  are

$$u = \sum_{m,n \in 2\mathbb{N}-1} \frac{16}{mn(m^2 + n^2)\pi^4} \sin(m\pi x) \sin(n\pi y) ,$$

$$|u|_{H^1(\Omega)}^2 = \sum_{m,n \in 2\mathbb{N}-1} \frac{64}{m^2n^2(m^2 + n^2)\pi^6} \approx 3.51442537 \times 10^{-2} .$$

We approximate  $u$  by the finite element solution  $\hat{u} \in V_1(\mathcal{T})$  on three different families of meshes, each indexed by a mesh parameter  $r$  that is inversely proportional to the characteristic diameter of its mesh cells, see Figure 3.3 for the case  $r = 16$  of each, together with the corresponding computed finite element solution  $\hat{u} \in V_1(\mathcal{T})$ . Since the cells are of uniform size,  $r$  is the number of cells touching each edge of  $\partial\Omega$ .

We refer to the first family of meshes as the Shuriken meshes, because it consists of shuriken elements, as seen in Figure 3.1), which are naturally modified at the boundary to properly fit it. There are three types of elements in this case, the corner elements, edge elements and interior elements. The second family is called the Pegboard meshes, and it consists of two types of elements, the half-washers and two-edge circles, as seen in Figure 3.1). The third family is called the Jigsaw meshes, and it has four different types of elements: corner pieces, two different types of edge pieces, and interior pieces. Of the nine different types of elements that appear in each of these families, only the two-edge circles are convex. In fact, none of the other types of elements are even star-shaped. Furthermore, each of the jigsaw elements have at least two non-convex corners, which implies that the local space  $V_1(K)$  for such an element will include functions that are singular, i.e. not in  $H^2(K)$ .

The discretization error  $|u - \hat{u}|_{H^1(\Omega)}$  satisfies  $|u - \hat{u}|_{H^1(\Omega)}^2 = |u|_{H^1(\Omega)}^2 - |\hat{u}|_{H^1(\Omega)}^2$ , making it straight-forward to compute once  $\hat{u} \in V_1(\mathcal{T})$  has been computed. These errors, and ratios of consecutive errors, are given in Table 3.1 for each of the families, demonstrating the expected linear convergence. As an interesting comparison, we also

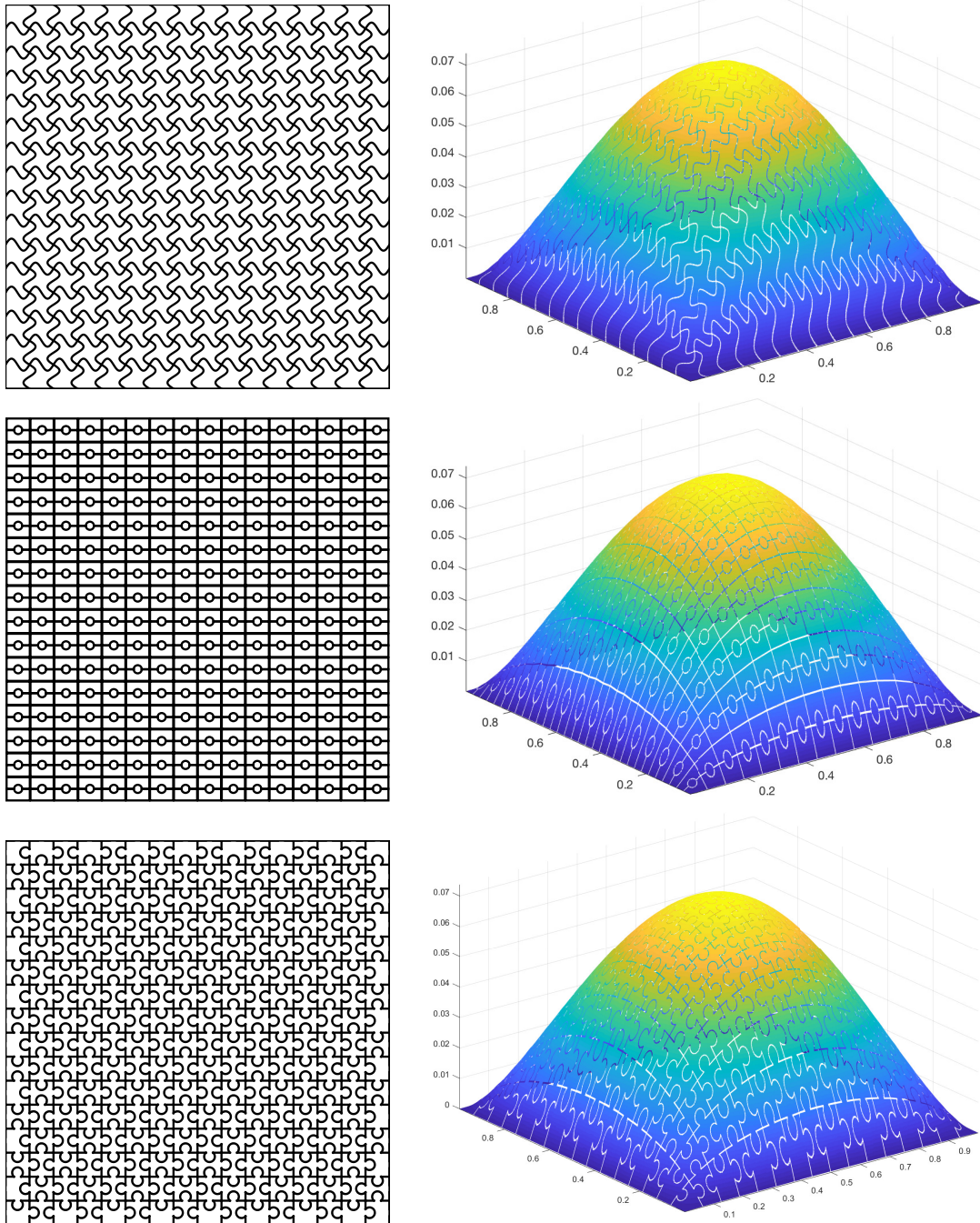


Figure 3.3: The Shuriken, Pegboard and Jigsaw meshes for  $r = 16$ , as well as the computed finite element solution  $\hat{u} \in V_1(\mathcal{T})$  on these meshes.

Table 3.1: Discretization errors,  $|u - \hat{u}|_1$ , and error ratios for the Shuriken, Pegboard, and Jigsaw meshes. For the Shuriken meshes, both Type 1 and Type 2 elements are used. For the other meshes, only Type 2 elements are used.

$r$	Shuriken, Type 1		Shuriken, Type 2		Pegboard		Jigsaw	
	$ u - \hat{u} _{H^1(\Omega)}$	ratio						
4	7.882e-02		5.629e-02		3.470e-02		3.209e-02	
8	8.200e-02	0.961	2.847e-02	1.977	1.726e-02	2.010	1.538e-02	2.086
16	8.813e-02	0.930	1.429e-02	1.993	8.537e-03	2.022	7.559e-03	2.035
32	9.232e-02	0.955	7.150e-03	1.998	4.233e-03	2.017	3.754e-03	2.014
64	9.470e-02	0.975	3.576e-03	1.999	2.106e-03	2.010	1.871e-03	2.006
128	9.600e-02	0.987	1.788e-03	2.000	1.050e-03	2.006	9.327e-04	2.006
256	9.662e-02	0.993	8.937e-04	2.001	5.239e-04	2.004	4.628e-04	2.015
512	9.694e-02	0.997	4.463e-04	2.003	2.611e-04	2.007	2.247e-04	2.060

include the errors and ratios for the discretizations that would arise had we chosen the Type 1 definition of  $\mathbb{P}_1(e)$  for the shuriken elements. This choice leads to local spaces having dimension 4 for mesh cells not touching the boundary, in contrast to the dimension 8 local spaces using the Type 2 definition of  $\mathbb{P}_1(e)$ . We recall that  $\mathbb{P}_1(K) \not\subset V_1(K)$  for Type 1 elements (unless  $K$  is a straight-edge polygon), and we see that there is no convergence at all in  $H^1$  in this case! In all three cases, optimal order convergence,  $|u - \hat{u}|_{H^1(\Omega)} = \mathcal{O}(h^2)$ , is obtained when Type 2 elements are used.

*Example 3.5.2 (Perturbed Triangle Mesh).* Let  $\Omega$  and  $u$  be as in the previous example. We again approximate  $u$  by its finite element solution  $\hat{u} \in V_1(\mathcal{T})$ , where the mesh  $\mathcal{T}$  consists perturbed triangular elements, as shown in Figure 3.4, each of which has one curved edge. Reference elements, one convex and the other non-convex, are obtained by splitting the unit square  $(0, 1) \times (0, 1)$  using a circular arc through the vertices  $(1, 0)$  and  $(0, 1)$  whose center is  $(-a, -a)$ , for some  $a > 0$ . The radius of curvature of this curved edge is  $\sqrt{a^2 + (1 + a)^2}$ , and it approaches a straight line as  $a$  increases. More specifically, the maximum distance between a point on the curved edge and the closest point to it on the line between  $(1, 0)$  and  $(0, 1)$  is  $(\sqrt{(2a + 1)^2 + 1} - (2a + 1))/\sqrt{2}$ , which behaves like  $1/(4a\sqrt{2})$  as  $a \rightarrow \infty$ . For the corresponding finite element meshes,

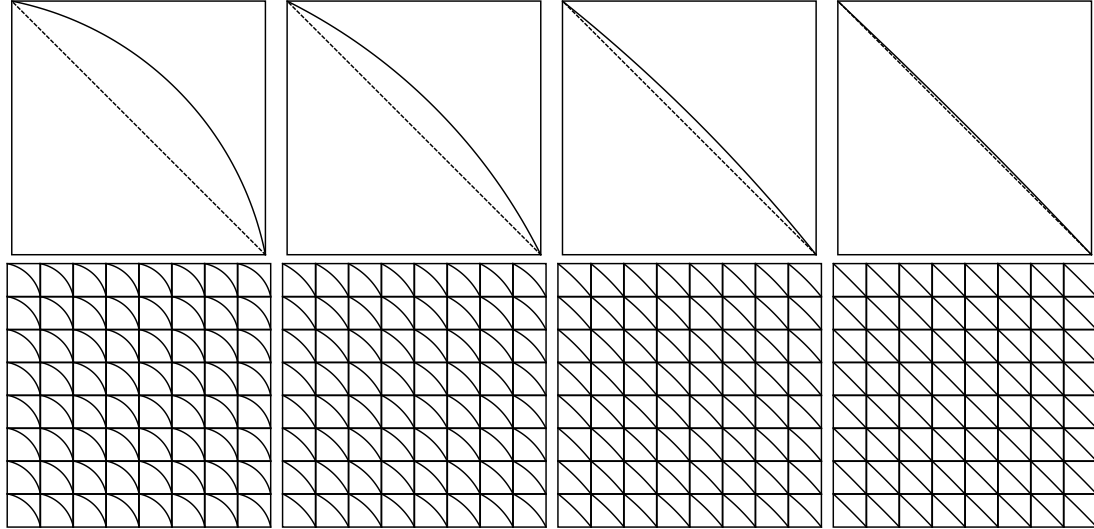


Figure 3.4: Reference elements (top) for the Perturbed Triangle meshes (bottom), shown with  $r = 8$ , for  $a = 1/4, 1, 4, 16$  from left to right. The dashed lines are straight ( $a = \infty$ ).

these reference element pairs are scaled so that their straight edges have length  $1/r$ .

In Figure 3.5, we report both the errors  $|u - \hat{u}|_{H^1(\Omega)}$  and the spectral condition numbers  $\kappa_2(A)$  of the stiffness matrices for Type 1 and Type 2 elements as the meshes is refined, for several values of  $a$ . For both types of elements,  $A$  is diagonally rescaled,  $a_{ij} \leftarrow a_{ij} / \sqrt{a_{ii}a_{jj}}$ , before computing the condition numbers. As expected, the Type 2 elements exhibit optimal order convergence throughout the refinements. For Type 1 elements, the convergence curves improve as the  $a$  is increased, in the sense that they stay roughly parallel to their Type 2 counterparts through more levels of refinement, but the convergence curves for Type 1 elements eventually level off, indicating a threshold beyond which the error does not decrease. The condition number plots for the Type 1 and Type 2 elements provide a complementary comparison, for which the Type 2 elements yield condition numbers that are *eventually* close to, and grow at the same rate as, those of the Type 1 elements, but may be significantly larger than their Type 1 counterparts for coarser meshes when the curved edges are nearly straight. The condition numbers for Type 1 elements grow like  $r^2$  as the mesh is

refined (i.e. like  $\dim(V)$ ), which is accordance with standard linear (bilinear) elements on triangular (rectangular) meshes. We observe, based on computations done for  $a = 1/4, 1, 4, \dots, 4096$ , that the condition numbers on the coarsest meshes ( $r = 4$ ) for Type 2 elements appear to grow quadratically in  $a$ . We also observe an apparent correlation between when the convergence curves for Type 1 elements tend to level off and when the condition numbers for Type 2 elements transition from a relatively flat phase to behaving like their Type 1 counterparts. It is a topic of future investigation to better understand how element shapes and “polynomial orders”  $p$  affect convergence and conditioning for both types of elements.

*Example 3.5.3 (L-Shaped Domain).* For our final set of experiments, we again consider the problem

$$-\Delta u = 1 \text{ in } \Omega \quad , \quad u = 0 \text{ on } \partial\Omega \quad ,$$

but on the (rotated) L-shaped domain  $\Omega = (-1, 1) \times (-1, 1) \setminus [0, 1] \times [-1, 0]$  (see Figure 3.6). This solution, though not known explicitly, is known to have a singularity at the origin, behaving asymptotically like  $|x|^{2/3}$  near the origin (cf. [46, 55, 87]). In standard finite element computations the efficient approximation of such a singular solution would be achieved by targeted refinement of mesh cells toward the singular point that is either guided by local error indicators (computed a posteriori) or by specific knowledge of the local singular behavior to determine an a priori mesh grading strategy. A head-to-head empirical comparison of these two types of refinement strategies is provided in [58]. Others have sought to address the issue of singularities by augmenting standard polynomial finite elements with (local) enrichment functions having the types of singularities expected of the solution based on a priori knowledge (cf. [37], [61] XFEM, [73] GFEM).

Our approach for this problem is different. We use the fact that, if a mesh cell

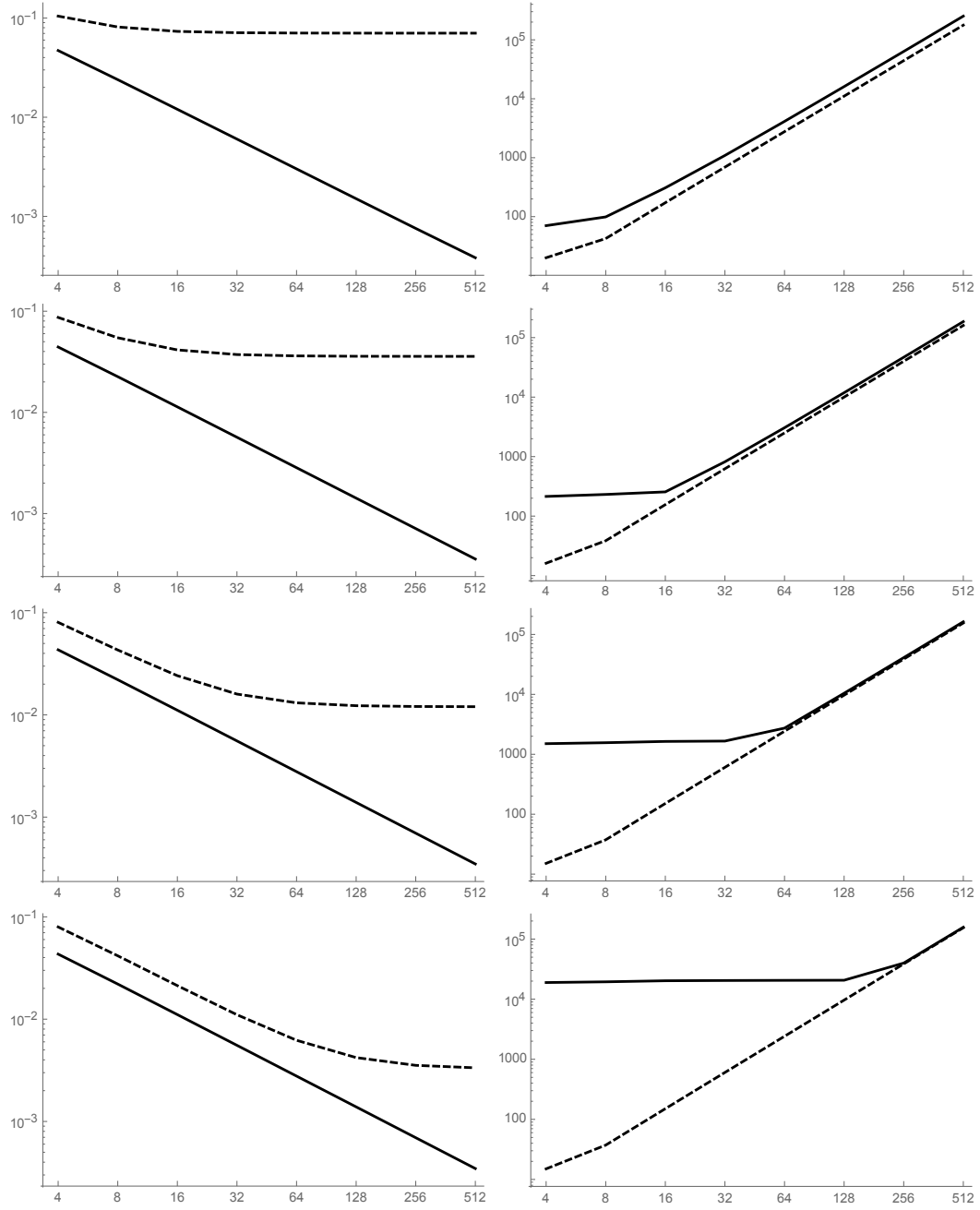


Figure 3.5: Log-Log plots of  $|u - \hat{u}|_{H^1(\Omega)}$  (left column) and  $\kappa_2(A)$  (right column) with respect to the mesh parameter  $r$  (horizontal axis), for Type 1 (dashed) and Type 2 (solid) elements on Perturbed Triangle mesh families  $a = 1/4, 1, 4, 16$  (from top to bottom).

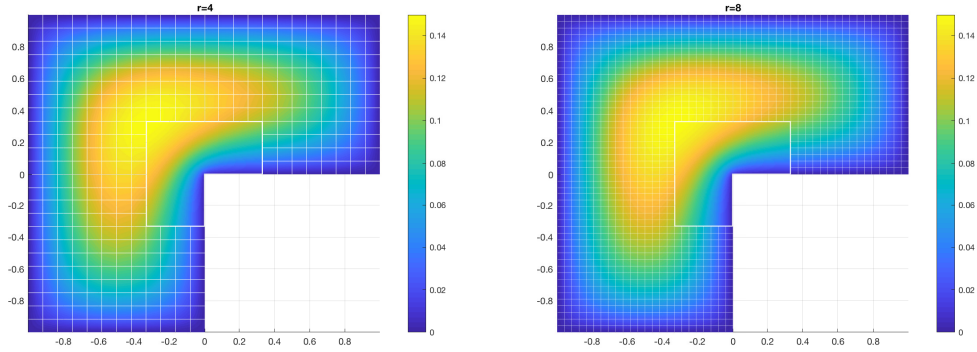


Figure 3.6: The L-shaped domain together with the meshes and contour plots of the computed solutions  $\hat{u} \in \tilde{V}_1(\mathcal{T})$  corresponding to  $r = 4$  (left) and  $r = 8$ .

$K$  has a non-convex corner, then the local space  $V_1(K)$  automatically contains functions having the correct type of singularity for that geometry. Remark 3.3.7 suggests improved approximation power for interpolation of functions having the same kind of singularities, and optimal order convergence was demonstrated in [3] for interpolation error in  $L^2(\Omega)$  of a harmonic function having an  $|x|^{2/3}$ -type singularity on precisely the kinds of meshes shown in Figure 3.6. That work did not, however, consider interpolation error or discretization error in  $H^1(\Omega)$  for such a problem. As before, we use a parameter  $r$  to describe the meshes in this family. The  $r$ th mesh in this family,  $\mathcal{T}_r$ , consists of one L-shaped element,  $K_L = (-1/3, 1/3) \times (-1/3, 1/3) \setminus [0, 1/3] \times [1/3, 0]$ , and  $24r^2$  congruent squares of size  $(3r)^{-1} \times (3r)^{-1}$ , see Figure 3.6. We note that there are  $r$  squares touching each of the short edges of  $\partial K \setminus \partial\Omega$ , and  $\partial K_L$  has  $6r + 2$  vertices. Although none of the edges in these meshes are curved, the optimal convergence rates enabled by the single L-shaped element illustrates how a result like (3.26) might be used to prove what is empirically observed. For this example, we provide such an analysis.

As with Example 3.5.1, we use a highly accurate approximation of  $|u|_{H^1(\Omega)}^2$ , together with the identity  $|u - \hat{u}|_{H^1(\Omega)}^2 = |u|_{H^1(\Omega)}^2 - |\hat{u}|_{H^1(\Omega)}^2$ . In the previous example, we

used a Fourier expansion to obtain our approximation of  $|u|_{H^1(\Omega)}^2$ . Here, we use the techniques developed in [65]. Letting  $w = -|x|^2/4$ , and recognizing that  $-\Delta w = 1$ , we have  $u = v + w$ , where  $\Delta v = 0$  in  $\Omega$  and  $v = -w$  on  $\partial\Omega$ , and it follows that

$$\begin{aligned} |u|_{H^1(\Omega)}^2 &= |w|_{H^1(\Omega)}^2 + |v|_{H^1(\Omega)}^2 + 2 \int_{\Omega} \nabla v \cdot \nabla w \, ds \\ &= \frac{1}{2} + \int_{\partial\Omega} \frac{\partial v}{\partial n} v \, ds + 2 \int_{\partial\Omega} \frac{\partial v}{\partial n} w \, ds \\ &= \frac{1}{2} - \int_{\partial\Omega} \frac{\partial v}{\partial n} v \, ds \approx 0.21407580269 . \end{aligned} \tag{3.33}$$

The integral  $\int_{\partial\Omega} \frac{\partial v}{\partial n} v \, ds$  is approximated using the techniques from [65].

For the square elements  $K$  in  $\mathcal{T}_r$ ,  $V_1(K)$  consists of the standard bilinear finite elements. The element stiffness matrices for these elements remain that same (up to symmetric permutation) for all meshes,

$$A_K = \frac{1}{6} \begin{pmatrix} 4 & -1 & -2 & -1 \\ -1 & 4 & -1 & -2 \\ -2 & -1 & 4 & -1 \\ -1 & -2 & -1 & 4 \end{pmatrix} .$$

The local space  $V_1(K_L)$  for single L-shaped element  $K_L$  changes from mesh to mesh, so its element stiffness matrix  $A_L$  must be recomputed on each mesh. The number of rows/columns of  $A_L$  on  $\mathcal{T}_r$  is  $6r + 2$ .

Revisiting the interpolation identity (3.20) in our present context, we have

$$\begin{aligned} |u - \mathcal{I}_K u|_{H^1(K)}^2 &= |u^K - \mathcal{I}_K^K u|_{H^1(K)}^2 + |u^{\partial K} - \mathcal{I}_K^{\partial K} u|_{H^1(K)}^2 \\ &= |u^K|_{H^1(K)}^2 + |u^{\partial K} - \mathcal{I}_K^{\partial K} u|_{H^1(K)}^2 , \end{aligned}$$

because  $V_1^K(K) = \{0\}$ . Since  $-\Delta u^K = 1$  in  $K$  and  $u^K = 0$  on  $\partial K$ , we have

$$|u^K|_{H^1(K)}^2 = \int_K u^K \, dx \leq |K|^{1/2} \|u^K\|_{L^2(K)} \leq |K|^{1/2} h_K |u^K|_{H^1(K)} .$$

For all of the square elements  $K$ , which shrink as  $r$  increases, the term  $|u^K|_{H^1(K)}$

is not problematic. However, the L-shaped element  $K = K_L$  does not shrink as  $r$  increases so the estimate  $|u^K|_{H^1(K)} \leq |K|^{1/2} h_K$  gives no guarantee of convergence at all, much less at the optimal rate. In fact, if we approximate  $u$  by  $\hat{u} \in V_1(\mathcal{T}_r)$  for this family of meshes, we do not get convergence in  $H^1(\Omega)$ !

This issue is simple to fix, however, and the remedy we now describe is suggestive of a more general principle that we aim to explore in detail in subsequent work. Because  $-\Delta u^K = -\Delta u = 1$  on  $K = K_L$ , we include the interior bubble function  $\phi \in V_2^K(K_L)$  satisfying  $-\Delta\phi = 1$  in  $K_L$  and  $\phi = 0$  on  $\partial K_L$ . The necessary quantities associated with  $\phi$  can be computed in the same manner as described (3.33) and its paragraph. We take  $\tilde{V}_1(K_L) = \text{span}(V_1(K_L) \cup \{\phi\})$  and  $\tilde{V}_1(\mathcal{T}_r) = \text{span}(V_1(\mathcal{T}_r) \cup \{\phi\})$ . We recall that  $\int_{\Omega} \nabla\psi \cdot \nabla\phi \, dx = \int_{K_L} \nabla\psi \cdot \nabla\phi \, dx = 0$  for all  $\psi \in V_1(\mathcal{T}_r)$ , so adding this function does not increase the cost of assembling and solving the necessary linear system.

With this enrichment by  $\phi$ , we have, on  $K = K_L$ ,

$$|u - \mathcal{I}_K u|_{H^1(K)} = |u^{\partial K} - \mathcal{I}_K^{\partial K} u|_{H^1(K)} .$$

Since  $u^{\partial K} - \mathcal{I}_K^{\partial K} u$  is harmonic on  $K_L$ , Dirichlet's principle ensures that, on  $K = K_L$ ,

$$|u^{\partial K} - \mathcal{I}_K^{\partial K} u|_{H^1(K)} = \inf\{|\xi|_{H^1(\Omega)} : \xi \in H^1(K_L) \text{ and } \xi = u^{\partial K} - \mathcal{I}_K^{\partial K} u \text{ on } \partial K_L\} .$$

This can be estimated by a technique similar in spirit to that given in [41, Theorem 4.1]. The argument involves creating a (fictitious) sub-triangulation of  $K_L$ , taking  $\phi$  to be the piecewise linear interpolant of  $u^{\partial K}$  (or  $u$ ) on this sub-triangulation, and using standard interpolation error estimates. However, unlike the estimate in [41, Theorem 4.1], which assumes  $H^2$  regularity of  $u^{\partial K}$ , we use geometrically graded sub-triangulations, as pictured in Figure 3.7, and use estimates from [7, 57] to deduce that  $|u^{\partial K} - \mathcal{I}_K^{\partial K} u|_{H^1(K)} \leq C_K r^{-1}$  on  $K = K_L$ , where  $C_K$  depends only on the mesh

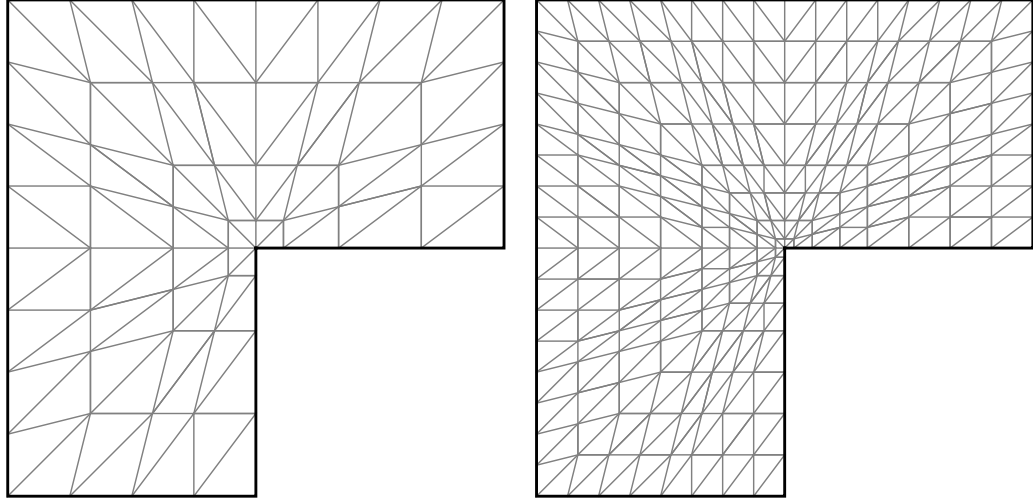


Figure 3.7: Sub-triangulations of the L-shaped element  $K_L$  that are geometrically graded toward the origin, corresponding to  $r = 4$  (left) and  $r = 8$ . These sub-triangulations are used merely as part of the argument to justify the interpolation error estimate, and are not used in the computation of  $\hat{u}$ .

grading parameter and the norm of  $u^{\partial K}$  (or  $u$ ) in an appropriate weighted Sobolev space. Combining this with the simple estimates from Theorem 3.3.8 for the square elements, and we see that  $|u - \mathcal{I}u|_{H^1(\Omega)} \leq Cr^{-1}$ , which is the rate of convergence observed in Table 3.2. We emphasize that sub-triangulations of  $K_L$  are purely for the purpose of this interpolation error estimate, and are not used at any point in the actual computations.

The number of rows and columns (and non-zeros) of the global stiffness matrix  $A$  grows quadratically with  $r$ , and the number of rows and columns of the (dense) submatrix  $A_L$  corresponding to  $V_1(K_L)$  grows linearly with  $r$ . We comment briefly on the condition numbers of these matrices, which are reported in Table 3.2. As with standard (low-order) finite elements, the condition number of  $A$  grows linearly with  $\dim(\tilde{V}_1(\mathcal{T}_r))$ , or quadratically with  $r$ . In contrast, the growth of the condition number of  $A_L$  seems to be leveling off—it is certainly not growing quadratically, or even linearly, with  $r$ . These issues of conditioning will be explored further in

Table 3.2: Discretization errors,  $|u - \hat{u}|_{H^1(\Omega)}$ , and error ratios for the sequence of meshes having one L-shaped cell of fixed size and increasingly fine square cells. Also included are the spectral condition numbers of the global (sparse) stiffness matrix  $A$  and the small (dense) stiffness matrix  $A_L$  associated with the basis functions on the L-shaped cell.

$r$	$ u - \hat{u} _{H^1(\Omega)}$	ratio	$\kappa_2(A)$	$\kappa_2(A_L)$
1	1.3629e-01		1.2908e+01	5.7834e+00
2	6.7610e-02	2.0158	3.7679e+01	7.5699e+00
4	3.3734e-02	2.0042	1.2527e+02	8.9390e+00
8	1.6855e-02	2.0014	4.6339e+02	9.8197e+00
16	8.4305e-03	1.9993	1.7919e+03	1.0377e+01
32	4.2289e-03	1.9935	7.0585e+03	1.0728e+01
64	2.1468e-03	1.9699	2.8029e+04	1.2450e+01

subsequent work.

In [3, Example 4.4] we compared interpolation errors in  $L^2(\Omega)$  for the harmonic function  $u = r^{2/3} \sin(2(\theta - \pi/2)/3)$  on  $\Omega = (-1, 1) \times (-1, 1) \setminus [0, 1] \times [0, 1]$ , a rotated version of the  $\Omega$  used here, on three different families of meshes. As noted above, one of these families of meshes was the one used here, and it led to optimal order convergence. The two other families yielded sub-optimal convergence at a theoretically predicted rate. One of these families of meshes consisted solely of congruent squares, and the other family was the same except right near the corner, where it had a single small L-shaped cell obtained by merging three of these squares. Although the local space on this L-shaped element could approximate the singular function at the optimal rate, the neighboring square elements, which got increasingly closer to the singularity on finer meshes, could not, so the overall convergence was spoiled. This motivates our choice to keep the L-shaped element of fixed size, as we have here. The particular size of this element is not crucial to the overall asymptotic behavior of convergence. In fact, we could have chosen  $K_L = \Omega$  in this case, and just solved the problem using integral equation techniques, as we did above for (3.33). The point of using the kinds of meshes that we did here is to demonstrate that they can offer a feasible alternative

to more traditional refinement techniques.

### 3.6. Conclusions

We have provided analysis and a practical low-order realization of a novel finite element method on meshes consisting of quite general curvilinear polygons. Allowing for such curved elements introduces both theoretical and computational challenges, including the proper definition and treatment of polynomial spaces defined on curves, determining an appropriate interpolation operator and obtaining meaningful error estimates, and efficiently computing with the implicitly-defined basis functions. Concerning the first of these challenges, we described and demonstrated simple methods for constructing a spanning set for a polynomial space on an edge, and then pairing it down to a basis. Concerning the second challenge, we proved local interpolation estimates in  $L^2$  and  $H^1$  for a projection-based scheme, showing that interpolation in these spaces is at least as good as interpolation in standard polynomial spaces on typical element shapes (e.g. triangles and quadrilaterals). The optimal order convergence of finite element approximations of a function having an unbounded gradient without employing small cells near the singularity, as well as the analysis provided for that specific example, indicates an even richer approximation theory that will be explored in subsequent work. In terms of practical computations, we described a boundary integral approach that was very recently developed with precisely these applications in mind. The numerical examples illustrated our convergence results on several families of meshes whose mesh cells are far from being simple perturbations of straight-edged polygons. We also numerically compared the approximation power of two types of harmonic bases on a mesh consisting of triangles with a single perturbed edge.

As highlighted at the end of Section 3.3, a better understanding of how geometric

features of elements and choice of  $p$  affect constants appearing in the interpolation analysis for  $V_p(K)$  is needed. Additionally, an accounting of errors made in the approximation of quantities required for the formation of element stiffness matrices, and those subsequently arising from quadratures, should be taken into account as part of a more complete analysis of the method. Since the experiments in this work really only involved harmonic basis functions, all quadratures were performed on the boundaries of elements, but higher-order elements will require volumetric quadratures as well, and the development of efficient and robust volumetric quadratures in our context is another topic for further investigation. The method should also be tested on PDEs modeling more complex phenomena, and problems in which there are curved (and moving) interfaces between materials are of particular interest in this regard. Extending this approach to 3D problems in which general curved cells are permitted presents both theoretical and practical/computational challenges beyond the obvious analogues discussed above, and we aim to address them in future work. Among these is a definition of  $V_p(K)$  that leads to a conforming space  $V_p(\mathcal{T})$  without making the dimension of  $V_p(K)$  much larger than is necessary to achieve optimal approximation properties. A second challenge is the efficient and accurate evaluation of quantities that are needed to form the local finite element linear systems; the approach outlined in Section 3.4 is inherently 2D, but there are integral equation approaches that may prove beneficial in our setting.

### 3.7. References

- [1] S. Adjerid, M. Aiffa, and J. E. Flaherty. Hierarchical finite element bases for triangular and tetrahedral elements. *Comput. Methods Appl. Mech. Engrg.*, 190(22-23):2925 – 2941, 2001.
- [2] B. Ahmad, A. Alsaedi, F. Brezzi, L. D. Marini, and A. Russo. Equivalent projectors for virtual element methods. *Comput. Math. Appl.*, 66(3):376–391, 2013.
- [3] A. Anand, J. S. Ovall, and S. Weißer. A Nyström-based finite element method on polygonal elements. *Comput. Math. Appl.*, 75(11):3971–3986, 2018.
- [4] P. Antonietti, M. Bruggi, S. Scacchi, and M. Verani. On the virtual element method for topology optimization on polygonal meshes: A numerical study. *Comput. Math. Appl.*, 74(5):1091 – 1109, 2017.
- [5] P. F. Antonietti, L. Beirão da Veiga, D. Mora, and M. Verani. A stream virtual element formulation of the Stokes problem on polygonal meshes. *SIAM J. Numer. Anal.*, 52(1):386–404, 2014.
- [6] P. F. Antonietti, S. Berrone, M. Verani, and S. Weißer. The virtual element method on anisotropic polygonal discretizations. In F. A. Radu, K. Kumar, I. Berre, J. M. Nordbotten, and I. S. Pop, editors, *Numerical Mathematics and Advanced Applications ENUMATH 2017*, pages 725–733, Cham, 2019. Springer International Publishing.
- [7] T. Apel, A.-M. Sändig, and J. R. Whiteman. Graded mesh refinement and error estimates for finite element solutions of elliptic boundary value problems in non-smooth domains. *Math. Methods Appl. Sci.*, 19(1):63–85, 1996.
- [8] L. Beirão da Veiga, F. Brezzi, L. D. Marini, and A. Russo. Virtual elements and curved edges, 2019. arXiv:1910.10184.
- [9] L. Beirão da Veiga, A. Chernov, L. Mascotto, and A. Russo. Basic principles of *hp* virtual elements on quasiuniform meshes. *Math. Models Methods Appl. Sci.*, 26(8):1567–1598, 2016.
- [10] L. Beirão da Veiga, A. Russo, and G. Vacca. The Virtual Element Method with curved edges. *ESAIM Math. Model. Numer. Anal.*, 53(2):375–404, 2019.
- [11] L. Beirão da Veiga, F. Brezzi, A. Cangiani, G. Manzini, L. D. Marini, and A. Russo. Basic principles of virtual element methods. *Math. Models Methods Appl. Sci.*, 23(1):199–214, 2013.
- [12] L. Beirão da Veiga, F. Brezzi, L. D. Marini, and A. Russo. The hitchhiker’s guide to the virtual element method. *Math. Models Methods Appl. Sci.*, 24(8):1541–1573, 2014.

- [13] L. Beirão da Veiga and G. Manzini. A virtual element method with arbitrary regularity. *IMA J. Numer. Anal.*, 34(2):759–781, 2014.
- [14] M. F. Benedetto, S. Berrone, A. Borio, S. Pieraccini, and S. Scialò. Order preserving SUPG stabilization for the virtual element formulation of advection-diffusion problems. *Comput. Methods Appl. Mech. Engrg.*, 311:18–40, 2016.
- [15] C. Bernardi. Optimal finite-element interpolation on curved domains. *SIAM J. Numer. Anal.*, 26(5):1212–1240, 1989.
- [16] S. Bertoluzza, M. Pennacchio, and D. Prada. High order VEM on curved domains. *Atti Accad. Naz. Lincei Cl. Sci. Fis. Mat. Natur.*, 30(2):391–412, 2019.
- [17] S. Beuchler and J. Schöberl. New shape functions for triangular  $p$ -FEM using integrated Jacobi polynomials. *Numer. Math.*, 103(3):339–366, 2006.
- [18] J. Bonelle, D. A. Di Pietro, and A. Ern. Low-order reconstruction operators on polyhedral meshes: application to compatible discrete operator schemes. *Comput. Aided Geom. Design*, 35/36:27–41, 2015.
- [19] J. Bonelle and A. Ern. Analysis of compatible discrete operator schemes for elliptic problems on polyhedral meshes. *ESAIM Math. Model. Numer. Anal.*, 48(2):553–581, 2014.
- [20] J. Bonelle and A. Ern. Analysis of compatible discrete operator schemes for the Stokes equations on polyhedral meshes. *IMA J. Numer. Anal.*, 35(4):1672–1697, 2015.
- [21] L. Botti and D. A. Di Pietro. Assessment of hybrid high-order methods on curved meshes and comparison with discontinuous Galerkin methods. *J. Comput. Phys.*, 370:58–84, 2018.
- [22] J. H. Bramble, J. E. Pasciak, and A. H. Schatz. The construction of preconditioners for elliptic problems by substructuring. I. *Math. Comp.*, 47(175):103–134, 1986.
- [23] S. C. Brenner and L. R. Scott. *The mathematical theory of finite element methods*, volume 15 of *Texts in Applied Mathematics*. Springer-Verlag, New York, second edition, 2002.
- [24] F. Brezzi, K. Lipnikov, and M. Shashkov. Convergence of mimetic finite difference method for diffusion problems on polyhedral meshes with curved faces. *Math. Models Methods Appl. Sci.*, 16(2):275–297, 2006.
- [25] F. Brezzi and L. D. Marini. Virtual element and discontinuous Galerkin methods. In *Recent developments in discontinuous Galerkin finite element methods for partial differential equations*, volume 157 of *IMA Vol. Math. Appl.*, pages 209–221. Springer, Cham, 2014.

- [26] P. G. Ciarlet. *The finite element method for elliptic problems*, volume 40 of *Classics in Applied Mathematics*. Society for Industrial and Applied Mathematics (SIAM), Philadelphia, PA, 2002. Reprint of the 1978 original [North-Holland, Amsterdam; MR0520174 (58 #25001)].
- [27] D. Copeland, U. Langer, and D. Pusch. From the boundary element domain decomposition methods to local Trefftz finite element methods on polyhedral meshes. In *Domain decomposition methods in science and engineering XVIII*, volume 70 of *Lect. Notes Comput. Sci. Eng.*, pages 315–322. Springer, Berlin, 2009.
- [28] J. A. Cottrell, T. J. R. Hughes, and Y. Bazilevs. *Isogeometric Analysis: Toward Integration of CAD and FEA*. Wiley Publishing, 1st edition, 2009.
- [29] L. T. Dechevski and W. L. Wendland. On the Bramble-Hilbert lemma. II. An improved estimate of the embedding constant. *Int. J. Pure Appl. Math.*, 33(4):433–464, 2006.
- [30] S. Dekel and D. Leviatan. The Bramble-Hilbert lemma for convex domains. *SIAM J. Math. Anal.*, 35(5):1203–1212, 2004.
- [31] L. Demkowicz and A. Buffa.  $H^1$ ,  $H(\text{curl})$  and  $H(\text{div})$ -conforming projection-based interpolation in three dimensions. Quasi-optimal  $p$ -interpolation estimates. *Comput. Methods Appl. Mech. Engrg.*, 194(2-5):267–296, 2005.
- [32] D. A. Di Pietro and A. Ern. A hybrid high-order locking-free method for linear elasticity on general meshes. *Comput. Methods Appl. Mech. Engrg.*, 283:1–21, 2015.
- [33] D. A. Di Pietro and A. Ern. Hybrid high-order methods for variable-diffusion problems on general meshes. *C. R. Math. Acad. Sci. Paris*, 353(1):31–34, 2015.
- [34] D. A. Di Pietro, A. Ern, and S. Lemaire. An arbitrary-order and compact-stencil discretization of diffusion on general meshes based on local reconstruction operators. *Comput. Methods Appl. Math.*, 14(4):461–472, 2014.
- [35] R. G. Durán. On polynomial approximation in Sobolev spaces. *SIAM J. Numer. Anal.*, 20(5):985–988, 1983.
- [36] A. Ern and J.-L. Guermond. *Theory and practice of finite elements*, volume 159 of *Applied Mathematical Sciences*. Springer-Verlag, New York, 2004.
- [37] G. J. Fix, S. Gulati, and G. I. Wakoff. On the use of singular functions with finite element approximations. *J. Computational Phys.*, 13:209–228, 1973.
- [38] M. Floater, A. Gillette, and N. Sukumar. Gradient bounds for Wachspress coordinates on polytopes. *SIAM J. Numer. Anal.*, 52(1):515–532, 2014.

- [39] M. S. Floater. Generalized barycentric coordinates and applications. *Acta Numer.*, 24:161–214, 2015.
- [40] A. L. Gain, C. Talischi, and G. H. Paulino. On the Virtual Element Method for three-dimensional linear elasticity problems on arbitrary polyhedral meshes. *Comput. Methods Appl. Mech. Engrg.*, 282:132–160, 2014.
- [41] A. Gillette and A. Rand. Interpolation error estimates for harmonic coordinates on polytopes. *ESAIM Math. Model. Numer. Anal.*, 50(3):651–676, 2016.
- [42] A. Gillette, A. Rand, and C. Bajaj. Error estimates for generalized barycentric interpolation. *Adv. Comput. Math.*, 37(3):417–439, 2012.
- [43] A. Gillette, A. Rand, and C. Bajaj. Construction of scalar and vector finite element families on polygonal and polyhedral meshes. *Comput. Methods Appl. Math.*, 16(4):667–683, 2016.
- [44] A. Greenbaum, L. Greengard, and G. B. McFadden. Laplace’s equation and the Dirichlet-Neumann map in multiply connected domains. *J. Comput. Phys.*, 105(2):267–278, 1993.
- [45] P. Grisvard. *Singularities in boundary value problems*, volume 22 of *Recherches en Mathématiques Appliquées [Research in Applied Mathematics]*. Masson, Paris, 1992.
- [46] P. Grisvard. *Elliptic problems in nonsmooth domains*, volume 69 of *Classics in Applied Mathematics*. Society for Industrial and Applied Mathematics (SIAM), Philadelphia, PA, 2011. Reprint of the 1985 original [MR0775683], With a foreword by Susanne C. Brenner.
- [47] M. Gu and L. Miranian. Strong rank revealing Cholesky factorization. *Electron. Trans. Numer. Anal.*, 17:76–92, 2004.
- [48] P. C. Hansen and P. Y. Yalamov. Computing symmetric rank-revealing decompositions via triangular factorization. *SIAM J. Matrix Anal. Appl.*, 23(2):443–458, 2001.
- [49] N. J. Higham. Analysis of the Cholesky decomposition of a semi-definite matrix. In *Reliable numerical computation*, Oxford Sci. Publ., pages 161–185. Oxford Univ. Press, New York, 1990.
- [50] C. Hofreither.  $L_2$  error estimates for a nonstandard finite element method on polyhedral meshes. *J. Numer. Math.*, 19(1):27–39, 2011.
- [51] C. Hofreither, U. Langer, and C. Pechstein. Analysis of a non-standard finite element method based on boundary integral operators. *Electron. Trans. Numer. Anal.*, 37:413–436, 2010.

- [52] C. Hofreither, U. Langer, and S. Weißer. Convection-adapted BEM-based FEM. *ZAMM Z. Angew. Math. Mech.*, 96(12):1467–1481, 2016.
- [53] R. A. Horn and C. R. Johnson. *Matrix analysis*. Cambridge University Press, Cambridge, second edition, 2013.
- [54] V. V. Karachik and N. A. Antropova. On the solution of a nonhomogeneous polyharmonic equation and the nonhomogeneous Helmholtz equation. *Differ. Uravn.*, 46(3):384–395, 2010.
- [55] V. A. Kozlov, V. G. Maz'ya, and J. Rossmann. *Elliptic boundary value problems in domains with point singularities*, volume 52 of *Mathematical Surveys and Monographs*. American Mathematical Society, Providence, RI, 1997.
- [56] M. Lenoir. Optimal isoparametric finite elements and error estimates for domains involving curved boundaries. *SIAM J. Numer. Anal.*, 23(3):562–580, 1986.
- [57] H. Li and V. Nistor. Analysis of a modified Schrödinger operator in 2D: regularity, index, and FEM. *J. Comput. Appl. Math.*, 224(1):320–338, 2009.
- [58] H. Li and J. S. Owall. A posteriori error estimation of hierarchical type for the Schrödinger operator with inverse square potential. *Numer. Math.*, 128(4):707–740, 2014.
- [59] G. Manzini, A. Russo, and N. Sukumar. New perspectives on polygonal and polyhedral finite element methods. *Math. Models Methods Appl. Sci.*, 24(8):1665–1699, 2014.
- [60] R. J. Y. McLeod and M. L. Baart. *Geometry and interpolation of curves and surfaces*. Cambridge University Press, Cambridge, 1998.
- [61] N. Moës, J. Dolbow, and T. Belytschko. A finite element method for crack growth without remeshing. *Internat. J. Numer. Methods Engrg.*, 46(1):131–150, 1999.
- [62] L. Mu, J. Wang, and X. Ye. A new weak Galerkin finite element method for the Helmholtz equation. *IMA J. Numer. Anal.*, 35(3):1228–1255, 2015.
- [63] L. Mu, J. Wang, and X. Ye. A weak Galerkin finite element method with polynomial reduction. *J. Comput. Appl. Math.*, 285:45–58, 2015.
- [64] L. Mu, J. Wang, and X. Ye. Weak Galerkin finite element methods on polytopal meshes. *Int. J. Numer. Anal. Model.*, 12(1):31–53, 2015.
- [65] J. S. Owall and S. E. Reynolds. A high-order methods for evaluating derivatives of harmonic functions in planar domains. *SIAM J. Sci. Comput.*, 40(3):A1915–A1935, 2018.

- [66] L. E. Payne and H. F. Weinberger. An optimal Poincaré inequality for convex domains. *Arch. Rational Mech. Anal.*, 5:286–292 (1960), 1960.
- [67] A. Rand, A. Gillette, and C. Bajaj. Quadratic serendipity finite elements on polygons using generalized barycentric coordinates. *Math. Comp.*, 83(290):2691–2716, 2014.
- [68] S. Rjasanow and S. Weißer. Higher order BEM-based FEM on polygonal meshes. *SIAM J. Numer. Anal.*, 50(5):2357–2378, 2012.
- [69] S. Rjasanow and S. Weißer. FEM with Trefftz trial functions on polyhedral elements. *J. Comput. Appl. Math.*, 263:202–217, 2014.
- [70] C. Schwab. *p- and hp-finite element methods*. Numerical Mathematics and Scientific Computation. The Clarendon Press, Oxford University Press, New York, 1998. Theory and applications in solid and fluid mechanics.
- [71] R. Scott. *Finite Element Techniques for Curved Boundaries*. PhD thesis, Massachusetts Institute of Technology, June 1973.
- [72] D. W. Spring, S. E. Leon, and G. H. Paulino. Unstructured polygonal meshes with adaptive refinement for the numerical simulation of dynamic cohesive fracture. *Intl. J. Fract.*, 189(1):33–57, Sep 2014.
- [73] T. Strouboulis, I. Babuška, and K. Copps. The design and analysis of the generalized finite element method. *Comput. Methods Appl. Mech. Engrg.*, 181(1-3):43–69, 2000.
- [74] B. Szabó and I. Babuška. *Finite element analysis*. A Wiley-Interscience Publication. John Wiley & Sons, Inc., New York, 1991.
- [75] A. Vaziri Astaneh, F. Fuentes, J. Mora, and L. Demkowicz. High-order polygonal discontinuous Petrov-Galerkin (PolyDPG) methods using ultraweak formulations. *Comput. Methods Appl. Mech. Engrg.*, 332:686–711, 2018.
- [76] R. Verfürth. A note on polynomial approximation in Sobolev spaces. *M2AN Math. Model. Numer. Anal.*, 33(4):715–719, 1999.
- [77] C. Wang and J. Wang. An efficient numerical scheme for the biharmonic equation by weak Galerkin finite element methods on polygonal or polyhedral meshes. *Comput. Math. Appl.*, 68(12, part B):2314–2330, 2014.
- [78] J. Wang and X. Ye. A weak Galerkin finite element method for second-order elliptic problems. *J. Comput. Appl. Math.*, 241:103–115, 2013.
- [79] J. Wang and X. Ye. A weak Galerkin mixed finite element method for second order elliptic problems. *Math. Comp.*, 83(289):2101–2126, 2014.

- [80] J. Wang and X. Ye. A weak Galerkin finite element method for the Stokes equations. *Adv. Comput. Math.*, 42(1):155–174, 2016.
- [81] S. Weißer. Residual error estimate for BEM-based FEM on polygonal meshes. *Numer. Math.*, 118(4):765–788, 2011.
- [82] S. Weißer. Arbitrary order Trefftz-like basis functions on polygonal meshes and realization in BEM-based FEM. *Comput. Math. Appl.*, 67(7):1390–1406, 2014.
- [83] S. Weißer. Residual based error estimate and quasi-interpolation on polygonal meshes for high order BEM-based FEM. *Comput. Math. Appl.*, 73(2):187–202, 2017.
- [84] S. Weißer. Anisotropic polygonal and polyhedral discretizations in finite element analysis. *ESAIM Math. Model. Numer. Anal.*, 52(2):475–501, 2019.
- [85] S. Weißer. *BEM-based Finite Element Approaches on Polytopal Meshes*, volume 130 of *Lecture Notes in Computational Science and Engineering*. Springer International Publishing, 1 edition, 2019.
- [86] S. Weißer and T. Wick. The dual-weighted residual estimator realized on polygonal meshes. *Comput. Methods Appl. Math.*, 18(4):753–776, 2018.
- [87] N. M. Wigley. Asymptotic expansions at a corner of solutions of mixed boundary value problems. *J. Math. Mech.*, 13:549–576, 1964.

## 4. Quadrature for Implicitly-defined Finite Element Functions on Curvilinear Polygons

### Full citation information:

Jeffrey S. Ovall and Samuel E. Reynolds. Quadrature for implicitly-defined finite element functions on curvilinear polygons. *Computers & Mathematics with Applications*, 107:1–16, 2022.

**Authors:** *Jeffrey S. Ovall<sup>1</sup> and Samuel E. Reynolds<sup>1</sup>*

### Author contribution statement:

- Jeffrey S. Ovall: established theoretical results, contributed to developing algorithms, contributed to drafting the paper, review and editing
- Samuel E. Reynolds: contributed to developing algorithms, contributed to drafting the paper, implemented numerical examples, review and editing

**DOI:** 10.1016/j.camwa.2021.12.003

### Hyperlink to the publication in PDXScholar:

<https://archives.pdx.edu/ds/psu/37923>

---

<sup>1</sup>Fariborz Maseeh Department of Mathematics and Statistics, Portland State University, Portland, OR 97201

## Abstract

$H^1$ -conforming Galerkin methods on polygonal meshes such as VEM, BEM-FEM and Trefftz-FEM employ local finite element functions that are implicitly defined as solutions of Poisson problems having polynomial source and boundary data. Recently, such methods have been extended to allow for mesh cells that are curvilinear polygons. Such extensions present new challenges for determining suitable quadratures. We describe an approach for integrating products of these implicitly defined functions, as well as products of their gradients, that reduces integrals on cells to integrals along their boundaries. Numerical experiments illustrate the practical performance of the proposed methods.

### 4.1. Introduction

The construction, analysis and implementation of finite element methods employing meshes consisting of non-standard cell shapes (e.g. fairly general polygons in 2D and polyhedra in 3D) have generated a lot of interest, and a sizable literature, in the last 10+ years. We do not attempt here to provide a representative sample of the literature, but instead highlight three closely-related approaches for second-order (linear) elliptic problems that yield  $H^1$ -conforming finite element spaces, and provide motivation for the problems considered in this work. Virtual Element Methods (VEM) (cf. [1, 4–6, 9–16, 22]), Boundary Element-Based Finite Element Methods (BEM-FEM) (cf. [28, 37–39, 44–49]) and Trefftz-type Finite Element Methods (Trefftz-FEM) (cf. [2, 3, 18, 26, 27]) all employ vector spaces that are implicitly defined, as in (4.1). The primary difference between VEM on the one hand, and BEM-FEM and Trefftz-FEM on the other, is how they work with such implicitly defined spaces in practice, particularly with regard to forming finite element linear systems. In

VEM, the space is treated “virtually” via degrees of freedom that provide enough information, up to a well-chosen stabilization term, to form the linear system; computations with basis functions (shape functions) are avoided. In contrast, BEM-FEM and Trefftz-FEM work more directly with basis functions, which are defined implicitly in terms of Poisson problems with explicitly given (polynomial) data. All computations involving these basis functions (e.g. pointwise evaluation of functions and some of their derivatives) are carried out using the solution of associated boundary integral equations. BEM-FEM and Trefftz-FEM differ primarily in the types of boundary integral equations that are solved (typically second-kind for Trefftz-FEM, and first-kind for BEM-FEM), and the discretizations employed for solving them (Nyström methods for recent versions of Trefftz-FEM, and BEM for BEM-FEM). Recently, Trefftz-FEM and VEM have been extended to allow for mesh cells that are curvilinear polygons (cf. [2, 3, 9, 10]). Such curved cells might naturally arise when standard (polygonal) cells abut a curved portion of the domain boundary or are transected by a (possibly evolving) curved interface, or multiple (small) curved inclusions in a material make it more computationally efficient to use mesh cells that have curved edges. Examples of such situations are given in Figure 4.1.

Determining suitable quadratures for finite elements on general polytopal meshes is clearly more challenging than for standard meshes, such as those involving only simplices and/or basic (affine) transformations of tensor product cells, for which polynomial-based quadratures of high order are readily available. Allowing for general curvilinear polygons and non-polynomial functions further complicates the matter. An obvious approach to quadrature on polytopes is to first partition it into such standard mesh cells, apply the known quadratures on each, and sum the result. This “brute-force” approach, though costly, remains popular because of the simplicity of its implementation. It is used, for example, in the BEM-FEM literature, whenever

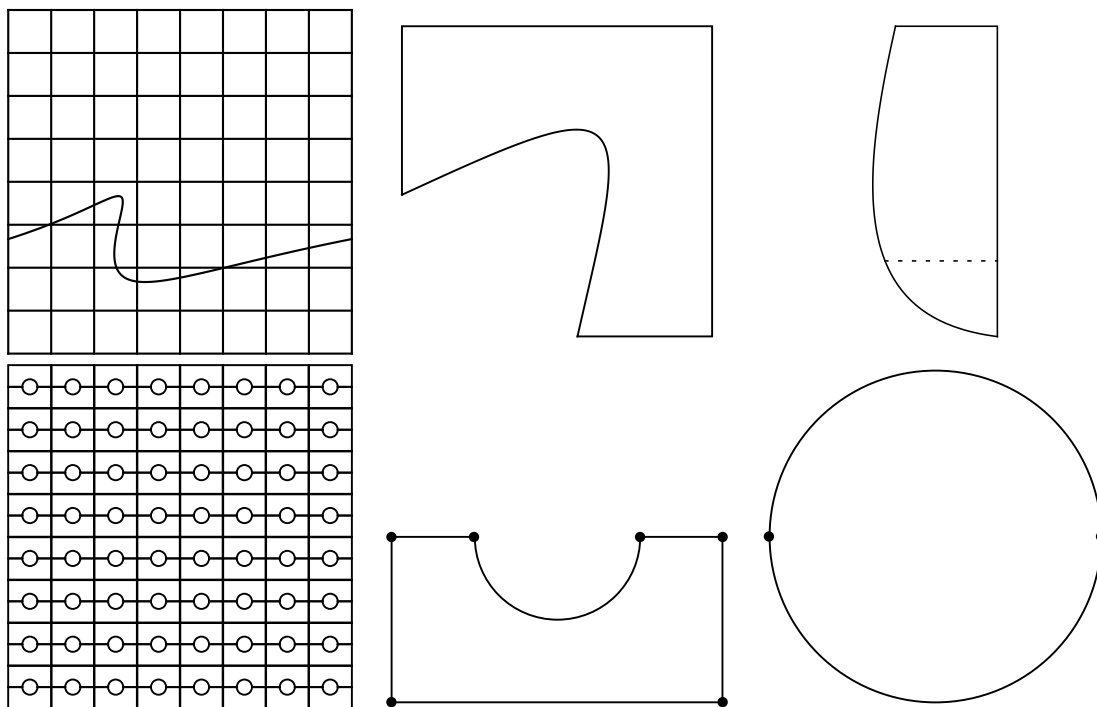


Figure 4.1: Top panel: a “background” mesh of squares cut by a curved interface, and two curved cells generated by this cutting, the second of which obtained by merging two smaller cells. Bottom panel: A domain with multiple small circular “inclusions” with a fitted mesh, and the two resultant cell types, the second of which is regarded as having two edges.

higher-order spaces, e.g. (4.1) for  $m > 1$ , are employed. Making no attempt at being exhaustive, we briefly describe some of the more sophisticated approaches—the introduction in [7] provides a good starting point for a more detailed exploration. In [40], the authors describe an approach yielding Gauss-like quadratures for polygons, which are exact for polynomials of a given degree  $2n - 1$ . An unattractive feature of the approach is that it often leads to quadrature points that lie outside the polygon. However, in many cases, including all convex polygons, a modified version of their approach yields all quadrature points in the polygon. In [41], the authors propose a similar approach which also allows for integration on polyhedra, and provide a more careful reporting of its practical efficiency. In [35], the authors first use a Schwarz-Christoffel (conformal) mapping to transform a polygon to the unit

disk, which is clearly tensorial in polar coordinates, and then any number of basic 1D quadratures (e.g. midpoint rule) may be applied in the radial and angular directions. The authors discuss numerical methods for determining the conformal map for each polygon. A more sophisticated subpartitioning approach is described in [43], with the aim of integrating non-polynomial (often rational) functions such as several variants of “generalized barycentric coordinates” naturally arising in Polygonal FEM (PFEM) (cf. [21, 29]). The contribution [42] describes methods for systematically “compressing” pre-existing quadrature rules, keeping a subset of the original nodes and recomputing quadrature weights, in order to retain as much of the effectiveness of the original quadrature while often drastically reducing the number of quadrature nodes. In [7], the authors consider the integration of polynomials on (flat-faced) polytopes in  $\mathbb{R}^d$ . A simple identity for homogeneous functions allows recursive reduction of the integral of a polynomial on the polytope to a sum of integrals lower-dimensional facets, ending in evaluation at the vertices. The first step in their reduction can also be used for curvilinear polygons, so we provide further details in Section 4.3. A very recent contribution [8] considers quadratures on curvilinear polygons whose curved edges are arcs of circles, and whose vertices are also the vertices of a convex polygon. This approach first partitions the cell into (curved) triangles and rectangles, each having at most once curved edge, generates quadratures for these specialized shapes, and then sums them to obtain a quadrature for the entire cell. Finally, a compression technique is used to reduce the number of quadrature points.

Given  $m \in \mathbb{Z}$ , we denote by  $\mathbb{P}_m$  the vector space of (real-valued) polynomials of total degree  $\leq m$  on  $\mathbb{R}^2$ , with the convention that  $\mathbb{P}_m = \{0\}$  when  $m < 0$ . We recall that  $\dim \mathbb{P}_m = \binom{m+2}{2}$ . For non-empty  $S \subset \mathbb{R}^2$ , we define  $\mathbb{P}_m(S)$  as the restriction of  $\mathbb{P}_m$  to  $S$ , and note that it is also a vector space. The dimension of  $\mathbb{P}_m(S)$  depends on the nature of  $S$ . For example, if  $S$  is open and connected, then  $\dim \mathbb{P}_m(S) =$

$\dim \mathbb{P}_m = \binom{m+2}{2}$ ; if  $S$  consists of a single point, then  $\dim \mathbb{P}_m(S) = 1$ ; if  $S$  is a straight line or a segment thereof, then  $\dim \mathbb{P}_m(S) = \binom{m+2}{2} - \binom{m+1}{2} = m + 1$ ; and if  $S$  is an arc of a curved conic section, then  $\dim \mathbb{P}_m(S) = \binom{m+2}{2} - \binom{m}{2}$ . Further discussion of  $\mathbb{P}_m(e)$ , where  $e$  is a simple (bounded) curve, is given in [2].

Let  $K \subset \mathbb{R}^2$  be open, bounded, simply connected, whose Lipschitz boundary  $\partial K$  is a union of smooth arcs with disjoint interiors, which we call edges. We refer to  $K$  as a curvilinear polygon. Points where adjacent edges meet are called vertices, and adjacent edges are allowed to meet at a straight angle. For  $m \in \mathbb{N}$ , we define  $\mathbb{P}_m^*(\partial K)$  to be the vector space of continuous functions on  $\partial K$  such that the restriction of such a function to an edge  $e$  of  $K$  is in  $\mathbb{P}_m(e)$ . It is clear that  $\mathbb{P}_m(\partial K) \subset \mathbb{P}_m^*(\partial K)$ . We define the space  $V_m(K)$  as

$$V_m(K) = \{v \in H^1(K) : \Delta v \in \mathbb{P}_{m-2}(K) \text{ in } K, v|_{\partial K} \in \mathbb{P}_m^*(\partial K)\} . \quad (4.1)$$

It is apparent from the definition that  $\mathbb{P}_m(K) \subset V_m(K)$ , and it can be shown that the only way in which equality is achieved is when  $m = 1$  and  $K$  is a triangle. A natural decomposition of  $V_m(K)$  is  $V_m(K) = V_m^{\partial K}(K) \oplus V_m^K(K)$ , where

$$V_m^{\partial K}(K) = \{v \in H^1(K) : \Delta v = 0 \text{ in } K, v|_{\partial K} \in \mathbb{P}_m^*(\partial K)\} , \quad (4.2a)$$

$$V_m^K(K) = \{v \in H^1(K) : \Delta v \in \mathbb{P}_{m-2}(K) \text{ in } K, v|_{\partial K} = 0\} . \quad (4.2b)$$

We see that  $\dim V_m^K(K) = \dim \mathbb{P}_{m-2}(K) = \binom{m}{2}$ , and that  $\dim V_m^{\partial K}(K) = \dim \mathbb{P}_m^*(\partial K)$ , the latter of which not only depends on  $m$ , but also on the number and nature of the edges of  $K$ .

We consider methods for efficiently approximating integrals of the forms

$$\int_K vw \, dx \quad , \quad \int_K \nabla v \cdot \nabla w \, dx \quad , \quad (4.3)$$

for  $v, w \in V_m(K)$ , by reducing the computations to integrals along the boundary

$\partial K$ . As we will see in subsequent sections, we will never need to evaluate functions or their gradients in the interior of  $K$  in order to evaluate the integrals in (4.3) for  $v, w \in V_m(K)$ . We will only need access to Dirichlet and Neumann traces of associated functions.

*Remark 4.1.1.* The primary contributions of this paper are: to show how the integrals (4.3), which are defined on a 2D cell  $K$ , can be reduced to integrals on  $\partial K$ ; and to provide a practical algorithm based on this reduction as an illustration that methods derived from in this way can provide efficient and accurate approximations of (4.3). The resulting boundary integrals, e.g. (4.10)-(4.15), involve both the Dirichlet trace (function value) and the Neumann trace (normal derivative) of functions that are given implicitly in terms of polynomial source and boundary data. The evaluation of these boundary integrals can be effected by using any number of quadrature routines, provided the user has an efficient Dirichlet-to-Neumann map. In the present work, we use second-kind integral equations, discretized using a quadrature-based method, more specifically a Nyström method, to obtain the Dirichlet-to-Neumann map, see [36]. Our Nyström method involves quadratures that are based on the variations of the trapezoid rule that can accommodate algebraic singularities near corners [31], and periodic logarithmic singularities [32–34]. Solving the associated (well-conditioned) Nyström linear system, and post-processing using the FFT, yields the Dirichlet-to-Neumann map at the quadrature points used in the Nyström discretization. Because of how, and where, we obtain the Dirichlet-to-Neumann map, the boundary integrals (4.10)-(4.15) are computed using the same trapezoid-based quadrature [31]. Other pairings of suitable quadratures, e.g. Gaussian quadratures and the Gauss-like approach of [19, 20], and Dirichlet-to-Neumann maps may be similarly effective, but we do not pursue such realizations of our general approach here.

The rest of the paper is organized as follows. In Section 4.2, we discuss algebraic

and computational techniques for determining functions whose Laplacian is either a polynomial or a harmonic function. Using these, we describe how the integrals (4.3) can be reduced to associated integrals on cell boundaries. Quadratures along the edges require evaluation of associated functions and their normal derivatives, which are provided algebraically for polynomials and via boundary integral equations for harmonic functions. Numerical experiments illustrating the practical performance of the approach are provided in Section 4.4. Section 4.5 contains further details, such as our chosen quadrature for edges, that are not as central to the discussion and would unnecessarily bog down the reading of the paper if they were included earlier.

## 4.2. Preliminary Results

It will be useful to have techniques for solving Poisson problems having polynomial or harmonic source terms. The following result is a corollary of [30, Theorem 2].

**Proposition 4.2.1.** Suppose  $p \in \mathbb{P}_n$ . There is a  $P \in \mathbb{P}_{n+2}$  such that  $\Delta P = p$ . More explicitly, if  $p(x) = \sum_{|\alpha| \leq n} c_\alpha (x - z)^\alpha$ , then we may choose

$$\begin{aligned}
 P(x) &= \sum_{|\alpha| \leq n} c_\alpha P_\alpha(x) \\
 P_\alpha(x) &= \frac{|x - z|^2}{4(|\alpha| + 1)!} \sum_{k=0}^{\lfloor |\alpha|/2 \rfloor} \frac{(-1)^k (|\alpha| - k)!}{(k + 1)!} \left( \frac{|x - z|^2}{4} \right)^k \Delta^k (x - z)^\alpha,
 \end{aligned} \tag{4.4}$$

where  $\lfloor s \rfloor$  is the integer part of  $s$ .

We note that  $P_\alpha$ , which satisfies  $\Delta P_\alpha = (x - z)^\alpha$ , is homogeneous of degree  $|\alpha| + 2$ , and that these polynomials may be computed *offline* and tabulated for  $|\alpha|$  up to some specified threshold, so that  $P$  may be computed efficiently from the coefficients  $c_\alpha$  of  $p$ . A polynomial  $q \in \mathbb{P}_j$  given with respect to a shifted monomial basis, as is  $p$  above, can be encoded as a coefficient array of length  $J = \binom{j+2}{2}$ , once a suitable enumeration

Table 4.1: An enumeration of multiindices for  $|\alpha| \leq 6$ , together with the indices and values of the non-zero coefficients of  $P_\alpha$  from Proposition 4.2.1.

$k$	$\alpha$	$P_\alpha$ indices	$P_\alpha$ coefficients
0	(0, 0)	(3, 5)	(1, 1)/4
1	(1, 0)	(6, 8)	(1, 1)/8
2	(0, 1)	(7, 9)	(1, 1)/8
3	(2, 0)	(10, 12, 14)	(7, 6, -1)/96
4	(1, 1)	(11, 13)	(1, 1)/12
5	(0, 2)	(10, 12, 14)	(-1, 6, 7)/96
6	(3, 0)	(15, 17, 19)	(3, 2, -1)/64
7	(2, 1)	(16, 18, 20)	(11, 10, -1)/192
8	(1, 2)	(15, 17, 19)	(-1, 10, 11)/192
9	(0, 3)	(16, 18, 20)	(-1, 2, 3)/64
10	(4, 0)	(21, 23, 25, 27)	(31, 15, -15, 1)/960
11	(3, 1)	(22, 24, 26)	(13, 10, -3)/320
12	(2, 2)	(21, 23, 25, 27)	(-1, 15, 15, -1)/360
13	(1, 3)	(22, 24, 26)	(-3, 10, 13)/320
14	(0, 4)	(21, 23, 25, 27)	(1, -15, 15, 31)/960
15	(5, 0)	(28, 30, 32, 34)	(9, 3, -5, 1)/384
16	(4, 1)	(29, 31, 33, 35)	(57, 35, -21, 1)/1920
17	(3, 2)	(28, 30, 32, 34)	(-3, 63, 55, -11)/1920
18	(2, 3)	(29, 31, 33, 35)	(-11, 55, 63, -3)/1920
19	(1, 4)	(28, 30, 32, 34)	(1, -21, 35, 57)/1920
20	(0, 5)	(29, 31, 33, 35)	(1, -5, 3, 9)/384
21	(6, 0)	(36, 38, 40, 42, 44)	(127, 28, -70, 28, -1)/7168
22	(5, 1)	(37, 39, 41, 43)	(15, 7, -1, 1)/672
23	(4, 2)	(36, 38, 40, 42, 44)	(-99, 2772, 2030, -812, 29)/107520
24	(3, 3)	(37, 39, 41, 43)	(-1, 7, 7, -1)/280
25	(2, 4)	(36, 38, 40, 42, 44)	(29, -812, 2030, 2772, -99)/107520
26	(1, 5)	(37, 39, 41, 43)	(1, -7, 7, 15)/672
27	(0, 6)	(36, 38, 40, 42, 44)	(-1, 28, -70, 28, 127)/7168

of the multiindices  $\alpha$  is chosen. Such an enumeration is given in Table 4.1 for  $|\alpha| \leq 6$ , and its extension to all multiindices is clear. The mappings  $\alpha \mapsto k$  and  $k \mapsto \alpha$  corresponding to Table 4.1 are

$$\alpha \mapsto \binom{|\alpha|+1}{2} + \alpha_2 \quad , \quad k \mapsto \left( |\alpha| - k + \binom{|\alpha|+1}{2}, k - \binom{|\alpha|+1}{2} \right) \quad (4.5)$$

where  $|\alpha| = \left\lfloor \frac{\sqrt{8k+1} - 1}{2} \right\rfloor$ .

Basic procedures such as computing the product of two polynomials, or computing the gradient of a polynomial, both of which are needed for the integral computations discussed in Section 4.3, can be performed efficiently in terms of coefficient arrays.

For “sparse” polynomials, i.e. those that involve relatively few non-zero coefficients, significant efficiency can be gained by storing only the non-zero coefficients and their indices. The polynomials  $P_\alpha$  from Proposition 4.2.1 are also given in Table 4.1 for  $|\alpha| \leq 6$ , expressed in terms their (few) non-zero coefficients and the indices of these coefficients. For example, we see that, for  $\alpha = (2, 3)$ ,  $P_\alpha$  is a linear combination of the shifted monomials associated with multiindices  $29 \mapsto (6, 1)$ ,  $31 \mapsto (4, 3)$ ,  $33 \mapsto (2, 5)$  and  $35 \mapsto (0, 7)$ . More specifically,

$$P_\alpha(x) = \frac{1}{1920} \left( -11(x-z)^{(6,1)} + 55(x-z)^{(4,3)} + 63(x-z)^{(2,5)} - 3(x-z)^{(0,7)} \right)$$

for  $\alpha = (2, 3)$  .

Though there are several patterns in the non-zero coefficients of  $P_\alpha$  that may be of interest (and some that might be exploited), we highlight only one: the alternating (in sign) sum of the coefficients of  $P_\alpha$  is 0. For example,  $(-11 + (-1)(55) + 63 + (-1)(-3))/1920 = 0$ , for  $\alpha = (2, 3)$ . An extension of Table 4.1, for  $7 \leq |\alpha| \leq 10$ , is given in Table 4.8 in Section 4.5 for convenience.

We recall that, for any function  $\phi$  that is harmonic in  $K$ , there is a *harmonic conjugate*  $\widehat{\phi}$ , satisfying  $\Delta\widehat{\phi} = 0$  and the Cauchy-Riemann equations,

$$\frac{\partial\phi}{\partial x_1} = \frac{\partial\widehat{\phi}}{\partial x_2} \quad , \quad \frac{\partial\phi}{\partial x_2} = -\frac{\partial\widehat{\phi}}{\partial x_1} \quad , \quad (4.6)$$

in  $K$ . Such a harmonic conjugate is unique, up to an additive constant, and the orthogonality of  $\nabla\phi$  and  $\nabla\widehat{\phi}$  implies that

$$\frac{\partial\phi}{\partial \mathbf{n}} = \frac{\partial\widehat{\phi}}{\partial \mathbf{t}} \quad , \quad \frac{\partial\widehat{\phi}}{\partial \mathbf{n}} = -\frac{\partial\phi}{\partial \mathbf{t}} \quad \text{on } \partial K \quad , \quad (4.7)$$

where  $\mathbf{n}$  is the outward unit normal, and  $\mathbf{t}$  is the unit tangent in the counter-clockwise

direction. We can compute a harmonic conjugate  $\widehat{\phi}$  by solving the Neumann problem

$$\Delta \widehat{\phi} = 0 \text{ in } K \quad , \quad \frac{\partial \widehat{\phi}}{\partial \mathbf{n}} = -\frac{\partial \phi}{\partial \mathbf{t}} \text{ on } \partial K \quad , \quad \int_{\partial K} \widehat{\phi} \, ds = 0 . \quad (4.8)$$

The condition  $\int_{\partial K} \widehat{\phi} \, ds = 0$  ensures that there is a unique solution of (4.8).

We are now ready to describe an approach to computing a function whose Laplacian is a given harmonic function.

**Proposition 4.2.2.** Suppose  $\phi$  is harmonic in  $K$ . The following construction provides a function  $\Phi$  such that  $\Delta \Phi = \phi$  in  $K$ .

- (a) Determine a solution of the Neumann problem:  $\Delta \widehat{\phi} = 0$  in  $K$ ,  $\partial \widehat{\phi} / \partial \mathbf{n} = -\partial \phi / \partial \mathbf{t}$  on  $\partial K$ .
- (b) Determine a solution of the Neumann problem:  $\Delta \rho = 0$  in  $K$ ,  $\partial \rho / \partial \mathbf{n} = (\phi, -\widehat{\phi}) \cdot \mathbf{n}$  on  $\partial K$ .
- (c) Determine a solution of the Neumann problem:  $\Delta \widehat{\rho} = 0$  in  $K$ ,  $\partial \widehat{\rho} / \partial \mathbf{n} = (\widehat{\phi}, \phi) \cdot \mathbf{n}$  on  $\partial K$ .
- (d) Set  $\Phi = (x_1 \rho + x_2 \widehat{\rho}) / 4$ .

It holds that  $\phi$  and  $\widehat{\phi}$  are harmonic conjugates, and that  $\rho$  and  $\widehat{\rho}$  are harmonic conjugates.

*Proof.* It follows from the Cauchy-Reimann equations (4.6) that both of the vector fields  $(\phi, -\widehat{\phi})$  and  $(\widehat{\phi}, \phi)$  are conservative in  $K$ , so there are functions  $\rho$  and  $\widehat{\rho}$  such that  $\nabla \rho = (\phi, -\widehat{\phi})$  and  $\nabla \widehat{\rho} = (\widehat{\phi}, \phi)$  in  $K$ . The potentials  $\rho$  and  $\widehat{\rho}$  are unique, up to additive constants. We note that  $\rho$  and  $\widehat{\rho}$  also satisfy the Cauchy-Reimann equations in  $K$ ,

$$\frac{\partial \rho}{\partial x_1} = \frac{\partial \widehat{\rho}}{\partial x_2} = \phi \quad , \quad \frac{\partial \rho}{\partial x_2} = -\frac{\partial \widehat{\rho}}{\partial x_1} = -\widehat{\phi} .$$

It also follows from the Cauchy-Reimann equations for  $\phi, \widehat{\phi}$  that  $\Delta\rho = \Delta\widehat{\rho} = 0$  in  $K$ . In other words,  $\rho$  and  $\widehat{\rho}$  are also harmonic conjugates. By continuously extending their gradients to the boundary, we see that their normal derivatives must satisfy

$$\frac{\partial\rho}{\partial\mathbf{n}} = \begin{pmatrix} \phi \\ -\widehat{\phi} \end{pmatrix} \cdot \mathbf{n} \quad , \quad \frac{\partial\widehat{\rho}}{\partial\mathbf{n}} = \begin{pmatrix} \widehat{\phi} \\ \phi \end{pmatrix} \cdot \mathbf{n}$$

on  $\partial K$ , which leads to the two Neumann problems given in the proposition. Finally, we have

$$\Delta\Phi = \frac{1}{4} \left( 2\frac{\partial\rho}{\partial x_1} + 2\frac{\partial\widehat{\rho}}{\partial x_2} \right) = \phi \quad \text{in } K \quad ,$$

which completes the proof. □

*Remark 4.2.3.* Taking  $\phi, \widehat{\phi}, \rho$  and  $\widehat{\rho}$  as in Proposition 4.2.2, we have  $\Delta\widehat{\Phi} = \widehat{\phi}$  for  $\widehat{\Phi} = (x_1\widehat{\rho} - x_2\rho)/4$ .

The approach described in Proposition 4.2.2 involves the solution of three Neumann problems, each of which can be made well-posed by imposing the vanishing boundary integral condition as in (4.8). There are many well-established techniques involving boundary integral equations for solving such Neumann problems, and we will use that described in [36], which employs Nyström discretizations of (well-conditioned) second-kind integral equations. We mention a few relevant features of the approach in [36] for the conjugate pair  $(\phi, \widehat{\phi})$ :

- $\phi$  is given implicitly in terms of its Dirichlet trace on  $\partial K$ , and supplies the boundary data for the Neumann problem for  $\widehat{\phi}$  via  $\partial\widehat{\phi}/\partial\mathbf{n} = -\partial\phi/\partial\mathbf{t}$ .
- A Neumann-to-Dirichlet map,  $\partial\widehat{\phi}/\partial\mathbf{n} \mapsto \widehat{\phi}$  on  $\partial K$ , is obtained directly as the solution of a boundary integral equation.
- A Dirichlet-to-Neumann map,  $\phi \mapsto \partial\phi/\partial\mathbf{n}$  on  $\partial K$ , is then obtained from  $\widehat{\phi}$  via taking its tangential derivative,  $\partial\phi/\partial\mathbf{n} = \partial\widehat{\phi}/\partial\mathbf{t}$ .

In each step, all computations occur only on  $\partial K$ .

### 4.3. Reducing Volumetric Integrals to Boundary Integrals

We begin with the integration of polynomials on  $K$ . Let  $r \in \mathbb{P}_n(K)$ . In the spirit of Proposition 4.2.1, we can reduce  $\int_K r dx$  to an integral along  $\partial K$ , by taking  $R \in \mathbb{P}_{n+2}(K)$  such that  $\Delta R = r$ . It then follows that  $\int_K r dx = \int_{\partial K} \partial R / \partial \mathbf{n} ds$ . Alternatively, we have a reduction to the boundary based on the Divergence Theorem and the following simple identity, which can be verified by direct computation,

$$\nabla \cdot [(x - z)^\alpha (x - z)] = (2 + |\alpha|)(x - z)^\alpha .$$

Here and following,  $z \in \mathbb{R}^2$  may be chosen arbitrarily—the barycenter of  $K$  is a natural choice. From this, it follows that

$$\int_K (x - z)^\alpha dx = \frac{1}{2 + |\alpha|} \int_{\partial K} (x - z)^\alpha (x - z) \cdot \mathbf{n} ds . \quad (4.9)$$

This type of reduction is the core of the method described in [7], where  $K$  is a polytope in  $\mathbb{R}^d$ . In this case  $2 + |\alpha|$  is replaced by  $d + |\alpha|$  above, and further reductions of the same type can be made due to the fact that the faces of  $K$  are flat. If  $F$  is such a flat face (we would take an edge  $e$  in our case), then  $(x - z) \cdot \mathbf{n}(x)$  is constant for  $x \in F$ . More specifically, for  $x \in F$ ,  $(x - z) \cdot \mathbf{n}(x)$  is the signed distance between  $z$  and the hyperplane containing  $F$ , taking the positive sign if  $z \in K$ . Factoring out this constant, the integral on  $F$  can be further reduced to integrals along its  $(d - 2)$ -dimensional (flat) facets, and so on. For generic curved boundaries, further simple reductions of  $\int_{\partial K} (x - z)^\alpha (x - z) \cdot \mathbf{n} ds$  are not available. Regardless, (4.9) allows for the efficient evaluation of  $\int_K r dx$  in terms of integrals along  $\partial K$ . We opt for the approach based on (4.9), as opposed to that based on  $\int_K r dx = \int_{\partial K} \partial R / \partial \mathbf{n} ds$ , because it is a bit cheaper.

The integration of  $\int_K \nabla v \cdot \nabla w \, dx$  can be naturally considered in three cases, the first two of which involve at least one function from  $V_m^{\partial K}(K)$ . These easier two integrals are reduced to

$$\int_K \nabla v \cdot \nabla w \, dx = 0 \text{ when } v \in V_m^{\partial K}(K), w \in V_m^K(K), \quad (4.10a)$$

$$\int_K \nabla v \cdot \nabla w \, dx = \int_{\partial K} \frac{\partial v}{\partial \mathbf{n}} w \, ds \text{ when } v, w \in V_m^{\partial K}(K). \quad (4.10b)$$

In the case of (4.10b), both  $v$  and  $w$  are given (implicitly) in terms of their Dirichlet data, so a Dirichlet-to-Neumann map,  $v \mapsto \partial v / \partial \mathbf{n}$  on  $\partial K$ , is needed to evaluate the boundary integral. This can be done as discussed in Section 4.2, or by some other method of choice.

Now suppose that  $v, w \in V_m^K(K)$ . These are given (implicitly) in terms of  $p, q \in \mathbb{P}_{m-2}(K)$  such that  $\Delta v = p$  and  $\Delta w = q$  in  $K$ . Let  $P, Q \in \mathbb{P}_m(K)$  be such that  $\Delta P = p$  and  $\Delta Q = q$ . We have

$$\begin{aligned} \int_K \nabla v \cdot \nabla w \, dx &= \int_K \nabla v \cdot \nabla Q \, dx + \int_K \nabla v \cdot \nabla(w - Q) \, dx \\ &= \int_K \nabla v \cdot \nabla Q \, dx = \int_{\partial K} \frac{\partial v}{\partial \mathbf{n}} Q \, ds - \int_K pQ \, dx. \end{aligned}$$

Summarizing, we have

$$\int_K \nabla v \cdot \nabla w \, dx = \int_{\partial K} \frac{\partial v}{\partial \mathbf{n}} Q \, ds - \int_K pQ \, dx \text{ when } v, w \in V_m^K(K). \quad (4.11)$$

Since  $pQ \in \mathbb{P}_{2m-2}(K)$ , the integral  $\int_K pQ \, dx$  can be addressed as discussed at the beginning of this section. The only term in the boundary integrals in (4.11) that requires further consideration is  $\partial v / \partial \mathbf{n}$ . Unlike (4.10b),  $v$  is not harmonic in this case, so an additional step is needed to determine  $\partial v / \partial \mathbf{n}$ . This can be done as

follows,

$$\frac{\partial v}{\partial \mathbf{n}} = \frac{\partial(v - P)}{\partial \mathbf{n}} + \frac{\partial P}{\partial \mathbf{n}} . \quad (4.12)$$

The term  $\partial P/\partial \mathbf{n}$  can be computed directly from the known polynomial  $P$ , and the term  $\partial(v - P)/\partial \mathbf{n}$  can be computed using a Dirichlet-to-Neumann map as discussed earlier, because  $v - P$  is harmonic, with known boundary trace,  $-P$ .

The integral  $\int_K vw \, dx$  is more challenging than its gradient counterpart, and we do not bother splitting into cases as before. To fix notation,

$$\begin{aligned} \Delta v &= p \in \mathbb{P}_{m-2}(K) \text{ in } K \quad , \quad v = f \in \mathbb{P}_m^*(K) \text{ on } \partial K \quad , \\ \Delta w &= q \in \mathbb{P}_{m-2}(K) \text{ in } K \quad , \quad w = g \in \mathbb{P}_m^*(K) \text{ on } \partial K \quad . \end{aligned}$$

As above,  $P, Q \in \mathbb{P}_m(K)$  satisfy  $\Delta P = p$  and  $\Delta Q = q$ . We have

$$\begin{aligned} \int_K vw \, dx &= \int_K (v - P)(w - Q) \, dx + \int_K (v - P)Q \, dx \\ &\quad + \int_K P(w - Q) \, dx + \int_K PQ \, dx . \end{aligned}$$

Now, take  $P^*, Q^* \in \mathbb{P}_{m+2}(K)$  such that  $\Delta P^* = P$  and  $\Delta Q^* = Q$ , and  $\Phi$  such that  $\Delta \Phi = v - P$  in  $K$ , as indicated in Proposition 4.2.2. At this stage, we have

$$\begin{aligned} \int_K vw \, dx &= \int_K \Delta \Phi (w - Q) \, dx + \int_K (v - P)\Delta Q^* \, dx \\ &\quad + \int_K \Delta P^* (w - Q) \, dx + \int_K PQ \, dx . \end{aligned}$$

The integrands in four of these integrals are the product of a harmonic function with the Laplacian of a second function. Using Green's identities to move the Laplacian

over to the harmonic function, we obtain

$$\begin{aligned}
\int_K vw \, dx &= \int_{\partial K} \frac{\partial \Phi}{\partial \mathbf{n}} (g - Q) - \Phi \frac{\partial(w - Q)}{\partial \mathbf{n}} \, ds \\
&+ \int_{\partial K} \frac{\partial Q^*}{\partial \mathbf{n}} (f - P) - Q^* \frac{\partial(v - P)}{\partial \mathbf{n}} \, ds \\
&+ \int_{\partial K} \frac{\partial P^*}{\partial \mathbf{n}} (g - Q) - P^* \frac{\partial(w - Q)}{\partial \mathbf{n}} \, ds + \int_K PQ \, dx .
\end{aligned} \tag{4.13}$$

As with (4.11), we handle the polynomial integral as discussed at the beginning of this section. In the case that  $w = r \in \mathbb{P}_n(K)$ , we have a much simpler formula for reducing the integral to the boundary. Let  $R \in \mathbb{P}_{n+2}(K)$  be such that  $\Delta R = r$ . We have

$$\int_K vw \, dx = \int_{\partial K} (f - P) \frac{\partial R}{\partial \mathbf{n}} - R \frac{\partial(v - P)}{\partial \mathbf{n}} \, ds + \int_K Pr \, dx . \tag{4.14}$$

This simpler formula may be convenient for integrating basis function against polynomial source terms in the formation of the righthand side (load vector) for the finite element system, for example. A different simplification of (4.13) may be given when both  $v$  and  $w$  are harmonic. In this case, we may take  $P = Q = P^* = Q^* = 0$  in (4.13), and the formula reduces to

$$\int_K vw \, dx = \int_{\partial K} \frac{\partial \Phi}{\partial \mathbf{n}} g \, ds - \int_{\partial K} \Phi \frac{\partial w}{\partial \mathbf{n}} \, ds . \tag{4.15}$$

*Remark 4.3.1.* Both (4.13) and its special case (4.15) involve the normal derivative of the function  $\Phi$  of Proposition 4.2.2. Taking  $\phi = v - P$  as above, and using the notation of Proposition 4.2.2, this normal derivative is given by

$$\frac{\partial \Phi}{\partial \mathbf{n}} = \begin{pmatrix} \rho + x_1 \phi + x_2 \hat{\phi} \\ \hat{\rho} - x_1 \hat{\phi} + x_2 \phi \end{pmatrix} \cdot \frac{\mathbf{n}}{4} .$$

The Dirichlet data of  $v$  is given, and  $P$  is readily obtained from  $p$  based on Proposition 4.2.1 and look-up tables such as Table 4.1, so we have easy access to the Dirichlet

data of  $\phi$ . The functions  $\widehat{\phi}$ ,  $\rho$  and  $\widehat{\rho}$  are all solutions of Neumann problems, and it is clear that we only need their Dirichlet data to evaluate  $\partial\Phi/\partial\mathbf{n}$ . The integral equations [36] (see also Section 4.5) that we employ provide such Neumann-to-Dirichlet maps directly.

#### 4.4. Numerical Illustrations

We illustrate the performance of our scheme to compute the target integrals (4.3) by reducing them to boundary integrals, as described in Section 4.3 and highlighted by the formulas (4.11) and (4.13), and special cases such as (4.15). Further details on the boundary integral equation techniques used to compute Dirichlet-to-Neumann and Neumann-to-Dirichlet used in our approach will be given in Section 4.5, where some discussion of the underlying quadrature(s) will also be provided. Here we merely state that these quadratures are governed by two parameters  $n$  and  $\sigma$ , where  $n$  dictates the number of quadrature points used on each edge of  $\partial K$ , and  $\sigma$  determines the “strength” of a change-of-variable used to define the quadrature. In the following experiments, we fix  $\sigma = 7$ , and vary  $n$  to illustrate rapid convergence with respect to this parameter. Several of the mesh cells chosen for our illustrations were selected not because they might naturally arise in applications such as those pictured in Figure 4.1, but because they pose computational challenges that are at least as difficult as those expected in practice, e.g. non-convex cells that may have corners giving rise to singularities in the local FEM spaces, and edges that are not circular arcs.

*Example 4.4.1 (Constant Functions).* Consider the case where  $v, w \in H^1(K)$  are harmonic and have a constant boundary trace  $v|_{\partial K} = w|_{\partial K} = 1$ . Clearly,  $v = w = 1$  in  $K$ , and  $\int_K vw \, dx = |K|$ . As a first basic test of our quadrature approach, we compare the computed value of  $\int_K vw \, dx$  to  $|K|$  in Table 4.2 for three different cases: the unit square ( $|K| = 1$ ), the unit circle ( $|K| = \pi$ ), the puzzle piece described in

Table 4.2: Absolute errors in the approximation of  $|K|$  via (4.15) in Example 4.4.1, for which  $\Delta v = \Delta w = 0$  in  $K$  and  $v = w = 1$  on  $\partial K$ .

$n$	unit square	unit circle	puzzle piece	shuriken
4	6.2674e-03	1.1254e-02	1.2107e-03	7.7162e-03
8	1.4776e-05	1.8674e-06	7.5746e-06	4.3152e-05
16	1.0118e-07	2.4451e-09	3.3861e-07	1.6385e-07
32	1.1940e-10	8.9906e-12	5.4846e-11	1.8183e-10
64	6.2350e-13	2.9310e-14	1.3824e-12	1.0436e-14

Example 4.4.4 ( $|K| = 1$ ), and the shuriken found in Example 4.4.5 with amplitude  $a = 0.25$  and area  $|K_a| = 1$ . We treat the circle as having two edges, with the two vertices at opposite ends of a diameter.

In this special case of constant functions, if we were to follow the construction described in Proposition 4.2.2 to obtain a  $\Phi$  such that  $\Delta\Phi = v = 1$  “by hand”, we could take  $\hat{v} = 0$  as the harmonic conjugate of  $v$ , and obtain  $\rho = x_1$  and  $\hat{\rho} = x_2$ , ultimately yielding the familiar  $\Phi = |x|^2/4$ . Using this  $\Phi$ , we see that (4.15) reduces to  $|K| = (1/2) \int_{\partial K} x \cdot \mathbf{n} ds$ , which can also be seen as a special case of (4.9), with  $\alpha = (0, 0)$  and  $z = (0, 0)$ . However, instead of approximating  $(1/2) \int_{\partial K} x \cdot \mathbf{n} ds$  directly, we proceed with the approach described by (4.15), which only “knows” that  $v$  and  $w$  are harmonic and have given Dirichlet data. Table 4.2 records the absolute errors in our quadrature approximations, and exhibits rapid convergence with respect the parameter  $n$  governing the number of quadrature points used on each edge.

*Example 4.4.2 (Unit Square).* Let  $K = (0, 1) \times (0, 1)$  be the unit square. It holds that  $\dim V_m(K) = m(m+7)/2$ . We make a brief comparison with the tensor product polynomials of degree  $\leq m$  in each variable,  $\mathbb{Q}_m = \text{span}\{x^i y^j : 0 \leq i, j \leq m\}$ , before testing our quadratures. Let  $\mathbb{Q}_m(K)$  denote the restriction of  $\mathbb{Q}_m$  to  $K$ . We have  $\dim \mathbb{Q}_m(K) = (m+1)^2 > \dim V_m(K)$  for  $m \geq 3$ . It holds that  $V_1(K) = \mathbb{Q}_1(K)$ . The fact that  $x(1-x)y(1-y) \in \mathbb{Q}_2(K) \setminus V_2(K)$  shows that  $V_2(K) \neq \mathbb{Q}_2(K)$ , although  $\dim V_2(K) = \dim \mathbb{Q}_2(K) = 9$ .

We will approximate several entries of the element mass and stiffness matrices associated with a basis of  $V_2(K)$ . The standard basis for  $V_1(K) = V_1^{\partial K}(K) = \mathbb{Q}_1(K)$  consists of the four “vertex functions”,

$$(v_0, v_1, v_2, v_3) = ((1-x)(1-y), x(1-y), xy, (1-x)y),$$

so called because  $\Delta v_j = 0$  and  $v_j(z_i) = \delta_{ij}$  for  $0 \leq i, j \leq 3$ , where

$$(z_0, z_1, z_2, z_3) = ((0, 0), (1, 0), (1, 1), (0, 1))$$

are the vertices given in counter-clockwise order. We add to this four “edge functions”, satisfying  $\Delta w_j = 0$  in  $K$  and  $w_j = v_j v_{j+1}$  on  $\partial K$ . Here, and elsewhere in this example, all subscripts should be understood modulo 4, e.g.  $v_4 = v_0$ ,  $v_5 = v_1$ ,  $v_6 = v_2$ . The vertex and edge functions together form a hierarchical basis for  $V_2^{\partial K}(K)$ . We complete a basis for  $V_2(K)$  by including the function satisfying  $\Delta \tilde{w} = -1$  in  $K$  and  $\tilde{w} = 0$  on  $\partial K$ . Using separation of variables, we can obtain series expansions of  $w_j$  and  $\tilde{w}$ . For example,

$$w_1 = \sum_{k \in 2\mathbb{N}-1}^{\infty} \frac{8 \sinh(k\pi x) \sin(k\pi y)}{(k\pi)^3 \sinh(k\pi)} \quad , \quad \tilde{w} = \sum_{k, \ell \in 2\mathbb{N}-1}^{\infty} \frac{16 \sin(k\pi x) \sin(\ell\pi y)}{k\ell(k^2 + \ell^2)\pi^4} .$$

Using these formulas, we obtain reference values for the desired integrals that are either exact, or obtained to very high precision from series expansions. For the approximated reference values, i.e. those that are given in decimal form, all digits are correct up to rounding in the final digit—MATHEMATICA was used to compute them, employing very high precision arithmetic. These reference values are used to test our quadrature on several combinations of the basis functions. Table 4.3 provides convergence data for these tests, as well as the reference values used to compute the errors. As in the previous example, we observe rapid convergence and small errors.

Table 4.3: Absolute errors for computing the  $L^2$  inner product  $\int_K vw \, dx$  and the  $H^1$  semi-inner product  $\int_K \nabla v \cdot \nabla w \, dx$  on the unit square, as described in Example 4.4.2. Following the notation in that example,  $v_j$  denotes the “vertex” functions,  $w_j$  denotes the “edge” functions, and  $\tilde{w}$  denotes the “bubble” function.

Functions	$n$	$L^2$ error	$H^1$ error	Reference Values
$v_j, v_j$	4	1.8197e-03	6.9331e-03	$L^2$ : 1/9
	8	5.0843e-06	3.6484e-05	$H^1$ : 2/3
	16	3.3700e-08	1.1758e-07	
	32	4.4464e-11	1.1843e-10	
	64	2.4278e-13	6.5759e-13	
$v_j, v_{j\pm 1}$	4	8.3471e-04	8.0181e-05	$L^2$ : 1/18
	8	6.3177e-07	7.4406e-06	$H^1$ : -1/6
	16	2.6840e-09	1.8098e-08	
	32	4.7440e-12	4.0427e-12	
	64	5.2902e-14	8.5895e-13	
$v_j, v_{j+2}$	4	2.7437e-04	7.5354e-03	$L^2$ : 1/36
	8	4.6195e-06	2.1527e-05	$H^1$ : -1/3
	16	2.1823e-08	8.1290e-08	
	32	2.3449e-11	1.1009e-10	
	64	1.0834e-13	4.6124e-13	
$v_0, w_1$	4	1.4790e-06	9.6344e-04	$L^2$ : 6.069682826514464e-03
	8	1.2707e-06	6.1960e-06	$H^1$ : -1/12
	16	6.8236e-09	3.1021e-08	
	32	6.8066e-12	4.5776e-11	
	64	2.3823e-14	4.1675e-14	
$v_1, w_1$	4	5.1158e-04	1.5100e-03	$L^2$ : 1.802485697075799e-02
	8	6.5354e-06	6.2160e-06	$H^1$ : 1/12
	16	9.6573e-09	3.1038e-08	
	32	1.1113e-11	4.5842e-11	
	64	8.9987e-14	6.6937e-13	
$w_j, w_j$	4	1.6966e-04	2.0778e-03	$L^2$ : 5.195037581961447e-03
	8	2.7239e-06	3.6914e-05	$H^1$ : 1.054327612163653e-01
	16	7.7508e-09	9.0495e-08	
	32	8.6327e-12	9.7762e-11	
	64	4.6582e-14	5.0088e-13	
$\tilde{w}, \tilde{w}$	4	6.6230e-06	1.1888e-03	$L^2$ : 1.702510524718458e-03
	8	1.8788e-07	5.8248e-06	$H^1$ : 3.514425373878843e-02
	16	1.8161e-09	3.1897e-08	
	32	2.3060e-12	3.1770e-11	
	64	1.1535e-14	1.5150e-13	
$v_j, \tilde{w}$	4	1.7543e-05	0	$L^2$ : 8.786063434697107e-3
	8	2.3409e-07	0	$H^1$ : 0
	16	2.5401e-09	0	
	32	3.3059e-12	0	
	64	1.4806e-14	0	
$w_j, \tilde{w}$	4	2.3668e-05	0	$L^2$ : 1.769711697503764e-03
	8	1.2301e-07	0	$H^1$ : 0
	16	7.4787e-11	0	
	32	4.3801e-14	0	
	64	1.9227e-15	0	

We now consider integrals involving  $v_\alpha \in V_m^K(K)$  satisfying

$$-\Delta v_\alpha = x^\alpha \text{ in } K \quad , \quad v_\alpha = 0 \text{ on } \partial K \quad ,$$

with  $|\alpha| \leq m$ . The integrals in (4.3) have the exact values

$$\int_K v_\alpha v_\beta dx = 4 \sum_{k=1}^{\infty} \sum_{\ell=1}^{\infty} \frac{S_{\alpha_1,k} S_{\alpha_2,\ell} S_{\beta_1,k} S_{\beta_2,\ell}}{\pi^4 (k^2 + \ell^2)^2} \quad , \quad (4.16a)$$

$$\int_K \nabla v_\alpha \cdot \nabla w_\alpha dx = 4 \sum_{k=1}^{\infty} \sum_{\ell=1}^{\infty} \frac{S_{\alpha_1,k} S_{\alpha_2,\ell} S_{\beta_1,k} S_{\beta_2,\ell}}{\pi^2 (k^2 + \ell^2)} \quad , \quad (4.16b)$$

where, for integers  $a \geq 0$  and  $\ell \geq 1$  we have, following from [23, Identity (3.761.5)], that

$$\begin{aligned} S_{a,\ell} &= \int_0^1 t^a \sin(\ell\pi t) dt \\ &= (-1)^{\ell+1} \sum_{j=0}^{\lfloor a/2 \rfloor} \frac{(-1)^j}{(\ell\pi)^{2j+1}} \frac{a!}{(a-2j)!} - (-1)^{\lfloor a/2 \rfloor} \frac{a!(a-2\lfloor a/2 \rfloor-1)}{(\ell\pi)^{a+1}} . \end{aligned} \quad (4.17)$$

As before, we obtain reference values that are exact in all digits shown, up to rounding in the final digit. Table 4.4 reports the absolute errors of both the  $L^2$  inner product as computed with (4.13), and the  $H^1$  semi-inner product as computed with (4.10) and (4.11). Again, we observe rapid convergence and small errors.

*Example 4.4.3 (Pac-Man).* For any constant  $\mu > 0$ , it holds that the function  $v = r^\mu \sin(\mu\theta)$  is harmonic in  $\mathbb{R}^2$ , except perhaps at the origin. We consider the case where  $1/2 < \mu < 1$ , so that  $v$  has an unbounded gradient at the origin, and take  $K$  to be the sector of the unit circle given in terms of polar coordinates by

$$K = \{(r, \theta) : 0 < r < 1, 0 < \theta < \pi/\mu\} .$$

The boundary  $\partial K$  is partitioned into three edges, one of which is a circular arc.

Table 4.4: Absolute errors for computing the  $L^2$  inner product  $\int_K v_\alpha v_\beta dx$  and the  $H^1$  semi-inner product  $\int_K \nabla v_\alpha \cdot \nabla v_\beta dx$  on the unit square, as described in Example 4.4.2.

$\alpha$	$\beta$	$n$	$L^2$ error	$H^1$ error	Reference Values
(0,0)	(0,0)	4	6.6230e-06	1.1888e-03	$L^2$ : 1.702510524718458e-03 $H^1$ : 3.514425373878843e-02
		8	1.8788e-07	5.8248e-06	
		16	1.8161e-09	3.1897e-08	
		32	2.3060e-12	3.1770e-11	
		64	1.1535e-14	1.5127e-13	
(1,0)	(0,0)	4	3.1495e-05	5.1747e-04	$L^2$ : 8.512552623592291e-04 $H^1$ : 1.757212686939421e-02
		8	1.3546e-07	3.0402e-06	
		16	1.2401e-09	1.6264e-08	
		32	1.5662e-12	1.6000e-11	
		64	6.4370e-15	1.6175e-14	
(1,1)	(1,0)	4	2.8944e-05	2.4156e-05	$L^2$ : 2.216128146808729e-04 $H^1$ : 4.876460403509895e-03
		8	1.5553e-07	1.0527e-06	
		16	1.2923e-09	4.2780e-09	
		32	1.6541e-12	2.9498e-12	
		64	3.6738e-15	7.3119e-14	
(2,1)	(0,2)	4	1.0205e-05	3.6082e-05	$L^2$ : 8.101386165180633e-05 $H^1$ : 1.905102279276017e-03
		8	7.0511e-08	1.6661e-07	
		16	6.1937e-10	8.0122e-10	
		32	7.9987e-13	2.4343e-12	
		64	7.3959e-15	7.0453e-14	
(4,1)	(3,2)	4	1.7520e-06	1.5966e-05	$L^2$ : 9.507439861840766e-06 $H^1$ : 3.269201405690909e-04
		8	2.6874e-08	2.4853e-07	
		16	1.8436e-10	1.1472e-09	
		32	2.1303e-13	8.4067e-13	
		64	4.7769e-16	9.2503e-15	
(5,1)	(3,3)	4	9.5548e-07	1.2468e-05	$L^2$ : 4.942357655448965e-06 $H^1$ : 1.881216015506745e-04
		8	1.4447e-08	1.1744e-07	
		16	1.0333e-10	4.0048e-10	
		32	1.2090e-13	1.0942e-13	
		64	4.3990e-16	3.8299e-17	
(4,2)	(4,2)	4	1.2419e-06	1.4192e-05	$L^2$ : 4.456767076898193e-06 $H^1$ : 1.792263895426231e-04
		8	1.8471e-08	2.1324e-07	
		16	1.2935e-10	1.0114e-09	
		32	1.4892e-13	7.2965e-13	
		64	3.0037e-16	1.1613e-14	

Let  $1/2 < \nu \leq \mu$ , and consider the three functions

$$v_1 = r^\mu \sin(\mu\theta) \quad , \quad v_2 = r^\nu \sin(\nu\theta) \quad , \quad v_3 = (1 - r^2)r^2 \sin(\theta) \sin(\theta - \pi/\mu) .$$

Although  $v_1$  and  $v_2$  are not in  $V_m(K)$  for any  $m$ , our methods for reducing integral involving them to boundary integral still apply, e.g. (4.15) still holds, and we use them below. Indeed, the construction of  $\Phi$  in Proposition 4.2.2 does not rely on the given Dirichlet data for  $v, w$  being in  $\mathbb{P}_p^*(\partial K)$ . One sees that  $v_3 \in V_4^{\partial K}(K)$ , as  $v = 0$  on  $\partial K$ , and

$$\begin{aligned} v_3 &= (1 - x^2 - y^2)(\cos(\pi/\mu) y - \sin(\pi/\mu) x)y , \\ \Delta v_3 &= 2 \cos(\pi/\mu) - 2 \cos(\pi/\mu) x^2 - 14 \cos(\pi/\mu) y^2 + 12 \sin(\pi/\mu) xy . \end{aligned}$$

We can compute the integrals (4.3) for these functions analytically,

$$\begin{aligned} \int_K v_1 v_2 \, dx &= \begin{cases} \frac{\pi}{4\mu(\mu+1)} , & \text{if } \nu = \mu , \\ \frac{\mu \sin(\nu\pi/\mu)}{(\mu + \nu + 2)(\mu^2 - \nu^2)} , & \text{if } \nu < \mu , \end{cases} \\ \int_K \nabla v_1 \cdot \nabla v_2 \, dx &= \begin{cases} \pi/2 , & \text{if } \nu = \mu , \\ \frac{\mu\nu \sin(\nu\pi/\mu)}{\mu^2 - \nu^2} , & \text{if } \nu < \mu , \end{cases} \\ \int_K v_2 v_3 \, dx &= \frac{2\nu \sin(\pi/\mu) \sin(\nu\pi/\mu) - 4 \cos(\pi/\mu) (1 - \cos(\nu\pi/\mu))}{\nu(\nu+4)(\nu+6)(\nu^2-4)} \\ \int_K \nabla v_2 \cdot \nabla v_3 \, dx &= 0 . \end{aligned}$$

In our experiments, we take  $\mu = 4/7$  and  $\nu = 2/7$ . The absolute errors and (exact) reference values are reported in Table 4.5. Although we again observe good convergence of the quadrature, it is not as rapid as what was observed in earlier examples, and the errors do not get near machine precision. This is due the strong singularities

Table 4.5: Absolute errors for the Pac-Man domain considered in Example 4.4.3, using  $v_1 = r^\mu \sin \mu\theta$  and  $v_2 = r^\nu \sin \nu\theta$  and  $v_3 = (1 - r^2)r^2 \sin(\theta) \sin(\theta - \pi/\mu)$ , with  $\mu = 4/7$  and  $\nu = 2/7$ .

Functions	$n$	$L^2$ error	$H^1$ error	Reference Values
$v_1, v_1$	4	9.4414e-02	2.1575e-01	$L^2$ : $49\pi/176$
	8	6.8100e-03	2.1041e-02	$H^1$ : $\pi/2$
	16	3.0614e-04	9.5614e-04	
	32	4.5945e-06	1.4420e-05	
	64	2.2640e-08	7.1147e-08	
$v_1, v_2$	4	8.9563e-02	2.5750e-01	$L^2$ : $49/60$
	8	8.5462e-03	3.7106e-02	$H^1$ : $2/3$
	16	6.2863e-04	3.5209e-03	
	32	1.6028e-05	1.0129e-04	
	64	1.6654e-07	5.6503e-07	
$v_1, v_3$	4	9.0079e-02	0	$L^2$ : $16807\sqrt{2}/264960$
	8	4.3964e-04	0	$H^1$ : 0
	16	1.7055e-05	0	
	32	2.5349e-07	0	
	64	1.2475e-09	0	
$v_2, w_3$	4	7.7313e-02	0	$L^2$ : $2401\sqrt{2}/31680$
	8	6.0152e-04	0	$H^1$ : 0
	16	5.1225e-05	0	
	32	1.4916e-06	0	
	64	1.6999e-08	0	

of the integrands  $v_1$  and  $v_2$  near the origin. In practice, the asymptotic behavior of functions in  $V_m(K)$  is known a priori, with the singular behavior near corners of  $K$  determined only by the angles at these corners (cf. [24, 25, 50]). Although we expect that the level of accuracy achieved by our current approach for such integrals is already sufficient for most practical computations, it should be possible to further improve the accuracy by exploiting the knowledge of the asymptotics near the corners. Singularity subtracting techniques (cf. [17, 51]) have been successfully used to this end in related contexts, and we may consider such modifications in future work.

*Example 4.4.4* (Puzzle Piece). In previous examples, we have examined the convergence rates of our method on relatively simple domains where the values of the integrals in (4.3) are known exactly, or highly accurate reference values can be computed using series expansions. We now consider a domain  $K$ , the puzzle piece depicted in Figure 4.2, for which such reference values are not available. The boundary  $\partial K$  is

partitioned into 12 edges, 4 of which are circular arcs. The cell  $K$  can be described in terms of two parameters, the radius  $r$  of the circular sectors, and the perpendicular distance  $b < r$  from the centers of these circles to the line containing the two adjacent straight edges. In our case,  $r = 0.22$  and  $b = 0.17$ . The length each of the straight edges is  $1/2 - \sqrt{r^2 - b^2} \approx 0.3604$ . In keeping with common terminology for jigsaw puzzles, we will refer to the circular protrusions as “tabs” and the circular indentions as “blanks”. The interior angle at four vertices where the tabs meet the straight edges is  $3\pi/2 + \arcsin(b/r) \approx \pi/0.5614$ , and the interior angle at the four vertices where the blanks meet the straight edges is  $\pi/2 - \arcsin(b/r) \approx \pi/4.5685$ . If the tabs are cut off and used to fill the blanks, the resulting shape is a unit square, which we used to assert that  $|K| = 1$  in Example 4.4.1.

In [2], we provide a detailed discussion of how to construct a spanning set, and then a basis, for  $\mathbb{P}_m^*(\partial K)$  when  $K$  has curved edges. Here, we will provide just enough detail to make sense of the corresponding numerical experiments. We begin by labeling the vertices  $z_0, \dots, z_{11}$ , starting at the lower left corner and proceeding counter-clockwise, as seen in Figure 4.2. As in Example 4.4.2, we let  $v_j$  denote a vertex function, i.e. the harmonic function satisfying  $v_j(z_i) = \delta_{ij}$  for each of the 12 vertices  $z_i$ , such that, along each edge, the trace of  $v_j$  is the trace of a linear function. On straight edges, this corresponds to our natural understanding of linear functions of a single variable such as arclength, but we must clarify what we use for linear functions on curved edges. Using the curved edge  $e$  (a circular arc) having  $z_4$  and  $z_5$  as its endpoints, we introduce a fictitious equilateral triangle that includes a fictitious point  $z$ , as seen in Figure 4.2. The three (linear) barycentric coordinates of this triangle are defined in all of  $\mathbb{R}^2$ , and we take their traces on  $e$  to define  $\mathbb{P}_1(e)$ . The traces on  $e$  of the barycentric coordinates associated with  $z_4$  and  $z_5$  provide part of the Dirichlet data for  $v_4$  and  $v_5$ . Analogous constructions are used for the other three

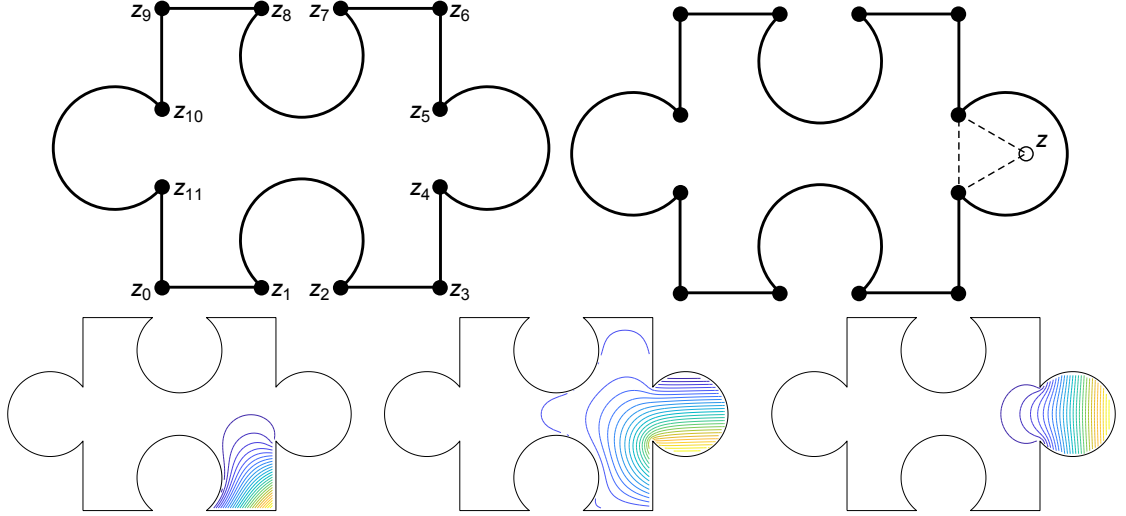


Figure 4.2: Top Left: The puzzle piece mesh cell considered in Example 4.4.4 (and Example 4.4.1). Top Right: The fictitious point  $z$  and equilateral triangle used to define  $\mathbb{P}_1(e)$  for the circular arc of the right tab; this construction was used to provide boundary values in the for the vertex functions  $v_4$  and  $v_5$ , and the edge function  $u_1$ . Bottom Panel: Contour plots of  $v_3, v_4, u_1 \in V_1^{\partial K}(K) = V_1(K)$ , left to right.

curved edges. This discussion also makes it clear that, in addition to the 12 vertex functions in  $V_1(K)$ , there are four “edge functions” in  $V_1(K)$ , associated with the four curved edges of  $\partial K$ , which are harmonic and vanish at every vertex, and whose trace on a curved edge is the trace of a linear function on that edge, as described above. We label these edge functions  $u_0, u_1, u_2, u_3$ , where the Dirichlet trace of  $u_0$  is supported on the curved edge of the bottom blank, that of  $u_1$  is supported on the curved edge of the right tab, that of  $u_2$  is supported on the curved edge of the top blank, and that of  $u_3$  is supported on the curved edge of the left tab. Although we will not need to evaluate any of these functions in (the interior of)  $K$  for our integral computations, we provide contour plots of three functions from  $V_1(K)$  to further clarify our constructions. We note that  $\dim V_1(K) = \dim \mathbb{P}_1^*(\partial K) = 16$ . For all curved edges, we choose the equilateral triangle so that the fictitious point is directed away from the center of  $K$ . This has the effect that non-zero Dirichlet values of  $u_1$  and  $u_3$  (associated with the tabs) are positive, and the non-zero Dirichlet values of

$u_0$  and  $u_2$  (associated with the blanks) are negative; so  $u_1, u_3 > 0$  and  $u_0, u_2 < 0$  in the interior of  $K$ .

On a straight edge  $e$ ,  $\dim \mathbb{P}_2(e) = 3$ , but on a circular edge  $e$ ,  $\dim \mathbb{P}_2(e) = 5$  (cf. [2, Proposition 2.1]). From this, it follows that  $\dim \mathbb{P}_2^*(\partial K) = 32$ . We can augment our basis of  $\mathbb{P}_1^*(\partial K)$  with 16 additional functions, whose traces on an edge  $e$  are traces of quadratic functions  $e$ , to obtain a basis of  $\mathbb{P}_2^*(\partial K)$ . These, in turn yield functions in  $V_2^{\partial K}(K)$  by harmonic extension, as before. We will only consider the following 12, which are sufficient for our quadrature illustrations:  $w_j \in V_2^{\partial K}(K)$  is the harmonic function satisfying  $w_j = v_j v_{j+1}$  on  $\partial K$ . As before, we take the ‘‘bubble function’’  $\tilde{w}$ , defined by  $\Delta \tilde{w} = -1$  in  $K$  and  $\tilde{w} = 0$  on  $\partial K$ .

In Table 4.6, we use our quadrature method to compute the integrals in (4.3) for several representative choices of  $v, w$  taken from the hierarchical basis of  $V_2(K)$  we have constructed above. Apart from the known value  $\int_K \nabla v \cdot \nabla w \, dx = 0$  for  $v \in V_2^{\partial K}(K)$  and  $w \in V_2^K(K)$ , exact values are not available, so we report the computed values to enough digits to observe convergence patterns. Comparing the values computed for  $n = 32$  and  $n = 64$ , we observe that the  $L^2$  inner products typically differ on the order  $10^{-8}$ , while the  $H^1$  semi-inner products typically differ by about  $10^{-6}$ . These observations are consistent with the absolute errors observed in Example 4.4.3, which similarly featured a domain with non-convex corners, giving rise to singular functions having unbounded gradients near such corners.

*Example 4.4.5 (Shuriken).* Consider the family of domains  $K_a$  with vertices lying on the unit square and with sinusoidal edges, as depicted in Figure 4.3, where the parameter  $a$  is taken to be the amplitude of each sinusoidal edge, e.g. its bottom edge can be parameterized by  $(t, a \sin(2\pi t))$  for  $t \in [0, 1]$ . We refer to  $K_a$  as a *shuriken*. We allow  $a \in [0, \bar{a})$ , where  $\bar{a} \approx 0.571991765$  satisfies  $-\bar{a} \sin(2\pi \bar{a}) = 1/4$ ; for  $a \geq \bar{a}$ , adjacent edges intersect at more than just the four vertices. The area

Table 4.6: Computed values of the  $L^2$  inner product  $\int_K vw \, dx$  and the  $H^1$  semi-inner product  $\int_K \nabla v \cdot \nabla w \, dx$  on the Puzzle Piece, as described in Example 4.4.4. Following the notation in that example,  $v_j$  denotes the linear vertex functions,  $u_j$  denotes the linear edge functions,  $w_j$  denotes the quadratic edge functions, and  $\tilde{w}$  denotes the bubble function.

$v$	$w$	$n$	$L^2$ computed	$H^1$ computed
$v_0$	$v_0$	4	0.013672210	0.726172648
		8	0.013916273	0.724767603
		16	0.013904164	0.725599803
		32	0.013904332	0.725576824
		64	0.013904335	0.725576695
$v_0$	$v_1$	4	0.010581850	-0.548518347
		8	0.009164142	-0.566262962
		16	0.009175002	-0.566136764
		32	0.009176187	-0.566201634
		64	0.009176188	-0.566201663
$v_0$	$w_0$	4	0.001817946	0.128954443
		8	0.002018093	0.124305855
		16	0.002010730	0.124548106
		32	0.002010408	0.124569497
		64	0.002010409	0.124569472
$v_1$	$u_0$	4	-0.008308089	-0.859205540
		8	-0.010886266	-1.102119080
		16	-0.010704997	-1.095933800
		32	-0.010705189	-1.095906920
		64	-0.010705190	-1.095906910
$u_0$	$u_0$	4	0.100392937	6.098079590
		8	0.127777179	7.384660560
		16	0.127439875	7.373140910
		32	0.127460415	7.373071500
		64	0.127460423	7.373070960
$u_0$	$u_4$	4	-0.005397524	0.130869343
		8	-0.003929706	0.096148951
		16	-0.003911636	0.094766919
		32	-0.003922668	0.095028432
		64	-0.003922684	0.095028843
$\tilde{w}$	$\tilde{w}$	4	0.000198651	0.011930104
		8	0.000136096	0.009876452
		16	0.000136275	0.009851928
		32	0.000136416	0.009856312
		64	0.000136416	0.009856322
$v_0$	$\tilde{w}$	4	0.000406902	0.000000000
		8	0.000235312	0.000000000
		16	0.000235317	0.000000000
		32	0.000235507	0.000000000
		64	0.000235507	0.000000000
$u_3$	$\tilde{w}$	4	-0.000549240	0.000000000
		8	-0.001071444	0.000000000
		16	-0.001066394	0.000000000
		32	-0.001067543	0.000000000
		64	-0.001067545	0.000000000

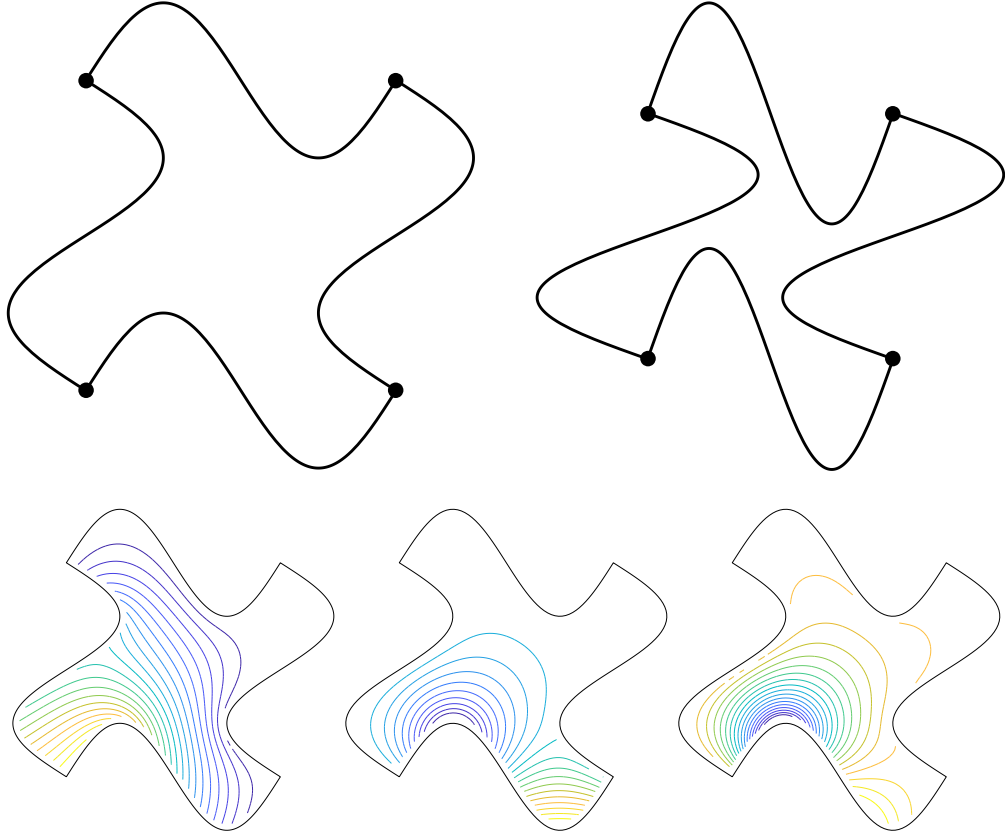


Figure 4.3: Top: Two examples of a shuriken  $K_a$ , as considered in Example 4.4.5. On the left,  $a = 0.25$ , and on the right,  $a = 0.45$ . Bottom: Contour plots of  $v_0$ ,  $u_0$ , and  $w_0$ , left to right, for  $a = 0.25$ .

of  $K_a$  is 1, and the length of each edge,  $\int_0^1 \sqrt{1 + (a \sin(2\pi t))^2} dt$ , increases with  $a$ . For the two cases considered in the experiments,  $a = 0.25$  and  $a = 0.45$ , the edge lengths are 1.4636955 and 2.1265300, respectively. It holds that  $\dim \mathbb{P}_2(e) = 6$  for each edge, so  $\dim \mathbb{P}_2^*(\partial K_a) = 24 - 4 = 20$ , and  $\dim V_2(K_a) = 21$ , with the final basis function being the bubble function  $\tilde{w}$  satisfying  $\Delta \tilde{w} = -1$  in  $K_a$ , and  $\tilde{w} = 0$  on  $\partial K_a$ . Starting with the lower left vertex, and enumerating counter-clockwise, we define  $v_0, v_1, v_2, v_3, u_0, u_1, u_2, u_3 \in V_1(K_a)$  as we did in Example 4.4.4. For the edge  $e$  having vertices  $z_j, z_{j+1}$ , there are three harmonic functions whose trace is quadratic on that edge and vanishes on  $\partial K_e \setminus e$ , but we only consider the one whose trace is  $v_j v_{j+1}$ , and label it  $w_j$ , as in Example 4.4.4.

In Table 4.7, we give the computed values of the integrals from (4.3) for two different shurikens, one with  $a = 0.25$  and another with  $a = 0.45$ . The functions  $v_j, w_j$  considered are taken from a hierarchical basis of  $V_2(K_a)$ , constructed just as in Example 4.4.4 for the Puzzle Piece. As before, we take the “bubble function”  $\tilde{w}$ , defined by  $\Delta\tilde{w} = -1$  in  $K$  and  $\tilde{w} = 0$  on  $\partial K$ . In Table 4.7, we do not exhaustively consider all combinations of products of basis functions, but instead choose a small representative subset. As with the Puzzle Piece, exact values for these integrals are not available, and so we provide enough digits of the computed values to observe convergence as the discretization parameter  $n$  increases. Comparing corresponding values at  $n = 64$  and  $n = 128$ , we see differences on the order of  $10^{-10}$  or better.

#### 4.5. Additional Details

In [36] we discuss, in detail, integral equation techniques to compute interior function values and derivatives, as well as the normal derivative, of harmonic functions with prescribed Dirichlet data. That paper also involves a detailed discussion of the so-called *Kress quadrature* that underlies much of the practical computations. Readers interested in that level of detail for these aspects of our present work are referred to that paper. Here, we merely outline key components to make this paper a bit more self-contained, and to explain the parameters  $n$  and  $\sigma$  used for the experiments in the Section 4.4.

A fundamental step in the techniques in [36] is the computation of a harmonic conjugate  $\hat{\phi}$  of a harmonic function  $\phi$  that is given implicitly by its Dirichlet data. The associated boundary value problem for  $\hat{\phi}$  is given in (4.8), and we emphasize its general form as a Neumann problem,

$$\Delta\hat{\phi} = 0 \text{ in } K \quad , \quad \frac{\partial\hat{\phi}}{\partial\mathbf{n}} = g \text{ on } \partial K \quad , \quad \int_{\partial K} \hat{\phi} ds = 0 \text{ .}$$

Table 4.7: Computed values of the  $L^2$  inner product  $\int_{K_a} vw \, dx$  and the  $H^1$  semi-inner product  $\int_{K_a} \nabla v \cdot \nabla w \, dx$  on two shuriken domains  $K_a$ , with  $a = 0.25$  and  $a = 0.45$ , as described in Example 4.4.5. As before,  $v_j$  denotes the linear vertex functions,  $u_j$  denotes the linear edge functions,  $w_j$  denotes the quadratic edge functions, and  $\tilde{w}$  denotes the bubble function.

$v$	$w$	$n$	$a = 0.25$		$a = 0.45$	
			$L^2$ computed	$H^1$ computed	$L^2$ computed	$H^1$ computed
$v_0$	$v_0$	8	0.122304484163	0.841197799625	0.171514539918	1.308227010771
		16	0.122284190374	0.841078224722	0.161649534123	1.285059888167
		32	0.122284167519	0.841078466578	0.161922544577	1.286968732102
		64	0.122284167335	0.841078466566	0.161922957483	1.286979554024
		128	0.122284167419	0.841078466698	0.161922957393	1.286979553929
$v_0$	$v_1$	8	0.044283489076	-0.188653733959	0.047081128807	-0.343127089202
		16	0.044283073196	-0.188546546255	0.047528869820	-0.324551380508
		32	0.044283007631	-0.188546629658	0.047453317056	-0.325394319115
		64	0.044283007451	-0.188546629678	0.047453075460	-0.325398144120
		128	0.044283007503	-0.188546629692	0.047453075355	-0.325398144019
$v_0$	$w_0$	8	0.087784366879	0.630102664349	0.135440998814	0.938133669372
		16	0.087785668489	0.630028986909	0.130038589885	0.926503662905
		32	0.087785657013	0.630029188476	0.130161374947	0.927407778671
		64	0.087785656854	0.630029188939	0.130161581076	0.927412815331
		128	0.087785656937	0.630029188799	0.130161580999	0.927412815472
$v_0$	$u_0$	8	0.009785147673	0.053403931094	0.015361998312	0.383596248396
		16	0.009797201099	0.053211804477	0.005563815566	0.321585504431
		32	0.009797258872	0.053211534064	0.005916108221	0.324871331510
		64	0.009797259015	0.053211533136	0.005916668964	0.324881204132
		128	0.009797258971	0.053211533453	0.005916669042	0.324881203630
$u_0$	$u_0$	8	0.004924824465	0.237480769718	0.021581633027	1.068284775604
		16	0.004932160428	0.237537650969	0.016630917230	1.026194691236
		32	0.004932173646	0.237537978641	0.016792540883	1.030136230562
		64	0.004932173705	0.237537979523	0.016792789460	1.030151873248
		128	0.004932173682	0.237537979226	0.016792789553	1.030151874144
$u_0$	$u_1$	8	0.000391360264	0.004984144499	-0.005503227525	-0.208598982465
		16	0.000392934007	0.004903204887	0.000982612276	-0.175841837434
		32	0.000392944534	0.004903322299	0.000788482846	-0.177472671981
		64	0.000392944547	0.004903322309	0.000788355410	-0.177474288985
		128	0.000392944547	0.004903322390	0.000788355417	-0.177474289201
$\tilde{w}$	$\tilde{w}$	8	0.000311621308	0.014364388949	-0.000283922410	0.007187496015
		16	0.000310412785	0.014331224233	0.000049393200	0.006055750660
		32	0.000310411357	0.014331099026	0.000049940608	0.006042215936
		64	0.000310411363	0.014331098676	0.000049939425	0.006042112045
		128	0.000310411359	0.014331098783	0.000049939433	0.006042111934
$v_0$	$\tilde{w}$	8	-0.003112915668	0.000000000000	-0.001626479966	0.000000000000
		16	-0.003108997951	0.000000000000	-0.001481515566	0.000000000000
		32	-0.003108991855	0.000000000000	-0.001484033797	0.000000000000
		64	-0.003108991818	0.000000000000	-0.001484035073	0.000000000000
		128	-0.003108991834	0.000000000000	-0.001484035053	0.000000000000
$u_0$	$\tilde{w}$	8	-0.000474699095	0.000000000000	-0.000037051472	0.000000000000
		16	-0.000473785530	0.000000000000	-0.000024127806	0.000000000000
		32	-0.000473782849	0.000000000000	-0.000026480483	0.000000000000
		64	-0.000473782842	0.000000000000	-0.000026493032	0.000000000000
		128	-0.000473782845	0.000000000000	-0.000026493015	0.000000000000

as such problems also arise in the construction described in Proposition 4.2.2. Here, the Neumann data  $g$  is specified by the user. We provide the associated integral equation employed in our work, whose solution yields a Neumann-to-Dirichlet map  $g \rightarrow \widehat{\phi}|_{\partial K}$ . We only present the equation in the case that  $\partial K$  has a single corner  $z$ . The case of multiple corners is dealt with analogously, and further details are provided in [36]. The associated integral equation is

$$\begin{aligned} |\partial K| \widehat{\phi}(z) + \frac{\widehat{\phi}(x) - \widehat{\phi}(z)}{2} + \int_{\partial K} \left( \frac{\partial G(x, y)}{\partial \mathbf{n}(y)} + 1 \right) (\widehat{\phi}(y) - \widehat{\phi}(z)) ds(y) \\ = \int_{\partial K} G(x, y) g(y) ds(y) , \end{aligned} \quad (4.18)$$

where  $G(x, y) = -(2\pi)^{-1} \ln |x - y|$  is the fundamental solution for the Laplacian in 2D. This integral equation is discretized by a Nyström method, which is a quadrature based method in which the integrals from (4.18) in the variable  $y$  are replaced by a quadrature that is suitable for these integrands regardless of the choice of  $x \in \partial\Omega$ , resulting in a “semi-discrete” equation. The semi-discrete equation is then sampled at the quadrature points to obtain a fully discrete (and well-conditioned) square linear system. We solve this system using GMRES. In the case that  $\widehat{\phi}$  is a harmonic conjugate of the harmonic function  $\phi$  having Dirichlet data  $f$ , a Dirichlet-to-Neumann map  $f \mapsto \partial\phi/\partial\mathbf{n}$  is obtained by taking the tangential derivative of  $\widehat{\phi}$ ,  $\partial\phi/\partial\mathbf{n} = \partial\widehat{\phi}/\partial\mathbf{t}$ . In our computations, an FFT is used to efficiently approximate  $\partial\widehat{\phi}/\partial\mathbf{t}$  at quadrature points from the approximation of  $\widehat{\phi}$  at these points that was obtained by solving the Nyström linear system.

The fundamental quadrature used in our discretization is due to Kress [31], and we briefly describe it here to explain the parameters  $n$  and  $\sigma$  used for the experiments. Suppose that a function  $F$  is continuous on  $[a, b]$ . For any suitable change-of-variable  $t = \lambda(\tau)$ ,  $\lambda : [a, b] \rightarrow [a, b]$ , we have  $\int_a^b F(t) dt = \int_a^b F(\lambda(\tau)) \lambda'(\tau) d\tau$ . A clever choice

of  $\lambda$  ensures that the new integrand,  $F(\lambda(\tau))\lambda'(\tau)$ , vanishes at the endpoints  $a$  and  $b$ , together with some of its derivatives. It is well-known that the trapezoid rule converges rapidly for such integrands, with the rate of convergence depending on the order at which  $F(\lambda(\tau))\lambda'(\tau)$  vanishes at these endpoints. *Kress quadrature* is obtained by using the trapezoid rule after the following sigmoidal change-of-variable, which is determined by single integer parameter  $\sigma \geq 2$ ,

$$\lambda(\tau) = (b - a) \frac{[c(\tau)]^\sigma}{[c(\tau)]^\sigma + [1 - c(\tau)]^\sigma} + a \quad , \quad c(\tau) = \left( \frac{1}{2} - \frac{1}{\sigma} \right) \theta^2 + \frac{\theta}{\sigma} + \frac{1}{2} \quad , \quad (4.19)$$

where  $\theta = (2\tau - a - b)/(b - a)$ . A key property of this change-of-variable is that  $\lambda'(\tau)$  has roots of order  $\sigma - 1$  at  $\tau = a$  and  $\tau = b$ . Letting  $h = (b - a)/m$  and  $\tau_k = a + kh$ , for  $0 \leq k \leq m$ , the corresponding quadrature is

$$\int_a^b F(t) dt \approx \sum_{k=0}^{m}{}'' F(t_k) w_k = \sum_{k=1}^{m-1} F(t_k) w_k \quad , \quad (4.20)$$

$$t_k = \lambda(\tau_k) \quad , \quad w_k = h\lambda'(\tau_k) \quad .$$

The double-prime notation in the first sum above indicates that its initial and final terms are halved. Since  $w_0 = w_m = 0$ , these terms can be dropped. Kress provides an analysis of this quadrature based on the Euler-Maclaurin formula in [31], and we provide a complementary analysis based on Fourier series in [36]. Depending on whether both, one or neither of the endpoints are counted, (4.20) involves between  $m - 1$  and  $m + 1$  quadrature points. It is convenient in our applications to consider it as an  $m$ -point quadrature by including only one of the endpoints, so that  $m$  points are “assigned” to each edge of  $\partial K$  via a parameterization of the boundary, and each vertex of  $\partial K$  is counted only once. It is also convenient in our implementation to take  $m = 2n$ . This choice applies both to the quadrature used for the Nyström linear system, which yields our discrete Dirichlet-to-Neumann map, and for the final boundary quadratures that employ this data to compute the target integrals (4.3) as

described in the introductory paragraph of Section 4.4. When the integer parameter  $n$  is used in Section 4.4, this is what it indicates.

We include an extension of Table 4.1 as a ready reference that may be used for higher degree polynomials. This is given in Table 4.8 and covers multiindices  $\alpha$  for which  $7 \leq |\alpha| \leq 10$ . We also make a brief note on computing the products of polynomials in our context. Given  $p, q \in \mathbb{P}_m(\mathbb{R}^2)$ , with

$$p(x) = \sum_{|\alpha| \leq m} c_\alpha (x - z)^\alpha, \quad q(x) = \sum_{|\beta| \leq m} d_\beta (x - z)^\beta,$$

the product  $pq \in \mathbb{P}_{2m}(\mathbb{R}^2)$  may be written as

$$(pq)(x) = \sum_{|\gamma| \leq 2m} \tilde{c}_\gamma (x - z)^\gamma,$$

where the coefficients are given by

$$\tilde{c}_\gamma = \sum_{\alpha + \beta = \gamma} c_\alpha d_\beta.$$

In the case where  $p, q$  are sparse, i.e. the majority of their coefficients are zero, as is the case for our experiments, we execute a double loop over the nonzero coefficients of  $p$  and  $q$ , and for each pair  $(\alpha, \beta)$ , we determine the integer  $n$  corresponding to the multi-index  $\alpha + \beta$ , according to the bijection described in (4.5). We then increment the coefficient  $\tilde{c}_\gamma$ , with  $\gamma$  corresponding to  $n$ , with  $\tilde{c}_\gamma \leftarrow \tilde{c}_\gamma + c_\alpha d_\beta$ .

All of the numerical experiments in this paper were implemented in MATLAB. Those interested in obtaining a copy of our code may do so at the GitHub repository found at

<https://github.com/samreynoldsmath/HigherOrderCurvedElementQuadrature>

Table 4.8: An enumeration of multiindices for  $7 \leq |\alpha| \leq 10$ , together with the indices and values of the non-zero coefficients of  $P_\alpha$  from Proposition 4.2.1.

$k$	$\alpha$	$P_\alpha$ indices	$P_\alpha$ coefficients
28	(7, 0)	(45, 47, 49, 51, 53)	(85, 12, -42, 28, -3)/6144
29	(6, 1)	(46, 48, 50, 52, 54)	(247, 84, -126, 36, -1)/14336
30	(5, 2)	(45, 47, 49, 51, 53)	(-73, 2628, 1554, -1036, 111)/129024
31	(4, 3)	(46, 48, 50, 52, 54)	(-489, 4564, 3906, -1116, 31)/215040
32	(3, 4)	(45, 47, 49, 51, 53)	(31, -1116, 3906, 4564, -489)/215040
33	(2, 5)	(46, 48, 50, 52, 54)	(111, -1036, 1554, 2628, -73)/129024
34	(1, 6)	(45, 47, 49, 51, 53)	(-1, 36, -126, 84, 247)/14336
35	(0, 7)	(46, 48, 50, 52, 54)	(-3, 28, -42, 12, 85)/6144
36	(8, 0)	(55, 57, 59, 61, 63, 65)	(511, 45, -210, 210, -45, 1)/46080
37	(7, 1)	(56, 58, 60, 62, 64)	(251, 60, -126, 60, -5)/18432
38	(6, 2)	(55, 57, 59, 61, 63, 65)	(-233, 10485, 4830, -4830, 1035, -23)/645120
39	(5, 3)	(56, 58, 60, 62, 64)	(-191, 2292, 1638, -780, 65)/129024
40	(4, 4)	(55, 57, 59, 61, 63, 65)	(1, -45, 210, 210, -45, 1)/12600
41	(3, 5)	(56, 58, 60, 62, 64)	(65, -780, 1638, 2292, -191)/129024
42	(2, 6)	(55, 57, 59, 61, 63, 65)	(-23, 1035, -4830, 4830, 10485, -233)/645120
43	(1, 7)	(56, 58, 60, 62, 64)	(-5, 60, -126, 60, 251)/18432
44	(0, 8)	(55, 57, 59, 61, 63, 65)	(1, -45, 210, -210, 45, 511)/46080
45	(9, 0)	(66, 68, 70, 72, 74, 76)	(93, 5, -30, 42, -15, 1)/10240
46	(8, 1)	(67, 69, 71, 73, 75, 77)	(1013, 165, -462, 330, -55, 1)/92160
47	(7, 2)	(66, 68, 70, 72, 74, 76)	(-11, 605, 210, -294, 105, -7)/46080
48	(6, 3)	(67, 69, 71, 73, 75, 77)	(-53, 795, 462, -330, 55, -1)/53760
49	(5, 4)	(66, 68, 70, 72, 74, 76)	(29, -1595, 9570, 8106, -2895, 193)/645120
50	(4, 5)	(67, 69, 71, 73, 75, 77)	(193, -2895, 8106, 9570, -1595, 29)/645120
51	(3, 6)	(66, 68, 70, 72, 74, 76)	(-1, 55, -330, 462, 795, -53)/53760
52	(2, 7)	(67, 69, 71, 73, 75, 77)	(-7, 105, -294, 210, 605, -11)/46080
53	(1, 8)	(66, 68, 70, 72, 74, 76)	(1, -55, 330, -462, 165, 1013)/92160
54	(0, 9)	(67, 69, 71, 73, 75, 77)	(1, -15, 42, -30, 5, 93)/10240
55	(10, 0)	(78, 80, 82, 84, 86, 88, 90)	(2047, 66, -495, 924, -495, 66, -1)/270336
56	(9, 1)	(79, 81, 83, 85, 87, 89)	(509, 55, -198, 198, -55, 3)/56320
57	(8, 2)	(78, 80, 82, 84, 86, 88, 90)	(-1981, 130746, 33165, -61908, 33165, -4422, 67)/12165120
58	(7, 3)	(79, 81, 83, 85, 87, 89)	(-681, 12485, 5742, -5742, 1595, -87)/1013760
59	(6, 4)	(78, 80, 82, 84, 86, 88, 90)	(743, -49038, 367785, 259644, -139095, 18546, -281)/28385280
60	(5, 5)	(79, 81, 83, 85, 87, 89)	(3, -55, 198, 198, -55, 3)/16632
61	(4, 6)	(78, 80, 82, 84, 86, 88, 90)	(-281, 18546, -139095, 259644, 367785, -49038, 743)/28385280
62	(3, 7)	(79, 81, 83, 85, 87, 89)	(-87, 1595, -5742, 5742, 12485, -681)/1013760
63	(2, 8)	(78, 80, 82, 84, 86, 88, 90)	(67, -4422, 33165, -61908, 33165, 130746, -1981)/12165120
64	(1, 9)	(79, 81, 83, 85, 87, 89)	(3, -55, 198, -198, 55, 509)/56320
65	(0, 10)	(78, 80, 82, 84, 86, 88, 90)	(-1, 66, -495, 924, -495, 66, 2047)/270336

#### 4.6. Concluding Remarks

We have described an approach for integrating products of functions and their gradients over curvilinear polygons, when the functions are given implicitly in terms of Poisson problems involving polynomial data. The efficient and accurate evaluation of such integrals is instrumental in the formation of linear systems associated with finite element methods such as Trefftz-FEM and VEM, which employ non-standard meshes. In our approach, integrals on curvilinear polygonal cells are reduced to integrals along their boundaries, using constructions that yield a function whose Laplacian is a given polynomial or harmonic function, together with integration by parts. The data for quadrature approximations of these boundary integrals is obtained using Dirichlet-to-Neumann and Neumann-to-Dirichlet maps that are computed using techniques based on second-kind integral equations. Numerical examples demonstrate rapid convergence and high accuracy of these quadratures.

## 4.7. References

- [1] B. Ahmad, A. Alsaedi, F. Brezzi, L. D. Marini, and A. Russo. Equivalent projectors for virtual element methods. *Comput. Math. Appl.*, 66(3):376–391, 2013.
- [2] A. Anand, J. S. Owall, S. E. Reynolds, and S. Weißer. Trefftz Finite Elements on Curvilinear Polygons. *SIAM J. Sci. Comput.*, 42(2):A1289–A1316, 2020.
- [3] A. Anand, J. S. Owall, and S. Weißer. A Nyström-based finite element method on polygonal elements. *Comput. Math. Appl.*, 75(11):3971–3986, 2018.
- [4] P. F. Antonietti, L. Beirão da Veiga, D. Mora, and M. Verani. A stream virtual element formulation of the Stokes problem on polygonal meshes. *SIAM J. Numer. Anal.*, 52(1):386–404, 2014.
- [5] P. F. Antonietti, S. Berrone, M. Verani, and S. Weißer. The virtual element method on anisotropic polygonal discretizations. In *Numerical mathematics and advanced applications—ENUMATH 2017*, volume 126 of *Lect. Notes Comput. Sci. Eng.*, pages 725–733. Springer, Cham, 2019.
- [6] P. F. Antonietti, M. Bruggi, S. Scacchi, and M. Verani. On the virtual element method for topology optimization on polygonal meshes: a numerical study. *Comput. Math. Appl.*, 74(5):1091–1109, 2017.
- [7] P. F. Antonietti, P. Houston, and G. Pennesi. Fast numerical integration on polytopic meshes with applications to discontinuous Galerkin finite element methods. *J. Sci. Comput.*, 77(3):1339–1370, 2018.
- [8] E. Artioli, A. Sommariva, and M. Vianello. Algebraic cubature on polygonal elements with a circular edge. *Comput. Math. Appl.*, 79(7):2057–2066, 2020.
- [9] L. Beirão da Veiga, F. Brezzi, L. D. Marini, and A. Russo. Polynomial preserving virtual elements with curved edges. *Math. Models Methods Appl. Sci.*, 30(8):1555–1590, 2020.
- [10] L. Beirão da Veiga, A. Russo, and G. Vacca. The virtual element method with curved edges. *ESAIM Math. Model. Numer. Anal.*, 53(2):375–404, 2019.
- [11] L. Beirão da Veiga, F. Brezzi, A. Cangiani, G. Manzini, L. D. Marini, and A. Russo. Basic principles of virtual element methods. *Math. Models Methods Appl. Sci.*, 23(1):199–214, 2013.
- [12] L. Beirão da Veiga, F. Brezzi, L. D. Marini, and A. Russo. The hitchhiker’s guide to the virtual element method. *Math. Models Methods Appl. Sci.*, 24(8):1541–1573, 2014.

- [13] L. Beirão da Veiga, A. Chernov, L. Mascotto, and A. Russo. Basic principles of *hp* virtual elements on quasiuniform meshes. *Math. Models Methods Appl. Sci.*, 26(8):1567–1598, 2016.
- [14] L. Beirão da Veiga and G. Manzini. A virtual element method with arbitrary regularity. *IMA J. Numer. Anal.*, 34(2):759–781, 2014.
- [15] M. F. Benedetto, S. Berrone, A. Borio, S. Pieraccini, and S. Scialò. Order preserving SUPG stabilization for the virtual element formulation of advection-diffusion problems. *Comput. Methods Appl. Mech. Engrg.*, 311:18–40, 2016.
- [16] F. Brezzi and L. D. Marini. Virtual element and discontinuous Galerkin methods. In *Recent developments in discontinuous Galerkin finite element methods for partial differential equations*, volume 157 of *IMA Vol. Math. Appl.*, pages 209–221. Springer, Cham, 2014.
- [17] O. P. Bruno, J. S. Owall, and C. Turc. A high-order integral algorithm for highly singular PDE solutions in Lipschitz domains. *Computing*, 84(3-4):149–181, 2009.
- [18] D. Copeland, U. Langer, and D. Pusch. From the boundary element domain decomposition methods to local Trefftz finite element methods on polyhedral meshes. In *Domain decomposition methods in science and engineering XVIII*, volume 70 of *Lect. Notes Comput. Sci. Eng.*, pages 315–322. Springer, Berlin, 2009.
- [19] G. Da Fies and M. Vianello. Trigonometric Gaussian quadrature on subintervals of the period. *Electron. Trans. Numer. Anal.*, 39:102–112, 2012.
- [20] G. Da Fies, M. Vianello, and A. Sommariva. SUBP: Matlab package for subperiodic trigonometric quadrature and multivariate applications. <https://www.math.unipd.it/~marcov/subp.html>, 2012. Accessed Nov. 17, 2021.
- [21] M. S. Floater. Generalized barycentric coordinates and applications. *Acta Numer.*, 24:161–214, 2015.
- [22] A. L. Gain, C. Talischi, and G. H. Paulino. On the Virtual Element Method for three-dimensional linear elasticity problems on arbitrary polyhedral meshes. *Comput. Methods Appl. Mech. Engrg.*, 282:132–160, 2014.
- [23] I. S. Gradshteyn and I. M. Ryzhik. *Table of integrals, series, and products*. Elsevier/Academic Press, Amsterdam, seventh edition, 2007. Translated from the Russian, Translation edited and with a preface by Alan Jeffrey and Daniel Zwillinger, With one CD-ROM (Windows, Macintosh and UNIX).
- [24] P. Grisvard. *Elliptic problems in nonsmooth domains*, volume 24 of *Monographs and Studies in Mathematics*. Pitman (Advanced Publishing Program), Boston, MA, 1985.

- [25] P. Grisvard. *Singularities in boundary value problems*, volume 22 of *Recherches en Mathématiques Appliquées [Research in Applied Mathematics]*. Masson, Paris, 1992.
- [26] C. Hofreither.  $L_2$  error estimates for a nonstandard finite element method on polyhedral meshes. *J. Numer. Math.*, 19(1):27–39, 2011.
- [27] C. Hofreither, U. Langer, and C. Pechstein. Analysis of a non-standard finite element method based on boundary integral operators. *Electron. Trans. Numer. Anal.*, 37:413–436, 2010.
- [28] C. Hofreither, U. Langer, and S. Weißer. Convection-adapted BEM-based FEM. *ZAMM Z. Angew. Math. Mech.*, 96(12):1467–1481, 2016.
- [29] K. Hormann and N. Sukumar, editors. *Generalized barycentric coordinates in computer graphics and computational mechanics*. CRC Press, Boca Raton, FL, 2018.
- [30] V. V. Karachik and N. A. Antropova. On the solution of a nonhomogeneous polyharmonic equation and the nonhomogeneous Helmholtz equation. *Differ. Uravn.*, 46(3):384–395, 2010.
- [31] R. Kress. A Nyström method for boundary integral equations in domains with corners. *Numer. Math.*, 58(2):145–161, 1990.
- [32] R. Kress. *Linear integral equations*, volume 82 of *Applied Mathematical Sciences*. Springer, New York, third edition, 2014.
- [33] R. Kussmaul. Ein numerisches Verfahren zur Lösung des Neumannschen Aussenraumproblems für die Helmholtzsche Schwingungsgleichung. *Computing (Arch. Elektron. Rechnen)*, 4:246–273, 1969.
- [34] E. Martensen. Über eine Methode zum räumlichen Neumannschen Problem mit einer Anwendung für torusartige Berandungen. *Acta Math.*, 109:75–135, 1963.
- [35] S. Natarajan, S. Bordas, and D. R. Mahapatra. Numerical integration over arbitrary polygonal domains based on Schwarz-Christoffel conformal mapping. *Internat. J. Numer. Methods Engrg.*, 80(1):103–134, 2009.
- [36] J. S. Owall and S. E. Reynolds. A high-order method for evaluating derivatives of harmonic functions in planar domains. *SIAM J. Sci. Comput.*, 40(3):A1915–A1935, 2018.
- [37] S. Rjasanow and S. Weißer. Higher order BEM-based FEM on polygonal meshes. *SIAM J. Numer. Anal.*, 50(5):2357–2378, 2012.

- [38] S. Rjasanow and S. Weißer. FEM with Trefftz trial functions on polyhedral elements. *J. Comput. Appl. Math.*, 263:202–217, 2014.
- [39] D. Seibel and S. Weißer. Recovery-based error estimators for the VEM and BEM-based FEM. *Comput. Math. Appl.*, 80(9):2073–2089, 2020.
- [40] A. Sommariva and M. Vianello. Product Gauss cubature over polygons based on Green’s integration formula. *BIT*, 47(2):441–453, 2007.
- [41] Y. Sudhakar, J. M. de Almeida, and W. A. Wall. An accurate, robust, and easy-to-implement method for integration over arbitrary polyhedra: Application to embedded interface methods. *J. Comput. Phys.*, 273:393 – 415, 2014.
- [42] Y. Sudhakar, A. Sommariva, M. Vianello, and W. A. Wall. On the use of compressed polyhedral quadrature formulas in embedded interface methods. *SIAM J. Sci. Comput.*, 39(3):B571–B587, 2017.
- [43] C. Talischi and G. H. Paulino. Addressing integration error for polygonal finite elements through polynomial projections: a patch test connection. *Math. Models Methods Appl. Sci.*, 24(8):1701–1727, 2014.
- [44] S. Weißer. Residual error estimate for bem-based fem on polygonal meshes. *Numer. Math.*, 118:765–788, 2011. 10.1007/s00211-011-0371-6.
- [45] S. Weißer. Arbitrary order Trefftz-like basis functions on polygonal meshes and realization in BEM-based FEM. *Comput. Math. Appl.*, 67(7):1390–1406, 2014.
- [46] S. Weißer. Residual based error estimate and quasi-interpolation on polygonal meshes for high order BEM-based FEM. *Comput. Math. Appl.*, 73(2):187–202, 2017.
- [47] S. Weißer. Anisotropic polygonal and polyhedral discretizations in finite element analysis. *ESAIM Math. Model. Numer. Anal.*, 53(2):475–501, 2019.
- [48] S. Weißer. *BEM-based Finite Element Approaches on Polytopal Meshes*, volume 130 of *Lecture Notes in Computational Science and Engineering*. Springer International Publishing, 1 edition, 2019.
- [49] S. Weißer and T. Wick. The dual-weighted residual estimator realized on polygonal meshes. *Comput. Methods Appl. Math.*, 18(4):753–776, 2018.
- [50] N. M. Wigley. Asymptotic expansions at a corner of solutions of mixed boundary value problems. *J. Math. Mech.*, 13:549–576, 1964.
- [51] N. M. Wigley. On a method to subtract off a singularity at a corner for the Dirichlet or Neumann problem. *Math. Comp.*, 23:395–401, 1969.

## 5. Evaluation of Inner Products of Implicitly-defined Finite Element Functions on Multiply Connected Planar Mesh Cells

### Full citation information:

Jeffrey S. Ovall and Samuel E. Reynolds. Evaluation of inner products of implicitly defined finite element functions on multiply connected planar mesh cells. *SIAM Journal on Scientific Computing*, 46(1):A338–A359, 2024.

**Authors:** *Jeffrey S. Ovall<sup>1</sup> and Samuel E. Reynolds<sup>1</sup>*

### Author contribution statement:

- Jeffrey S. Ovall: investigation, review and editing
- Samuel E. Reynolds: established theoretical results, developed algorithms, implemented numerical examples, drafted the paper

**DOI:** 10.1137/23M1569332

### Hyperlink to the publication in PDXScholar:

Not yet available.

---

<sup>1</sup>Fariborz Maseeh Department of Mathematics and Statistics, Portland State University, Portland, OR 97201

**Additional information:** This work was partially supported by the National Science Foundation through NSF grant DMS-2012285 and NSF RTG grant DMS-2136228.

## Abstract

In recent years, there has been significant interest in the development of finite element methods defined on meshes that include rather general polytopes and curvilinear polygons. In the present work, we provide tools necessary to employ multiply connected mesh cells in planar domains, i.e. cells with holes, in finite element computations. Our focus is efficient evaluation the  $H^1$  semi-inner product and  $L^2$  inner product of implicitly-defined finite element functions of the types arising in boundary element based finite element methods (BEM-FEM) and virtual element methods (VEM). Such functions are defined as solutions of Poisson problems having polynomial source term and continuous boundary data. We show that the integrals of interest can be reduced to integrals along the boundaries of mesh cells, thereby avoiding the need to perform any computations in cell interiors. The dominating cost of this reduction is solving a relatively small Nyström system to obtain a Dirichlet-to-Neumann map, as well as the solution of two more Nyström systems to obtain an “anti-Laplacian” of a harmonic function, which is used for computing the  $L^2$  inner product. Several numerical examples demonstrate the high-order accuracy of this approach.

### 5.1. Introduction

Let  $K \subset \mathbb{R}^2$  be an open, bounded, and connected planar region with a piecewise  $C^2$  smooth boundary  $\partial K$ . Assume the boundary  $\partial K$  is partitioned into a finite number of *edges*, with each edge being  $C^2$  smooth and connected. Edges are permitted to meet at interior angles strictly between 0 and  $2\pi$ , so that  $\partial K$  has no cusps or slits.

Consider the problem of computing the  $H^1$  semi-inner product and  $L^2$  inner product,

$$\int_K \nabla v \cdot \nabla w \, dx , \tag{5.1}$$

$$\int_K v w \, dx , \tag{5.2}$$

where  $v, w$  are implicitly defined elements of a *local Poisson space*  $V_p(K)$ , which we define as follows. Fix a natural number  $p$ , and let  $V_p(K)$  consist of the functions  $v \in H^1(K)$  such that:

- (a) for  $p = 1$ ,  $v$  is harmonic in  $K$ ;
- (b) for  $p \geq 2$ , the Laplacian  $\Delta v$  is a polynomial of degree at most  $p - 2$  in  $K$ ;
- (c) the trace  $v|_{\partial K}$  is continuous;
- (d) the trace  $v|_e$  along any edge  $e \subset \partial K$  is the trace of a polynomial of degree at most  $p$  (defined over all of  $\mathbb{R}^2$ ).

Note, for instance, that  $V_p(K)$  contains all of the polynomials of degree at most  $p$ . Such subspaces of  $H^1(K)$  arise naturally in the context of finite element methods posed over *curvilinear meshes*, whose mesh cells have curved edges. Our present interest is extending the application of these spaces to curvilinear meshes with *punctured* (i.e. multiply connected) mesh cells; see Figure 5.1.

Such spaces of implicitly-defined functions, whether arising from curvilinear, polygonal, or more conventional tetrahedral meshes, have appeared in the literature frequently in the last several years. Many readers are likely to be familiar with Virtual Element Methods (VEM), which have gained significant popularity in the last decade and have a large body of recent publications [5, 7–9], some of which concern employing curvilinear mesh cells [1, 6, 11, 36]. Our approach is more closely aligned with Boundary Element Based Finite Element Methods (BEM-FEM) and

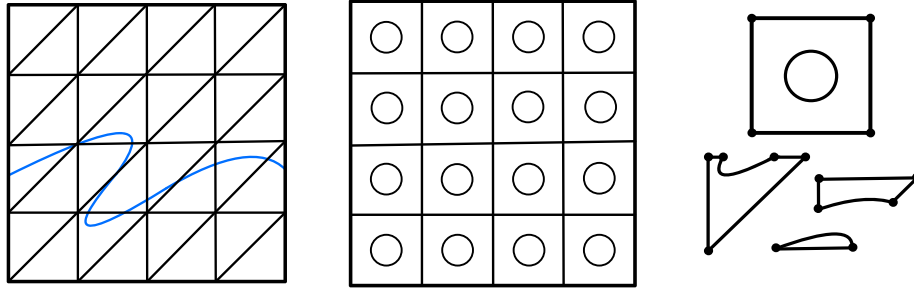


Figure 5.1: Left: A curvilinear mesh of a square domain featuring a curvilinear interface. Center: A curvilinear mesh of a square domain with circular punctures. Right: A few of the cells found in these meshes.

Trefftz methods [10, 15, 17–19, 30–35]. In contrast to VEM, we actually construct a basis of  $V_p(K)$  and do not require projections and so-called stabilization terms. Furthermore, although the computations needed for computing these integrals do not require the evaluation of the implicitly defined functions, or their derivatives, in the interior of a mesh cells, our approach allows us to provide such quantities with very high accuracy. The basic framework for our approach was proposed in [2], where we introduced methods for construction of a basis that automatically preserves  $H^1$  conformity, and proved estimates for associated interpolation operators. Subsequently, in [27], we demonstrated that practical computation of  $H^1$  semi-inner products and  $L^2$  inner products of functions in  $V_p(K)$  are feasible whenever  $K$  is simply connected (i.e. has no holes). Indeed, we showed that these volumetric integrals can be reduced to boundary integrals, thereby circumventing any need to develop 2D quadratures for the unconventional geometries present in curvilinear meshes. The goal of this work is to extend these results to the case where  $K$  is multiply connected.

In Section 5.2, we briefly summarize how (5.1) and (5.2) may be computed in the case when  $K$  is simply connected. In Section 5.3, we address how these calculations can be modified in order to accomodate multiply connected mesh cells. We provide illustrative numerical examples in Section 5.4, and concluding remarks in Section 5.5.

## 5.2. Simply Connected Mesh Cells

Let  $K$  be simply connected, and suppose that  $v, w \in V_p(K)$ . The objective of this section is to provide an overview of some of the techniques used to compute the integrals (5.1) and (5.2). In particular, we will see that each of these volumetric integrals can be reduced to boundary integrals over  $\partial K$ . These were discussed in detail in [27], although since its publication we have made some improvements that reduce computational cost, which we present here.

**5.2.1. The  $H^1$  Semi-inner Product:** Given  $v, w \in V_p(K)$ , note that  $\Delta v$  and  $\Delta w$  are given polynomials of degree at most  $p - 2$ . Let  $P$  and  $Q$  be polynomials of degree at most  $p$  satisfying

$$\Delta(v - P) = 0, \quad \Delta(w - Q) = 0.$$

As pointed out in [20], such polynomials  $P$  and  $Q$  can be explicitly constructed term-by-term by observing that

$$P_\alpha(x) = \frac{|x|^2}{4(|\alpha| + 1)!} \sum_{k=0}^{\lfloor |\alpha|/2 \rfloor} \frac{(-1)^k (|\alpha| - k)!}{(k + 1)!} \left( \frac{|x|^2}{4} \right)^k \Delta^k(x^\alpha) \quad (5.3)$$

is a polynomial anti-Laplacian of  $x^\alpha = x_1^{\alpha_1} x_2^{\alpha_2}$  for a multi-index  $\alpha = (\alpha_1, \alpha_2)$ , i.e.  $\Delta P_\alpha(x) = x^\alpha$ . Note that, in practice,  $P_\alpha$  is obtained only by manipulation of polynomial coefficients, and poses no computational barrier. The same can be said of other operations involving polynomials, such as gradients, etc.

Since the functions

$$\phi = v - P, \quad \psi = w - Q$$

are harmonic, we have the expansion

$$\begin{aligned} \int_K \nabla v \cdot \nabla w \, dx &= \int_K \nabla \phi \cdot \nabla w \, dx + \int_K \nabla P \cdot \nabla \psi \, dx + \int_K \nabla P \cdot \nabla Q \, dx \\ &= \int_{\partial K} w \frac{\partial \phi}{\partial \mathbf{n}} \, ds + \int_{\partial K} P \frac{\partial \psi}{\partial \mathbf{n}} \, ds + \int_K \nabla P \cdot \nabla Q \, dx . \end{aligned} \quad (5.4)$$

For the first two integrals in the final expression, the normal derivatives  $\partial\phi/\partial\mathbf{n}$  and  $\partial\psi/\partial\mathbf{n}$  may be computed using the Dirichlet-to-Neumann map discussed below. Furthermore,  $\nabla P \cdot \nabla Q$  is clearly a polynomial of degree at most  $2p - 2$ . As noted in [3], a straightforward application of the Divergence Theorem and Euler's Homogeneous Function Theorem shows that

$$\int_K x^\alpha \, dx = \frac{1}{2 + |\alpha|} \int_{\partial K} (x \cdot \mathbf{n}) x^\alpha \, ds . \quad (5.5)$$

In this fashion, we reduce the volumetric integral  $\int_K \nabla v \cdot \nabla w \, dx$  to readily computable boundary integrals.

*Remark 5.2.1.* The result (5.5) is a special case of analogous reduction-to-the-boundary integration formulas, such as those introduced by Lasserre [23,24] for more general homogeneous functions (as well as logarithms and exponentials). In [3], the authors exploit these reduction properties repeatedly to reduce the integration of a polynomial on a (flat faced) polytope to a computation that only involves evaluation of the integrand and its derivatives at the vertices of the polytope. The motivating application in [3] was the efficient computation of integrals associated with discretizations of PDEs via discontinuous Galerkin methods. Our motivation is quite similar, but the functions we need to integrate include more than polynomials, and the edges of our mesh cells are not flat (or level sets of homogeneous functions). As such, we can reduce our integrals to computations along the boundaries of mesh cells, but not to their vertices.

**5.2.2. A Dirichlet-to-Neumann Map:** Consider the problem of determining the normal derivative of a harmonic function  $\phi$  given its Dirichlet trace  $\phi|_{\partial K}$ . Recall that  $\widehat{\phi}$  is a harmonic conjugate of a harmonic function  $\phi$  whenever  $\phi, \widehat{\phi}$  are continuously twice differentiable on  $K$  and satisfy the Cauchy-Riemann equations:

$$\frac{\partial \phi}{\partial x_1} = \frac{\partial \widehat{\phi}}{\partial x_2}, \quad \frac{\partial \phi}{\partial x_2} = -\frac{\partial \widehat{\phi}}{\partial x_1}.$$

Given that  $\phi$  is harmonic on a simply connected domain  $K$ , the existence of a harmonic conjugate of  $\phi$  is guaranteed, and  $\widehat{\phi}$  is unique up to an additive constant. If  $\partial K$  is smooth, for every  $x \in \partial K$  it holds that

$$\frac{1}{2} \widehat{\phi}(x) + \int_{\partial K} \frac{\partial G(x, y)}{\partial \mathbf{n}(y)} \widehat{\phi}(y) dS(y) = \int_{\partial K} G(x, y) \frac{\partial \widehat{\phi}}{\partial \mathbf{n}}(y) dS(y) \quad (5.6)$$

where  $G(x, y) = -(2\pi)^{-1} \ln |x - y|$  is the fundamental solution of the Laplacian in  $\mathbb{R}^2$ . Supposing that the boundary  $\partial K$  is traversed counterclockwise, we let  $\mathbf{t}$  denote the unit tangent vector and  $\mathbf{n}$  denote the outward unit normal vector, so that the normal and tangential derivatives of  $\phi$  and  $\widehat{\phi}$  are related by

$$\frac{\partial \phi}{\partial \mathbf{n}} = \frac{\partial \widehat{\phi}}{\partial \mathbf{t}}, \quad \frac{\partial \widehat{\phi}}{\partial \mathbf{n}} = -\frac{\partial \phi}{\partial \mathbf{t}}, \quad (5.7)$$

from which the right-hand side in (5.6) can be computed. Since  $\widehat{\phi}$  is unique only up to an additive constant, we impose  $\int_K \widehat{\phi} ds = 0$ , which we add to the left-hand side above to obtain

$$\frac{1}{2} \widehat{\phi}(x) + \int_{\partial K} \left( \frac{\partial G(x, y)}{\partial \mathbf{n}(y)} + 1 \right) \widehat{\phi}(y) dS(y) = - \int_{\partial K} G(x, y) \frac{\partial \phi}{\partial \mathbf{t}}(y) dS(y). \quad (5.8)$$

In practice, we solve this integral equation numerically for  $\widehat{\phi}$  on  $\partial K$  using a Nyström method, where the right-hand side is computed using the tangential derivative of  $\phi$ , which is readily accessible from its trace  $\phi|_{\partial K}$ . Having obtained values of the harmonic conjugate  $\widehat{\phi}$  on the boundary  $\partial K$ , we may obtain its tangential derivative

$\partial\widehat{\phi}/\partial\mathbf{t}$  via numerical differentiation, which then yields values of the normal derivative  $\partial\phi/\partial\mathbf{n}$ . Indeed, if  $x(t)$  is a sufficiently smooth parameterization of  $\partial K$  and we define  $G(t) = \widehat{\phi}(x(t))$ , then

$$G'(t) = \frac{\partial\widehat{\phi}}{\partial\mathbf{t}}(x(t)) |x'(t)| = \frac{\partial\phi}{\partial\mathbf{n}}(x(t)) |x'(t)| . \quad (5.9)$$

Since  $G(t)$  is periodic, a natural choice to obtain  $G'(t)$  is to write a Fourier expansion  $G(t) = \sum_{k=-\infty}^{\infty} \omega_k e^{ikt}$  and obtain an approximation of  $G'(t)$  by truncating the series

$$G'(t) = \sum_{k=-\infty}^{\infty} ik \omega_k e^{ikt} . \quad (5.10)$$

In practice, a Fast Fourier Transform (FFT) may be used on a discretization of  $G(t)$ , and an inverse FFT used on the coefficients  $ik\omega_k$  to obtain the approximate values of  $G'(t)$ .

Details of such calculations, including the case where  $\partial K$  has corners, are discussed in [26].

**5.2.3. The  $L^2$  Inner Product:** Let  $v = \phi + P$  and  $w = \psi + Q$  be as above. We have the expansion

$$\int_K v w \, dx = \int_K \phi \psi \, dx + \int_K Q \phi \, dx + \int_K P \psi \, dx + \int_K P Q \, dx . \quad (5.11)$$

Notice that the last integral can be computed with (5.5), whereas the two middle integrals have the form

$$\int_K r \eta \, dx$$

where  $r$  is a polynomial and  $\eta$  is harmonic. Using (5.3), let  $R$  be a polynomial such that

$$\Delta R = r ,$$

then applying Green's Second Identity, we have

$$\int_K r \eta \, dx = \int_K \eta \Delta R \, dx = \int_{\partial K} \left[ \eta \frac{\partial R}{\partial \mathbf{n}} - R \frac{\partial \eta}{\partial \mathbf{n}} \right] ds . \quad (5.12)$$

The remaining integral to be computed in (5.11) is the  $L^2$  inner product of the two harmonic functions  $\phi$  and  $\psi$ . Toward this end, suppose that  $\Phi$  is an anti-Laplacian of the harmonic function  $\phi$ , that is,

$$\Delta \Phi = \phi .$$

Then using Green's Second Identity again yields

$$\int_K \phi \psi \, dx = \int_K \psi \Delta \Phi \, dx = \int_{\partial K} \left[ \psi \frac{\partial \Phi}{\partial \mathbf{n}} - \Phi \frac{\partial \psi}{\partial \mathbf{n}} \right] ds . \quad (5.13)$$

The problem of determining such a  $\Phi$ , in particular its trace  $\Phi|_{\partial K}$  and normal derivative  $\partial \Phi / \partial \mathbf{n}$ , is addressed below.

**5.2.4. Anti-Laplacians of Harmonic Functions:** Notice that if  $\Phi$  is an anti-Laplacian of  $\phi$ , it holds that  $\Phi$  is *biharmonic*, that is,  $\Delta^2 \Phi = 0$ . It is well-known (cf. [12, pg. 269]) that every biharmonic function is of the form

$$\Phi(x) = \operatorname{Re} [\bar{z}f(z) + g(z)] ,$$

where  $f, g$  are some analytic functions,  $\operatorname{Re} [z]$  denotes the real part of  $z \in \mathbb{C}$ ,  $\bar{z}$  denotes the complex conjugate, and we use the natural identification of the complex plane with  $\mathbb{R}^2$  via  $x = (x_1, x_2) \mapsto z = x_1 + ix_2$ . Since any anti-Laplacian of  $\phi$  will suffice for

our purposes, we will take  $g = 0$  and write

$$\Phi(x) = \frac{x_1 \rho(x) + x_2 \widehat{\rho}(x)}{4},$$

where  $\rho = 4(\operatorname{Re} f)$  is a harmonic function and  $\widehat{\rho} = 4(\operatorname{Im} f)$  is a harmonic conjugate of  $\rho$ . It follows from the Cauchy-Riemann equations that

$$\phi = \Delta \Phi = \frac{\partial \rho}{\partial x_1} = \frac{\partial \widehat{\rho}}{\partial x_2},$$

and that the gradients of  $\rho$  and  $\widehat{\rho}$  must take the form

$$\nabla \rho = \begin{pmatrix} \phi \\ -\widehat{\phi} \end{pmatrix}, \quad \nabla \widehat{\rho} = \begin{pmatrix} \widehat{\phi} \\ \phi \end{pmatrix},$$

where  $\widehat{\phi}$  is a harmonic conjugate of  $\phi$ .

*Remark 5.2.2.* Note that the gradient of  $\Phi$  is given by

$$\nabla \Phi(x) = \frac{1}{4} \begin{pmatrix} \rho(x) \\ \widehat{\rho}(x) \end{pmatrix} + \frac{1}{4} \begin{pmatrix} x_1 & x_2 \\ x_2 & -x_1 \end{pmatrix} \begin{pmatrix} \phi(x) \\ \widehat{\phi}(x) \end{pmatrix}$$

from which we may obtain the normal derivative  $\partial \Phi / \partial \mathbf{n}$ .

*Remark 5.2.3.* For any fixed constants  $a$  and  $b$ , we have that

$$\frac{x_1(\rho(x) + a) + x_2(\widehat{\rho}(x) + b)}{4}$$

is also an anti-Laplacian of  $\phi$ , since  $(ax_1 + bx_2)/4$  is harmonic.

In order to compute  $\rho$  and  $\widehat{\rho}$ , consider the following. For the sake of illustration, we assume that the boundary  $\partial K$  is smooth, but a similar approach works when  $\partial K$  is only piecewise smooth, using some minor modifications. Given the traces of  $\phi$  and  $\widehat{\phi}$  on  $\partial K$ , we have access to the tangential derivative of  $\rho$  via

$$\frac{\partial \rho}{\partial \mathbf{t}} = \begin{pmatrix} \phi \\ -\widehat{\phi} \end{pmatrix} \cdot \mathbf{t}.$$

Given a sufficiently smooth parameterization  $x(t) : [0, 2\pi] \rightarrow \partial K$  of the boundary, we

define  $g : [0, 2\pi] \rightarrow \mathbb{R}$  by

$$g(t) = \frac{\partial \rho}{\partial \mathbf{t}}(x(t)) |x'(t)| .$$

By the Fundamental Theorem of Calculus, we may obtain an anti-derivative  $G$  via

$$G(t) = \int_0^t g(\tau) d\tau = \int_0^t \nabla \rho(x(\tau)) \cdot x'(\tau) d\tau = \rho(x(t)) .$$

Note that  $g$  is  $2\pi$ -periodic and admits a Fourier expansion

$$g(t) = \sum_{k=-\infty}^{\infty} \omega_k e^{ikt} .$$

As mentioned above, in practice we truncate this series and compute the Fourier coefficients  $\omega_k$  using an FFT. Integrating termwise yields

$$\rho(x(t)) = G(t) = C + \omega_0 t + \sum_{\substack{k=-\infty \\ k \neq 0}}^{\infty} \frac{\omega_k}{ik} e^{ikt}$$

for an arbitrary constant  $C$ . In light of Remark 5.2.3, we may pick  $C$  arbitrarily; for instance, choose  $C = 0$ . Moreover, since  $\rho(x(t))$  is  $2\pi$ -periodic, we also see that  $\omega_0 = 0$ . In the computational context, we apply an inverse FFT to the coefficients  $-\mathbf{i}\omega_k/k$  in order to obtain approximate values of  $\rho$  on the boundary. We apply an analogous procedure to obtain values of  $\hat{\rho}$  on the boundary, using the tangential derivative data

$$\frac{\partial \hat{\rho}}{\partial \mathbf{t}} = \begin{pmatrix} \hat{\phi} \\ \phi \end{pmatrix} \cdot \mathbf{t}$$

and computing an anti-derivative of

$$\hat{g}(t) = \frac{\partial \hat{\rho}}{\partial \mathbf{t}}(x(t)) |x'(t)| .$$

**5.2.5. Piecewise Smooth Boundaries:** In our discussion so far, we have assumed the cell boundary  $\partial K$  to be smooth. In that setting, we employ the trapezoid rule for all integrals under consideration, because of its simplicity and its exponential convergence rate when applied to smooth periodic functions such as those that we encounter in this context (cf. [28] and references therein). In this section, we will briefly address how the calculations described above are modified when  $\partial K$  has one or more corners. Elaboration on these modifications can be found in [26].

Each edge of the mesh cell  $K$  is discretized into  $2n + 1$  points, including the endpoints, so that the boundary is discretized into  $N = 2n \times (\# \text{ edges of } K)$  points, with redundant endpoints being neglected. When an edge  $e \subseteq \partial K$  is a  $C^2$  smooth closed contour, the boundary points are assumed to be sampled according a *strongly regular parameterization*  $x(t)$  of  $e$  (i.e.  $|x'(t)| \geq \delta$  for all  $x(t) \in e$  and for some fixed  $\delta > 0$ ). In the case where  $e$  terminates at a corner, we employ a *Kress reparameterization*, defined as follows (cf. [21]). Suppose that  $x(t)$  is a strongly regular parameterization of  $e$  for  $t \in [0, 2\pi]$ , then define  $\tilde{x}(u) = x(\tau(u))$  using

$$\tau(u) = \frac{2\pi[c(u)]^\sigma}{[c(u)]^\sigma + [1 - c(u)]^\sigma},$$

$$c(u) = \left(\frac{1}{2} - \frac{1}{\sigma}\right) \left(\frac{u}{\pi} - 1\right)^2 + \frac{1}{\sigma} \left(\frac{u}{\pi} - 1\right) + \frac{1}{2}, \quad u \in [0, 2\pi]$$

where the *Kress parameter*  $\sigma \geq 2$  is fixed. The Kress reparameterization is not regular, with  $\tilde{x}'(u)$  vanishing at the endpoints. Indeed,  $\tau'(u)$  has roots at 0 and  $2\pi$  of order  $\sigma - 1$ , which leads to heavy sampling of the boundary near corners. This effect is amplified for larger values of  $\sigma$ . *Kress quadrature*, which applies the trapezoid rule after the aforementioned change of variable, was introduced in [21], and an analysis of its convergence properties and how they relate to the associated Nyström system is provided there (see also [26]). It provides a simple high-order quadrature that is

very effective for the kinds of singular and nearly singular integrands that naturally arise when corners are present.

Recall that the boundary integrals we must approximate have the form

$$\int_{\partial K} w \frac{\partial \eta}{\partial \mathbf{n}} ds = \int_{t_0}^{t_1} w(x(t)) \frac{\partial \eta}{\partial \mathbf{n}}(x(t)) |x'(t)| dt = \int_{t_0}^{t_1} w(x(t)) \frac{\partial \hat{\eta}}{\partial \mathbf{t}}(x(t)) |x'(t)| dt ,$$

where  $\eta$  is a harmonic on  $K$ , with a harmonic conjugate  $\hat{\eta}$ . We emphasize that the normal derivative of  $\eta$ , or the tangential derivative of  $\hat{\eta}$ , is always weighted by the Jacobian  $|x'(t)|$  in these expressions. Note that, whenever  $\hat{\eta}$  has a sufficiently smooth Dirichlet trace, we can compute the *weighted tangential derivative*,

$$\frac{d}{dt} \hat{\eta}(x(t)) = \frac{\partial \hat{\eta}}{\partial \mathbf{t}}(x(t)) |x'(t)| ,$$

by using, for instance, the FFT-based approach described by (5.10). From this, the *weighted normal derivative*

$$\frac{\partial \eta}{\partial \mathbf{n}}(x(t)) |x'(t)| ,$$

is also obtained. Of course, we may replace  $x(t)$  by  $\tilde{x}(u) = x(\tau(u))$  in these expressions when a Kress reparameterization is used. Accurate recovery of tangential or normal derivatives near corners in the case of Kress reparameterization is problematic because  $|\tilde{x}'(u)|$  vanishes at corners, but we again emphasize that we only ever need the weighted versions of these quantities in our computations. As such, we report on approximations of weighted boundary derivatives in Section 5.4.

Note that, for the sake of effectively applying an FFT, we assume that the parameter  $t$  is sampled at equispaced nodes  $t_k = hk$ ,  $h = \pi/n$ ,  $0 \leq k \leq 2n + 1$ , and likewise for the parameter  $u$  when using a Kress reparameterization.

**5.2.6. Summary of Simply Connected Case:** Thus far, we have all the necessary tools to compute the target integrals (5.1) and (5.2) in the case where  $K$  is simply connected. It is worth reiterating that both of these volumetric integrals have been successfully reduced to contour integrals along the boundary  $\partial K$ , and there is no need for 2-dimensional quadratures as *all necessary computations occur only on  $\partial K$* .

We have the option, though, of obtaining interior values of  $v \in V_p(K)$  as follows. Write  $v = \phi + P$  as above, and determine a harmonic conjugate  $\widehat{\phi}$  of  $\phi$ . Then  $f = \phi + i\widehat{\phi}$  is an analytic function, and for any fixed interior point  $z = x_1 + ix_2 \in K$  we have Cauchy's integral formula

$$f(z) = \frac{1}{2\pi i} \oint_{\partial K} \frac{f(\zeta)}{\zeta - z} d\zeta . \quad (5.14)$$

Furthermore, we can obtain interior values of  $\nabla\phi$  by observing that

$$f' = \frac{\partial\phi}{\partial x_1} - i \frac{\partial\phi}{\partial x_2} , \quad f'(z) = \frac{1}{2\pi i} \oint_{\partial K} \frac{f(\zeta)}{(\zeta - z)^2} d\zeta .$$

Interior values of higher derivatives, such as the components of the Hessian, can be obtained in similar fashion if so desired.

We conclude this section with a few remarks about computational complexity. Assume the boundary  $\partial K$  is parameterized and then discretized using  $N$  points. The Nyström system resulting from (5.8) is dense, though well-conditioned, and simple linear solvers come with a computational cost  $\mathcal{O}(N^3)$ . Using more sophisticated methods, such as GMRES, make an improvement, but in general will never be better than  $\mathcal{O}(N^2)$ . Although even more sophisticated methods, such as those based on hierarchical matrices [14] or hierarchical semiseparable matrices [37], can reduce the computational complexity even further, for relatively small problems such as those considered here, GMRES is sufficient.

The FFT calls used for numerical differentiation have a computational cost of

$\mathcal{O}(N \log N)$ , and integration along  $\partial K$  (using, say, the trapezoid rule) takes  $\mathcal{O}(N)$  operations. Operations on polynomials, such as computing anti-Laplacians, can be performed by manipulation of the coefficients and do not meaningfully contribute to the computational cost. So, despite the many terms we have encountered in the expansion of the integrals (5.1) and (5.2), in practice these expansions are relatively cheap in comparison to the cost of obtaining the Dirichlet trace of the harmonic conjugate. Note that the latter computation need only happen once for each function  $v \in V_p(K)$  considered.

Additionally, we can use trigonometric interpolation to reduce computational cost even further, as was explored in [26]. With the boundary discretized into  $N$  points, we can solve the the Nyström system obtained from (5.8) as usual to obtain the harmonic conjugate  $\hat{\phi}$  at these  $N$  points. While performing numerical differentiation with FFT as proposed, we have the Fourier coefficients at our disposal, which allows for rapid interpolation to, say,  $M = 2^m N$  points. We then compute the boundary integrals obtained from expanding (5.1) and (5.2) using standard 1D quadratures on the larger collection of  $M$  points. The heuristics presented in [26] suggest that, for modest values of  $m$  (e.g.  $m = 1, 2$ ), the procedure described above achieves similar levels of accuracy when compared the values obtained by solving the associated  $M \times M$  Nyström system directly.

### 5.3. Punctured Cells

We now consider the case with  $K$  being multiply connected. That is, we take  $K_0, K_1, \dots, K_m \subset \mathbb{R}^2$  to be simply connected, open, bounded regions, such that:

- (a) for each  $1 \leq j \leq m$ , we have that  $\overline{K_j}$  is a proper subset of  $K_0$ —that is,  $\overline{K_j} \subset K_0$ ;
- (b) for each  $1 \leq i < j \leq m$ , the closures of  $K_i$  and  $K_j$  are disjoint—that is,

$$\overline{K}_i \cap \overline{K}_j = \emptyset.$$

Additionally, we will require that for each  $0 \leq j \leq m$ , the boundary  $\partial K_j$  is piecewise  $C^2$  smooth without slits or cusps. We then take  $K$  to be the region

$$K = K_0 \setminus \bigcup_{j=1}^m \overline{K}_j.$$

We refer to  $K_j$  as the  $j$ th *hole* (or *puncture*) of  $K$ . We sometimes call  $\partial K_0$  the *outer boundary* of  $K$ , and  $\partial K_j$  the  $j$ th *inner boundary*. The outer boundary is assumed to be oriented counterclockwise, and the inner boundaries oriented clockwise, with the unit tangential vector  $\mathbf{t}$ , wherever it is defined, oriented accordingly. The outward unit normal  $\mathbf{n}$  is therefore always a  $\pi/2$  clockwise rotation of  $\mathbf{t}$ .

In the simply connected case, we made liberal use of the notion of harmonic conjugates. However, in multiply connected domains, a given harmonic function is not guaranteed to have a harmonic conjugate. For example,  $\ln|x|$  has no harmonic conjugate on any annulus centered at the origin. The following theorem, a proof of which can be found in [4], implies that logarithmic functions are essentially the only harmonic functions in a multiply connected domain that can fail to have a harmonic conjugate.

**Theorem 5.3.1** (Logarithmic Conjugation Theorem). *For each of the  $m$  holes of a multiply connected domain  $K$ , fix a point  $\xi_j \in K_j$ . Suppose that  $\phi$  is a harmonic function on  $K$ . Then there are real constants  $a_1, \dots, a_m$  such that, for each  $x \in K$ ,*

$$\phi(x) = \psi(x) + \sum_{j=1}^m a_j \ln|x - \xi_j|$$

where  $\psi$  is the real part of an analytic function. In particular,  $\psi$  has a harmonic conjugate  $\widehat{\psi}$ .

To simplify the notation in what is to come, it will be convenient to define

$$\lambda_j(x) = \ln |x - \xi_j|, \quad x \in K, \quad 1 \leq j \leq m. \quad (5.15)$$

In a minor notational shift from Section 5.2, note that, in this section, we will reserve  $\psi$  to represent a “conjugable part” of a harmonic function  $\phi$ , rather than treat  $\phi$  and  $\psi$  as independent harmonic functions as we did in the previous section.

**5.3.1. A Dirichlet-to-Neumann Map for Punctured Cells:** Our present goal is to determine the coefficients  $a_1, \dots, a_m$ , as in the statement of Theorem 5.3.1, given the trace of a harmonic function  $\phi$ . We will see that we simultaneously determine  $\widehat{\psi}$  by solving an integral equation similar to (5.8), and thereby arrive at the Dirichlet-to-Neumann map

$$\phi|_{\partial K} \mapsto \frac{\partial \phi}{\partial \mathbf{n}} = \frac{\partial \widehat{\psi}}{\partial \mathbf{t}} + \sum_{j=1}^m a_j \frac{\partial \lambda_j}{\partial \mathbf{n}}. \quad (5.16)$$

Assume for now that the boundary  $\partial K$  is  $C^2$  smooth. The case with corners is handled with Kress reparameterization, as discussed in the previous section. Our current task is to generalize the technique described by (5.8) in the case where  $K$  is multiply connected. An alternative approach to the method we discuss here is presented in [13], which is comparable to our method in terms of cost and accuracy when all boundary edges are smooth, but does not achieve similar levels of accuracy when corners are present.

Let  $\widehat{\psi}$  denote a harmonic conjugate of  $\psi$  satisfying  $\int_{\partial K} \widehat{\psi} \, ds = 0$ . Just as in the simply connected case, we have

$$\frac{1}{2} \widehat{\psi}(x) + \int_{\partial K} \left( \frac{\partial G(x, y)}{\partial \mathbf{n}(y)} + 1 \right) \widehat{\psi}(y) \, dS(y) = \int_{\partial K} G(x, y) \frac{\partial \widehat{\psi}}{\partial \mathbf{n}}(y) \, dS(y).$$

Making the replacement

$$\frac{\partial \widehat{\psi}}{\partial \mathbf{n}} = -\frac{\partial \psi}{\partial \mathbf{t}} = -\frac{\partial \phi}{\partial \mathbf{t}} + \sum_{j=1}^m a_j \frac{\partial \lambda_j}{\partial \mathbf{t}}$$

and rearranging yields

$$\begin{aligned} \frac{1}{2} \widehat{\psi}(x) + \int_{\partial K} \left( \frac{\partial G(x, y)}{\partial \mathbf{n}(y)} + 1 \right) \widehat{\psi}(y) dS(y) - \sum_{j=1}^m a_j \int_{\partial K} G(x, y) \frac{\partial \lambda_j}{\partial \mathbf{t}}(y) dS(y) \\ = - \int_{\partial K} G(x, y) \frac{\partial \phi}{\partial \mathbf{t}}(y) dS(y) . \end{aligned} \quad (5.17)$$

This integral equation is underdetermined due to the  $m$  additional degrees of freedom  $a_1, \dots, a_m$ , in contrast to (5.8). To resolve this, we multiply both sides of  $\phi = \psi + \sum_{j=1}^m a_j \lambda_j$  by the normal derivative  $\partial \lambda_\ell / \partial \mathbf{n}$  and integrate over  $\partial K$  to obtain

$$\int_{\partial K} \phi \frac{\partial \lambda_\ell}{\partial \mathbf{n}} ds = \int_{\partial K} \psi \frac{\partial \lambda_\ell}{\partial \mathbf{n}} ds + \sum_{j=1}^m a_j \int_{\partial K} \lambda_j \frac{\partial \lambda_\ell}{\partial \mathbf{n}} ds .$$

Invoking Green's Second Identity and the Cauchy-Riemann equations yields

$$\int_{\partial K} \psi \frac{\partial \lambda_\ell}{\partial \mathbf{n}} ds = \int_{\partial K} \lambda_\ell \frac{\partial \psi}{\partial \mathbf{n}} ds = \int_{\partial K} \lambda_\ell \frac{\partial \widehat{\psi}}{\partial \mathbf{t}} ds .$$

To write this in a form more conducive to computation, observe that the Fundamental Theorem of Calculus for contour integrals implies that

$$\int_{\partial K} \frac{\partial(\widehat{\psi} \lambda_\ell)}{\partial \mathbf{t}} ds = 0$$

since  $\partial K$  consists of  $m + 1$  closed contours. From the Product Rule, we obtain

$$\int_{\partial K} \lambda_\ell \frac{\partial \widehat{\psi}}{\partial \mathbf{t}} ds = - \int_{\partial K} \widehat{\psi} \frac{\partial \lambda_\ell}{\partial \mathbf{t}} ds .$$

Therefore,  $\widehat{\psi}$  ought to satisfy

$$- \int_{\partial K} \widehat{\psi} \frac{\partial \lambda_\ell}{\partial \mathbf{t}} ds + \sum_{j=1}^m a_j \int_{\partial K} \lambda_j \frac{\partial \lambda_\ell}{\partial \mathbf{n}} ds = \int_{\partial K} \phi \frac{\partial \lambda_\ell}{\partial \mathbf{n}} ds , \quad 1 \leq \ell \leq m . \quad (5.18)$$

In summary, we have obtained a system of equations (5.17) and (5.18) for simultaneously determining the trace of  $\widehat{\psi}$  on  $\partial K$  and the coefficients  $a_1, \dots, a_m$ . Discretizing the boundary into  $N$  points, as we did for the simply connected case, this system of equations yields a square augmented Nyström system in  $N + m$  variables, which we may solve with the same techniques used for solving (5.8). The case when  $\partial K$  has corners can be handled using a Kress reparameterization, just as in the simply connected case.

**5.3.2. Anti-Laplacians of Harmonic Functions on Punctured Cells:** Next, we wish to construct an anti-Laplacian of a harmonic function

$$\phi = \psi + \sum_{j=1}^m a_j \lambda_j$$

as in the statement of Theorem 5.3.1. It is simple to verify that

$$\Lambda_j(x) = \frac{1}{4} |x - \xi_j|^2 (\ln |x - \xi_j| - 1)$$

is an anti-Laplacian of  $\lambda_j(x) = \ln |x - \xi_j|$ , so if  $\Psi$  is an anti-Laplacian of  $\psi$ , then we have that

$$\Phi = \Psi + \sum_{j=1}^m a_j \Lambda_j \tag{5.19}$$

is an anti-Laplacian of  $\phi$ . The normal derivative can be computed using

$$\nabla \Phi = \nabla \Psi + \sum_{j=1}^m a_j \nabla \Lambda_j, \quad \nabla \Lambda_j(x) = \frac{1}{4} (2 \ln |x - \xi_j| - 1) (x - \xi_j).$$

Analogous to the simply connected case, we might seek potentials  $\rho, \widehat{\rho}$  of the vector fields

$$\mathbf{F} = \begin{pmatrix} \psi \\ -\widehat{\psi} \end{pmatrix}, \quad \widehat{\mathbf{F}} = \begin{pmatrix} \widehat{\psi} \\ \psi \end{pmatrix}.$$

While  $\mathbf{F}$  and  $\widehat{\mathbf{F}}$  both have vanishing curls, this is not sufficient to guarantee that they are both conservative on a multiply connected domain—a simple counterexample being

$$\psi(x) = \frac{x_1}{|x|^2}, \quad \widehat{\psi}(x) = -\frac{x_2}{|x|^2},$$

taken on a circular annulus centered at the origin.

An elementary observation from complex analysis is that an analytic function  $g = \psi + i\widehat{\psi}$  has an antiderivative if and only if  $\mathbf{F} = (\psi, -\widehat{\psi})$  and  $\widehat{\mathbf{F}} = (\widehat{\psi}, \psi)$  are conservative vector fields. Indeed,  $G = \rho + i\widehat{\rho}$  satisfies  $G' = g$  for  $\nabla\rho = \mathbf{F}$  and  $\nabla\widehat{\rho} = \widehat{\mathbf{F}}$ . This simple fact inspires us to decompose  $g$  as  $g_0 + g_1$ , where  $g_0$  has an antiderivative and the real part of  $g_1$  has an anti-Laplacian which can be computed a priori. The following proposition reveals such a decomposition. The proof is inspired by that given in [4] and is unlikely to surprise a reader familiar with elementary complex analysis, but we include it for the sake of completeness.

**Proposition 5.3.2.** Let  $g = \psi + i\widehat{\psi}$  be analytic on a multiply connected domain  $K$ . Let  $\zeta_j \in K_j$  denote a point fixed in the  $j$ th hole of  $K$ . Then there are complex constants  $\alpha_j \in \mathbb{C}$  such that

$$g(z) = g_0(z) + \sum_{j=1}^m \frac{\alpha_j}{z - \zeta_j},$$

where  $g_0$  has an antiderivative.

*Proof.* For each  $1 \leq j \leq m$ , let

$$\alpha_j = -\frac{1}{2\pi i} \oint_{\partial K_j} g \, dz$$

where  $\partial K_j$  is the boundary of the  $j$ th hole traversed clockwise, and define

$$g_0(z) := g(z) - \sum_{j=1}^m \frac{\alpha_j}{z - \zeta_j} .$$

We wish to show that  $g_0$  has an antiderivative, i.e. there is an analytic function  $G_0$  for which  $G_0' = g_0$ . It will suffice to show that  $\oint_{\gamma} g_0 dz = 0$  for any closed contour  $\gamma$  in  $K$ . To see why, fix any point  $z_0 \in K$  and define

$$G_0(z) = \int_{\gamma(z_0, z)} g_0(\zeta) d\zeta$$

where  $\gamma(z_0, z)$  is any contour in  $K$  starting at  $z_0$  and terminating at  $z \in K$ . Since this integral would be path independent, it would hold that  $G_0$  is well defined and  $G_0' = g_0$ .

Let  $\gamma$  be a closed contour in  $K$ . If  $\gamma$  is homotopic to a point, then

$$\oint_{\gamma} g_0 dz = \oint_{\gamma} g dz - \sum_{j=1}^m \oint_{\gamma} \frac{\alpha_j}{z - \zeta_j} dz = 0$$

holds because  $g$  and  $(z - \zeta_j)^{-1}$  are analytic in any simply connected open subset of  $K$ . If  $\gamma$  is homotopic to  $\partial K_{\ell}$ , then by the Deformation Theorem [25, Theorem 2.2.2] we have

$$\begin{aligned} \oint_{\gamma} g_0 dz &= \oint_{\partial K_{\ell}} g_0 dz \\ &= \oint_{\partial K_{\ell}} g dz - \sum_{j=1}^m \oint_{\partial K_{\ell}} \frac{\alpha_j}{z - \zeta_j} dz \\ &= -2\pi i \alpha_{\ell} - \oint_{\partial K_{\ell}} \frac{\alpha_{\ell}}{z - \zeta_{\ell}} dz = 0 . \end{aligned}$$

Note that the same conclusion holds when  $\gamma$  is oriented opposite to  $\partial K_{\ell}$ . Finally, if  $\gamma$  is any closed contour in  $K$  that is not homotopic to a point, it holds that  $\gamma$  can be

decomposed as a closed chain (cf. Theorem 2.4 in [22])

$$\gamma \sim m_1 \gamma_{\ell_1} + \cdots + m_n \gamma_{\ell_n}, \quad n \leq m$$

with  $\gamma_{\ell_j}$  being homotopic to  $\partial K_j$  and  $m_j$  being the winding number of  $\gamma$  with respect to  $\zeta_j$ . Then

$$\oint_{\gamma} g_0 dz = \sum_{j=1}^n m_j \oint_{\gamma_{\ell_j}} g_0 dz = 0$$

holds by the previous conclusion. Therefore  $\int_{\gamma} g_0 dz = 0$  for any closed contour in  $\gamma$ . As remarked above, this is sufficient to show that  $g_0$  has an antiderivative.  $\square$

*Remark 5.3.3.* For  $\alpha_j = b_j + ic_j$  in the proof above, we have

$$b_j = -\frac{1}{2\pi} \int_{\partial K_j} (\widehat{\psi}, \psi) \cdot \mathbf{t} ds, \quad c_j = \frac{1}{2\pi} \int_{\partial K_j} (\psi, -\widehat{\psi}) \cdot \mathbf{t} ds \quad (5.20)$$

are real-valued contour integrals around the boundary of the  $j$ th hole. Again, note that the inner boundary  $\partial K_j$  is taken to be oriented clockwise, with  $\mathbf{t}$  behaving accordingly.

Using the above results, we may decompose  $g = \psi + i\widehat{\psi}$  into one part that has an antiderivative

$$g_0 = \psi_0 + i\widehat{\psi}_0,$$

and another part that is a linear combination of rational functions

$$\sum_{j=1}^m \frac{\alpha_j}{z - \zeta_j} = \sum_{j=1}^m (b_j \mu_j - c_j \widehat{\mu}_j) + i \sum_{j=1}^m (c_j \mu_j + b_j \widehat{\mu}_j), \quad \begin{pmatrix} \mu_j \\ -\widehat{\mu}_j \end{pmatrix} = \nabla \ln |x - \xi_j|,$$

where we use  $\zeta_j = \xi_j \cdot (1, i)$ , with  $\xi_j$  being chosen when Theorem 5.3.1 is applied.

Easy calculations verify that

$$M_j(x; b_j, c_j) = \frac{1}{2}(b_j, c_j) \cdot (x - \xi_j) \ln |x - \xi_j|$$

satisfies  $\Delta M_j = b_j \mu_j - c_j \widehat{\mu}_j$ , and whose normal derivative can be directly obtained from

$$\nabla M_j(x; b_j, c_j) = \frac{1}{2}(b_j \mu_j - c_j \widehat{\mu}_j) (x - \xi_j) + \frac{1}{2} \ln |x - \xi_j| (b_j, c_j) .$$

Suppose that we have computed  $b_j, c_j$ ,  $1 \leq j \leq m$ , using Remark 5.3.3 and thereby obtained  $g_0 = \psi_0 + i\widehat{\psi}_0$  as in Proposition 5.3.2. Since  $g_0$  has an antiderivative, we have that the vector fields

$$\mathbf{F}_0 = \begin{pmatrix} \psi_0 \\ -\widehat{\psi}_0 \end{pmatrix} , \quad \widehat{\mathbf{F}}_0 = \begin{pmatrix} \widehat{\psi}_0 \\ \psi_0 \end{pmatrix}$$

are conservative. Let  $\rho_0, \widehat{\rho}_0$  be their corresponding potentials, then it follows from the Cauchy-Riemann equations that  $\widehat{\rho}_0$  is a harmonic conjugate of  $\rho_0$ , and their Neumann data is supplied with

$$\frac{\partial \rho_0}{\partial \mathbf{n}} = \mathbf{F}_0 \cdot \mathbf{n} , \quad \frac{\partial \widehat{\rho}_0}{\partial \mathbf{n}} = \widehat{\mathbf{F}}_0 \cdot \mathbf{n} .$$

The solution to the Neumann problem  $\Delta \rho_0 = 0$ ,  $\nabla \rho_0 \cdot \mathbf{n} = \mathbf{F}_0 \cdot \mathbf{n}$  is unique up to an additive constant, and similarly for  $\widehat{\rho}_0$ . Given the conclusion of Remark 5.2.3, we may fix these constants arbitrarily, and we make the choice to impose

$$\int_{\partial K} \rho_0 \, ds = 0 , \quad \int_{\partial K} \widehat{\rho}_0 \, ds = 0 .$$

Using the same techniques used to solve (5.8), we may determine the traces of  $\rho, \widehat{\rho}$  by

solving

$$\begin{aligned} \frac{1}{2}\rho_0(x) + \int_{\partial K} \left( \frac{\partial G(x, y)}{\partial \mathbf{n}(y)} + 1 \right) \rho_0(y) dS(y) \\ = \int_{\partial K} G(x, y) \mathbf{F}_0(y) \cdot \mathbf{n}(y) dS(y) , \end{aligned} \quad (5.21)$$

$$\begin{aligned} \frac{1}{2}\widehat{\rho}_0(x) + \int_{\partial K} \left( \frac{\partial G(x, y)}{\partial \mathbf{n}(y)} + 1 \right) \widehat{\rho}_0(y) dS(y) \\ = \int_{\partial K} G(x, y) \widehat{\mathbf{F}}_0(y) \cdot \mathbf{n}(y) dS(y) . \end{aligned} \quad (5.22)$$

In summary, we have the following recipe to determine an anti-Laplacian  $\Phi$  of a given harmonic function  $\phi$  on a multiply connected domain  $K$ :

(a) Write  $\phi = \psi + \sum_j a_j \lambda_j$  as in Theorem 5.3.1, and determine  $\widehat{\psi}$  and  $a_1, \dots, a_m$  using (5.17) and (5.18).

(b) Determine  $b_1, \dots, b_m, c_1, \dots, c_m$  by computing (5.20).

(c) Set

$$\psi_0 = \psi - \sum_{j=1}^m (b_j \mu_j - c_j \widehat{\mu}_j) , \quad \widehat{\psi}_0 = \widehat{\psi} - \sum_{j=1}^m (c_j \mu_j + b_j \widehat{\mu}_j) .$$

(d) Solve (5.21) and (5.22) using  $\mathbf{F}_0 = (\psi_0, -\widehat{\psi}_0)$  and  $\widehat{\mathbf{F}}_0 = (\widehat{\psi}_0, \psi_0)$ .

(e) Set

$$\Phi(x) = \frac{1}{4} (x_1 \rho_0(x) + x_2 \widehat{\rho}_0(x)) + \sum_{j=1}^m M_j(x; b_j, c_j) + \sum_{j=1}^m a_j \Lambda_j(x) .$$

**5.3.3. Summary of Multiply Connected Case:** The strategies outlined in Section 5.2 for expanding the  $H^1$  semi-inner product and  $L^2$  inner product and reducing each term to integrals along the boundary  $\partial K$  still hold in the multiply connected case. The two primary ways in which the computations have changed in the multiply

connected case is (i) the Dirichlet-to-Neumann map for harmonic functions, and (ii) obtaining an anti-Laplacian of a harmonic function.

We also note that the FFT-based method (5.10) can still be used to obtain  $\partial\widehat{\psi}/\partial\mathbf{t}$  from  $\widehat{\psi}|_{\partial K}$ , *but must be used on each component  $\partial K_0, \partial K_1, \dots, \partial K_m$  of the boundary separately*. An astute reader may also notice that similar concerns would thwart our attempts to obtain  $\rho_0, \widehat{\rho}_0$  with an FFT-based approach when  $K$  is multiply connected, in contrast to the simply connected case.

Should we wish to obtain interior values of

$$v(x) = \psi(x) + P(x) + \sum_{j=1}^m a_j \lambda_j(x) ,$$

which we emphasize is optional, we may proceed as follows. The values of  $P$  and  $\lambda_j$  may be obtained through direct computation. To see how to obtain interior values of  $\psi$ , consider the complex contour integral of  $f = \psi + i\widehat{\psi}$  along the outer boundary  $\partial K_0$ . Let  $\gamma$  be the positively oriented boundary of a closed disk that lies in  $K$  and is centered at a fixed  $z \in K$ . Then  $\partial K_0$  can be decomposed into the chain

$$\partial K_0 \sim \gamma - \partial K_1 - \dots - \partial K_m$$

with the inner boundaries oriented clockwise. So integrating and applying Cauchy's integral formula to  $\gamma$  yields

$$\oint_{\partial K_0} \frac{f(\zeta)}{\zeta - z} d\zeta = 2\pi i f(z) - \sum_{j=1}^m \oint_{\partial K_j} \frac{f(\zeta)}{\zeta - z} d\zeta ,$$

and rearranging gives the familiar formula

$$f(z) = \frac{1}{2\pi i} \oint_{\partial K} \frac{f(\zeta)}{\zeta - z} d\zeta , \quad z \in K ,$$

provided that we orient the boundary components properly. The same argument can be applied to show that the components of the gradient can be obtained in the interior

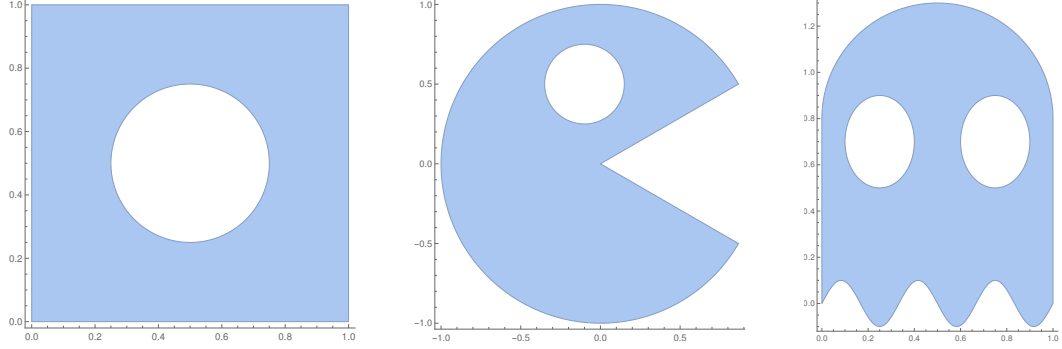


Figure 5.2: Punctured cells used for numerical experiments in Section 5.4.

by applying the above result to  $f'$ , and similarly for higher derivatives.

#### 5.4. Numerical Examples

For each of the following examples, we pick explicit functions  $v, w \in H^1(K)$  of the form

$$v = \phi + P, \quad w = \psi + Q,$$

where  $\phi, \psi$  are harmonic functions and  $P, Q$  are polynomials. While we will pick  $v, w$  to be explicitly-defined, note that only the boundary traces  $v|_{\partial K}, w|_{\partial K}$  and the coefficients of the polynomial Laplacians  $\Delta v, \Delta w$  are supplied as input for the computations. Using explicitly defined functions is convenient for convergence studies, but in practice the computations will work the same for implicitly-defined functions.

Unless otherwise noted, we keep the Kress parameter  $\sigma = 7$  fixed, as we observed that this value of the Kress parameter gave satisfactory results under a wide range of circumstances. Boundary integrals are evaluated by applying the trapezoid rule. We use the SciPy package [29] for GMRES using default parameters (except for the convergence tolerance, which we set to  $10^{-12}$ ), and we use the NumPy package [16] to execute FFT calls.

Table 5.1: Errors in intermediate quantities for  $v$  on the square with a circular hole in Example 5.4.1: the logarithmic coefficient  $a_1$ , the trace of the harmonic conjugate  $\widehat{\psi}$ , the weighted normal derivative wnd, and the trace of the anit-Laplacian  $\Phi$ . The latter three are given in the  $L^2$  boundary norm.

$n$	$a_1$ error	$\widehat{\psi}$ error	wnd error	$\Phi$ error
4	1.7045e-03	3.5785e-02	2.8201e-01	8.3234e-03
8	3.5531e-07	2.6597e-04	1.2855e-03	3.9429e-05
16	1.0027e-09	1.1884e-06	3.7415e-06	3.3785e-07
32	3.5905e-13	2.3095e-09	1.0434e-08	1.9430e-09
64	1.8874e-14	1.6313e-12	6.4780e-11	7.0728e-12

In each example, reference values for the  $H^1$  and  $L^2$  (semi-)inner products were obtained with *Wolfram Mathematica*. The mesh cell  $K$  was defined using `ImplicitRegion[]`, and volumetric integrals were computed using `NIntegrate[]`. We remark that our implementation, albeit far from optimized, was significantly faster than *Mathematica* for computing these kinds of integrals. (In fairness, we compute these integrals as boundary integrals, whereas it seems that *Mathematica* implements general-purpose adaptive 2D quadrature over the volume, so perhaps the comparison in performance is unjustified.) For each reference value, we also give the error estimate that was provided by *Mathematica*.

Each of the numerical examples in this section is presented with Jupyter Notebook in the GitHub repository

<https://github.com/samreynoldsmath/PuncturedFEM>

which also contains the Python source code implementing the numerical methods we have described in this work.

*Example 5.4.1 (Punctured Square)*. Let  $K_0 = (0, 1) \times (0, 1)$  be a unit square, and let  $K_1 = \{x \in \mathbb{R}^2 : |x - \xi| < 1/16\}$  be a disk of radius  $1/4$  centered at  $\xi = (1/2, 1/2)$ . The cell under consideration is the square with the disk removed,  $K = K_0 \setminus \overline{K_1}$ , as

depicted in the left-hand side of Figure 5.2. Define

$$v(x) = e^{x_1} \cos x_2 + \ln |x - \xi| + x_1^3 x_2 + x_1 x_2^3 .$$

Notice that  $v$  can be decomposed into

$$v = \phi + P , \quad \phi(x) = e^{x_1} \cos x_2 + \ln |x - \xi| , \quad P(x) = x_1^3 x_2 + x_1 x_2^3 ,$$

with  $\phi$  being harmonic and the polynomial  $P$  having the Laplacian

$$\Delta v(x) = \Delta P(x) = 12x_1 x_2 .$$

Furthermore,  $\phi$  can be decomposed as

$$\phi(x) = \psi(x) + a_1 \ln |x - \xi_1|$$

with  $a_1 = 1$  and  $\xi_1 = \xi = (1/2, 1/2)$ . In Table 5.1, we report the errors in the computed approximations of  $a_1$ ,  $\widehat{\psi}$ , the weighted normal derivative (wnd) of  $\phi$ , and the trace of the anti-Laplacian  $\Phi$ . Since a harmonic conjugate  $\widehat{\psi}$  is unique only up to an additive constant, we compute the error as

$$\left( \int_{\partial K} (\widehat{\psi}_{\text{exact}} - \widehat{\psi}_{\text{computed}} + c)^2 ds \right)^{1/2} ,$$

where  $c$  is a constant minimizing the  $L^2(\partial K)$  distance between the traces of  $\widehat{\psi}_{\text{exact}}$  and  $\widehat{\psi}_{\text{computed}}$ , namely

$$c = -\frac{1}{|\partial K|} \int_{\partial K} (\widehat{\psi}_{\text{exact}} - \widehat{\psi}_{\text{computed}}) ds .$$

In general, an anti-Laplacian  $\Phi$  is unique only up to the addition of a harmonic function, which is much less restrictive. However, we see from Remark 5.2.3 that two different anti-Laplacians computed using the techniques described will differ by the addition of a linear function  $c_1 x_1 + c_2 x_2$  for some constants  $c_1, c_2$ . It follows that

difference between  $\Phi_{\text{computed}}$  and

$$\Phi_{\text{exact}}(x) = \frac{1}{4}e^{x_1}(x_1 \cos x_2 + x_2 \sin x_2) + \frac{1}{4}|x - \xi|^2(\ln|x - \xi| - 1)$$

ought to be well-modeled by  $c_1x_1 + c_2x_2$ , and we choose to determine optimal constants  $c_1, c_2$  via least-squares. Upon doing so, we compute the error in  $\Phi$  with

$$\left( \int_{\partial K} (\Phi_{\text{exact}} - \Phi_{\text{computed}} + c_1x_1 + c_2x_2)^2 ds \right)^{1/2}.$$

In Table 5.1, we list the absolute error in the logarithmic coefficient  $a_1$ , as well as the  $L^2$  boundary norm of the errors in the harmonic conjugate trace  $\widehat{\psi}|_{\partial K}$ , the weighted normal derivative of  $\phi$ , and the trace of the anti-Laplacian  $\Phi$ . We observe superlinear convergence in these quantities with respect to the boundary discretization parameter  $n$ . In Table 5.2, we provide the errors in the  $H^1$  semi-inner product and  $L^2$  inner product of  $v$  and  $w$ , where

$$w(x) = \frac{x_1 - 0.5}{(x_1 - 0.5)^2 + (y - 0.5)^2} + x_1^3 + x_1x_2^2.$$

The reference values

$$\int_K \nabla v \cdot \nabla w dx \approx 4.46481780319135 \pm 9.9241 \times 10^{-15},$$

$$\int_K v w dx \approx 1.39484950156676 \pm 2.7256 \times 10^{-16}$$

were obtained with *Mathematica*, as noted above. Notice that the convergence trends in these quantities parallels those of the intermediate quantities found in Table 5.1.

*Example 5.4.2 (Pac-Man).* For our next example, we consider the Pac-Man domain  $K = K_0 \setminus \overline{K_1}$ , where  $K_0$  is the sector of the unit circle centered at the origin for  $\theta_0 < \theta < 2\pi - \theta_0$ ,  $\theta_0 = \pi/6$ , and  $K_1$  is a disk of radius  $1/4$  centered at  $(-1/10, 1/2)$ .

Table 5.2: Absolute errors in the  $H^1$  semi-inner product and  $L^2$  inner product for the Punctured Square (Example 5.4.1), Pac-Man (Example 5.4.2), and Ghost (Example 5.4.3).

$n$	Punctured Square		Pac-Man		Ghost	
	$H^1$ error	$L^2$ error	$H^1$ error	$L^2$ error	$H^1$ error	$L^2$ error
4	1.5180e-02	3.4040e-03	7.2078e-02	2.1955e-02	2.4336e+00	5.9408e-03
8	2.6758e-04	8.3812e-05	3.3022e-02	5.4798e-03	1.0269e-02	1.3086e-02
16	8.4860e-07	3.8993e-08	1.2495e-03	1.0159e-04	1.5273e-03	1.3783e-04
32	1.0860e-09	2.8398e-11	6.5683e-06	4.6050e-07	5.3219e-07	8.1747e-07
64	9.5390e-13	1.1036e-13	4.6834e-08	2.1726e-09	1.5430e-11	4.6189e-11

(See Figure 5.2, center.) The function

$$v(x) = r^\alpha \sin(\alpha\theta)$$

specified in polar coordinates  $(r, \theta)$  is harmonic everywhere except possibly the origin for any fixed  $\alpha > 0$ . For the choice  $0 < \alpha < 1$ , we have that the gradient of  $v$  is unbounded near the origin; indeed,  $|\nabla v| = \alpha r^{\alpha-1}$ . Noting that the boundary  $\partial K$  intersects the origin, it follows that normal derivative of  $v$  is also unbounded near the origin. To test whether our strategy is viable for such functions, we compute the  $H^1$  seminorm and  $L^2$  norm of  $v$  for  $\alpha = 1/2$ . The results are given in Table 5.2, using the reference values

$$\int_K |\nabla v|^2 dx \approx 1.20953682240855912 \pm 2.3929 \times 10^{-18},$$

$$\int_K v^2 dx \approx 0.97793431492143971 \pm 3.6199 \times 10^{-19}.$$

Although convergence is still rapid in this case, it is less so than in the previous example, as may be expected when considering more challenging integrands, as we have here.

*Example 5.4.3 (Ghost).* Our final example demonstrates that our method works when  $K$  has more than one puncture, as well as when the boundary has edges that are not line segments or circular arcs. The lower edge of the Ghost is the sinusoid  $x_2 = 0.1 \sin(6\pi x_1)$  for  $0 < x_1 < 1$ , the sides are vertical line segments, the upper boundary

is a circular arc of radius  $1/2$  centered at  $(0.5, 0.8)$ , and the inner boundaries are ellipses with  $0.15$  and  $0.2$  as the semi-minor and semi-major axes, respectively, with one centered at  $(0.25, 0.7)$  and the other at  $(0.75, 0.7)$ . (See Figure 5.2, right.) The functions we choose to integrate are

$$v(x) = \frac{x_1 - 0.25}{(x_1 - 0.25)^2 + (x_2 - 0.7)^2} + x_1^3 x_2 + x_2^2,$$

$$w(x) = \ln [(x_1 - 0.75)^2 + (x_2 - 0.7)^2] + x_1^2 x_2^2 - x_1 x_2^3.$$

Notice that these functions have singularities in the holes of  $K$ , one rational and the other logarithmic. In Table 5.2, we compare the computed  $H^1$  and  $L^2$  (semi-)inner products to the reference values

$$\int_K \nabla v \cdot \nabla w \, dx \approx -6.311053612386 \pm 3.6161 \times 10^{-12},$$

$$\int_K v w \, dx \approx -3.277578636852 \pm 1.0856 \times 10^{-13}.$$

We conjecture that for  $n = 4$ , the error in the  $H^1$  semi-inner product is significantly worse than in the other two examples because this level of boundary discretization is insufficient to fully capture the oscillatory behavior of the lower edge.

Lastly, we demonstrate the ability to obtain interior values of  $v$  and  $\nabla v$  in the interior of  $K$  in Figure 5.3. All computations used to generate these values used the boundary discretization parameter  $n = 64$ . Values and errors are given only for points that are at least  $0.02$  units away from the nearest quadrature point on the boundary. As seen in the figure, the pointwise errors in these computations are extremely small away from the boundary, and significantly increase near the boundary. This error increase is due fact that the integrand Cauchy's integral formula is nearly singular (large derivatives) for points near the boundary because the factor(s) of  $\zeta - z$  in the denominator of the integrand, which reduces the accuracy of the types of quadratures

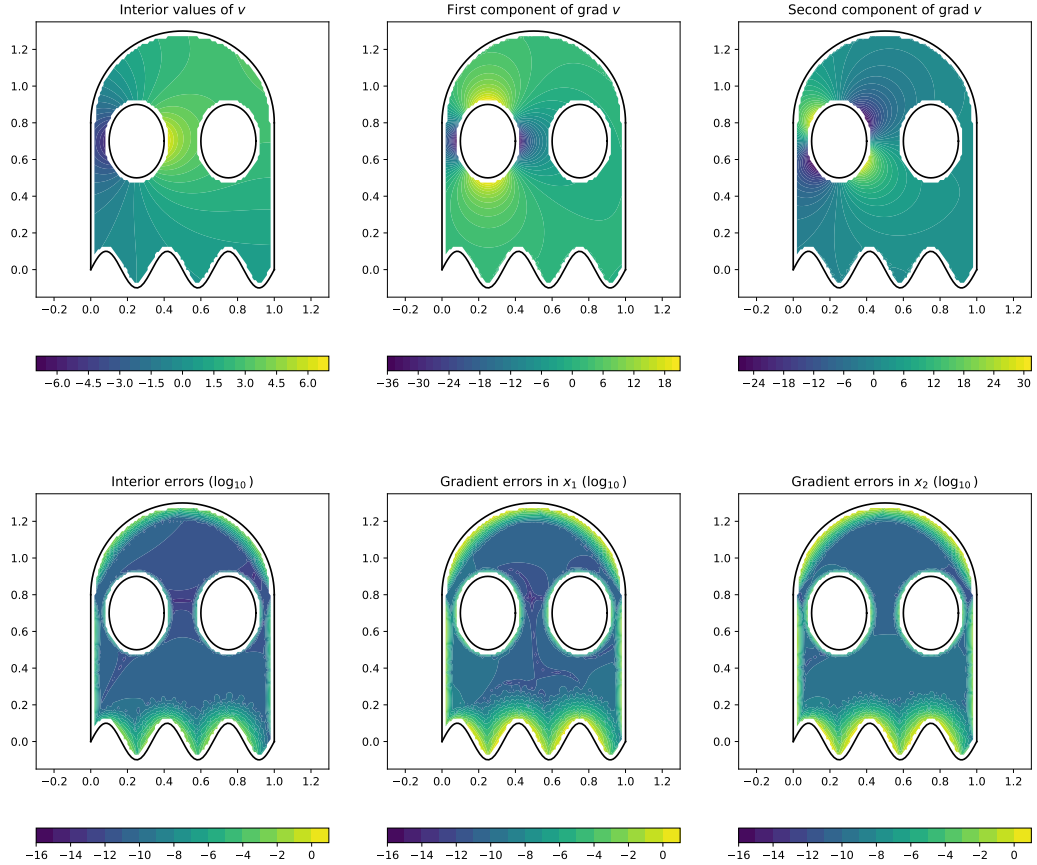


Figure 5.3: Interior values of  $v$  and  $\nabla v$  in Example 5.4.3. In the left column, we have the computed values of  $v$  on top, and the base 10 logarithm of the absolute error on bottom. This setup is repeated in the middle and right columns for the components of the gradient.

we employ. There are well-known approaches for combating such negative effects near the boundary, such as interpolation between the highly accurate values in the interior and the known, or highly accurate, values on the boundary. We have not incorporated such improvements here, because the focus of the present work is on the efficient and accurate evaluation of the two target integrals, not on point evaluations in the interior.

### 5.5. Conclusion

We have seen that, given implicitly-defined functions  $v, w$  of the type that arise in a finite element setting, we can efficiently compute the  $H^1$  semi-inner product and  $L^2$

inner product of  $v$  and  $w$  over multiply connected curvilinear mesh cells. All of the necessary computations occur only on the boundary of mesh cells, although we have the option of obtaining interior values of these functions and their derivatives using quantities obtained in the course of these calculations. Two key computations needed for our approach are (i) a Dirichlet-to-Neumann map for harmonic functions, and (ii) finding the trace and normal derivative of an anti-Laplacian of a harmonic function. We have described how both of these computations may be feasibly accomplished on planar curvilinear mesh cells with holes. Numerical examples demonstrate high accuracy and rapid convergence with respect to the number of sampled boundary points.

Some aspects of our approach to reduce integrals on  $K$  to integrals on  $\partial K$  carry over naturally to higher dimensions, with little or no change. For example, the identities (5.4) and (5.11)-(5.13) are dimension-independent, and the identities (5.3) and (5.5) have natural analogues in  $d$  dimensions (cf. [20] and [24]). However, certain aspects of our approach, which were central to achieving efficient, high-order quadratures, are inherently two-dimensional. These aspects include the use of complex function theory and harmonic conjugates in the computation of Dirichlet-to-Neumann maps, as well as computations related to the anti-Laplacian of a harmonic function. Obtaining efficient quadratures in three dimensions for integrals such as (5.1)-(5.2) involving functions in  $V_p(K)$  on general mesh cells  $K$  remains an open challenge.

## 5.6. References

- [1] F. Aldakheel, B. Hudobivnik, E. Artioli, L. Beirão da Veiga, and P. Wriggers. Curvilinear virtual elements for contact mechanics. *Comput. Methods Appl. Mech. Engrg.*, 372:113394, 19, 2020.
- [2] A. Anand, J. S. Owall, S. E. Reynolds, and S. Weißer. Trefftz Finite Elements on Curvilinear Polygons. *SIAM J. Sci. Comput.*, 42(2):A1289–A1316, 2020.
- [3] P. F. Antonietti, P. Houston, and G. Pennesi. Fast numerical integration on polytopic meshes with applications to discontinuous Galerkin finite element methods. *J. Sci. Comput.*, 77(3):1339–1370, 2018.
- [4] S. Axler. Harmonic functions from a complex analysis viewpoint. *Amer. Math. Monthly*, 93(4):246–258, 1986.
- [5] L. Beirão da Veiga, F. Brezzi, L. D. Marini, and A. Russo. Polynomial preserving virtual elements with curved edges. *Math. Models Methods Appl. Sci.*, 30(8):1555–1590, 2020.
- [6] L. Beirão da Veiga, A. Russo, and G. Vacca. The virtual element method with curved edges. *ESAIM Math. Model. Numer. Anal.*, 53(2):375–404, 2019.
- [7] L. Beirão da Veiga, F. Brezzi, A. Cangiani, G. Manzini, L. D. Marini, and A. Russo. Basic principles of virtual element methods. *Math. Models Methods Appl. Sci.*, 23(1):199–214, 2013.
- [8] L. Beirão da Veiga, F. Brezzi, L. D. Marini, and A. Russo. The hitchhiker’s guide to the virtual element method. *Math. Models Methods Appl. Sci.*, 24(8):1541–1573, 2014.
- [9] F. Brezzi and L. D. Marini. Virtual element and discontinuous Galerkin methods. In *Recent developments in discontinuous Galerkin finite element methods for partial differential equations*, volume 157 of *IMA Vol. Math. Appl.*, pages 209–221. Springer, Cham, 2014.
- [10] D. Copeland, U. Langer, and D. Pusch. From the boundary element domain decomposition methods to local Trefftz finite element methods on polyhedral meshes. In *Domain decomposition methods in science and engineering XVIII*, volume 70 of *Lect. Notes Comput. Sci. Eng.*, pages 315–322. Springer, Berlin, 2009.
- [11] F. Dassi, A. Fumagalli, D. Losapio, S. Scialò, A. Scotti, and G. Vacca. The mixed virtual element method on curved edges in two dimensions. *Comput. Methods Appl. Mech. Engrg.*, 386:Paper No. 114098, 25, 2021.

- [12] P. R. Garabedian. *Partial Differential Equations*. John Wiley & Sons, New York, 1964.
- [13] A. Greenbaum, L. Greengard, and G. B. McFadden. Laplace’s equation and the Dirichlet-to-Neumann map in multiply connected domains. *Journal of Computational Physics*, 105(1):267–278, 1993.
- [14] W. Hackbusch. *Hierarchical matrices: algorithms and analysis*, volume 49 of *Springer Series in Computational Mathematics*. Springer, Heidelberg, 2015.
- [15] H. Hakula. Resolving boundary layers with harmonic extension finite elements. *Mathematical and Computational Applications*, 27(4), 2022.
- [16] C. R. Harris, K. J. Millman, S. J. van der Walt, R. Gommers, P. Virtanen, D. Cournapeau, E. Wieser, J. Taylor, S. Berg, N. J. Smith, R. Kern, M. Picus, S. Hoyer, M. H. van Kerkwijk, M. Brett, A. Haldane, J. F. del Río, M. Wiebe, P. Peterson, P. Gérard-Marchant, K. Sheppard, T. Reddy, W. Weckesser, H. Abbasi, C. Gohlke, and T. E. Oliphant. Array programming with NumPy. *Nature*, 585(7825):357–362, Sept. 2020.
- [17] C. Hofreither.  $L_2$  error estimates for a nonstandard finite element method on polyhedral meshes. *J. Numer. Math.*, 19(1):27–39, 2011.
- [18] C. Hofreither, U. Langer, and C. Pechstein. Analysis of a non-standard finite element method based on boundary integral operators. *Electron. Trans. Numer. Anal.*, 37:413–436, 2010.
- [19] C. Hofreither, U. Langer, and S. Weißer. Convection-adapted BEM-based FEM. *ZAMM Z. Angew. Math. Mech.*, 96(12):1467–1481, 2016.
- [20] V. V. Karachik and N. A. Antropova. On the solution of a nonhomogeneous polyharmonic equation and the nonhomogeneous Helmholtz equation. *Differ. Uravn.*, 46(3):384–395, 2010.
- [21] R. Kress. A Nyström method for boundary integral equations in domains with corners. *Numer. Math.*, 58(2):145–161, 1990.
- [22] S. Lang. *Complex analysis*, volume 103 of *Graduate Texts in Mathematics*. Springer-Verlag, New York, fourth edition, 1999.
- [23] J. B. Lasserre. Integration on a convex polytope. *Proc. Amer. Math. Soc.*, 126(8):2433–2441, 1998.
- [24] J. B. Lasserre. Integration and homogeneous functions. *Proc. Amer. Math. Soc.*, 127(3):813–818, 1999.

- [25] J. E. Marsden and M. J. Hoffman. *Basic complex analysis*. W. H. Freeman and Company, New York, second edition, 1987.
- [26] J. S. Owall and S. E. Reynolds. A high-order method for evaluating derivatives of harmonic functions in planar domains. *SIAM J. Sci. Comput.*, 40(3):A1915–A1935, 2018.
- [27] J. S. Owall and S. E. Reynolds. Quadrature for implicitly-defined finite element functions on curvilinear polygons. *Computers & Mathematics with Applications*, 107:1–16, 2022.
- [28] L. Trefethen and J. Weideman. The exponentially convergent trapezoidal rule. *SIAM Review*, 56(3):385–458, 2014.
- [29] P. Virtanen, R. Gommers, T. E. Oliphant, M. Haberland, T. Reddy, D. Cournapeau, E. Burovski, P. Peterson, W. Weckesser, J. Bright, S. J. van der Walt, M. Brett, J. Wilson, K. J. Millman, N. Mayorov, A. R. J. Nelson, E. Jones, R. Kern, E. Larson, C. J. Carey, Í. Polat, Y. Feng, E. W. Moore, J. VanderPlas, D. Laxalde, J. Perktold, R. Cimrman, I. Henriksen, E. A. Quintero, C. R. Harris, A. M. Archibald, A. H. Ribeiro, F. Pedregosa, P. van Mulbregt, and SciPy 1.0 Contributors. SciPy 1.0: Fundamental Algorithms for Scientific Computing in Python. *Nature Methods*, 17:261–272, 2020.
- [30] S. Weißer. Residual error estimate for bem-based fem on polygonal meshes. *Numer. Math.*, 118:765–788, 2011. 10.1007/s00211-011-0371-6.
- [31] S. Weißer. Arbitrary order Trefftz-like basis functions on polygonal meshes and realization in BEM-based FEM. *Comput. Math. Appl.*, 67(7):1390–1406, 2014.
- [32] S. Weißer. Residual based error estimate and quasi-interpolation on polygonal meshes for high order BEM-based FEM. *Comput. Math. Appl.*, 73(2):187–202, 2017.
- [33] S. Weißer. Anisotropic polygonal and polyhedral discretizations in finite element analysis. *ESAIM Math. Model. Numer. Anal.*, 53(2):475–501, 2019.
- [34] S. Weißer. *BEM-based Finite Element Approaches on Polytopal Meshes*, volume 130 of *Lecture Notes in Computational Science and Engineering*. Springer International Publishing, 1 edition, 2019.
- [35] S. Weißer and T. Wick. The dual-weighted residual estimator realized on polygonal meshes. *Comput. Methods Appl. Math.*, 18(4):753–776, 2018.
- [36] P. Wriggers, B. Hudobivnik, and F. Aldakheel. A virtual element formulation for general element shapes. *Comput. Mech.*, 66(4):963–977, 2020.

- [37] J. Xia, S. Chandrasekaran, M. Gu, and X. S. Li. Fast algorithms for hierarchically semiseparable matrices. *Numer. Linear Algebra Appl.*, 17(6):953–976, 2010.

## 6. Conclusion

### 6.1. Summary

In the four papers above, we have explored both a theoretical and computational framework sufficient to implement a finite element method using implicitly-defined Poisson functions spaces defined in terms of a curvilinear mesh, including those incorporating multiply connected mesh cells. While virtual element methods use the same function spaces and can be adapted to use the same kind of meshes, our approach to forming the global linear system is decisively “nonvirtual” in that we construct a basis of such a space and compute the entries of the linear system directly, rather than projecting these functions onto polynomial spaces and introducing stabilization terms.

These computations are not as computationally expensive as might be expected, since all relevant volumetric integrals can be reduced to boundary integrals along the boundaries of mesh cells, so that all important computations take place on the mesh skeleton. Despite this, we are able to recover the values of basis functions in the interior, thanks to Cauchy’s integral formula; we can similarly obtain interior derivatives, such as the gradient and Hessian.

A principal component of this method is the ability to determine a harmonic conjugate of a given harmonic function, which is key to obtaining a Dirichlet-to-Neumann map, but also plays a role in constructing an anti-Laplacian of a harmonic function. In the punctured cell case, the existence of a harmonic conjugate, modulo

certain logarithmic terms, permits the same types of computations for these types of mesh cells. The fact that planar domains can be identified as lying in the complex plane, and then bringing to bear the many fundamental results of complex analysis, were instrumental in the development of this method.

## 6.2. Future Work

There are a number of ways in which the work that has been presented here could be extended. Also see Appendix A.

**6.2.1. Comparison Studies:** One of the motivations of developing this method was to hopefully reduce overall computational cost of solving a finite element system by reducing the number of degrees of freedom, that is, when those degrees of freedom are the consequence of mesh refinement due to curved geometry. A numerical study comparing our method to others, including conventional methods like Lagrange finite elements and more experimental ones like VEM, might provide useful insight into what types of problems each of these tools is best suited for.

**6.2.2. *hp*-Refinement:** Our current implementation does not include automatic mesh generation or refinement algorithms, and order  $p > 5$  can result in incorrect dimensions of generated local Poisson spaces in some cases. If these issues can be overcome and combined with *a posteriori* error estimation, an *hp*-refinement method could be achieved.

**6.2.3. Applications to Time-dependent Problems:** Time-dependent problems (e.g. the heat equation) can be solved numerically by repeated linear solve calls. While more conventional finite element spaces, such as Lagrange finite elements, have a relatively cheap assembly cost, the potential for a large number of degrees

freedom implies that each linear solve call is relatively expensive. Assembly cost in the method proposed in this work is more expensive, but the resulting global system has the potential to be much smaller, which could lead to significant speedup. Similar benefits could extend to other methods that use the formed linear system repeatedly.

**6.2.4.  $H(\text{div})$ - and  $H(\text{curl})$ -conforming Spaces:** As we have seen, the normal and tangential derivatives of functions in local Poisson spaces appear frequently in computations, and it is not difficult to imagine that a normally-continuous  $H(\text{div})$ -conforming space analogous to a Raviart-Thomas space using implicitly-defined Poisson-type functions could be constructed. Similarly, a tangentially-continuous  $H(\text{curl})$ -conforming space analogous to a Nédélec space seems plausible as well. The approximation properties of these spaces warrant investigation.

**6.2.5. 3-dimensional Domains:** As we have seen in some detail, complex analysis plays an important role in our method, at least computationally, to create both a Dirichlet-to-Neumann map for harmonic functions and to construct anti-Laplacians of harmonic functions. In a 3D domain, we can no longer identify the domain as a subset of the complex plane, in which case tools analogous to those developed in this work will need to be developed.

## Appendix A. Extensions

This appendix is devoted to ideas which are natural extensions of the work presented in this dissertation, but have not yet been published.

### A.1. Advection Terms

Let  $K$  be a connected mesh cell and consider the integral

$$\int_K (b \cdot \nabla v) w \, dx \tag{A.1}$$

for  $v, w \in V_p(K)$  and a constant vector  $b$ . Writing  $v = \phi + P$  and  $w = \psi + Q$  with  $\phi, \psi$  harmonic and  $P, Q \in \mathbb{P}_p(K)$ , we have the expansion

$$\begin{aligned} \int_K (b \cdot \nabla v) w \, dx &= \int_K (b \cdot \nabla \phi) \psi \, dx + \int_K (b \cdot \nabla \phi) Q \, dx \\ &+ \int_K (b \cdot \nabla P) \psi \, dx + \int_K (b \cdot \nabla P) Q \, dx . \end{aligned} \tag{A.2}$$

Note that the final integral is that of a polynomial, which we have seen is computable. Moreover,  $\int_K (b \cdot \nabla P) \psi \, dx$  is the  $L^2$  inner product between the harmonic function  $\psi$  and the polynomial  $b \cdot \nabla P$ , which we have seen is also computable. Observe that  $\beta(x) = b \cdot x$  is a harmonic polynomial satisfying  $\nabla \beta = b$  and

$$b \cdot \nabla \phi = \frac{1}{2} \Delta(\beta \phi) .$$

Applying Green's Second Identity, we obtain

$$\int_K (b \cdot \nabla \phi) \psi \, dx = \frac{1}{2} \int_K \psi \Delta(\beta \phi) \, dx = \frac{1}{2} \int_{\partial K} \left[ (b \cdot \mathbf{n}) \phi \psi + \beta \psi \frac{\partial \phi}{\partial \mathbf{n}} - \beta \phi \frac{\partial \psi}{\partial \mathbf{n}} \right] ds .$$

Similarly, we have that

$$\int_K (b \cdot \nabla \phi) Q \, dx = \frac{1}{2} \int_{\partial K} \left[ (b \cdot \mathbf{n}) \phi Q + \beta Q \frac{\partial \phi}{\partial \mathbf{n}} - \beta \phi \frac{\partial Q}{\partial \mathbf{n}} \right] ds + \frac{1}{2} \int_K \phi \beta \Delta Q \, dx .$$

Note that the latter integral is the  $L^2$  inner product between the harmonic function  $\phi$  and the polynomial  $\beta \Delta Q$ .

We therefore have that the integral (A.1) can be computed using the same tools developed in the course of this work.

## A.2. Generalized Diffusion Operators

Let  $A$  be a symmetric positive definite  $2 \times 2$  constant matrix, and for  $v, w \in H^1(K)$  consider the integral

$$\int_K \nabla v \cdot A \nabla w \, dx . \tag{A.3}$$

Notice that  $A$  admits a Cholesky factorization  $A = LL^\top$ , which yields

$$\nabla v \cdot A \nabla w = (L^\top \nabla v) \cdot (L^\top \nabla w) .$$

This inspires us to think of  $L$  as the Jacobian of a linear coordinate transform

$$x = Ly , \quad x \in K ,$$

and noting that  $\text{rank } A = 2$  implies that  $L$  is nonsingular we define the transformed domain

$$L^{-1}K := \{L^{-1}x : x \in K\} .$$

Suppose we define  $\tilde{v} \in H^1(L^{-1}K)$  by

$$\tilde{v}(y) := v(Ly) , \quad y \in L^{-1}K ,$$

then the chain rule gives

$$\nabla \tilde{v} = L^\top \nabla v .$$

Let us likewise define  $\tilde{w}(y) := w(Ly)$ , then we have

$$\int_K \nabla v \cdot A \nabla w \, dx = |\det L| \int_{L^{-1}K} \nabla \tilde{v} \cdot \nabla \tilde{w} \, dy , \quad (\text{A.4})$$

where we used the fact that  $\det L$  is constant to push it out from under the integral.

In addition to the integral (A.4), we can compute the other quantities of interest

$$\int_K v w \, dx = |\det L| \int_{L^{-1}K} \tilde{v} \tilde{w} \, dy \quad (\text{A.5})$$

and

$$\begin{aligned} \int_K (b \cdot \nabla v) w \, dx &= \int_K w (L^{-1}b) \cdot (L^\top \nabla v) \, dx \\ &= |\det L| \int_{L^{-1}K} \tilde{w} (L^{-1}b) \cdot \nabla \tilde{v} \, dy \end{aligned} \quad (\text{A.6})$$

So, if we suppose that  $\tilde{v}, \tilde{w} \in V_p(L^{-1}K)$ , the integrals appearing in (1.2) can be computed with the machinery we have devised in this work. Now, if  $\tilde{v}, \tilde{w} \in V_p(L^{-1}K)$ , simple computations suggest that  $v, w \notin V_p(K)$ , but they do belong to a ‘‘perturbed’’ space, which we define presently.

Let  $V_p(K; A)$  denote the subspace of  $H^1(K)$  such that for each  $v \in V_p(K; A)$  we have

$$(a) \quad \operatorname{div} A \nabla v \in \mathbb{P}_{p-2}(K),$$

$$(b) \quad v|_{\partial K} \in C(\partial K),$$

(c)  $v|_e \in P_p(e)$  for each edge  $e \subseteq \partial K$ .

We might call  $V_p(K; A)$  the *A-perturbed Poisson space*. Note that the chain rule gives

$$\operatorname{div} A \nabla v = \Delta \tilde{v}$$

where  $\tilde{v} = v \circ L$  as before. Moreover, notice that  $f \in \mathbb{P}_p(K)$  if and only if  $f \circ L \in \mathbb{P}_p(L^{-1}K)$ , so

$$\operatorname{div} A \nabla v \in \mathbb{P}_{p-2}(K) \iff \Delta \tilde{v} \in \mathbb{P}_{p-2}(L^{-1}K)$$

and

$$v|_{\partial K} \in \mathbb{P}_p^*(\partial K) \iff \tilde{v}|_{\partial L^{-1}K} \in \mathbb{P}_p^*(\partial L^{-1}K) .$$

Combining these facts, we have that

$$v \in V_p(K; A) \iff v \circ L = \tilde{v} \in V_p(L^{-1}K) . \quad (\text{A.7})$$

These results suggest that  $V_p(K; A)$  is a computationally attractive space for solving the full weak form stated in (1.2). We conjecture that the approximation properties of  $V_p(K; A)$  are the same as those of  $V_p(K)$ , in the sense discussed in Chapter 3, up to a multiplicative constant depending only on  $A$ . Note that  $\|\cdot\|_{H^1(K)}$  and  $\|\cdot\|_{H^1(K;A)}$  defined by

$$\|v\|_{H^1(K;A)} := \left( \int_K \nabla v \cdot A \nabla v \, dx \right)^{1/2} \quad (\text{A.8})$$

are equivalent norms, due to the fact that  $\sqrt{x^\top x}$  and  $\sqrt{x^\top A x}$  are norms on the finite-dimensional vector space  $\mathbb{R}^d$ , and are therefore equivalent.

## Appendix B. Implementation

In Chapter 3, we saw numerical examples of implementing a finite element method on a curvilinear mesh of the unit square, attempting to solve the model problem

$$-\Delta u = 1 \text{ in } \Omega, \quad u = 0 \text{ on } \partial\Omega.$$

While we were pleased with the results, the MATLAB implementation used for those examples was far from a usable tool. In the years since that paper's publication, we have been developing the "PuncturedFEM" Python package, which is still a work-in-progress but is already more capable, efficient, and user-friendly. At the time of writing, it is capable of solving the more general problem

$$-a\Delta u + cu = f \text{ in } \Omega, \quad u = 0 \text{ on } \partial\Omega, \tag{B.1}$$

where  $a, c$  are constant scalars and  $f$  is a polynomial. Furthermore, the package is capable of handling more interesting meshes, such as the "Pac-Man" mesh seen in

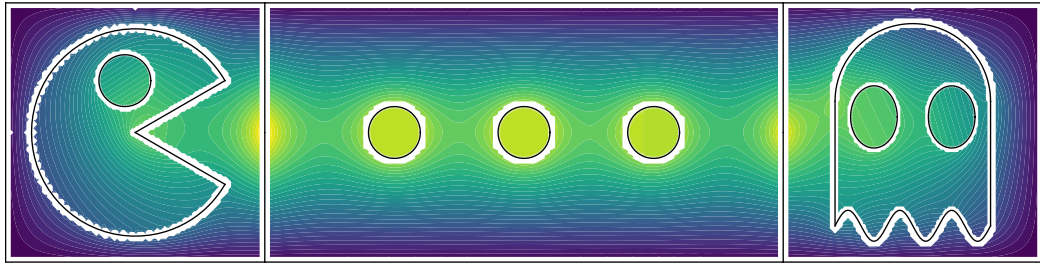


Figure B.1: An approximate solution to  $-\Delta u + u = 1$  on a rectangle with a zero Dirichlet boundary condition. The mesh consists of 11 cells, 5 of which are multiply connected, and all have curvilinear boundaries.

Figure B.1. The package can be installed with Python's package manager `pip` using the command

```
pip install puncturedfem
```

and the GitHub repository

```
https://github.com/samreynoldsmath/PuncturedFEM
```

contains some numerical examples in addition to the source code.